December 2012

Investigation of Heat Transfer and Flow Using Ribs Within Gas Turbine Blade Cooling Passage: Experimental and Hybrid Les/rans Modeling

Sourabh Kumar
University of Wisconsin-Milwaukee

INVESTIGATION OF HEAT TRANSFER AND FLOW USING RIBS WITHIN GAS TURBINE BLADE COOLING PASSAGE: EXPERIMENTAL AND HYBRID LES/RANS MODELING

By

Sourabh Kumar

A Dissertation Submitted in

Partial Fulfillment of the

Requirements for the Degree of

Doctor of Philosophy

In Engineering

at

The University of Wisconsin-Milwaukee

December 2012

ABSTRACT

INVESTIGATION OF HEAT TRANSFER AND FLOW USING RIBS WITHIN GAS TURBINE BLADE COOLING PASSAGE: EXPERIMENTAL AND HYBRID LES/RANS MODELING

By

Sourabh Kumar

The University of Wisconsin-Milwaukee, 2012
Under the supervision of Dr Ryo S. Amano

Gas turbines are extensively used for aircraft propulsion, land based power generation and various industrial applications. Developments in innovative gas turbine cooling technology enhance the efficiency and power output, with an increase in turbine rotor inlet temperatures. These advancements of turbine cooling have allowed engine design to exceed normal material temperature limits. For internal cooling design, techniques for heat extraction from the surfaces exposed to hot stream are based on the increase of heat transfer areas and on promotion of turbulence of the cooling flow. In this study, it is obtained by casting repeated continuous V and broken V shaped ribs on one side of the two pass square channel into the core of blade. Despite extensive research on ribs, only few papers have validated the numerical data with experimental results in two pass channel. In the present study, detailed experimental investigation is carried out for two pass square channels with 180^{o} turn. Detailed heat transfer distribution occurring in the ribbed passage is reported for steady state experiment. Four different combinations of 60^{o}

V and Broken 60^{o} V ribs in channel are considered. Thermocouples are used to obtain the temperature on the channel surface and local heat transfer coefficients are obtained for various Reynolds numbers, within the turbulent flow regime. Area averaged data are calculated in order to compare the overall performance of the tested ribbed surface and to evaluate the degree of heat transfer enhancement induced by the ribs with. Flow within the channels is characterized by heat transfer enhancing ribs, bends, rotation and buoyancy effects. Computational Fluid Dynamics (CFD) simulations were carried out for the same geometries using different turbulence models such as *k*-ω Shear stress transport (SST) and Reynolds stress model (RSM). These CFD simulations were based on advanced computing in order to improve the accuracy of three dimensional metal temperature prediction which can be applied routinely in the design stage of turbine cooled vanes and blades.

This study presents an attempt to collect information about Nusselt number inside the ribbed duct and a series of measurement is performed in steady state eliminating the error sources inherently connected with transient method. A Large Eddy Simulation (LES) is carried out on the best V and Broken V rib arrangements to analyze the flow pattern inside the channel. A novel method is devised to analyze the results obtained from CFD simulation. Hybrid LES/Reynolds Averaged Navier Strokes (RANS) modeling is used to modify Reynolds stresses using Algebraic Stress Model (ASM).

TABLE OF CONTENTS

LIST OF FIGURES

LIST OF TABLES

LIST OF ABBREVIATIONS

ASM Algebraic Stress Model

AC Alternating Current

CFD Computational Fluid Dynamics

CFM Cubic feet per Minute

CPU Central Processing Unit

DNS Direct Numerical Simulation

LES Large Eddy Simulation

MB Mega Byte

NiCr Nickel-Chromium

RSM Reynolds Stress Model

SST Shear Stress Transport

TBC Thermal Barrier Coating

URANS Unsteady Reynolds Average Navier Strokes

WALE Wall Adapting Local Eddy Viscosity

LIST OF SYMBOLS

A	Wall surface area
A_{gas}	Surface Area of gas flow
AR	Channel Aspect ratio
b	Channel divider wall thickness
c_p	Specific heat at constant pressure
$C_{\emptyset 1}$	Pressure strain Coefficient = 2.3
$C_{\emptyset 2}$	Pressure strain Coefficient = 0.4
d	Distance to the closest wall
D	Channel width
D_H	Hydraulic diameter
D_ω	Cross diffusivity term
e	Rib height
E	exponent
^oF	Fahrenheit
g	Acceleration due to gravity
$\overline{g}_{ij}$	Gradient velocity tensor
$\tilde{G}_K$	Generation of turbulence kinetic energy due to mean velocity gradients
G_w	Generation of ω
h	Heat transfer coefficient
H_{gas}	Enthalpy of Gas

H	Height of the channel
I	Current
in^2	Inch square
k	Turbulence kinetic Energy
k'	Von karman constant
k_p	Turbulence kinetic Energy at node P
k_T	Fluid thermal conductivity
K	Kelvin
l_t	Test section length
L	Channel Length
L_S	Mixing length for subgrid scales
$\dot{m}$	Mass Flow Rate
Nu	Nusselt number
Nu_o	Theoretical Nusselt Number
p	Pressure
$\bar{p}$	Resolvable scale pressure
p''	Sub grid scale pressure
P	Rib Pitch
P_{ij}	Reynolds Stress Production Term
P_k	Rate of production of kinetic energy
Pr	Prandtl number = 0.71
Pr_T	Turbulent Prandtl Number for Temperature =0.9

q_{w}	Wall heat flux
Q_{el}	Electrical Heat Supplied
Q''_{el}	Electrical Heat Flux
Q''_{con}	Conduction Heat Flux
Q''_{dis}	Dissipated Heat Flux
Q''_{net}	Net Heat Flux
Re	Reynolds number, $Re=\rho U_{in} D_{\mathrm{h}}/\mu$
Re_{D}	Reynolds number based on Hydraulic Diameter
$\overline{S_{ij}}$	Rate of strain tensor
S_K	User defined source term
S_ω	User defined source term
T_w	Wall Temperature
T	Temperature
T_a	Atmospheric Temperature
T_b	Compressor exit temperature
T_c	Turbine Inlet Temperature
T_d	Turbine outlet Temperature
T_s	Temperature surface across the channel
T_{bx}	Temperature bulk across the channel length
T_{gas}	Firing temperature for blade
$T_{bulk\ metal}$	Average metal temperature

$T_{coolant\ supply}$	Temperature of coolant entering the airfoil
u	Fluctuating velocity in x direction
u_i, u_j, u_j	Velocity in *i, j, k* direction
$\bar{u}_1$	Resolvable scale velocity
u_i''	Sub grid scale velocity
$\overline{u'_i u'_J}$	Reynolds Stress
U_p	Velocity at node p
U_{in}	Mean Inlet Velocity
v	Fluctuating velocity in y direction
V	Volume of computational cell
w	Fluctuating velocity in z direction
W	Channel Width
x_i , x_j, x_k	Spatial Coordinate
Y_K	Dissipation of *k* due to turbulence
Y_ω	Dissipation of ω due to turbulence

Greek symbols

α	Rib Angle
Γ_k	Effective diffusivity of *k*
Γ_ω	Effective diffusivity of ω

δ_{ij}	Kronecker delta
∂	Derivative
ε	Rate of Dissipation of turbulent kinetic Energy
$\vec{\varepsilon}$	Spatial filtering
ε_{jkm}	Alternating Tensor
η_{ther}	Thermal Efficiency
θ	Temperature
$\mathbf{\Lambda}$	$\mathbf{\Lambda}$ Function
μ	Dynamic viscosity
μ_t	Subgrid scale turbulent viscosity
v	Kinematic viscosity
ρ	Fluid density
σ	Prandtl number
σ_T	Turbulent Prandtl number
τ_w	Wall shear stress
$\tau_{ij}{}^{r}$	Residual stress tensor
τ_{kk}	Subgrid scale stresses
ω	Specific Dissipation
Ω, R	Resistance

Ω_k	Angular Velocity

Subscript

i,j,k,l,m	tensor notation

ACKNOWLEDGEMENTS

I would like to express my deep appreciation and gratitude to my advisor, Dr R.S Amano for his patient guidance and mentorship, all the way from my start of PhD program to the completion of degree. I am truly fortunate to have the opportunity to work with him. He has been very supportive throughout the project and had helped me continuously, suggesting improvements related to this manuscript. I would like thank the entire committee member for their support and help over the years. I would like to express my sincere regards and thanks to all the professors in Department of Mechanical Engineering at University of Wisconsin-Milwaukee for constantly and passionately guiding and helping me to complete my effort.

I would like to express my thanks and gratitude to all those who provided help and encouragement along this journey. To my parents and friends who have been the vehicle that has guided and encouraged me in each and every aspect of my life.

Finally, I would like to thank my wife, Pankhuree for providing the encouragement and unconditional support I needed to complete this effort.

CHAPTER 1: INTRODUCTION

Gas turbines play a vital role in today's industrial environment. As the demand for power and energy increases, improvement in power output and thermal efficiency of gas turbine is essential, this can be achieved by efficient cooling methods. The cooling of gas turbine components using internal convective flow of a single phase gas has been used for last 50 years; from simple smooth cooling passage to very complex geometries involving many different surfaces, architectures and fluid-surface interaction. The main goal is to obtain high overall cooling effectiveness with lowest possible penalty on thermodynamic performance cycle. An advanced gas turbine engine operates at a high temperature of 1500^{o} C to improve thermal efficiency and power output. This high temperature at rotor blade can exceed the melting temperature of the metal. It is mandatory for the blades and vanes to be cooled so that they withstand these high temperatures. 20% to 30% of the compressed air at 650^{o} C is extracted from the compressor and passed through the high pressure turbine. With cool compressed air, the blade temperature can be lowered to approximately 1000^{o} C, which is needed for safe operation of the engine. For these high temperature turbine blades, cooling methods require key and innovative technologies. The metal temperature of the turbine cooled vanes and blades should be predicted in design stages as accurately as possible, to reduce the period of product development cycle and to accurately predict the life of blades and vanes; as these are dependent on the metal temperature. The life of turbine blades is dependent upon accurate mapping of blade surface temperature, local heat transfer coefficients and prevention of local hot spots. Figure 1.1 shows the cross sectional view of the turbine vane and blade. Complex flow around the vanes and blades makes prediction of metal temperature difficult. The trend of

heat flux is similar in both vane and blade, on suction side the flow transition from laminar to turbulent increases the heat transfer coefficient flux. Similar change occurs on the pressure side.

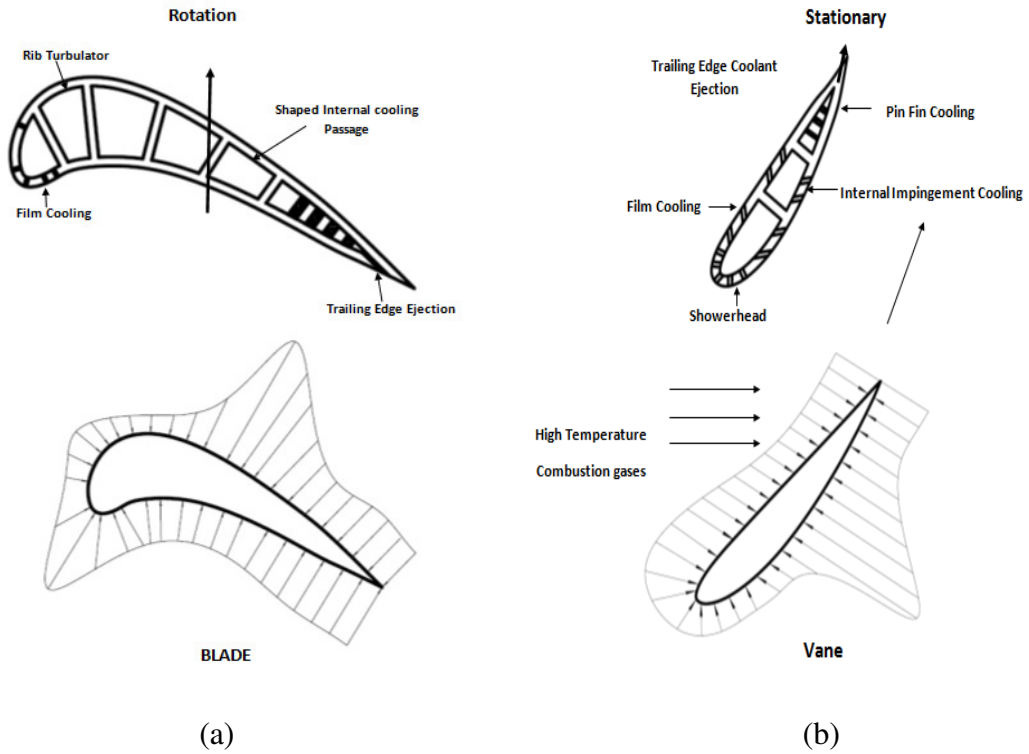

Figure 1.1: Cross sectional view and heat flux distribution of (a) vane and (b) blade.

Due to high velocity and complex flow around the gas turbine, it is important to obtain data that will help in designing efficient cooling technologies. Detailed hot gas path heat transfer distribution and film cooling data are needed for airfoil. A stator vane surface heat transfer is affected by combustor developed high turbulence, laminar to turbulent transition, acceleration, film cooling flow, platform secondary flow and surface roughness. These factors as well as the rotational, centrifugal forces and blade tip clearance and leakage must be considered in the rotating blades. After the hot spots on

the turbine and vanes are known, the vane and blade cooling performance can be improved by new and innovative heat transfer data. It is also essential to understand the flow physics and to improve the current internal cooling design. Many techniques have been developed to enhance the heat transfer in these passages. Near the leading edge of the blade, jet impingement (coupled with film cooling) is one such technique. The cooling passage located in the middle of the airfoil is often used with rib turbulator while pin fins and dimples can be used in the trailing edge portion of the vanes and blades. A number of traditional cooling concepts are used in various combinations to adequately cool the turbine vanes and blades.

Testing allows experimenters to measure the temperature contours and pressure variation. Periodic ribs are frequently employed in various ducts to enhance the heat transfer process for many applications including gas turbine cooling systems and compact heat exchangers. These arrangements of ribs have important influence on the thermal and hydraulic performances of these ducts. Due to favorable longitudinal secondary flow, angled ribs are more favorable than perpendicular ribs when both heat transfer and pressure drop are concerned. In this study, the ribs being used are 60^{o} continuous V rib and 60^{o} broken V rib in various combinations. In addition to the experimental results, effort has been made to address the numerical simulation of these ribs so that they can be used effectively. Additionally, the comparisons of Computational Fluid Dynamics (CFD) results with experimental results are useful for the prediction of blade temperature and can be applied routinely in design stage. In this work, the average heat transfer coefficient in square channel of aspect ratio (AR) of 1 is used. The pitch to rib height

(P/e) is considered to be 10. Reynolds Numbers considered for this experiment are in the turbulent region. This experiment is done in steady state.

CHAPTER 2: BACKGROUND AND LITERATURE REVIEW ON GAS TURBINE COOLING

2.1 Gas Turbine:

Gas turbine is used extensively in many areas including air craft propulsions, land based power generation and industrial applications. The main advantages of a gas turbine are exceptional reliability, high thrust to weight ratio, and relative freedom from vibration. Gas turbine, also called a combustion turbine, is a rotary engine that extracts energy from a flow of combustion gases. It has an upstream compressor coupled with a downstream turbine, and a combustion chamber in-between. Gas turbine may also refer to just the turbine component. The turbine consists of the following main parts: an inlet, a compressor, a combustor, a turbine and an exhaust.

There are three primary modules in a gas turbine

• Compressor module

In this module, the pressure of air is increased in several stages. The rotation of the compressor increases the velocity of the air and diffusers converts dynamic pressure to the static pressure. The compressor is connected to the turbine through a shaft running through the center of the engine.

• Combustion module

The operation of a gas turbine is based on the principle that the power gained from the turbine exceeds the power absorbed by the compressor. This is achieved by the addition of energy in the combustor by igniting fuel in special purpose burners.

• Turbine module

The highly energetic gas from the combustor is expanded through a turbine to achieve high power output.

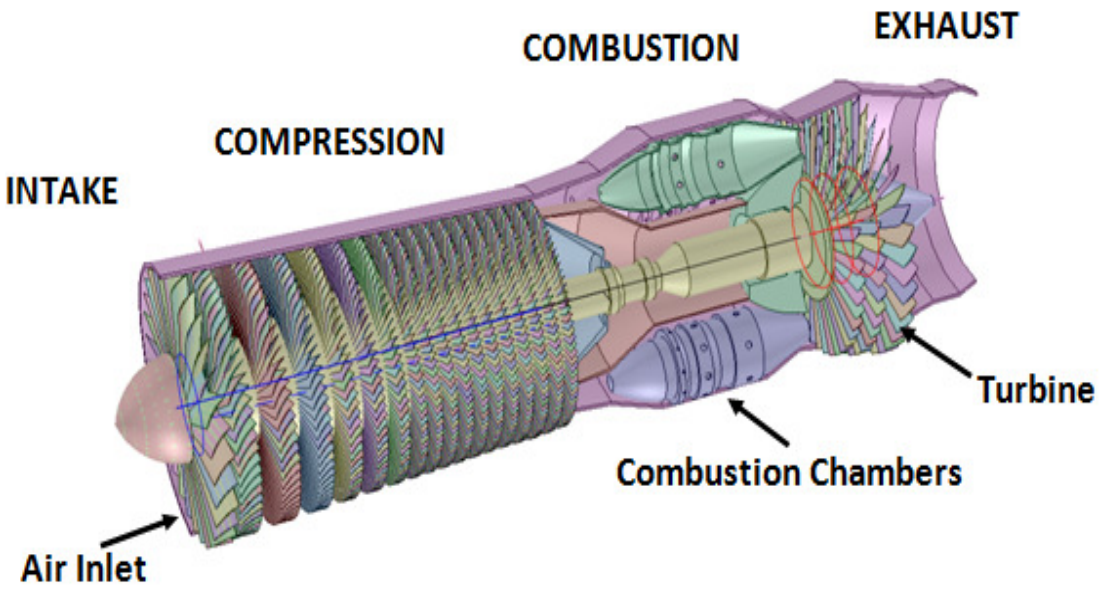

Figure 2.1: Gas turbine Jet Engine

There are multiple causes for gas turbine blade failure. Some of the important reasons are listed below.

1. High temperatures: High temperature causes increased blade temperature and higher temperature gradients, both of which can have a detrimental impact on service life. High temperatures are the main causes of creep and corrosion failure.

2. High stresses in the turbine blades causes centrifugal force and fluid forces which causes fracture, yielding and creep failure.

3. High vibration in the turbine section cause fatigue failure.

2.2 Efficiency of Gas Turbine:

The gas turbine industry is trying to reach both higher turbine temperature as well as increased pressure ratio, both of which will lead to improved efficiency and effectiveness of the engines. Ideal Brayton cycle efficiency is calculated based on Eq. (2.1).

$$\eta_{ther} = 1 - \frac{T_a}{T_b} \tag{2.1}$$

The condition for maximum work in Brayton cycle is different than that for maximum efficiency. Maximum power for ideal Brayton cycle is determined using Eq. (2.2) [1]

$$Power = \dot{m} c_p T_a \left[\frac{T_C}{T_a} - 2\sqrt{\frac{T_C}{T_a}} + 1\right] \tag{2.2}$$

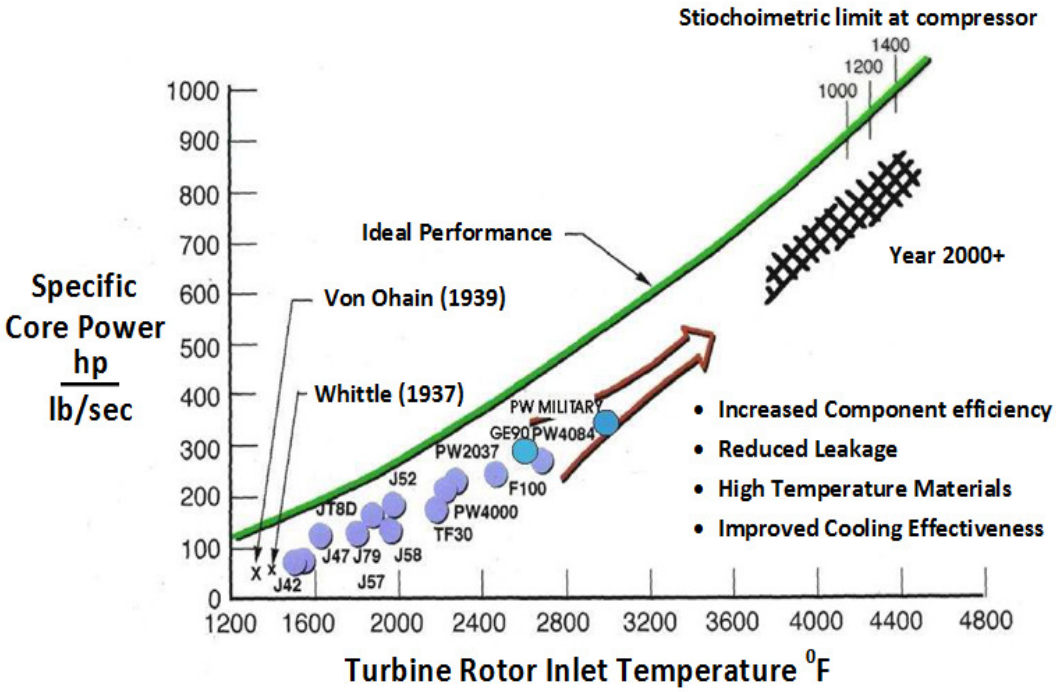

Figure 2.2: Specific core power with turbine rotor inlet temperature
Reference: http://mit.edu/16.unified/www/FALL/thermodynamics/notes/node28.html

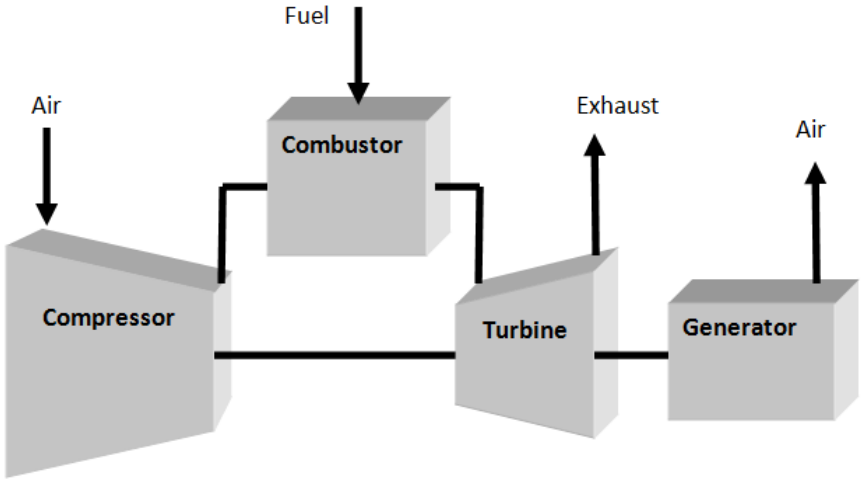

(a)

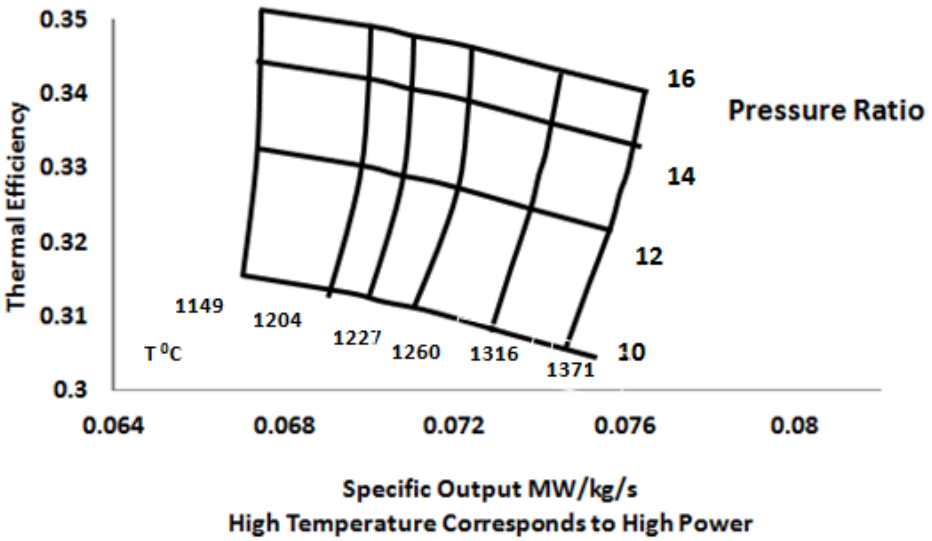

(b)

Figure 2.3: Brayton Cycle (a) and thermal efficiency (b) of gas turbine

Figures 2.2 and 2.3 show that with higher turbine inlet temperature, the power output can be greatly improved. In Fig. 2.2, J42, J47, J79 etc. are the engine names developed by

Pratt & Whitney and GE. The desire for better performance and improved efficiency will continue the trend towards higher inlet temperature. In turn, high turbine inlet temperature provides a challenging environment for the turbine blades, which are subject to a variety of damage mechanisms. Thus, engine design must strike a balance between thermodynamic performance and component life. Based on different aspects of turbine blade designs methods are devised to improve the efficiency and power. Some of the methods are listed below.

Methods Employed

1. 25% compressor gas utilization.

   With an increase of the temperature, about 25% of compressor gas is used as a coolant for the blade.

2. Improvements in blade materials--alloys.

   A limiting factor in jet engines was the materials used but better materials like nickel based alloy and new manufacturing techniques have ameliorated this problem.

3. Use of Combined Cycle to achieve a good efficiency.

   In case of stationary power plants, combining two or more thermodynamic cycles improves overall efficiency.

4. Improvements in blade cooling technology.

   Different innovative cooling technologies developed like internal cooling, film cooling etc has vastly improved the tolerance level of blade materials.

5. Thermal Barrier Coating.

TBCs improve corrosion and oxidation resistance, both of which become greater concerns as temperatures increase.

As this study is based on improvements in blade cooling technologies, I have discussed these in detain in the following sections.

2.3 Cooling Technology Design:

Cooling technologies used in gas turbine vanes and blades are mainly composed of five main elements [1].

1. Internal convective cooling
2. External surface film cooling
3. Material
4. Thermal Mechanical design
5. Selection and pretreatment of the coolant fluid.

Internal convective cooling is the method of directing coolant to the regions of the components requiring cooling and in turn increasing the heat transfer coefficient. The internal cooling which is main basis of this study will be discussed in detail in the next segment. Film cooling is bleeding internal cooling flow into the exterior skin of the components to provide heat flux reducing cooling layer. Film cooling is tied to internal cooling techniques. Different methods of film cooling can be seen in Fig. 2.4. Materials used are high temperature, high strength nickel or cobalt based super alloy coated with yttria-stabilized zirconia oxide ceramics (thermal barrier coating, TBC). This protective ceramic coating is used to actively enhance the cooling capability of internal cooling techniques. Thermal stresses, coating strains, oxidation limits, creep rupture properties

and aero mechanical response are important factors for thermal mechanical design. The bleed air from the compressor functions as the cooling fluid. The main constraints of turbine blade design are pressure losses, material temperature, component stresses, geometry and volume, aerodynamics, fouling and coolant conditions.

Cooling design analysis can be studied in stages as shown in Fig. 2.5.

Level 1 is the preliminary design concept of the components which are based on nominal target conditions excluding the surrounding environment. Component design includes several depths of analyses, from 1D estimate, to detailed 2D analyses, to complete 3D computational predictions.

Level 2 cooling analysis is a more detailed inclusion of surrounding effect and constraints from aerodynamics, material properties, mechanical loading, lifting limitations and clearance. This level is involves thermo-mechanical analysis performed at both steady state and full load conditions.

Level 3 analysis brings in operational transient aspects.

Level 0 is the preliminary design and primarily deals with the efficiency, cost of electricity, power sizing and number of start. It mainly deals with coolant consumption, turbine airfoil life and inspection intervals.

As the main objective of this research is to study Level 0 and Level 1 design strategies, more emphasis will be given on parameters involved in these stages.

Level 0: Preliminary Cooling Design Analysis

Cooling analysis at this is simply looking projected coolant flow rates based on design goals. Temperatures may be altered by various cycle combinations, surface area by overall power requirements or aerodynamics, coolant specific heat by selecting coolant

fluid, airfoil temperatures by cooling mass flow rate; these affect efficiency, emission, life and cost.

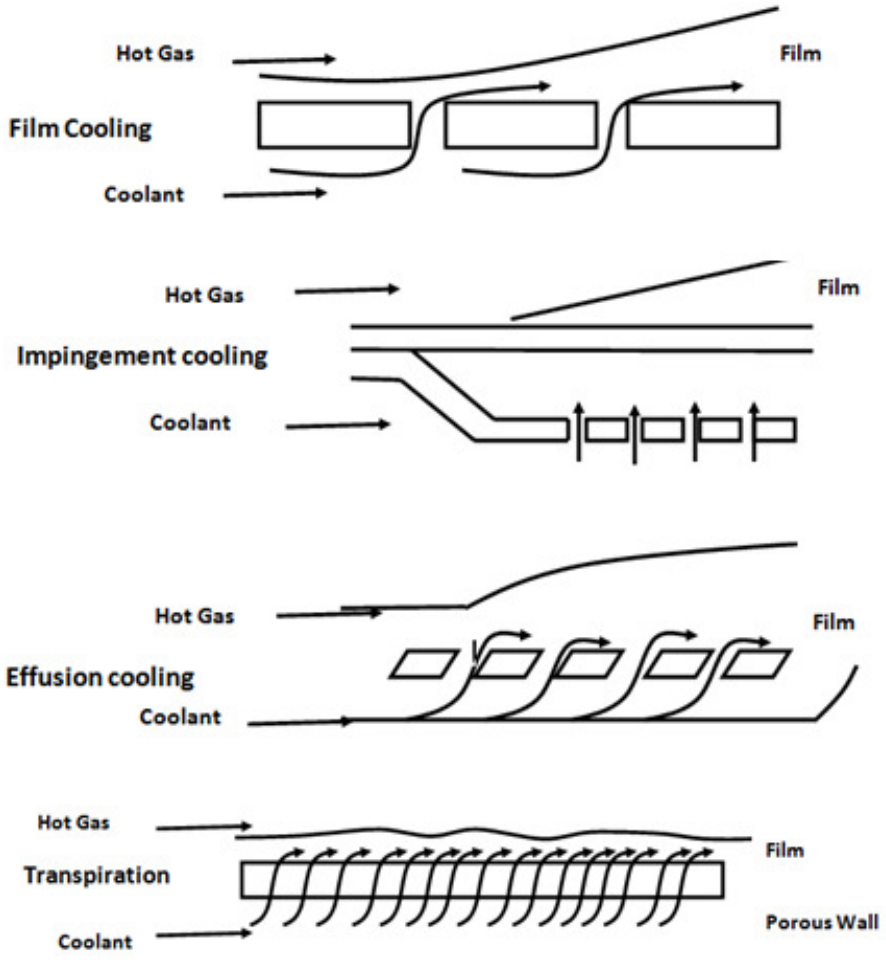

Figure 2.4: Different cooling Technology

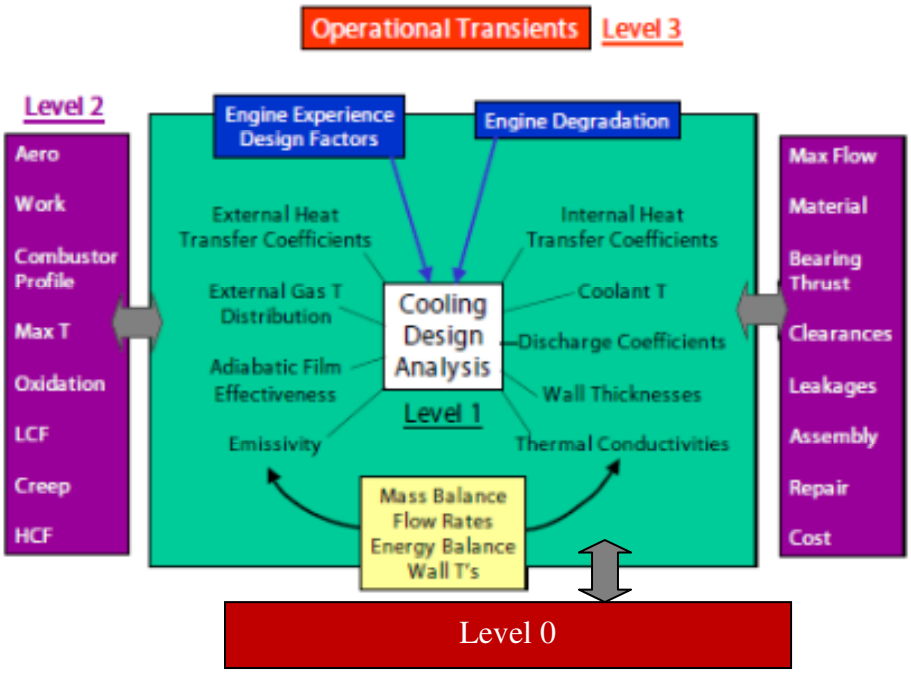

Figure 2.5: Cooling design Analysis system [1]

Cooling technology performance chart provides basis for performance characteristic of cooling technologies which can be seen in Fig. 2.6.

$$Gross\ cooling\ effectiveness = \frac{(T_{gas} - T_{bulk\ metal})}{(T_{gas} - T_{coolant\ supply})} \tag{2.3}$$

$$Heat\ loading\ parameter = \frac{(m_{coolant} * c_{p\ coolant})}{(2 * H_{gas} * A_{gas})} \tag{2.4}$$

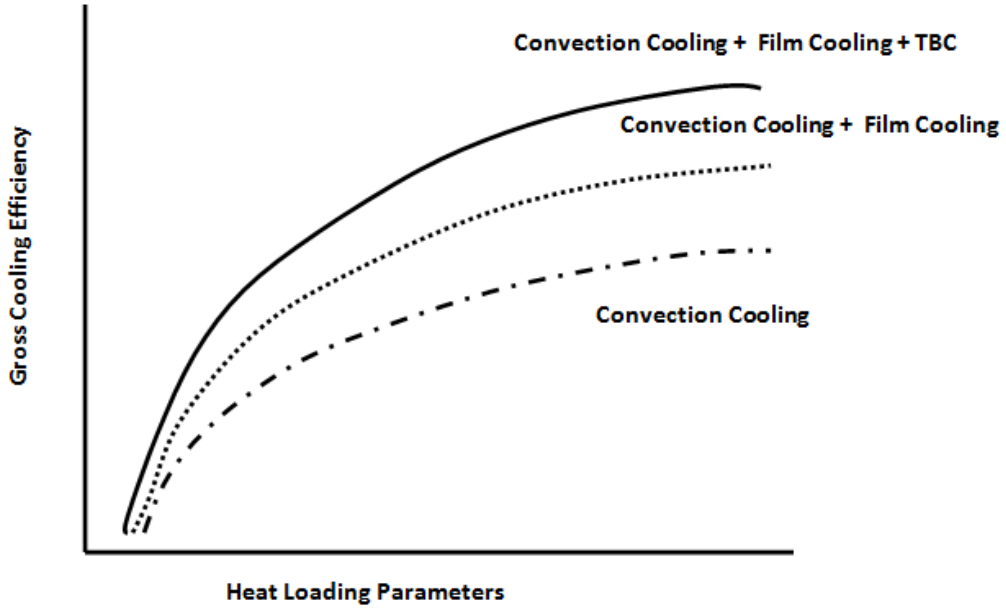

Figure 2.6: Cooling technology performance chart [1]

Level 1: Conceptual Cooling Design Analysis

Component design can be started with preliminary design, extended to 2D analysis and to 3D computational prediction. Preliminary design uses mostly bulk quantities and one dimensional simplified equation to reach meaningful estimations of temperature and flow requirements. 2D analysis incorporates boundary layer analysis, network flow and energy balance and some thermal gradients to estimate the local temperature and flow prediction. Three dimensional analyses may use complete CFD (Computational Fluid Dynamics) and heat transfer models to obtain detailed predictions of local thermal effects and flow losses.

This work is based on a detailed analysis of Level 1 3D, which is done mainly for internal cooling of blades with 60^{o} V continuous and 60^{o} broken V rib turbulators. The next

section demonstrates a detailed study of internal cooling of turbine blades with emphasis on the mid section cooling which is the main objective.

2.4 Internal Cooling Technologies:

A number of traditional internal cooling concepts have been used in blades and vanes. This section will briefly describe the developments done through the years; with more emphasis on internal cooling of rib turbulated cooling. The experimental and computational efforts made on cooling are discussed in this section. Figure 2.7 shows how the turbine entry temperatures have been improved by the introduction of various cooling technologies during the past several years. Figure 2.7 clearly depicts that with passage of time; new improved cooling technologies are developed along with new materials.

Enhanced internal cooling of turbine Vanes:

Figure 2.8 shows that the turbine vane is hollow and coolant air from the compressor is extracted for impingement and pin fin cooling. The leading edge is cooled using jet impingement techniques while the trailing edge is cooled using pin fins.

Impingement Cooling: This section describes the internal cooling of turbine vanes. Impingement cooling is suitable for the leading edge of the airfoil because of thick blade wall in this area as well as high heat loads. Various factors such as jet hole size & distribution, cooling channel cross section and target surface shape should be considered for cooling channel heat transfer distribution.

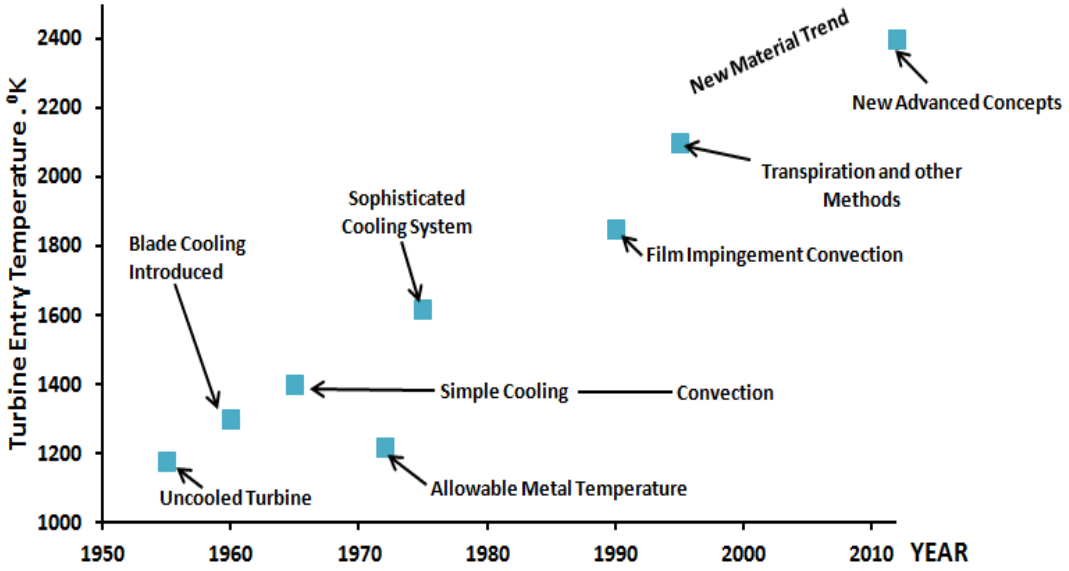

Figure 2.7: Development of cooling technology in gas turbine blade

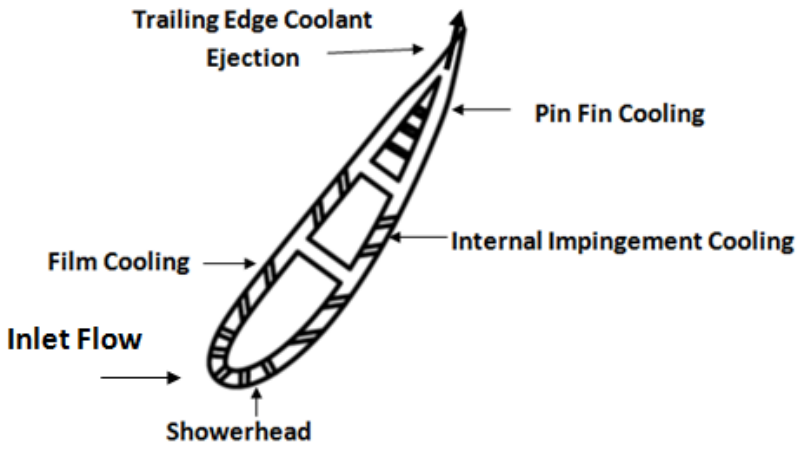

Figure 2.8: Turbine Vane cross-section with impingement and trailing edge pin-fin cooling

a) Jet Impingement from Multiple Jets

Metzger et al [2] showed that multiple jets perform differently from a single jet striking. They concluded that Nusselt number is dependent on Reynolds number and has no

dependence on jet to target spacing. Florschuetz et al. [3] & Koopman et al. [4] showed that one jet can alter the performance of others. To estimate the heat transfer enhancement from an array of impinging jets, correlations based on experimental data were developed by Kercher et al. [5] and Florschuetz et al. [6].

b) Jet Impingement on a Curved Surface

Near the leading edge of the airfoil curvature of target surface creates different cross flow behavior. Chupp et al. [7] studied and concluded that Nusselt Number ratio increases as the curvature of target plate increases. Bunker et al. [8] concluded that sharper nose radius yielded more uniform Nusselt number distribution compared to smooth-nosed chamber. In addition if the bleed from the pressure and suction are equal greatest reduction in Nusselt number occurs.

Pin Fin Cooling: Pin fins are at the trailing edge due to the narrowness of the area at this end. An array of pins is used and when coolant flows past the pins, the flow separates, wakes are shed and horseshoe vortex formed upstream. These flow patterns create additional mixing and in turn increases the heat transfer coefficient. There are various factors to be considered while designing these pin fins.

a) Pin array arrangement

There are two commonly used array arrangement of the pin fins: inline and staggered array. Metzger et al. [10] used staggered array of circular pins which is a closer spaced array. A closer spaced array shows a higher heat transfer coefficient and also increases the pressure drop. Chyu et al [11] showed that heat transfer coefficient is high for both arrays. Experimental results by Metzger et al. [10] and Van Fossen [12] predicted Nusselt Number. The surface containing pins is not affected by the pin tip clearance. Whereas the

opposite surface, that does not have pins, shows a decrease in heat transfer coefficient with an increase in the pin tip clearance. The friction factor is lower for partial pins compared to full-length pins. In general, the heat transfer coefficient decreases with partial length pins.

b) Effect of Flow Convergence and Turning

The flow channel in the trailing edge of an airfoil has a reducing cross section where flow accelerates resulting in increase in heat transfer coefficient [13].

c) Pin-Fin Cooling With Ejection

Trailing edge pin fin channel has ejection holes. Kumran et al. [14] investigated the effect of length of these coolant ejection holes on the heat transfer coefficient. Higher coolant ejection reduces the Nusselt number significantly.

Dimple Cooling: Dimpled cooling is used as alternative to pin fin cooling because of moderate heat transfer and low pressure loss penalty. The dimple size, dimple depth, distribution, shapes (cylindrical, hemispheric, teardrop) each effect the heat transfer distribution. There is no dependence on Reynolds number and channel aspect ratio [15-19].

Enhanced Internal cooling of Turbine Blade

There are three major cooling zones. The leading edge is cooled by jet impingement, pin fin with ejection is used near the trailing edge and the middle portion is cooled by serpentine rib roughened coolant passage. Although the techniques used to cool the blades are similar to those used to cool vanes, there are some difference in the heat transfer trends because of rotation.

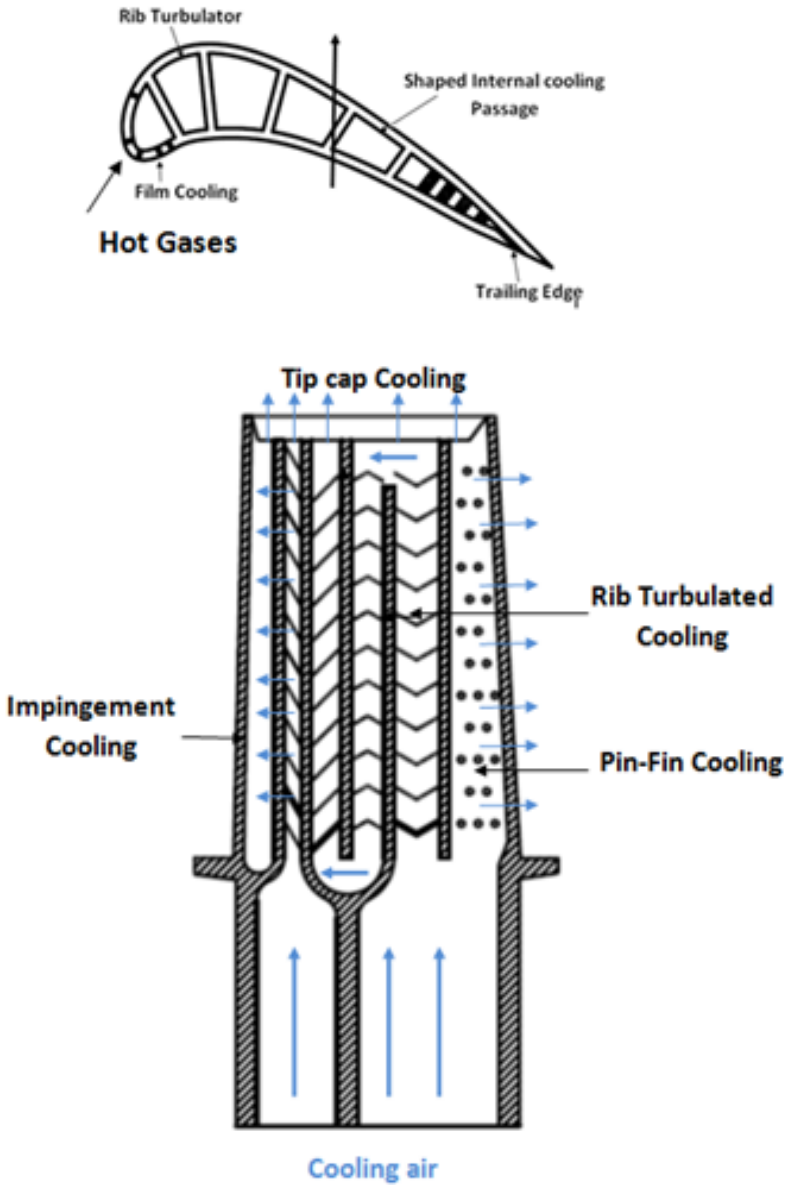

(a) Schematic of a Modern Gas Turbine Blade with Common Cooling Techniques

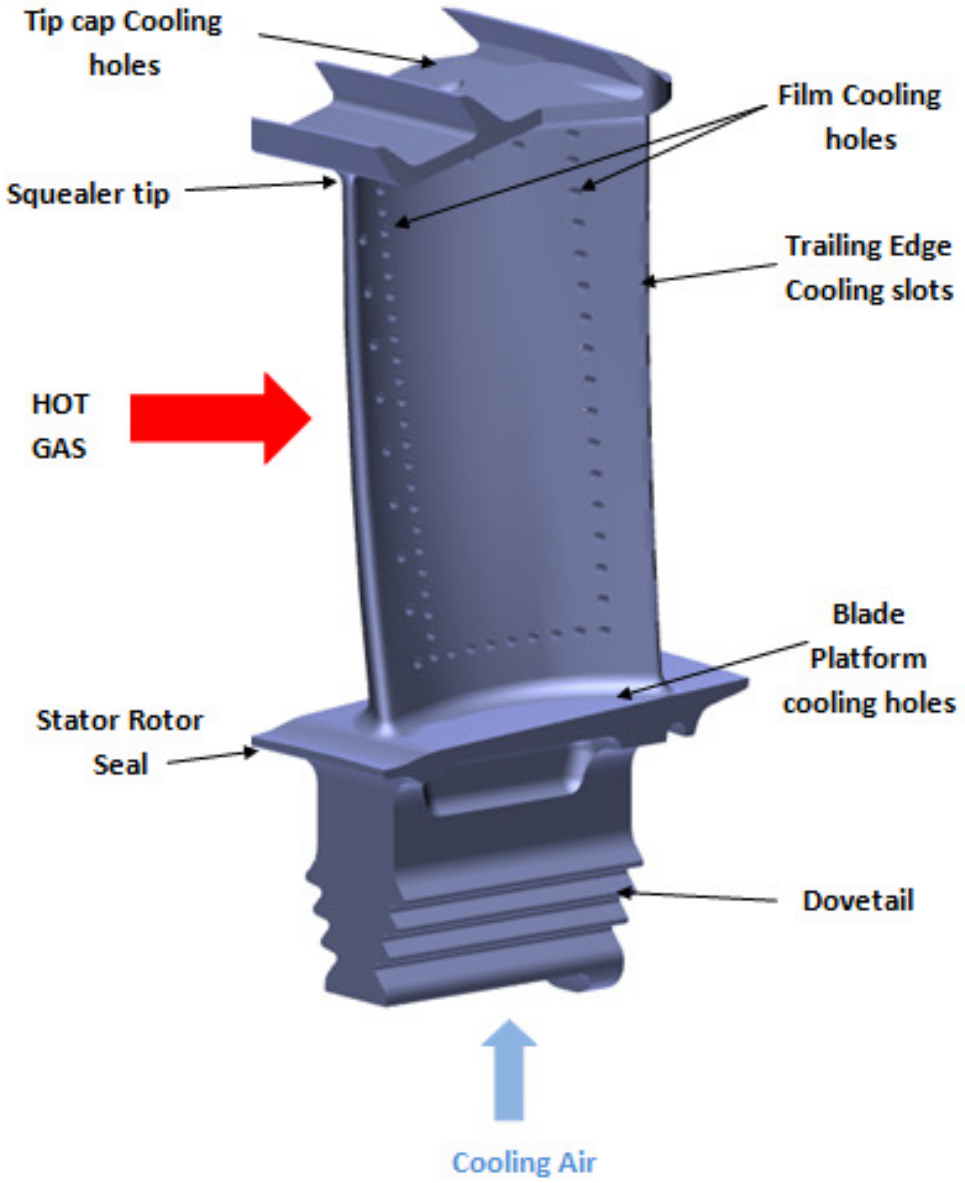

(b) Modern Gas Turbine Blade

Figure 2.9: Airfoil cooling schemes for High pressure turbine

Figure 2.9 shows the cooling schemes for high pressure turbine on all the sections of the air foil. Since main focus of this study is the rib roughened cooling of the turbine blade a detailed literature survey on the same is essential. Turbulators in the form of trip strips

placed transverse to the bulk flow directions were one of the major improvements made to cooling channels and hence many investigations were done into the heat transfer and friction characteristics. Most of the research which resulted in widely used data and correlation were carried by Webb et al. [20], Burggraf [21] and Han et al. [22].

In advanced gas turbine blades, repeated rib turbulators are used on the two opposite walls of the internal cooling passage to enhance heat transfer. Thermal energy is transferred from external pressure and suction surface of turbine blades to the inner zones, and the heat is extracted by internal cooling. The internal cooling passages are mostly modeled as short square or rectangular channels with various aspect ratios. The heat transfer augmentation in rectangular coolant passages with rib turbulators primarily depends on channel aspect ratio, rib turbulator geometry, (such as rib size, shape, distribution, flow-attack angle) and flow Reynolds number. Many fundamental studies have been conducted to understand the coolant flow through a stationary ribbed channel. Rib turbulators disturb only the near wall flow for heat transfer enhancement. Therefore, the pressure drop penalty caused by rib turbulators is affordable in blade internal cooling design. There have been basic studies by Han et al to understand the heat transfer augmentation verses the pressure drop penalty by flow separation caused by rib turbulator [23-26].

Figure 2.10 shows symmetric and staggered rib arrangement in opposite walls of a cooling channel which was investigated by Han et al [1]. This research used symmetric and staggered ribs to show the effect on heat transfer. Figure 2.11 shows schematic of flow separation from ribs reattach on the floors between ribs thus increasing the heat transfer coefficients of the ribs and the floors. Reattachment following separation causes

boundary layer to reattach to channel wall. This thinner, reattached boundary layer increases the heat transfer coefficient.

The flow in a ribbed channel can be divided in two parts, main core flow and near wall flow. The flow phenomenon near the wall can be seen in Fig. 2.12. The structure is dependent upon the geometrical ration of *p/e* [1].

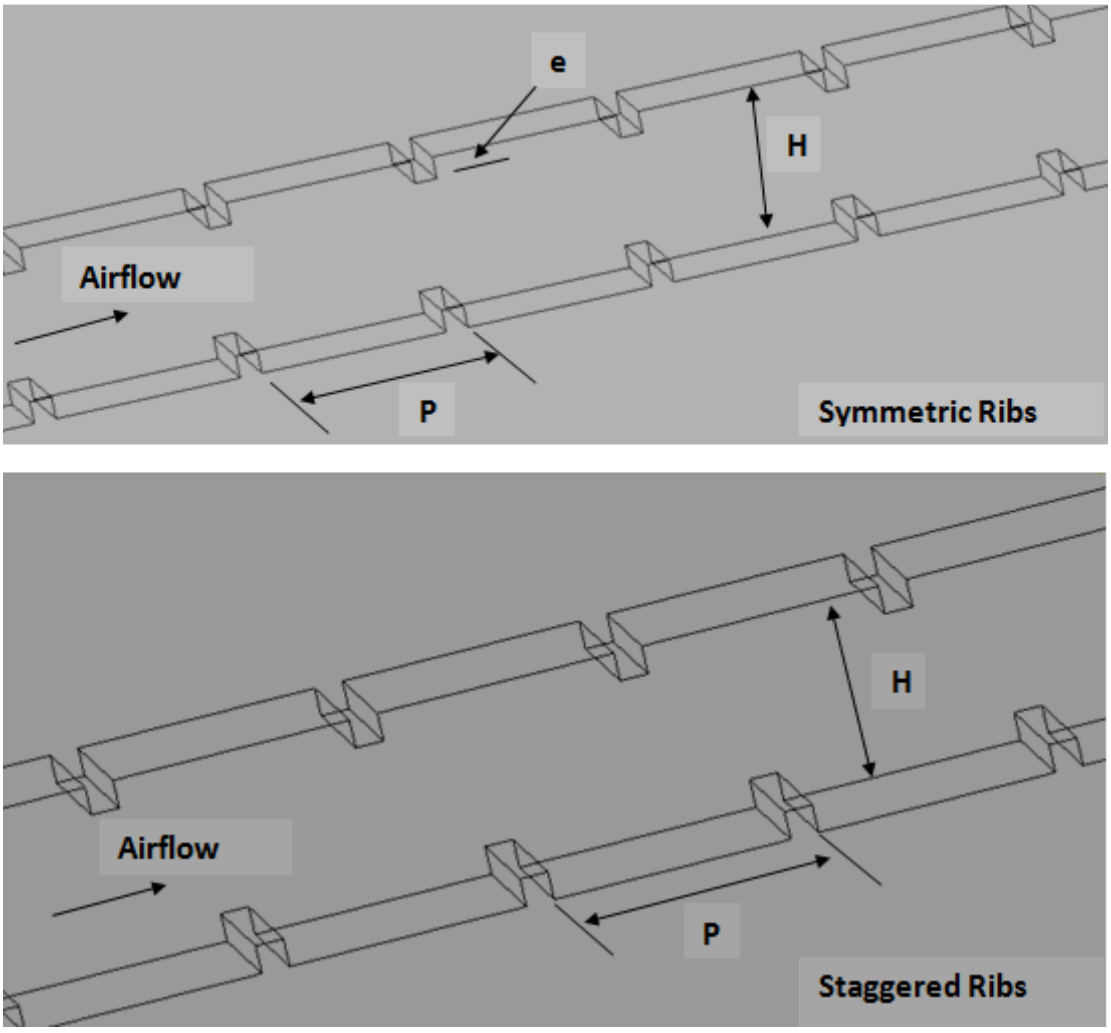

Figure 2.10: Symmetric and staggered ribs arranged on opposite wall of coolant passage.

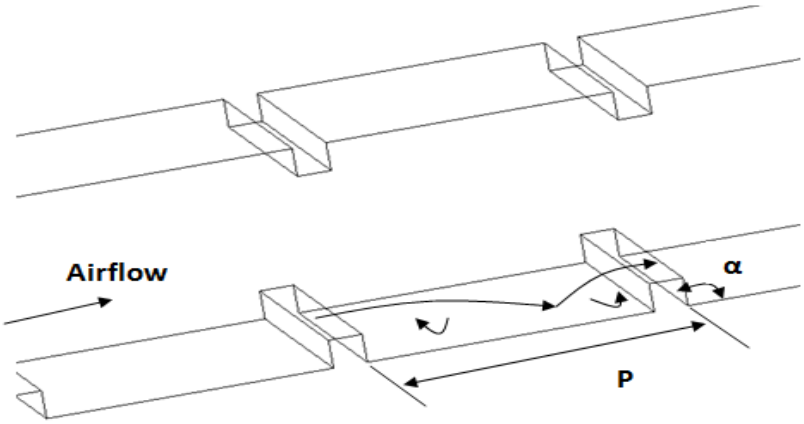

Figure 2.11: Flow separation from ribs and secondary flow between angled ribs in cooling channel

Three different separated flow regions can be observed, a) In front of the rib, a separated recirculation zone exists; b) on top of each rib a separation bubble forms due to upstream facing step; c) behind the rib, a separated recirculation region exists which can extend up to 7 rib height downstream, before flow reattaches. Fig. 2.11 shows the flow effect of separation and reattachment due to the presence of ribs. As p/e=10, there is no flow separation on the rib and recirculation and reattachment occurs downstream and upstream of the flow which makes the ratio optimum. However the Reynolds number effect cannot be ruled out for the flow. The core flow develops rapidly in a ribbed channel compared to a smooth one. The presence of the ribs increases turbulence and induces secondary flow that tends to move fluid from the main core towards the walls. However the airfoil being used now-a-days have complicated shapes and smaller gas turbines have high blockage ribs at closer spacing.

Due to curved asymmetrical shape of the turbine blades, cooling channel near trailing edge has broader aspect ratio and those near the leading edge have narrow aspect ratio.

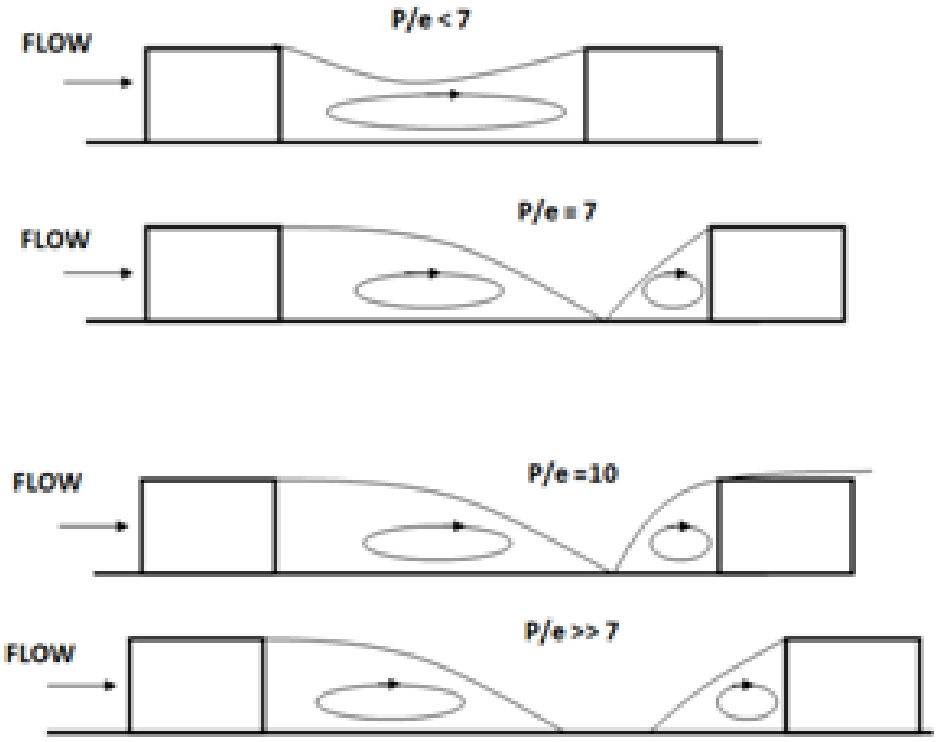

Figure 2.12: Flow structure in the vicinity of rib in cooling channel

Ribs with angle of attack α of 90^o are called orthogonal or transverse ribs; those with an angle of attack other than 90^o are called skewed or angled ribs. The skewed or angled ribs develop secondary flow in the cross stream direction. In general, the repeated ribs that are used for coolant passages with a channel aspect ratio varying from 1/4 (near blade leading edge) to 4 (near blade trailing edge), are nearly square in cross section with a typical relative rib height of 5-10% of coolant channel hydraulic diameter [28]. Figure 2.13 shows the aspect ratio variation in the turbine blade. If the rib turbulators are skewed to the mainstream flow direction, counter rotating vortices are created. These ribs are instrumental in increased turbulent mixing in the areas of flow separation which leads to effective heat dissipation with affordable pressure penalty.

Han et al [23-27] developed correlations for both pressure penalty and heat transfer enhancement in various arrangements of ribs in cooling channels. Ribs being most popular heat transfer enhancement techniques for the serpentine cooling passage, many studies have been conducted to look the effects of channel cross-section, rib configuration and coolant flow Reynolds number.

Recent studies were mainly in the range of 50,000 but advanced gas turbine requires Reynolds number up to 500,000. The height of the ribs is mostly taken to be 5-10% of the channel hydraulic diameter, and the rib spacing to height ratio varies from 5-15%. There are studies which focus on more closely spaced ribs with much larger blockage ratio. With angled ribs providing higher heat transfer enhancement, there were studies on wide variety of rib configuration. Han et al [28-29] and Ekkad et al. [30-31] showed that V shaped ribs outperform the angled rib for a given pressure drop. Ekkad et al [31] showed that the regional averaged Nusselt Number ratio for different rib orientation are almost identical with or without bleed hole extraction. This study showed 20 to 25% reduction of main flow can be used for film cooling without significantly affecting the ribbed channel cooling performance. It also demonstrated that heat transfer near the holes can be enhanced if the ribs are placed near the bleed holes. In an effort to study heat transfer enhancement, various discrete ribs were also considered.

The majority of the ribs used in the experimental studies have a square cross-section, but there are numerous studies on various profiled ribs. Han et al [32] studied the delta shaped ribs which show higher heat transfer enhancements than traditional angled ribs. Bunker et al. [33] studied the performance of ribs leaning towards or away from the flow and they concluded that the traditional square ribs give greater heat transfer

enhancements and less frictional losses than the ribs leaning towards or away from the flow. Taslim et al [34] considered ribs to have rounded edges as it is unlikely to have sharp edges when the blades are cast. They concluded from their experiments that rounding decreases the level of heat transfer enhancement in the cooling channel. Ribs with a higher aspect ratio (taller ribs) are more sensitive to the rounding effect. Square ribs are only slightly affected by rounded edges.

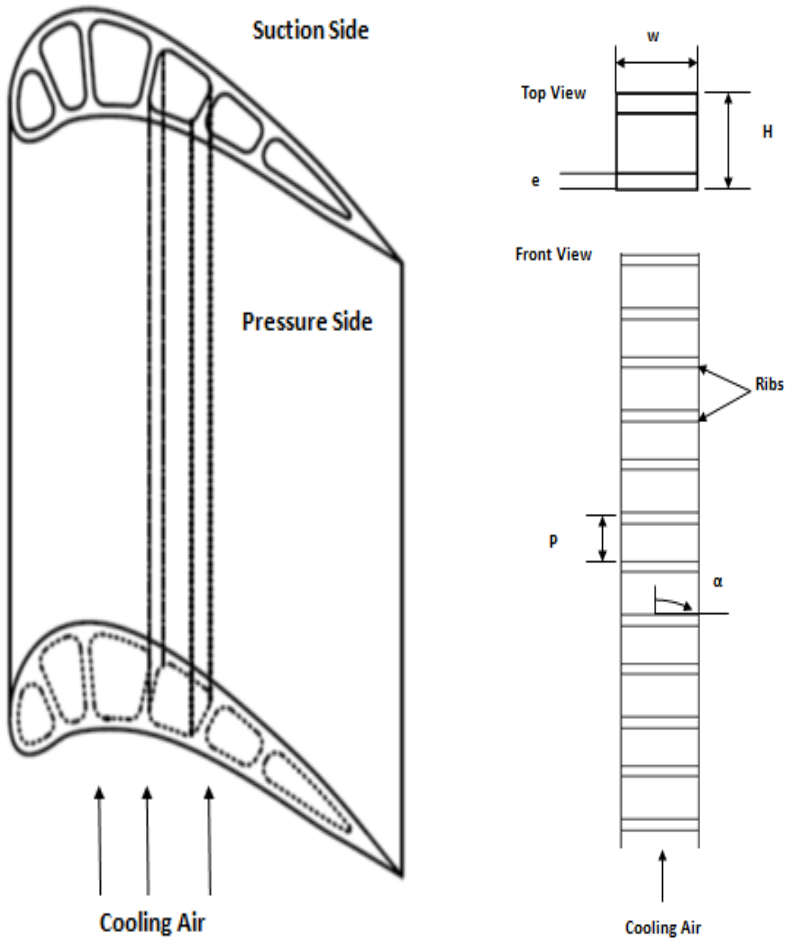

Figure 2.13: Coolant channel in turbine airfoil and internal rib arrangement

However, the pressure drop is significantly less in channels with rounded ribs. Bailey et al. [35] and Taslim et al. [36] showed that with more effective blockage, the heat transfer coefficient can increase but it comes at the cost of significant increase in pressure penalty.

Modern turbine airfoil has ribs in the internal coolant channel and film cooling for outside surfaces. The presence of periodic ribs and holes in gas turbine blades creates strong axial and spanwise variations in the heat transfer distributions on the passage surface. Shen et al [37] and Thurman et al [38] studied heat transfer enhancement by ribs in the presence of coolant extraction. These studies showed that heat transfer coefficients in the near hole region increases.

Review of rotational effect on rib turbulator cooling

In this section a brief overview of rotational effect in blades are discussed which need to be studied in future research work. Heat transfer pattern in rotating coolant passages are very different from stationary cooling passages as both Coriolis and buoyancy forces change the flow and temperature profile in the rotor and in turn affect their surface heat transfer coefficient distribution [39-40]. It is very important to take into consideration the coolant to blade temperature difference (buoyancy effect) and rotating conditions. Coolant passage cross section and the orientation are important factors for heat transfer.

Figure 2.14 shows a channel with angled ribs where there are two counter rotating vortices formed in the cross-section of the cooling passage. If V-shaped rib turbulators are used, four vortices are generated. These additional counter-rotating vortices associated with the V-shaped have resulted in increase in heat transfer enhancement when

compared with angled ribs. Figure 2.14 shows how counter rotating vortices are generated in 45^{o} angled V shape.

As in Fig. 2.15 the secondary flow in two pass channel are different for radial outflow and radial inflow passes. Coriolis force being dependent on direction of rotation acts in different directions for the two passes [41]. For radial outward flow, the Coriolis force shifts the flow towards the trailing walls causing them to have higher heat transfer. Rotational buoyancy is caused by a strong centrifugal force that pushes cooler, heavier fluid away from center of rotation. As shown in Fig. 2.15, in first pass Coriolis force and buoyancy force further increase the heat transfer at the trailing edge but in second pass they favors the leading side. Wall heating condition affects rotating coolant passage leading to different trailing wall temperature from leading side temperature. This study was done by Parson et al [42] and Zhang et al [43]. Combined effect of rotation and rib shape on the heat transfer in rotating channels was investigated by Acharya et al [44]. Effect of channel cross section and channel orientation on rotating channel heat was studied by Wagner et al [45].

As modern gas turbines operate at extremely high temperatures, cooling technology of blades have become extremely important. Internal heat transfer is enhanced with jet impingement, pin-fin cooling and rib turbulators. In recent years, numerous studies have been done to look at factors affecting heat transfer distribution in cooling channels. There have been studies based on rotating as well as non-rotating blades. High performance rib turbulators under realistic, thermal and coolant flow are needed to be looked at.

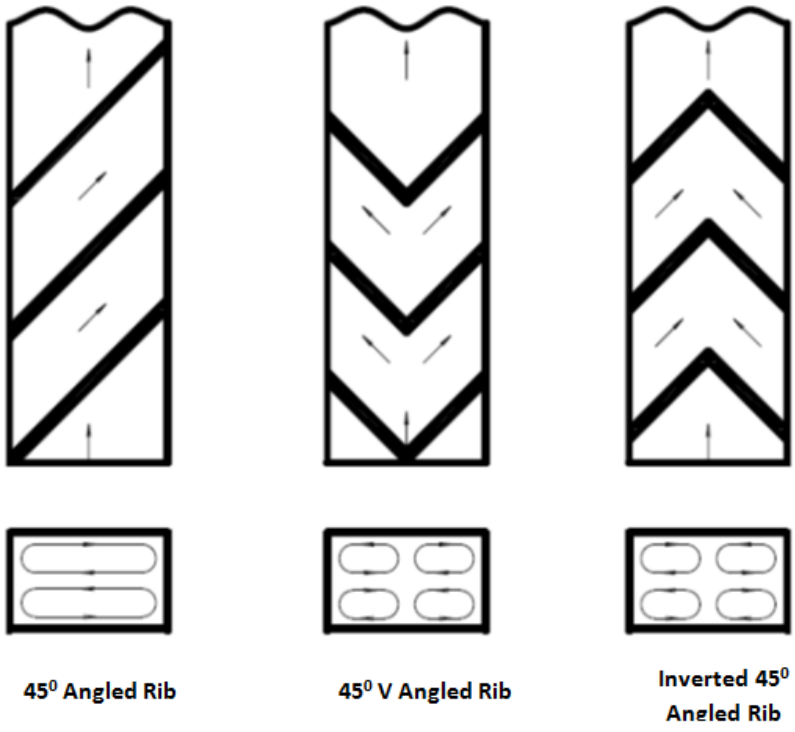

Figure 2.14: Secondary flow vortices induced by 45^{O} angled and 45^{O} V-Shaped ribs

Flow phenomenon inside turbine blade:

In this section, the flow phenomenon occurring inside the turbine vane and blade is discussed in detail. Gas turbine engine consists of several stages of both stationary and rotating sets of blades. To guide the flow from an axial to a tangential direction, stationary rows are positioned upstream the rotating row. The turbine blades are stressed to rotational as well as temperature loads. The Table 2.1 below shows the enforced flow phenomenon due to physical effects in two pass channel used for internal cooling of blades. In this table, only the main and direct effects are listed.

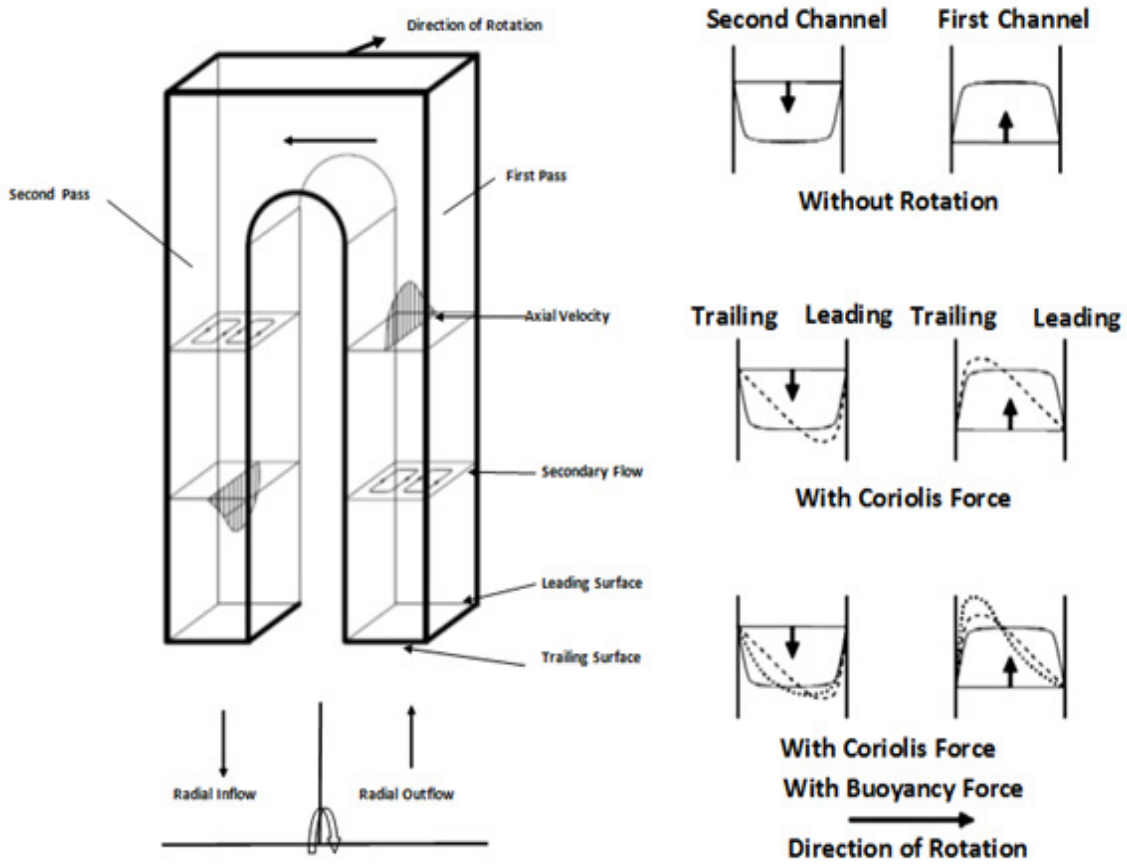

Figure 2.15: Coolant flow through two pass rotating channel

Table 2.1: Effect of physical condition of channel on flow phenomenon

Flow Effect / Physical Condition	Shearing	Secondary flow	Separation	Accelerate-Decelerate	Stabilizing	Buoyancy
Bends	x	x	x	x		
Corners		x				
Heating					x	x
Ribs	x	x	x	x		
Rotation		x			x	x
Walls	x					

2.5 Goals and objectives of the research:

Detailed review of literature reveals that further research is required especially for local heat transfer distribution in the presence of continuous and broken V ribs with different arrangements. Since the orientation of V ribs along the flow is important criteria for heat transfer enhancement, evaluation method have to be developed to demonstrate the performance advantage relative to smooth passage of equal hydraulic diameter.

The goal of this study is to look at the effects of several combinations of continuous and broken V ribs on heat transfer enhancement. The aspect ratio of the channel is taken to be 1:1 and the flow and heat transfer is done for two pass stationary channel. To my knowledge this is the first attempt to look at extensive experimental and numerical simulations of these combinations.

To summarize the main goals of this study include:

(1) To develop an experimental setup for gas turbine blade cooling.

(2) To present high resolution heat transfer results of complex three dimensional channel flows experimentally.

(3) To develop numerical simulation models for these cases.

(4) To validate these numerical simulation results with experimental results obtained.

(5) To use the best V rib configuration and do a LES model analysis for further flow analysis.

(6) To develop a Hybrid LES/RANS modeling with ASM and modify Reynolds stresses using ASM to analyze the results.

CHAPTER 3: BACKGROUND AND LITERATURE SURVEY ON TURBULENCE SIMULATION TECHNIQUES

3.1 Introduction:

This section reviews the literature in gas turbine blade internal cooling with ribs using Large Eddy Simulation. The main aim of this section is to summarize the research work done in last few decades in this area. Most of the present studies use Reynolds averaged Navier Strokes (RANS) model, which is dependent on semi empirical models to analyze the fluid flow and heat transfer for cooling channel of gas turbine blades. This is because of higher computational overhead associated with Direct Numerical Simulation (DNS). There is a need to use models which are highly accurate and reliable. With the development of High Performance Computing (HPC), Large Eddy simulations (LES) are possible now-a-days. LES has been applied to engineering work but is still in its nascent stage in its implementation in the area of internal cooling channels. The ability of LES calculations to fully resolve turbulence at large scales and model only the universal smallest scales produces accurate results. This simulation work includes Large Eddy Simulation for two pass channel. The objective of the study is to simulate the flow for two pass channel with 60^o V broken and 60^o V continuous ribs.

3.2 Large Eddy Simulation (LES):

The efficient design of internal cooling ducts in gas turbine blades and nozzles requires a detailed knowledge of flow and heat phenomenon inside the blade cooling channel. DNS is the solution of the whole field without modeling, which is very expensive. Hence LES models are used which are intermediate between DNS and Detached Eddy Simulations

(DES). LES uses empirical constants and functions; however as modeling of turbulence is being confined to sub grid-scale only, there is less effect of empirical modeling on results as compared to RANS model. The main advantages of LES over RANS are reliability, repeatability and universality. LES model is used to simulate the Inlet V and Outlet Inverted V for both continuous and broken ribs in two pass channel. These channels are the best among the combination of V upstream and downstream in the channel analyzed. In LES, large eddies are resolved directly and smaller eddies are modeled. LES modeling are becoming gradually more predominant in recent years with increase in computational resources.

Kajishima et al [47] discussed the origin of turbulence driven secondary flow and the validity of eddy viscosity models for prediction of turbulent flow in a stationary square duct on the basis of the LES. Choi et al [48] studied the extension of LES from an Euler/RANS code in stationary square duct, which was inherently to reduce the computing power. Hebrard et al [49] studied the effect of the spatial development of turbulent flow inside the duct with high temperatures suddenly imposed at one of the duct walls. They also studied the case of an S-shaped duct for both convex and concave curvature. All these studies were for stationary duct flow using LES model.

Pallares et al [50-51] studied turbulent flow at low Reynolds Numbers in a rotating straight square duct using LES technique. The pressure driven flow was assumed to be fully developed, isothermal and incompressible. Computations were carried out using a second-order finite volume code with a localized one-equation dynamic subgrid scale model. Simulations of rotating channel flows were initially carried out and were seen to be in agreement with experiments and DNS reported in the literature. The study of the

flow in a rotating square duct revealed the influence of the Coriolis force on the spatial distribution of the average velocity fields and Reynolds stresses. It was found that, globally at the low Reynolds Number studied, rotation tends to significantly reduce the overall turbulence level of flow. They also studied turbulent heat transfer at low Reynolds Numbers in stationary and rotating straight square ducts. Simulations of mixed convection arising from the centrifugal buoyancy effect showed that the turbulence level of the flow was strongly influenced by centrifugal buoyancy effect. These studies were with rotating channels without ribs.

Yang et al [52] studied application of dynamic subgrid-scale model to a LES of turbulent channel flow with a square rib mounted on one wall. Near-wall structures were resolved with no-slip boundary condition. The results show better agreement with DNS than LES with a fixed model constant, verifying the value of the dynamic subgrid-scale model for simulating complex turbulent flows.

Murata et al [53] investigated the effects of transverse ribs, the Coriolis force, and cross-sectional aspect ratios on turbulence. The large eddy simulation was performed changing the rotation number and the aspect ratio. It was shown that the heat transfer enhancement caused by the rotation number and the aspect ratio. It was shown that the heat transfer enhancement caused by the rotation was larger for the higher aspect ratios because of intensified Coriolis induced secondary flow. The Reynolds Number considered for this study was 30,000. Murata et al [54] studied heat transfer in a rib-roughened duct using second-order finite difference method in coordinates fitted to transverse or angled ribs. Turbulent and laminar cases, of which Reynolds Number was 350 and 50 respectively, were computed for rib angles of 60^{O} and 90^{O}. The comparison between the laminar and

turbulent results showed clear differences in heat transfer distribution because the higher momentum fluid of the turbulent case was more disturbed by the ribs as compared to the laminar case. The above studies were using ribs for duct flow.

Murata et al [55-56] studied heat transfer in a rotating two-pass square channel with 180^o sharp turns using large eddy simulation with lagrangian dynamic subgrid-scale model. In the rotating condition, the high momentum fluid on the upstream pressure side formed one strong vortex in the turn that transported the high momentum and low temperature fluid to the suction surface side where the heat transfer is increased. They also studied centrifugal buoyancy effect on heat transfer in a rotating two-pass square channel with 180^o sharp turns using large eddy simulation. The effect of the siding/opposing buoyancy contributions was seen in different longitudinal vortex structure near the pressure surface. This was dependent on the radial flow direction and in large buoyancy induced variation of the heat transfer on the pressure surface than that on the suction surface. The heat transfer efficiency index is slightly increased by the buoyancy. These studies were based on two pass smooth channel.

Murata et al [57] studied the flow and pressure loss within a ribbed duct. They showed that in rotating condition, the highest rotating speed caused deteriorated heat transfer on the pressure surface of the straight pass. The friction factor was much more sensitive to both the rib arrangement and channel rotation than the heat transfer.

Jordan [58] studied the turbulent character and pressure loss produced by periodic symmetric ribs in a circular duct. Pollard et al [59] studied fully developed turbulent flow in a straight square annular duct using large eddy simulation. The flow Reynolds Number was 200 based on the mean friction velocity and half the hydraulic diameter of the

annular duct. The mean flow field and the turbulent statistics were compared with existing experimental and numerical data for square duct flow and acceptable agreement was obtained.

Feiz et al [60] studied fully developed, incompressible turbulent channel flows for stationary and rotating circular pipes. A dynamic model and the Smagorinsky model were used and compared with DNS results. The features of the flow at two Reynolds Numbers of 4900 and 7400 and for rotation speeds of 0, 1 and 2 are discussed and compared to available literature.

Reynolds number of 15,000 for two dimensional flow and heat transfer through sudden expansion pipe with an expansion ratio of 2 was studied by Sugawara et al [61] using LES. The traditional Smagorinsky model was used and time averaged velocity, flow rate and turbulence fluctuation compared very well experiments.

Braun et al [62] studied experimental and numerical results of local heat transfer coefficients on the rib roughened wall of a channel with turbulent flow with Reynolds Number of 6000 based on channel height. The numerical results were obtained from large eddy simulation and the experimental results from ammonia-absorption technique. Numerical computations were done for a periodic element of the channel with periodically fully developed flow. The experiments even after the eighth period did not show an exact periodically fully developed condition and under predicted the values, similar to that observed in this study.

Saha et al [63] studied comparison between unsteady RANS calculation (URANS) across a wide range of Reynolds Number and an LES calculation of Reynolds Number of 12,500 in periodic ribbed duct flow. The LES results are based on a higher- order

accurate finite difference scheme with a dynamic Smagorinsky model for the subgrid stresses. The URANS procedure utilizes a two equation k-ϵ model for the turbulent stresses. It was done to investigate the accuracy gained over the computational cost involved. URANS calculation showed much less unsteadiness than the LES calculation. The LES results clearly reflect the importance of coherent structure in the flow, and the unsteady dynamics associated with these structures.

An alternative to LES for industrial flows can then be unsteady RANS also called URANS (Unsteady RANS). The URANS equations are the usual RANS equations, but with transient (unsteady) term retained. The URANS momentum equation and the LES momentum equation are exactly the same, except that the term used in URANS is turbulent viscosity and in LES, is subgrid scale viscosity. In URANS, much more of the turbulence is modeled than in LES, and, hence, the turbulent viscosity is much larger than the SGS (subgrid scale) viscosity. The common definition of URANS is that the turbulent length scale is not determined by the grid, whereas in LES it is.

Tyagi et al [64] studied instantaneous flow and heat transfer fields in fully developed periodic ducts. LES was done for Reynolds number of 12500 and focused on a large scale coherent structure, which was very important for fluid mixing and heat transfer.

Ahn et al [65] studied sharp edged circular ribs for Reynolds Number of 30,000 and concluded that heat transfer increase was similar for both cases but friction factor was slightly less in the case of rounded rib. Thermal performance of the ribs was increased in the case of round ribs.

Tafti et al [66] compared LES for Dynamic Smagorinsky model and no model for different grid resolutions and reported mean flow, turbulence and heat transfer. All the

results showed Dynamic Smagorinsky model predicted results comparable to the experimental results. Tafti et al [67] studied fully developed flow and heat transfer LES calculations in a rotating duct with both Coriolis and buoyancy forces included.

Takahashi et al [68] studied high Reynolds number LES calculation of a periodic duct with crossed 60^{O} angled ribs and different aspect ratio ducts. The results showed that rib induced separation vortex behind the rib and vortex shedding is strongly related to channel heat transfer. These studies were based on ribbed channel flow.

Most of the LES studies were done on smaller ducts with periodic ribs. The assumptions of periodic ribs will not be able to take in account the turning effect in case of serpentine passages. In addition, there is no LES done on V and Broken V case. To the authors knowledge only Murata et al [55-56] have looked at two pass channel using LES for low Reynolds Number. To take it a step further, a complete two pass square channel with high Reynolds Number of 56000 flow domain has been studied as part of this thesis. Heat transfer pattern and flow phenomena are studied using LES for Inlet V and Outlet Inverted V for both continuous and broken ribs.

3.3 Hybrid LES/RANS modeling with ASM:

A novel approach is devised to calculate the heat transfer for the channel flow with continuous and broken V rib. Algebraic stress model (ASM) is a compromise between simplicity of turbulent energy method & universality and greater range of predictability of Reynolds stress methods. It is an economical way of accounting for anisotropy of Reynolds stress.

LES model provides good results for velocity and velocity gradient. RSM model provides values for initial Reynolds stresses. Using these values modified Reynolds stresses are calculated by ASM and are used to analyze heat transfer results. These results provide very good agreement with the experimental results. To the authors knowledge no one has used this approach till date. Hybrid LES/RANS modeling with ASM produces better results because it takes the best predicted parameters from LES (velocity and velocity gradient) and RANS (Reynolds stresses) and uses ASM model to calculate the modified Reynolds stresses. These modified Reynolds stresses are used to calculate the kinetic energy at the first grid point. These modified kinetic energy, velocity and wall shear stress from the LES model are instrumental in getting accurate heat transfer predictions.

CHAPTER 4: EXPERIMENTAL APPARATUS AND DATA REDUCTION

4.1 Introduction:

The experimental system was designed to simulate a stationary two pass internal cooling channel. The system includes a test rig, test sections and data acquisition system. Temperature and velocity data are measured to obtain the heat transfer across the channel. This chapter discusses the test rig development, calculation done for the selection of blower and test rig manufacturing. Different rib arrangements to be tested are discussed at length.

4.2 Experimental setup:

The objective was to create an experimental setup for measuring local heat transfer coefficient in turbulent flow through a two pass square channel with 180^{o} bent. It consisted of constructing the two pass square channel with Plexiglas and assembling the model with nuts, bolts, acrylic cement and weather seal. A high resistance wire matrix as heating element was used to heat the bottom surface of the channel. To measure the surface temperature of heating element, a thermocouple array was positioned. These arrays of thermocouples were attached to a data acquisition system which provided the output temperature of the surface and air in channel. Blower was selected based on the output pressure loss calculation of the overall channel arrangement which provided high Reynolds Number. In line flow, sensors were used to get velocity and pressure at inlet and outlet. Complete setup of the experiment can be seen in Fig. 4.1. Details of the selection of blower and other equipments will be discussed in latter sections.

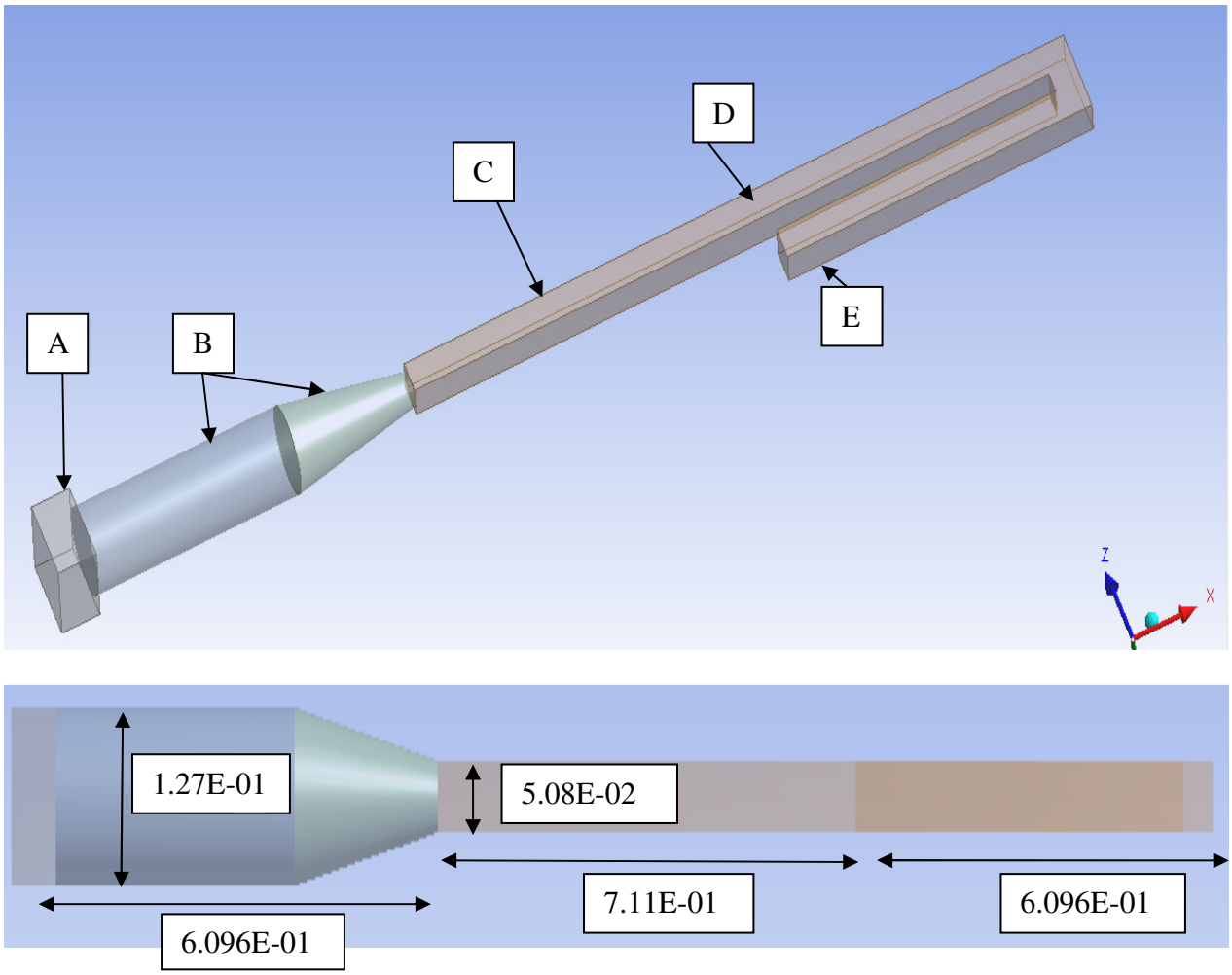

Figure 4.1: Design of the test rib (All dim in m)

A- Blower with 8.02E-02 m^3/s with static pressure of 1992 N/m^2

B- Ducting used for connection

C- Inlet duct

D- Point where the average velocity and Pressure is to be calculated.

E -Point where pressure is to be calculated (open to atmosphere).

Cross section of the duct is 5.08E-02*5.08E-02 m

This section discusses all procedural steps in the experimental setup. These aspects are divided in two different sections named as such

i) Construction of Experimental Setup

ii) Measuring Equipments for Experiments

a) Experimental Setup

i) Construction of Experimental Setup

Main elements required for the construction of experimental setup are as follows

1. Plexiglas Channel

Test section is made up of Plexiglas. Plexiglas acrylic sheet selected had maximum temperature of 200^{o} F. These were selected to withstand the temperature of the heating elements. Table 4.1 shows the dimensions used for this experiment. For flow to be developed, a fully developed length using Eq. 4.1 was used. The length was considered based on maximum Reynolds Number. The overall channel was a simple design as it consisted of four rectangular walls, a flat top piece and a base plate. For the remainder of this report, the term “top plate” will refer to the fixed plate that is attached to the channel walls, and the term “base plate” will refer to either of the removable plates constructed for the purpose of observing the heat transfer of the channel. The Plexiglas piece was modeled using Pro-Engineer. The walls, top, and two bottom base plates of the channel were constructed out of 6.35E-03 m thick Plexiglas. Using solvent cement, the wall pieces and top plate were assembled into a permanent fixture. The two base plates have the same outside dimensions as the top piece. These base plates were designed to be interchangeable as they will have two different surface geometries for the comparison of their heat transfer rates and flow pattern characteristics. To make the bottom plate interchangeable, hex nuts were used for mounting. Original cuts produced leaky joints in the structure, so a high quality carbide table saw was used for accurate tolerances. To seal

the top plate and walls to the base plate, weather sealant foam was put along the contact edge to give an effective airtight seal, as well as retaining the removability of the base plate.

Turbulence entry length correlation:

$$\frac{L_e}{D_H} = 1.6(Re_D)^{0.25} \quad (4.1)$$

2. Rib used for test section:

Ribs used for the test were made of Plexiglas with height and width of 6.35E-03 m. The ribs were made such that the angle of ribs is 60^o V. In addition to continuous ribs, broken ribs were also considered for analysis. These ribs were wrapped in copper foil and soldered on to the test section copper foil. Broken ribs are one third of the overall length of continuous ribs.

3. Heating Elements:

A variety of heating elements were considered with the goal of choosing an element which would provide the necessary combination of high electrical and low thermal resistivity. Sample tests with this material using a DC power supply were conducted, resulting in a viable heating element solution. Flexible silicone rubber heat sheets and strips were used to heat the surface of the channel uniformly. Heating element was selected based on uniformity of heat supply for the copper foil used. These were of the sizes considered for testing. These flexible silicone rubber heat strips could provide 1.55E04 W/m^2 with a maximum temperature of 450^o F. The details of heating element can be seen in appendix A.

Table 4.1: Dimensions of the model used for Experimental setup of smooth and ribbed channel

Channel Aspect Ratio (AR)	1:1
Hydraulic diameter (D_H)	5.08 E-02 m
Passage height (H)	5.08 E-02 m
Passage width (W)	5.08 E-02 m
Test section length (l_t)	6.096 E-01 m
Rib height (e)	6.35 E-03 m
Rib-to-rib pitch (p_r)	6.35 E-02 m
Rib Height to Hydraulic Diameter (e/ D_H)	1.25 E-01
Rib Angle (α)	60^o

Exact size of the heat sheets were used as heating elements provided by McMasters. A 140 V AC variance power supply was acquired and used to send a current through the wire. Due to the varying resistivity of wire, calibration of the wire was required. These calibrations were used to approximate the required voltage by the matrix in order to get a constant heat flux.

4. Honeycomb:

Honey comb was made manually using 50 mm diameter straw which were glued to each other. This was placed at the entrance of the test section to achieve uniform flow. Insulation was used below the test section to avoid heat losses. Weather strip was used for closing the gaps to prevent air leakage in the system when the top surface is closed.

5. Copper Foil:

Copper foil was selected as the heating surface. The thickness of copper foil selected is very thin in order to neglect the conduction effect of the foil. These copper foils were wrapped around the heating element and then placed on the surface of the channel under

investigation. Copper foil used for experiment was 2.54E-05 m thick. Fig. 4.2 shows the copper foil wrapped heating element for testing. Fig. 4.3 shows schematic representation of the arrangement of copper foil and the heating element.

Figure 4.2: Copper sheet wrapped on heating element used for testing.

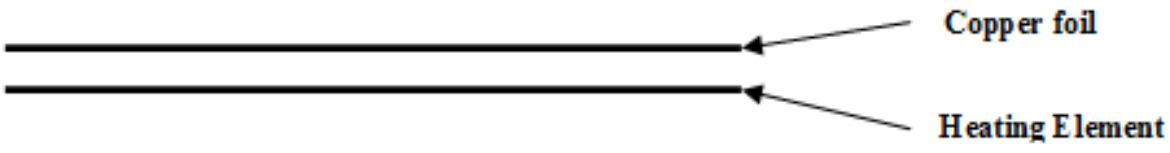

Figure 4.3: Schematic of the test section

ii) Measuring Equipments for Experiments

This section discusses the various components of the experimental setup which measured temperature and velocity. This section will briefly discuss the blower selection as well.

1. Thermocouples

The channel was equipped with 32 T-type thermocouples. Six of these monitored the air temperature, while the remaining were used to monitor base plate/heating element temperature at consistently spaced points along the base plate. Each thermocouple was inserted into a data acquisition interface (DAQ unit) which relayed temperature data to a program specifically obtained from Omega known as TracerDAQ Pro. It can record data for 20 samples which can be used for Uncertainty analysis. All the surface temperatures were measured using an array of thermocouples on the surface of the heated copper foil. Four of these DAQs were used to capture the surface temperature. Figure 4.4 shows the location of the air temperature thermocouples to measure the air bulk temperature.

2. Velocity Meter and Pressure Measurement:

In-line flow sensor was used to get flow rate. This was attached to a differential pressure transmitter. This flow sensor eliminates the need for traversing the flowing stream because of its multiple sensing points and build-in averaging capability. Velocity and pressure was measured using a Dwyer Magnesense brand digital readout meter which was connected to the In line flow sensor.

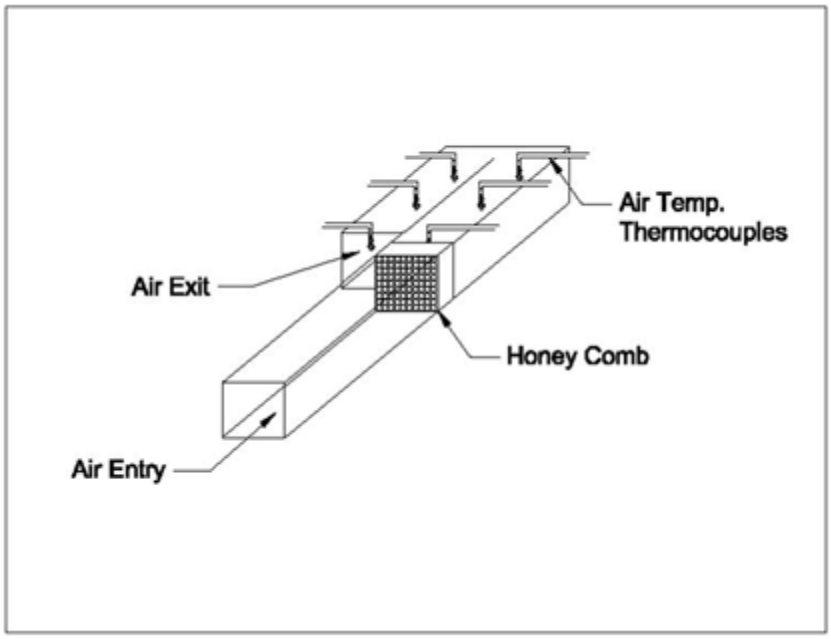

Figure 4.4: A diagram of the six thermocouples reading air temperature, the honeycomb mesh to smooth air flow, and the air entry/exit.

The range of the equipment was considered based on the maximum Reynolds Number required and the pressure loss across the channel. In line flow sensor was specially considered based on channel cross section of 0.0508 m. Magnesense Differential Pressure Transmitter is an extremely versatile transmitter for monitoring pressure and air velocity. It has features of selecting English and Metric units with digital display.

3. Blower and Duct Design:

Duct design was created for connecting the blower to the test section. Once the design of duct was determined, a pressure loss calculation was done for the overall channel considering a Reynolds number of 90,000. After the calculations were carried out operating curve for blower was obtained for selecting correct blower flow rate. Canvas was used to connect duct assembly to the blower. The blower consisted of damper to

change flow rate in the channel to get different velocities at the inlet. These dampers increase the pressure loss across the channel and in turn decrease the velocity.

This was an effective way to achieve different velocities. An iterative design procedure was used to calculate the pressure loss throughout the duct arrangements used for the experiment. Pressure loss across the test section was based on 100,000 Reynolds number. Once the pressure loss was calculated, Cincinnati Blower with a pressure loss of 8 in. water column was selected based on the system and operating curve of the blower selected.

Once the blower was selected, a final recalculation of the ducting pressure loss was completed based on the outlet of the blower. Final specifications of the blower selected can be seen in appendix A. As mentioned above, a damper was used to regulate the velocity of the air being used for the experiment.

4.3 Assembled Experimental Setup:

Figure 4.5 shows the complete experimental setup. The blowers were rigidly bolted and supported on the experimental frame and the test section was arranged such that the flow is horizontal throughout the test section. All the DAQs were arranged on the test setup support unit. The control units for heating element were also attached to the frame. Thermocouples were numbered so that they could be suitably identified. Fig. 4.6 shows the blower being attached to the canvas which in turn is attached to the duct system. At the entrance of the blower, dampers were placed to change velocity for testing.

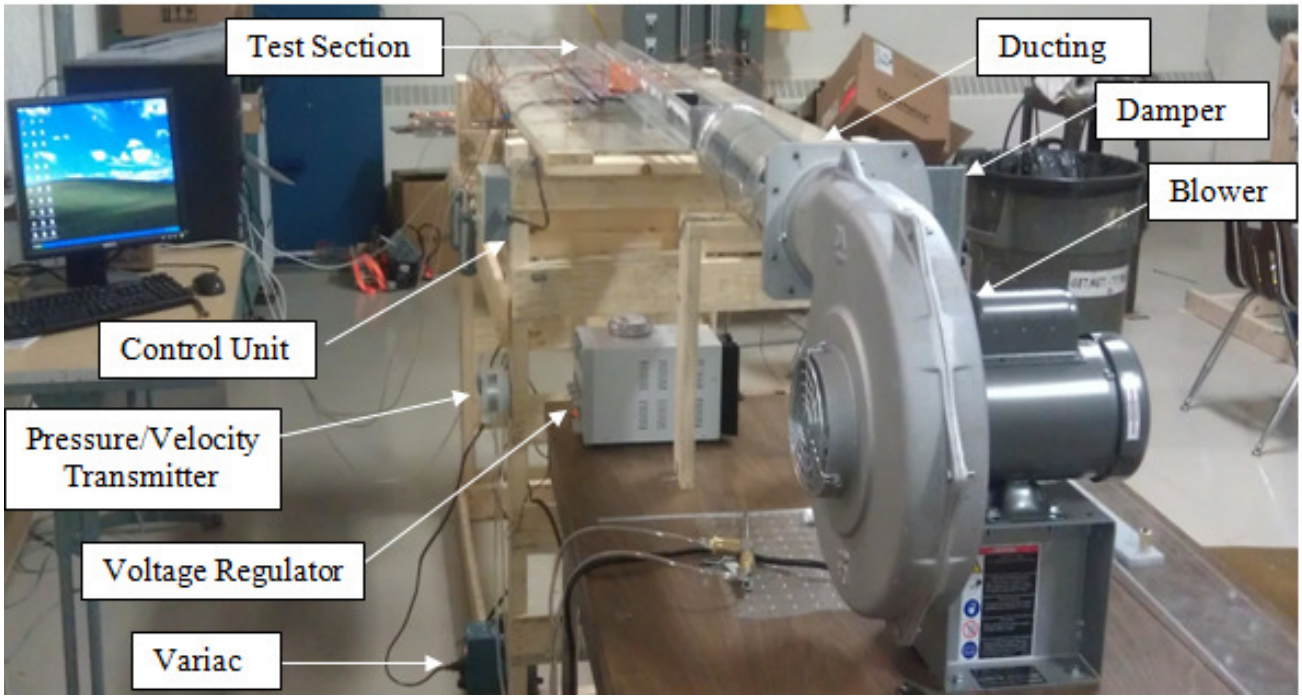

Figure 4.5: Complete experimental setup

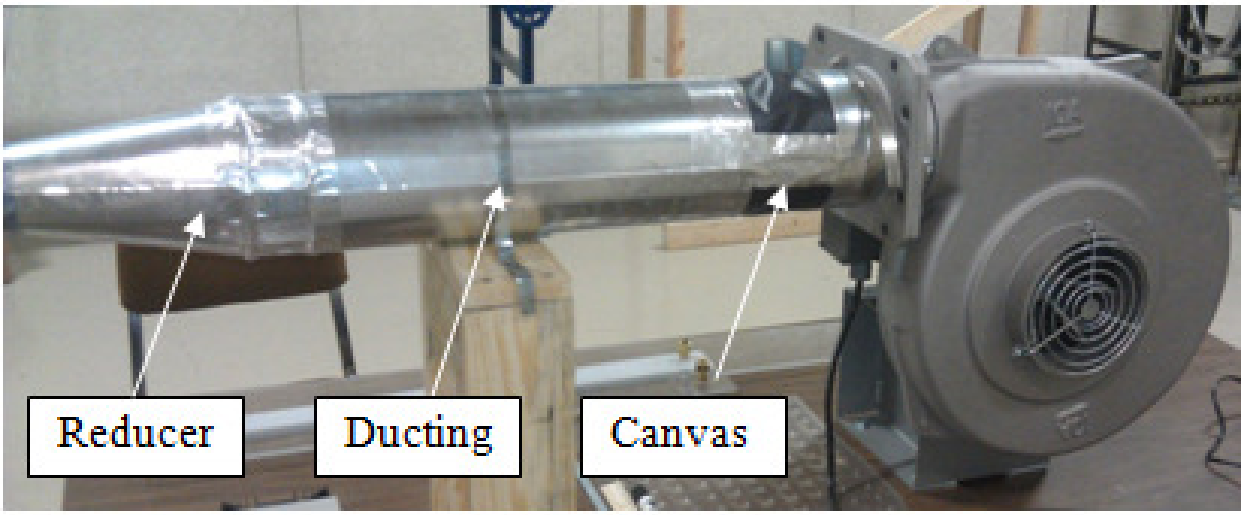

Figure 4.6: Blower assembled with Canvas and Ducting

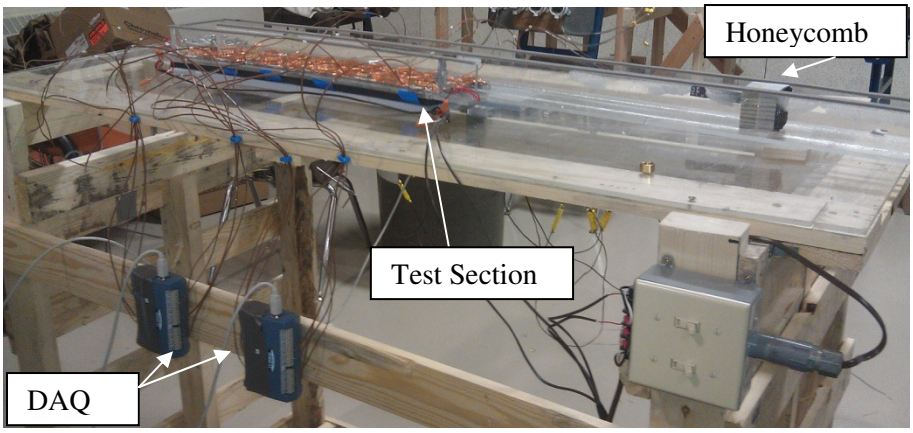

Figure 4.7: Test section with DAQ and control units

Figure 4.7 shows the test section with the control unit and the DAQs arranged beside the test section. These DAQs were attached to a computer for temperature output measurements using TracerDAQ Pro. Figure 4.8 (a) shows front view of the test section. Below the test section, insulations were used to minimize the heat loss during heating. In line sensor was placed on top of the test section to measure the velocity as shown in Fig. 4.8 (b). Figure 4.9 shows the complete schematic setup. The arrangement is such that different test section can be tested as well. The top section is removable and other ribs could be tested as well. Figure 4.10 shows the entire experimental loop diagram.

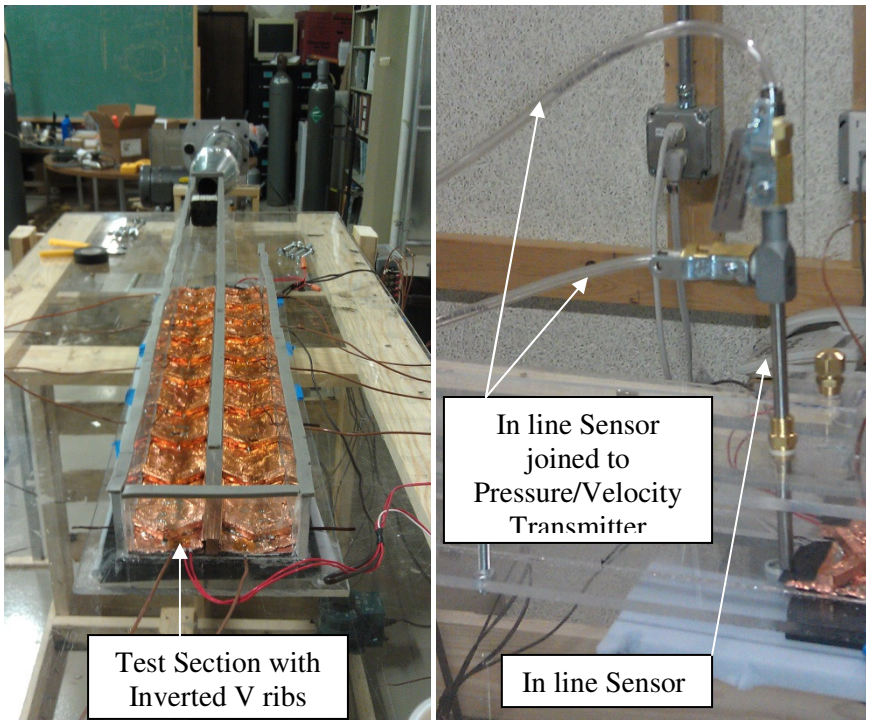

Figure 4.8: a) Test section from front b) Inline flow sensors

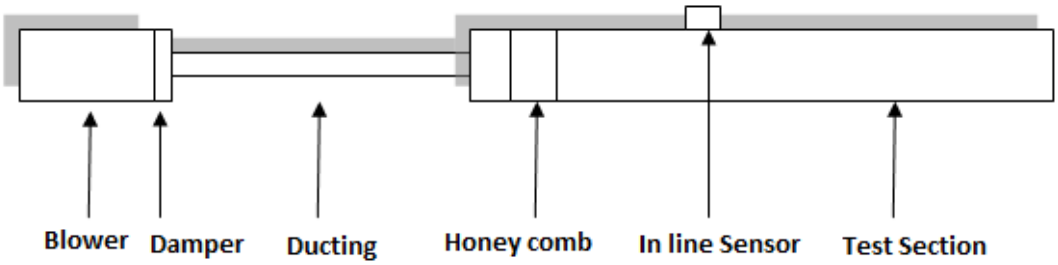

Figure 4.9: Schematic of the proposed setup for Experiment

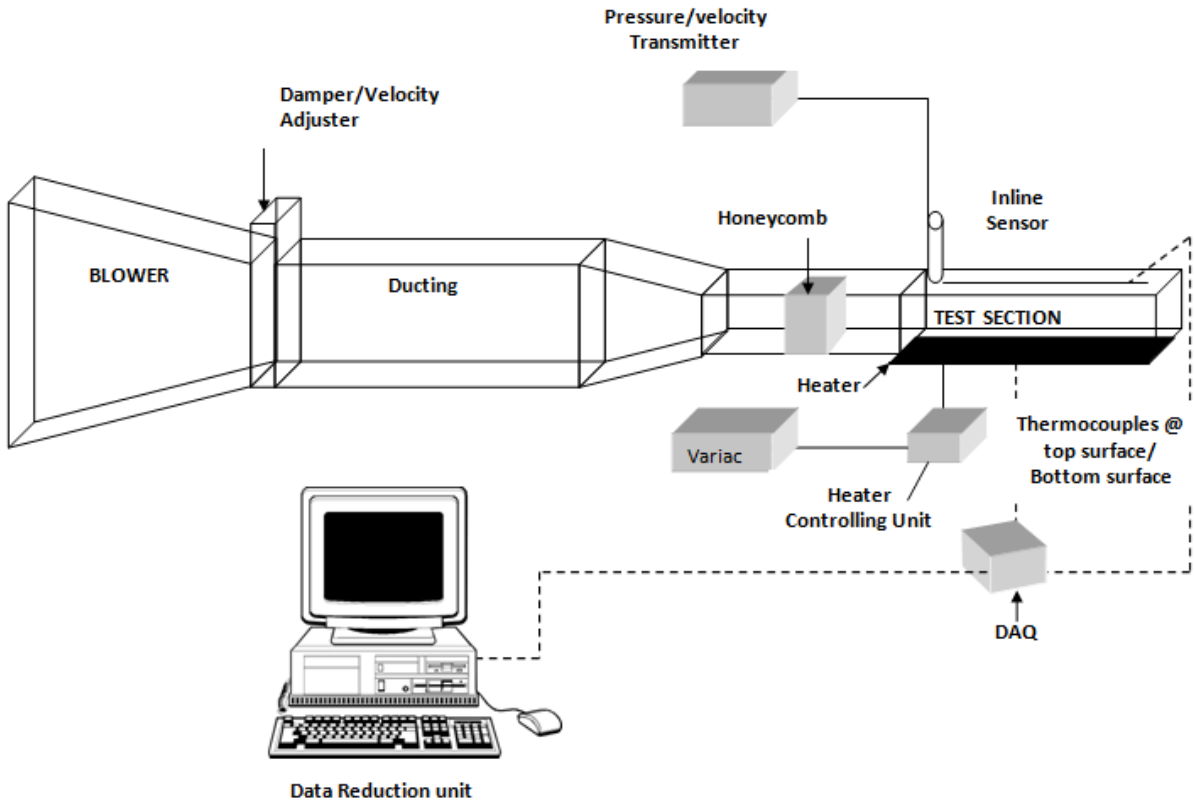

Figure 4.10: Entire view of experimental loop diagram

4.4 Rib arrangement used for testing:

On the surface of the test section, different arrangements of ribs were considered for testing. There were four cases each for Continuous and Broken ribs considered for the experimental work.

A) Continuous V ribs:

Case I: 60^{o} V rib (V_C)

Case 2: 60^{o} inverted V rib (IV_C)

Case 3: 60^{o} V rib at inlet and 60^{o} inverted V rib at outlet (V-IV_C)

Case4: 60^{o} inverted V rib at inlet and 60^{o} V rib at outlet (IV-V_C)

B) Broken V ribs:

Case I: 60^o Broken V rib (V_B)

Case 2: 60^o Broken inverted V rib (IV_B)

Case 3: 60^o Broken V rib at inlet and 60^o Broken inverted V rib at outlet (V-IV_B)

Case4: 60^o Broken inverted V rib at inlet and 60^o Broken V rib at outlet (IV-V_C)

Table 4.2: Experimental and Numerical parameters (m)

Channel Aspect Ratio (W:H)	1:1
Channel Width (W)	5.08 E-02
Channel Height (H)	5.08 E-02
Rib Height (e)	6.35 E-03
Hydraulic Diameter(D_H)	5.08 E-02
Rib Height to Hydraulic Diameter (e/D_H)	1.25 E-01
Rib Pitch to Rib Height(P/e)	10
Reynolds Number	21,000 , 56000, 85000
Surface Geometry	60^O Angled Continuous and Broken
Channel Orientation	90^o

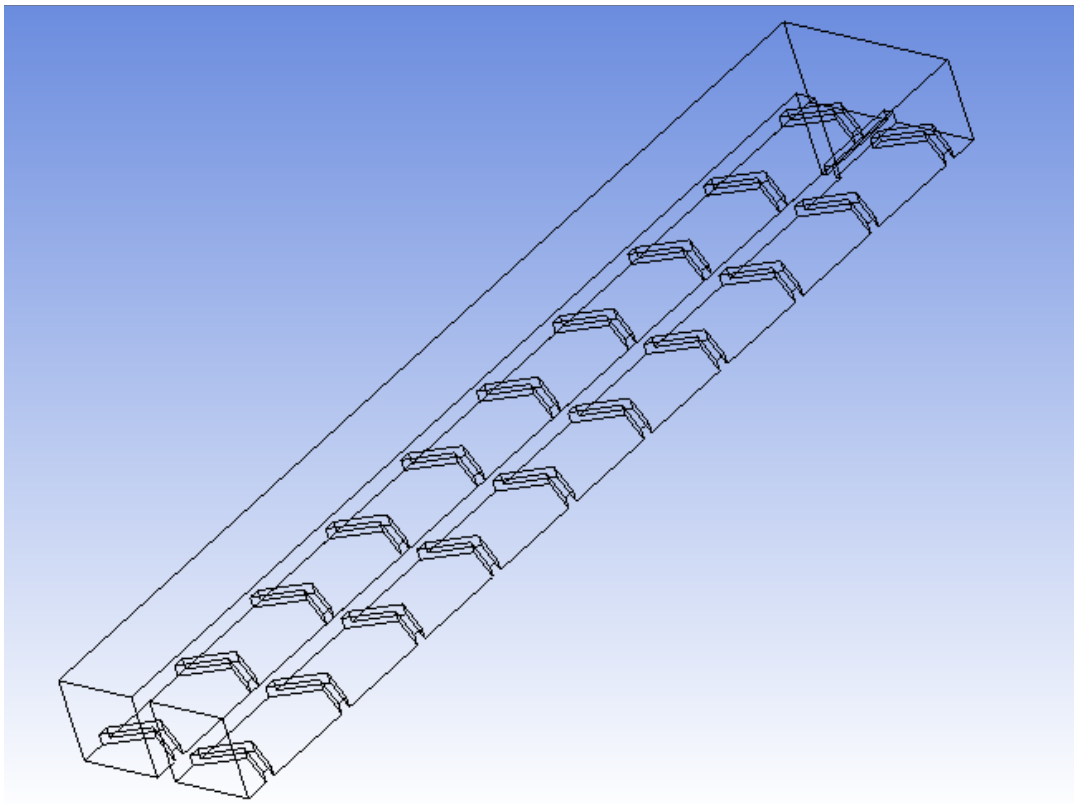

Figure 4.11(a): Inverted V Rib

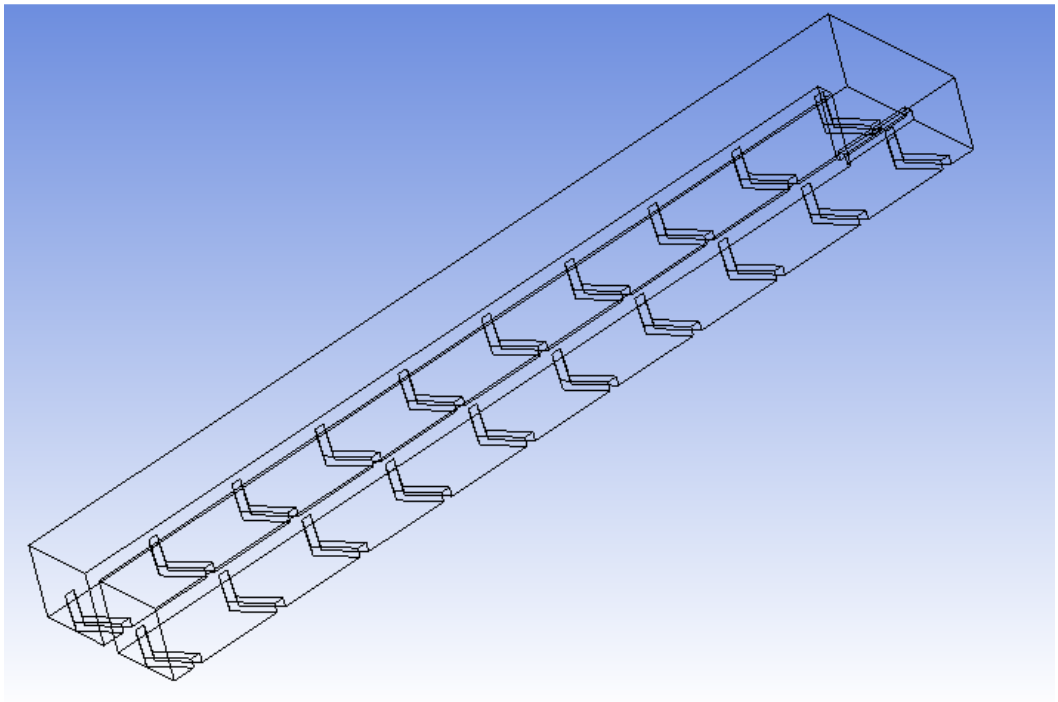

Figure 4.11(b): V Rib

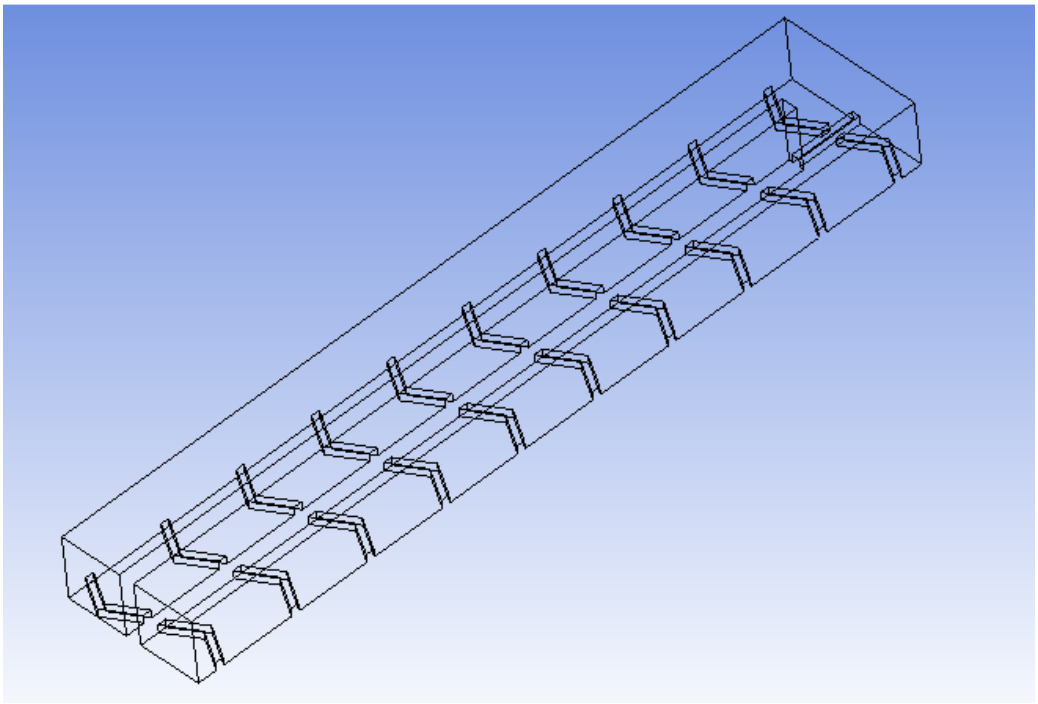

Figure 4.11(c): Inlet V and Outlet Inverted V Rib

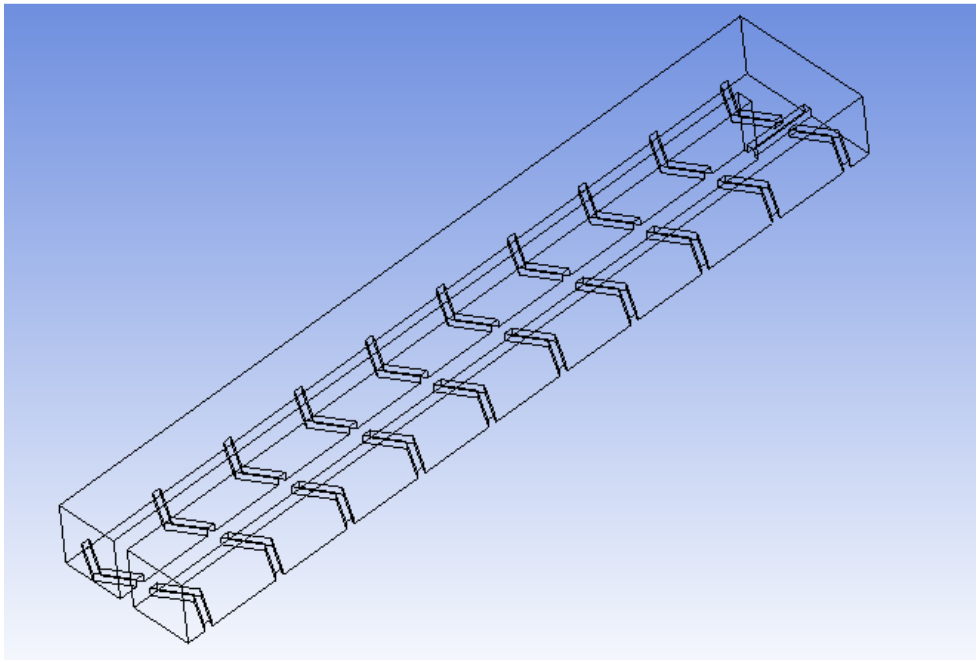

Figure 4.11(d): Inlet Inverted V and Outlet V Rib

Figure 4.11: Different shapes of Continuous 60^{o} V Rib turbulators

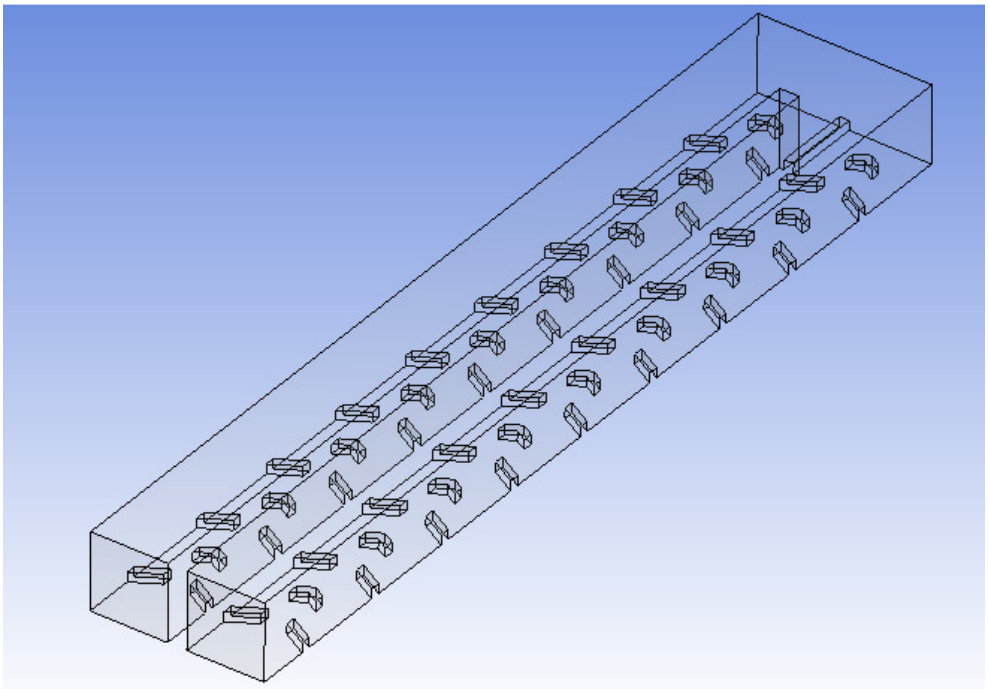

Figure 4.12 (a): Inverted Broken V Rib

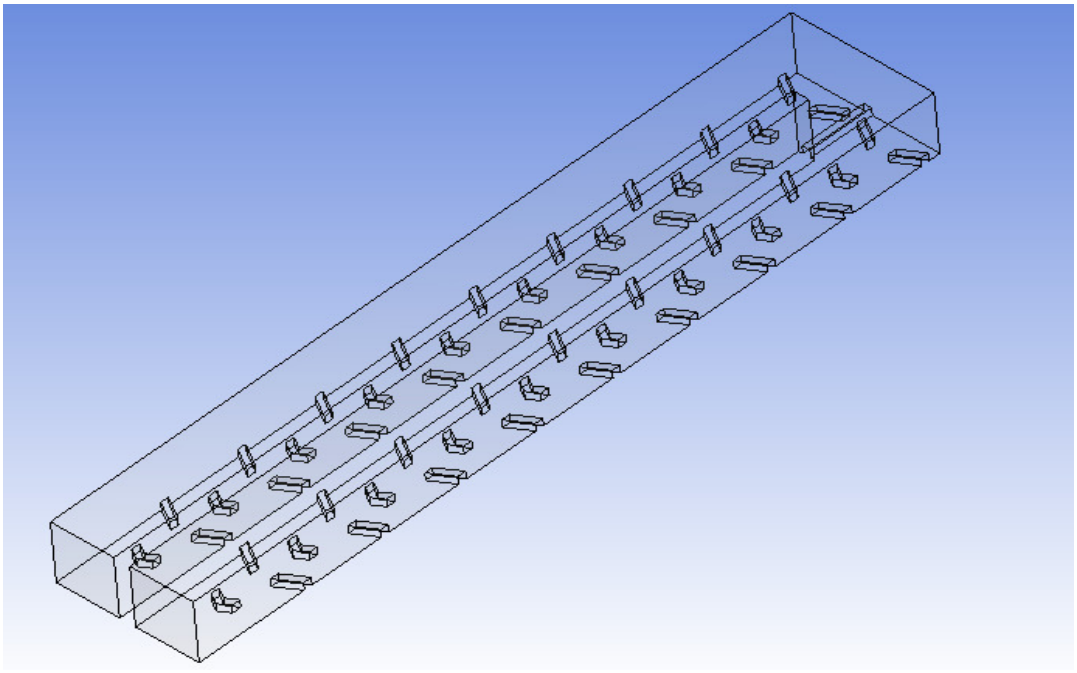

Figure 4.12 (b): Broken V Rib

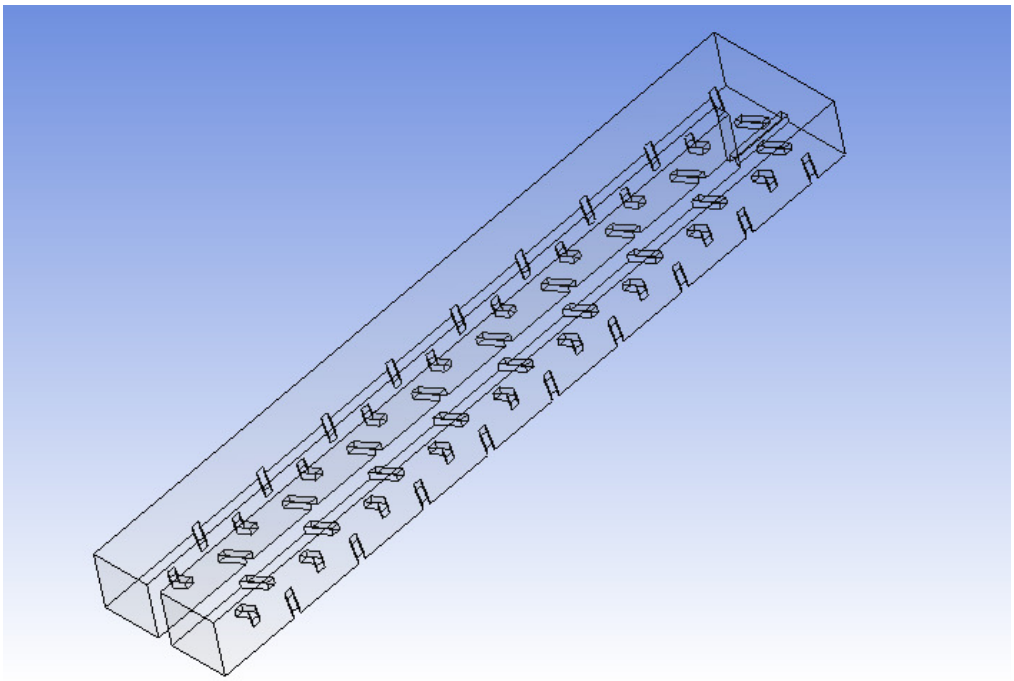

Figure 4.12(c): Inlet V and Outlet Inverted Broken V Rib

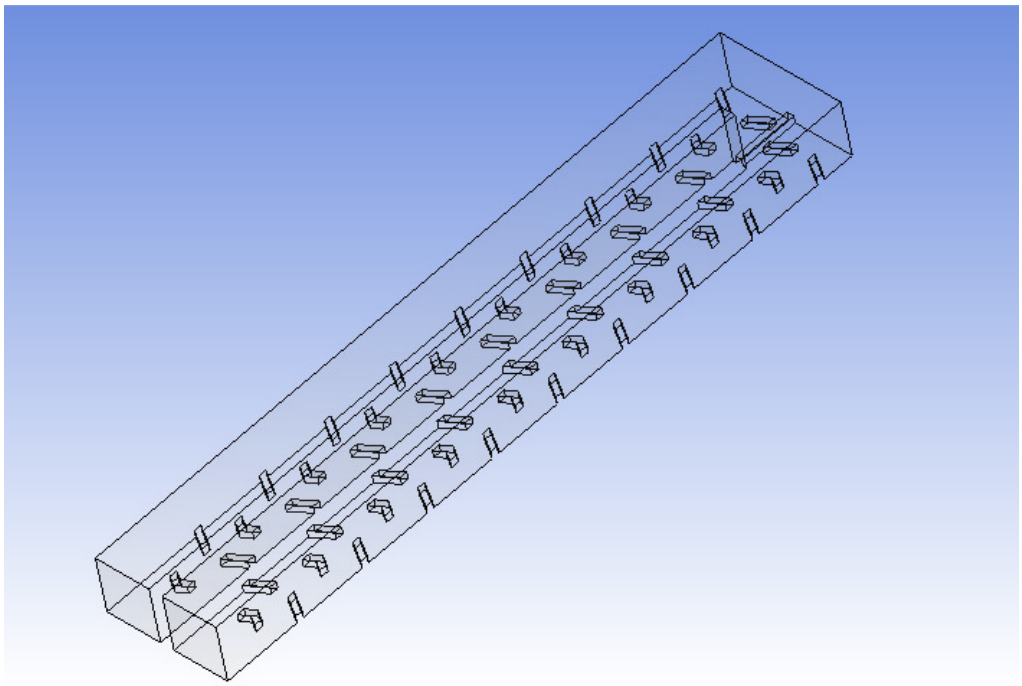

Figure 4.12(d): Inlet Inverted V and outlet V Broken Rib

Figure 4.12: Different shapes of Broken 60^{o} V Rib turbulators

Table 4.2 shows the experimental parameters selected for experimental analysis. Figures 4.11 and 4.12 show all the rib configurations being considered for experimental test.

4.5 Data Reduction and Operating Procedures:

Array of thermocouples were placed on test section. The velocity was adjusted to a prescribed value and then the variac was switched on to supply heat to the heating element. The Tracer DAQ pro was opened and monitored to achieve a steady temperature for the test section. Once the test section was completely heated the blower was switched on to achieve a steady state. Velocity was measured using In line sensor and the temperature recorded for each case at different Reynolds number. Once data for all cases was collected data, processing was carried out to get the required results for heat transfer.

Heat Transfer Enhancement:

This study investigates the regionally averaged heat transfer coefficient at various locations within the channel. The heat transfer coefficient is determined by net heat transferred from the heated plate, surface area of heated plate, the regionally averaged temperature of the plate and the local bulk mean temperature.

In order to calculate the Nusselt numbers required, different theoretical equations was used. Velocity was experimentally found, and used to calculate mass flow rate in Eq. 4.2. The Reynolds number was calculated from Eq. 4.3 based upon the measured velocity, and assuming properties at 300 K. The heat into the system was equal to the electrical power input, Eq. 4.4, and this value was converted to a heat flux over the area of the plates in Eq. 4.5. The electrical input was calculated using electrical properties

namely, current supplied and resistance of the heating element. These values were calculated for voltage used for heating using variac. The net heat transfer was calculated using the external heat losses from the test section. The losses considered in this experiment include conduction through the Plexiglas and the dissipation of heat from the surface of test section.

The heat loss calibration was done by using insulation on the heated test section to eliminate the natural convection. Now using energy conservation, the heat loss and effective heat flux were calculated using Eq. 4.6. The losses calculated were around 10% of the overall heat flux supplied.

It is critical to note that heat fluxes in the experiments are the same, as an increase in surface area does not represent an increase in heat into the system.

$$\dot{m} = \rho * U_{in} * A \tag{4.2}$$

$$Re = (\rho * U_{in} * D_H)/\mu \tag{4.3}$$

$$Q_{el} = R * I^2 \tag{4.4}$$

$$Q''_{el} = R * I^2/A \tag{4.5}$$

Nusselt numbers was calculated once h, convective heat transfer was calculated, using Eq. 4.7. This value was then used along with the hydraulic diameter and the conductive heat coefficient of the working fluid, air, to attain an experimental Nusselt number. The theoretical Nusselt number was calculated using Dittus Boelter Eq. 4.9, as our system had turbulent flow with a Prandlt number 0.71.

$$Q''_{net} = Q''_{el} - Q''_{con} - Q''_{dis} \tag{4.6}$$

$$h = Q''_{net}/(T_s - T_{bx}) \tag{4.7}$$

$$Nu = h * \mathrm{D_H}/\mathrm{k} \tag{4.8}$$

$$Nu_o = 0.023 * Re^{\frac{4}{5}} * Pr^{.4} \tag{4.9}$$

Mean and surface temperatures were obtained from Tracer DAQ Pro. The main idea behind the project was to compare local Nusselt numbers in the ribbed channel with smooth channel. Ratio of Experimental Nusselt number with theoretical Nusselt numbers for both the cases were plotted against the channel length.

Uncertainty Analysis:

Uncertainty analysis is the prediction of the uncertainty interval which should be associated with experimental results, based on observations of the scatter in the raw data used in calculating the results. Uncertainty is a quantification of the doubts about the measured results. Uncertainty analysis was based on the method proposed by Moffat [69].

By using the equations given above in this section Nusselt Number ratio can be expressed as

$$\frac{Nu}{Nu_0} = \left(\frac{D_H}{k}\right)\left(\frac{Q_{net}}{A(T_S - T_{bx})}\right)\left(\frac{1}{0.023 * Re^{\frac{4}{5}} * Pr^{.4}}\right) \tag{4.10}$$

The uncertainty of the following variables is estimated:

Heat Transfer Area (A)

Air Conductivity (k)

Hydraulic Diameter (D_H)

Prandtl Number (Pr)

Reynolds Number (Re)

Temperature (T)

Using the combined effect of all the parameters affecting the Nusselt Number ratio an overall uncertainty can be calculated. The complete uncertainty analysis is discussed chapter 5.

CHAPTER 5: HEAT TRANSFER RESULTS AND DISCUSSION-EXPERIMENTAL

5.1 Introduction:

The main objective of this chapter is to present experimental results for all different types of rib configuration considered for continuous V ribs and broken V ribs. Results for three different Reynolds Number 21000, 56000 and 85000 are compared. The results shows that secondary flow and three dimensional accelerated flow in two pass square channel increases the heat transfer.

5.2 Description of the Problem:

The main aim is to predict and compare heat transfer phenomenon throughout the two pass channel and to get the best arrangement of rib in the channel. The two pass channels are casted with 60^o continuous V and 60^o Broken V ribs on the surface of the channel. There are four different arrangements of ribs throughout the channel for each 60^o continuous V and 60^o Broken V considered for experiments. As described in Table 4.1 in chapter 4, the aspect ratio of the channel under investigation is 1:1, where aspect ratio is the ratio of width of the channel with the height of the channel. Hydraulic diameter is 508E-02 m, which is effective diameter based on area of the cross-section and perimeter. Orientation of the channel is 90^o, the ribs are placed on one surface of the test section. For this experiment Rib pitch to rib height, which means the ratio of distance between two ribs to the height is 10. Reynolds number 21000, 56000 and 85000 are used for this experiment. Ribs arrangement classifications are mentioned in chapter 4.4 for both continuous and broken cases are considered.

These eight set up of rib arrangement are basically divided into two parts one of continuous and the other being broken rib. Each of these comprises of four different arrangements of ribs. V ribs are ribs which are placed such that the pointed part is pointing towards upstream in the first pass and away from in second pass. Definition of Inverted V is that the pointed portion is away in the first pass and in second pass the pointed portion is towards the flow. In all cases a 90^o rib is placed at the turn. V rib at inlet and Inverted V rib at outlet means that in the inlet section the pointed portion is upstream and again in second pass the ribs are upstream. Inverted V rib at inlet and V rib at outlet are pointed portion is away from upstream and again in second pass the pointed V is away from upstream. With these combination experiments are carried out for three different Reynolds Number for each cases.

Table 4.2 in chapter 4 briefly outlines the experimental conditions or the parameters used for the experiments. Rib aspect ratio is considered to be 1:1 with channel width and height 0.0508 m. The angle of the ribs placed is considered to be 60^o and the channel orientation being 90^o . In this work, V-IV is Inlet V and Outlet Inverted V, IV is Inlet Inverted V and Outlet Inverted V, IV-V is Inlet Inverted V and Outlet V and V is Inlet V and Outlet V. C is for continuous Ribs and B is for broken ribs. For all the ribs the angle of the rib is considered 60^o.

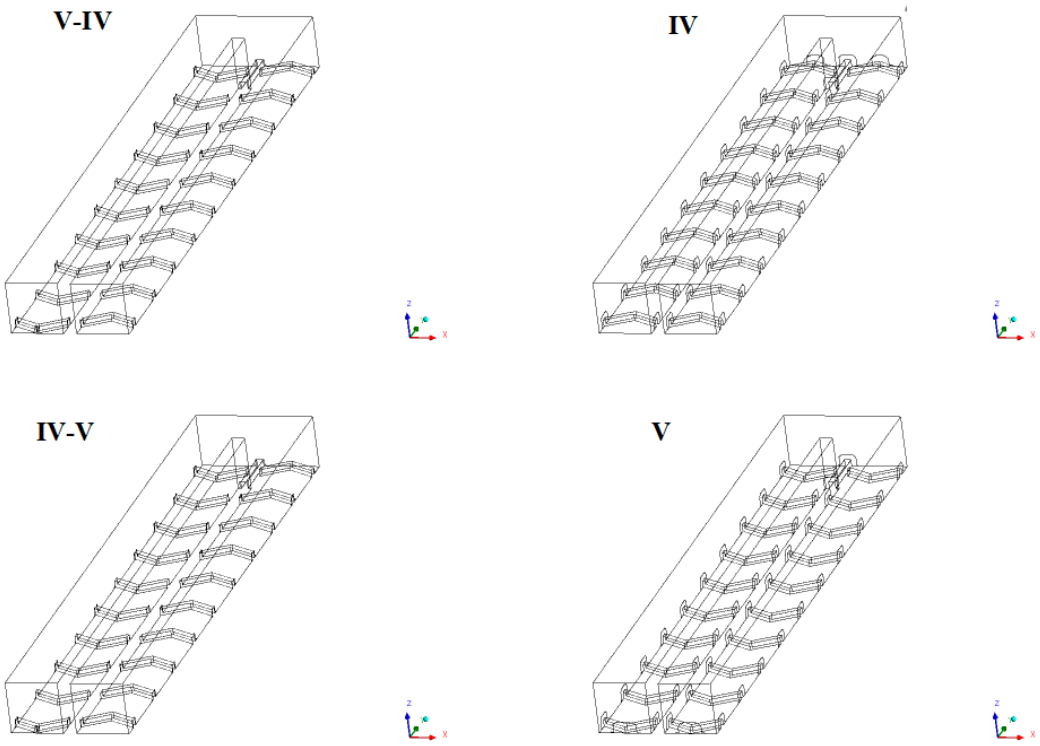

Figure 5.1 Isometric View of all the continuous Rib arrangement

Figures 5.1 and 5.2 show the isometric and top view of continuous rib test section. In Fig. 5.1 the arrangement and orientation of the ribs can be clearly seen which shows how the ribs are arranged on one surface of channel. The ribs are placed on the bottom side of the channel which is given constant heat flux. There is a 90^{o} ribs in the turn section for all the section considered. These ribs enhance heat transfer which are calculated and compared for different Reynolds Number.

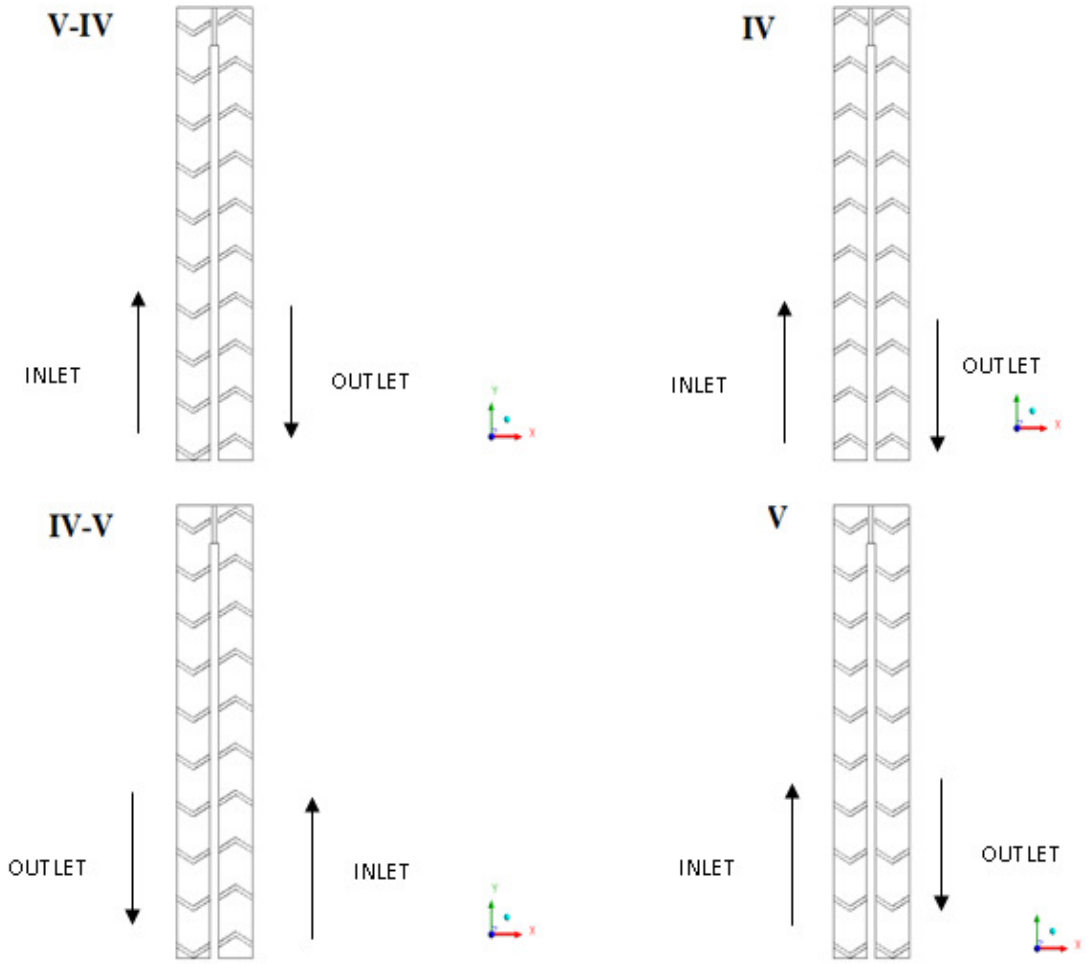

Figure 5.2 Front View of all the continuous Rib arrangement

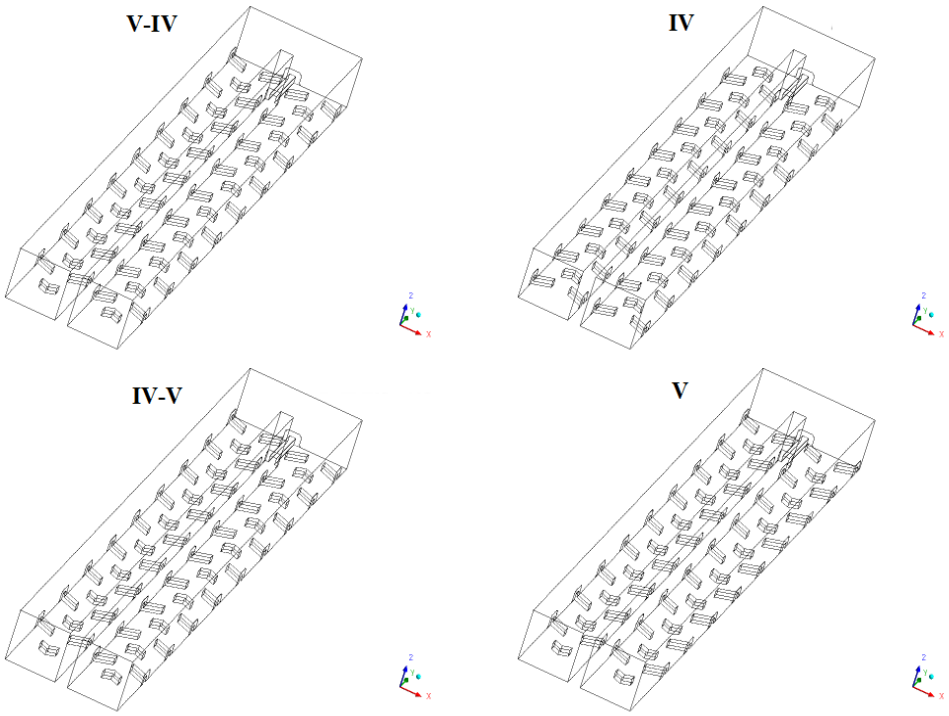

Figure 5.3 Isometric View of all the broken Rib arrangement

Figures 5.3 and 5.4 show the isometric and top view of broken rib test section. In Fig. 5.3, the arrangement and orientation of the broken ribs is on one surface of the cooling channel. The ribs are placed on the bottom side of the channel which is given heat flux. There is a 90^{o} ribs in the turn section for all the section considered for broken ribs as well.

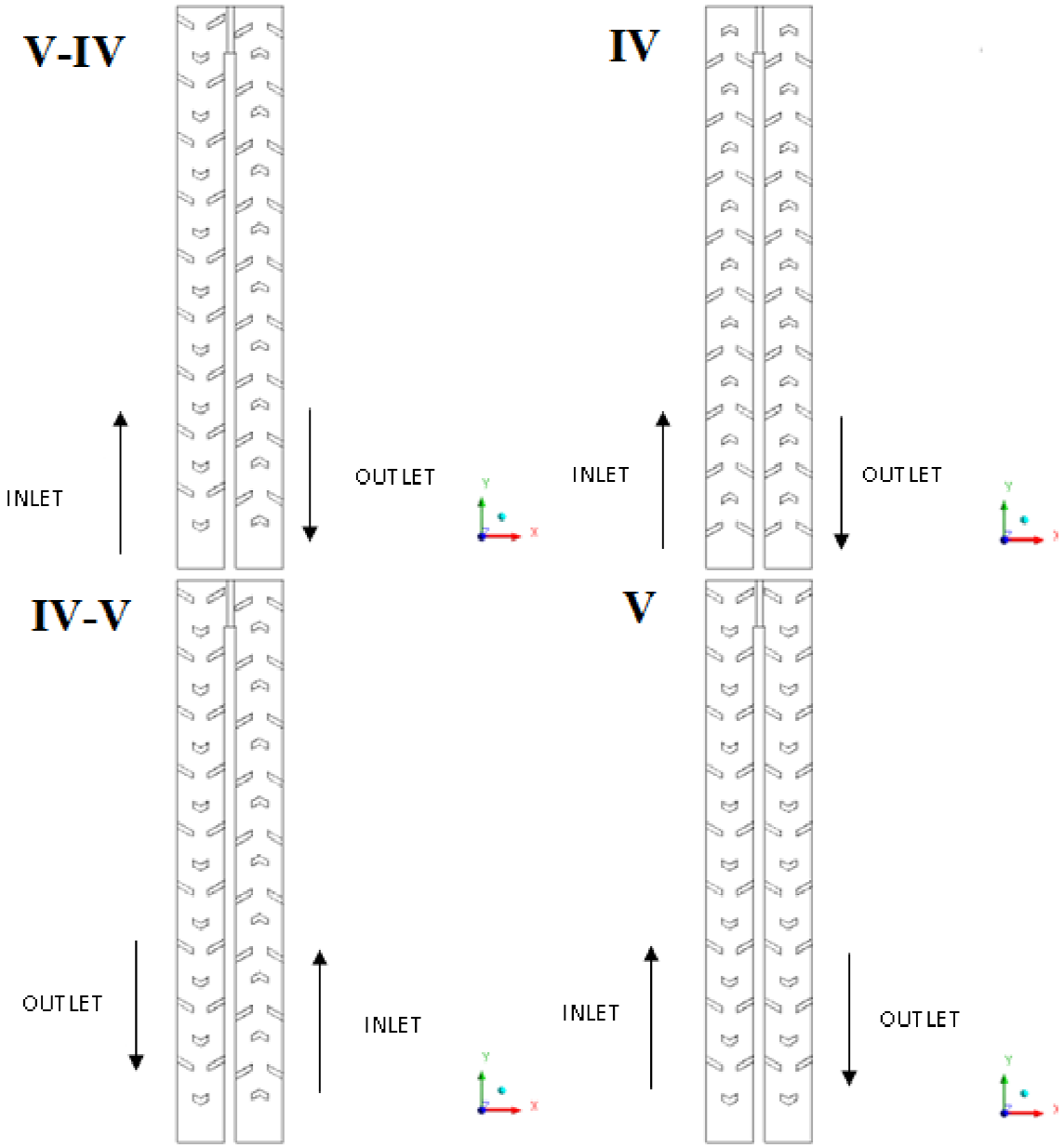

Figure 5.4 Front View of all the broken Rib arrangement

5.3 Heat Transfer Calculation:

First step of experimental work is to calculate the total heat flux being provided to the heating element. For calculating the heat transfer, average temperature of the overall heating surface is calculated using the arrays of thermocouple on heating surface. This temperature provides the overall temperature but for accurate prediction of surface temperature, the heat loss due to convection and conduction are also considered for overall heat transfer prediction during the experiments. To exclude the convection losses during experiment, heating surfaces are insulated and once again an array of thermocouples is used to get the temperature of heated surface. To calculate or exclude the conduction losses temperature of the lower surface of the Plexiglas are calculated. Insulation is provided for Plexiglas lower surface to reduce the loss below. Once conduction losses and convection losses are calculated then net heat supplied can be calculated using Eq. 4.5.

After a series of trails finally variac was kept at 48.4 V supply and the resistance of the heating section used during the experiment is measured to be 29.1 Ω . The thermal conductivity of the Plexiglas is 0.2 W/m-K which is used to calculate the loss. For this average temperature at the bottom of the surface calculated is used.

After getting the values the Eqs. 4.5 and 4.6 were used to get the total heat supplied to the heating element.

$$Q''_{net} = 2087.6 \text{ W/m}^2 \tag{5.1}$$

Once the net heat flux supplied is calculated based on the temperatures of different conditions to calculate conduction and convection losses, this net heat flux is used for post processing of all the results. This will provide accurate prediction of heat transfer

enhancement for the cases considered in this study. For comparison with numerical simulation the same heat flux are used.

5.4 Results and Discussion:

A. Continuous Ribs Results:

This section discusses Nusselt Number ratio which are depiction of how the heat transfer enhancement is changing throughout the channel which can be used for heat transfer coefficient prediction. Figs. 5.5, 5.6 and 5.7 show the Nusselt number ratio comparison for all the continuous ribs at different Reynolds Number of 21,000, 56,000 and 85,000. The experimental Nusselt Number being normalized with theoretical Nusselt number. From these figures, it is clearly depicted that the best arrangement for heat transfer is V-IV as compared to other ribs. In the turn region because of turning effect and Coriolis effect of the flow the heat transfer is enhanced for all cases and leading to a spike in Nusselt number ratio.

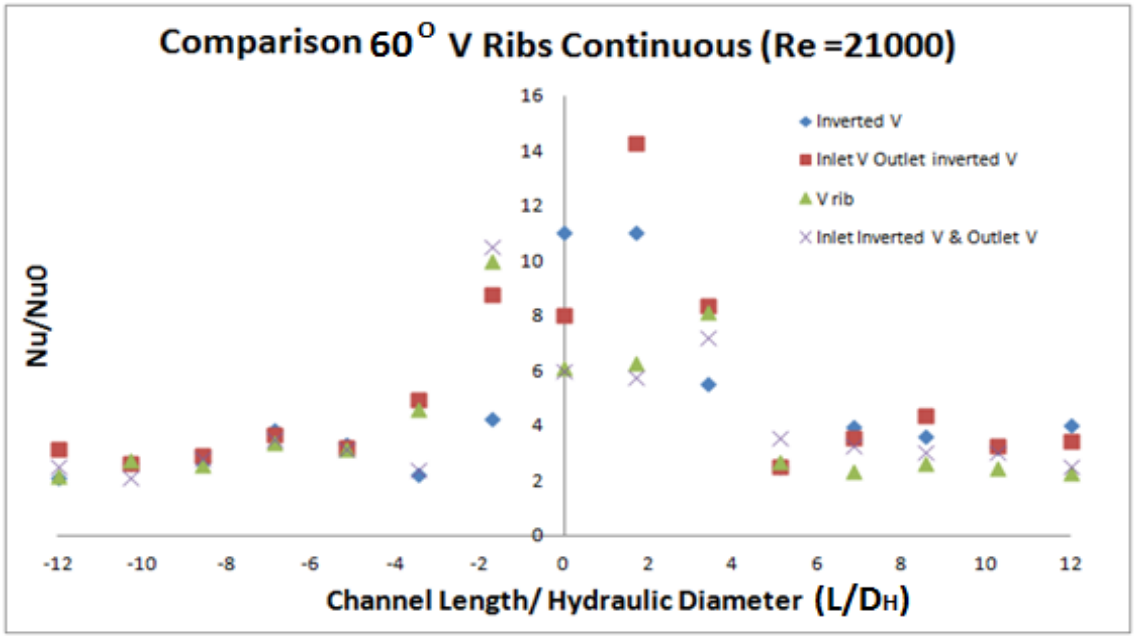

Figure 5.5 Comparison of continuous rib Nusselt Number @ Re =21000

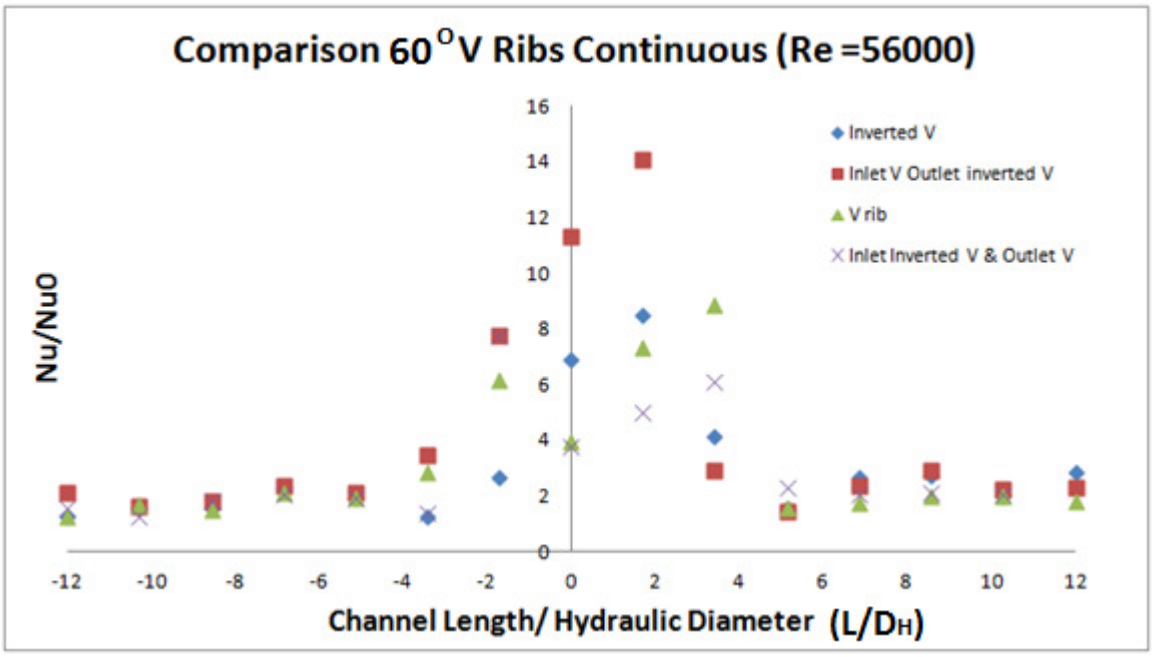

Figure 5.6 Comparison of continuous rib Nusselt Number @ Re =56000

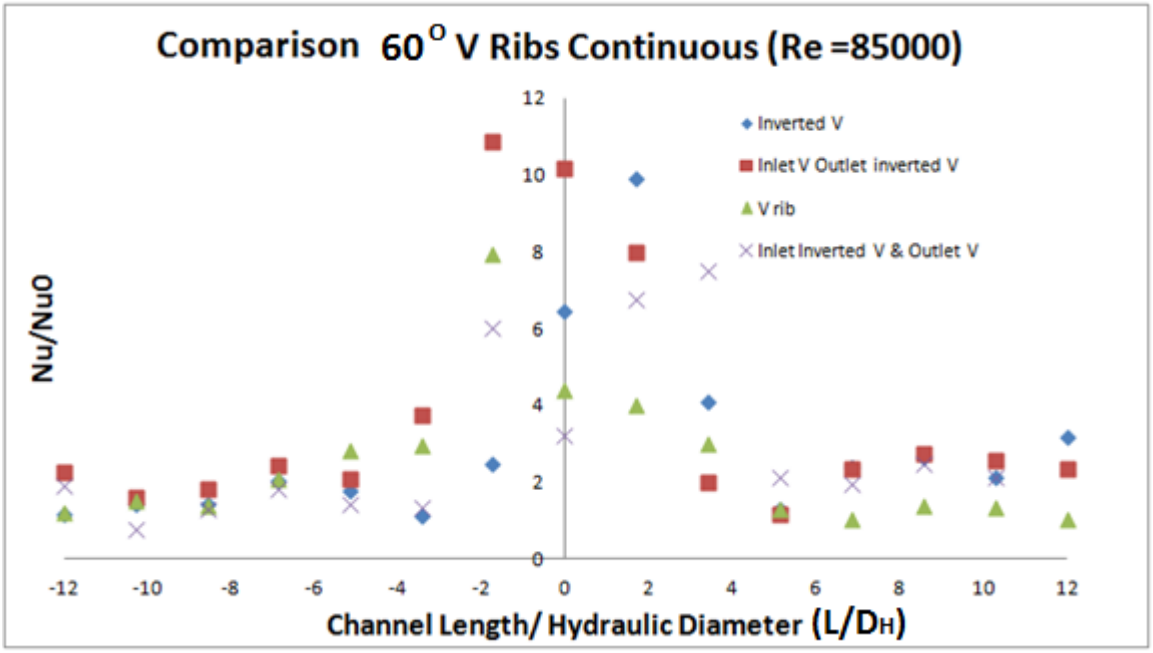

Figure 5.7 Comparison of continuous rib Nusselt Number @ Re =85000

Negative values on X axis depicts the Inlet section and positive values are post turn section that is second pass of the cooling channel. -2 to 2 is the turn section for channel. Zero value on abscissa (X-axis) are the middle of the bend section in cooling channels considered. The important thing to see in Fig. 5.5 is that for Reynolds number 21,000 in the first pass the Nusselt Number ratio is almost around 3-5 and in the second pass it is around 2-4 for all the cases. The ratio spikes in the turn region for all the cases which is because of turning effect and the flow impinges on the surface post turn. These spikes are further enhanced because of the ribs in the channel. If the ratios are closely monitored they can clearly predict that the ratio are high for V-IV continuous rib as compared to the other configurations. V rib are the next best configurations with higher in post turn section. Inverted ribs are next to V rib configurations and the IV-V are the worst performer in terms of heat transfer. Similar profiles of Nusselt Number are observed in Figs. 5.6 and 5.7 for Reynolds Number 56,000 and 85,000 except the ratio are slightly less.

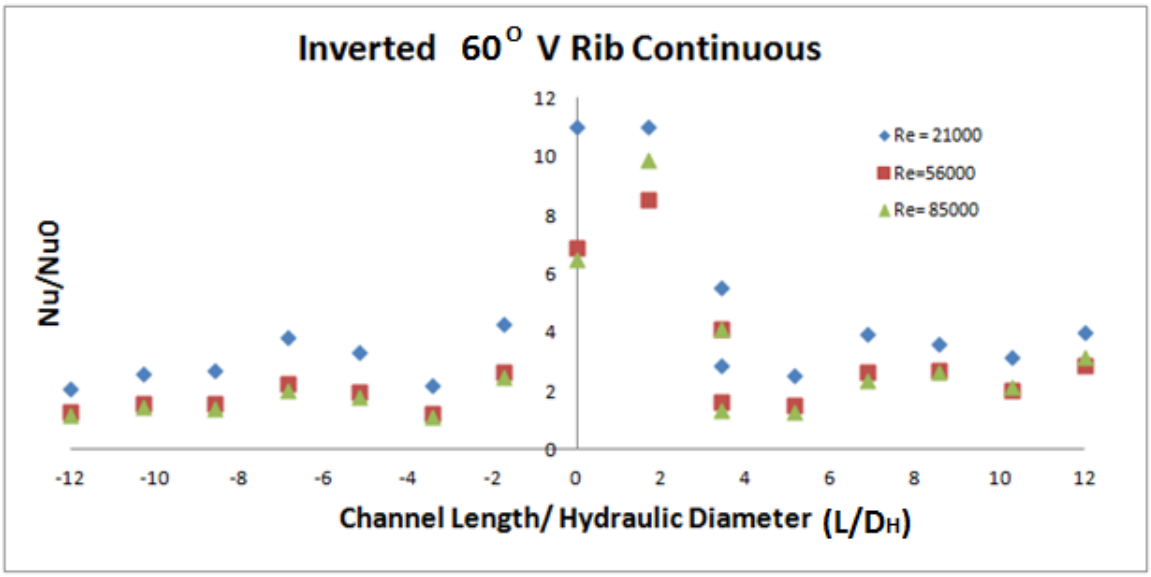

Figure 5.8 Comparision of Inverted 60° continuous rib for different Reynolds Number

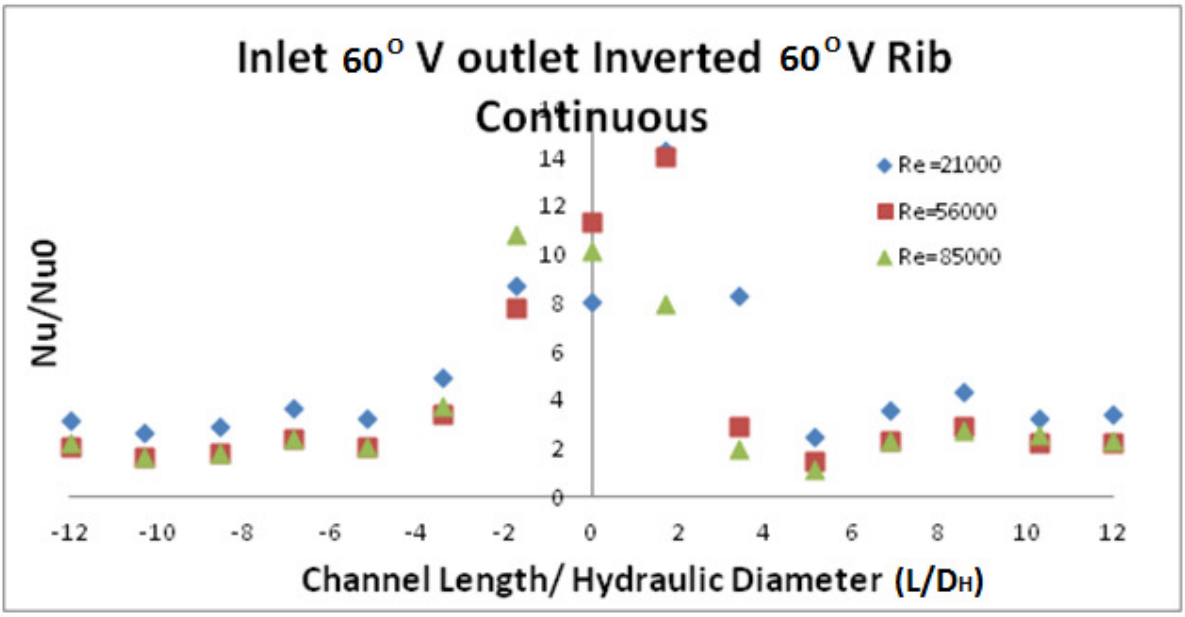

Figure 5.9 Comparision of Inlet 60° V and outlet 60° V Rib continuous rib for different Reynolds Number

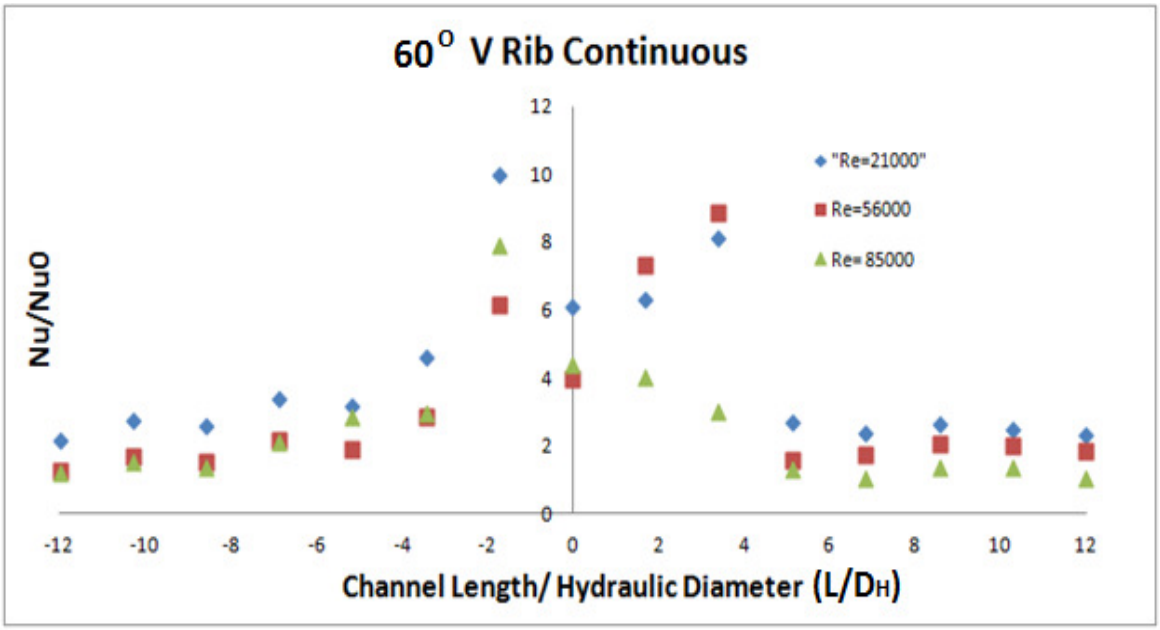

Figure 5.10 Comparision of 60° V Rib continuous rib for different Reynolds Number

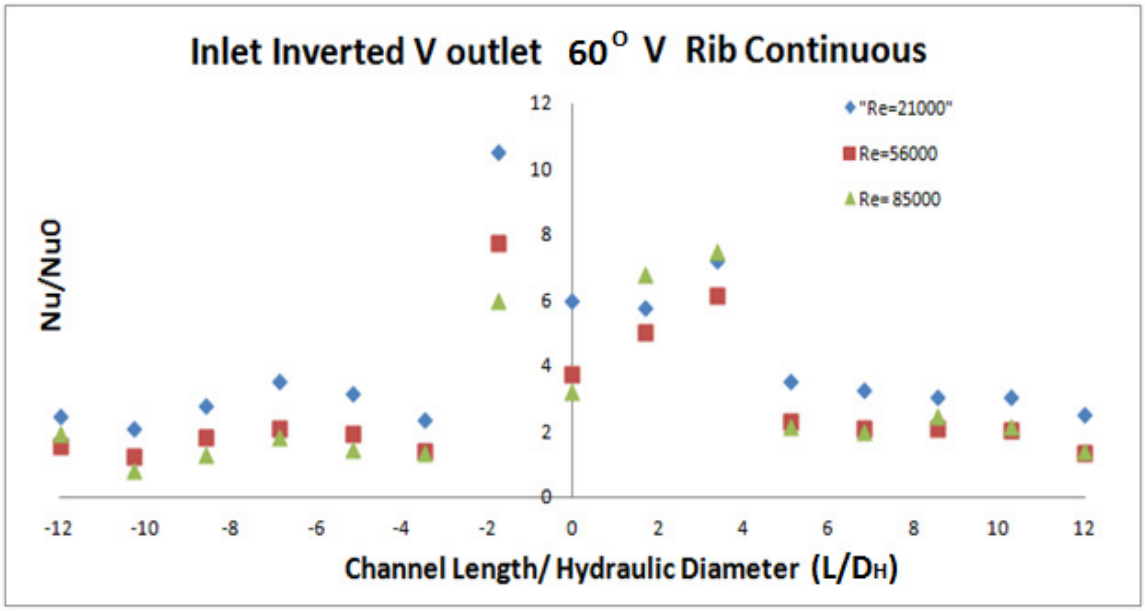

Figure 5.11 Comparison of 60° Inlet Inverted V and Outlet 60° V Rib continuous rib for different Reynolds Number

Figure 5.8 shows comparison of IV continuous rib at different Reynolds number to show the effect of Reynolds Number on heat transfer. This figure shows how in the throughout channel Nusselt Number ratio decreases with increase in Reynolds Number. The same nature of profile can be seen in the Fig. 5.9 for V-IV, Fig. 5.10 for V and Fig. 5.11 for IV-V. Overall the best configuration is V-IV and the worst being the IV-V. The important conclusion being V pointing towards the upstream always enhances the heat transfer. For this reason V-IV is the best profile.

Broken Ribs Results:

This section discusses Nusselt Number ratio throughout the channel for Broken V ribs. The experimental Nusselt Number being normalized with theoretical Nusselt number. Figs. 5.12, 5.13 and 5.14 show the Nusselt number ratio comparison for all the continuous ribs at different Reynolds Number of 21,000, 56,000 and 85,000. The

experimental Nusselt Number being normalized with theoretical Nusselt number. From these figure it is clearly depicted that the best arrangement for heat transfer is again V-IV for broken ribs as compared to other ribs. In the turn region because of turning effect and Coriolis effect of the flow the heat transfer is enhanced for all cases and hence a spike in Nusselt number ratio.

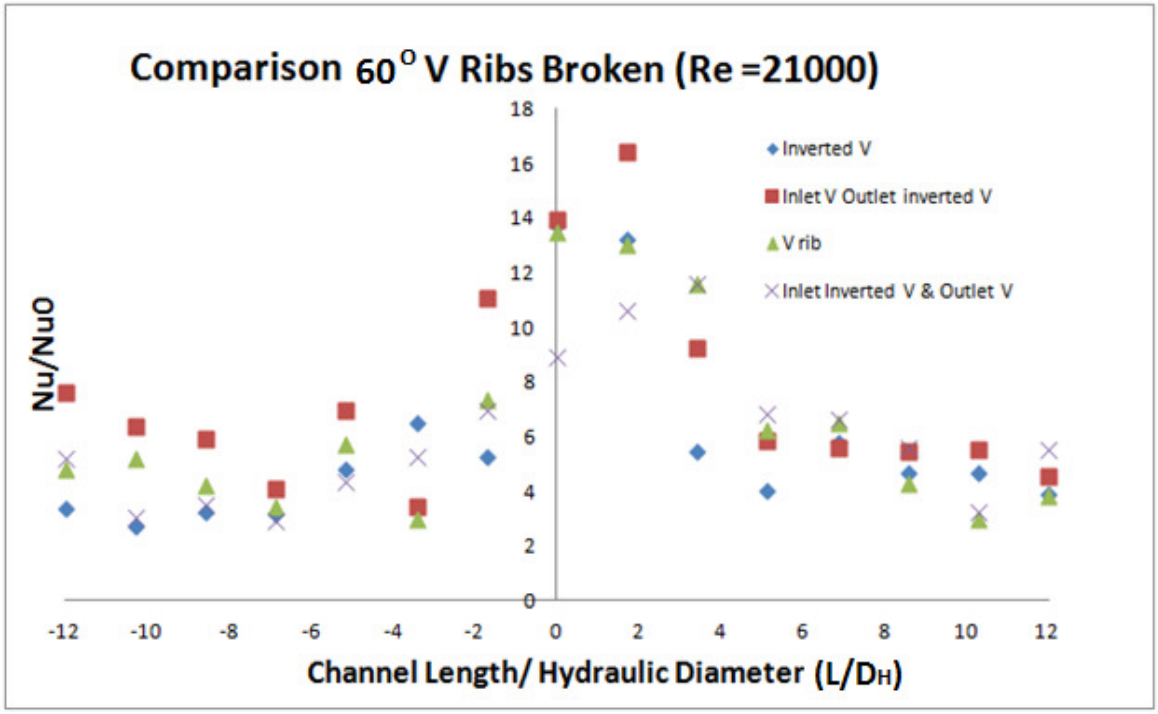

Figure 5.12 Comparison of broken rib Nusselt Number @ Re =21000

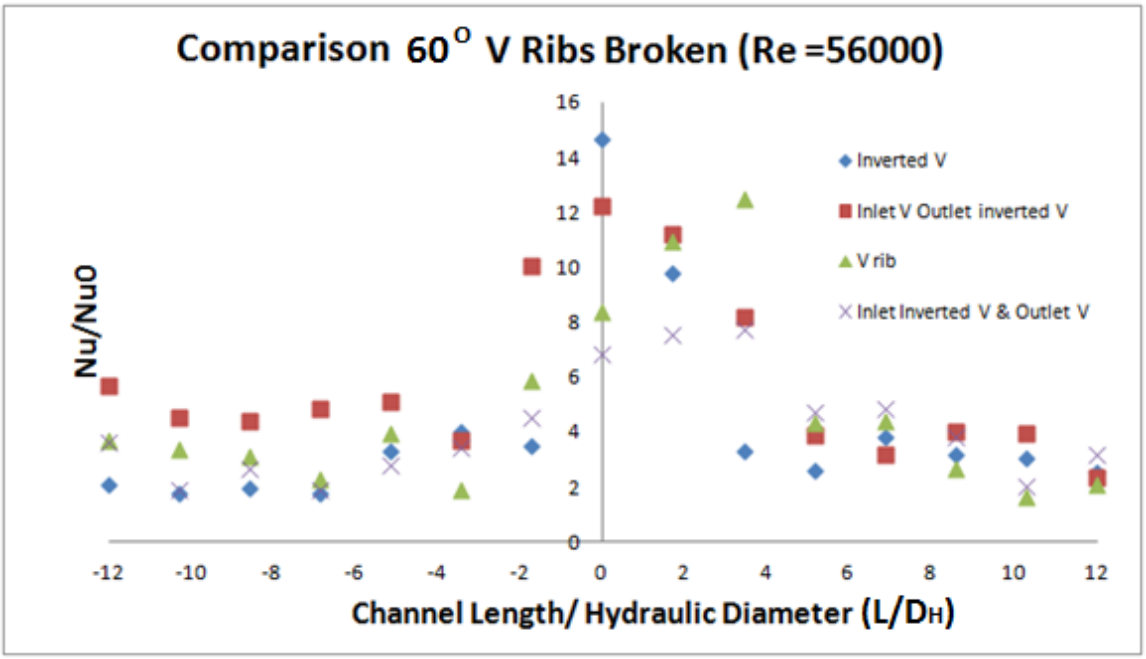

Figure 5.13 Comparison of broken rib Nusselt Number @ Re =56000

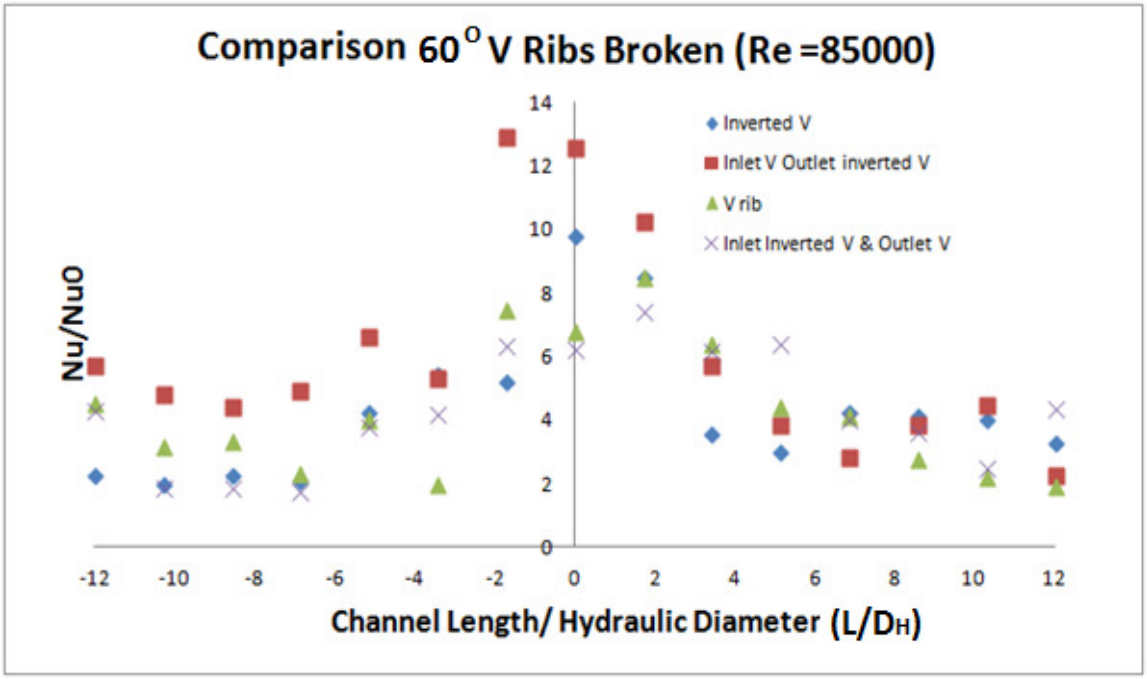

Figure 5.14 Comparison of broken rib Nusselt Number @ Re =85000

Negative values on X axis depicts the Inlet section and positive values are post turn section that is second pass of the cooling channel. -2 to 2 is the turn section for channel.

The important point in Fig. 5.12 is that for Reynolds number 21,000 in the first pass the Nusselt Number ratio is almost around 3-7 and in the second pass it is around 3-6 for all the cases. The ratio spikes in the turn region for all the cases and that is because of turning effect and the flow impinges on the surface post turn. These spikes are further enhanced because of the ribs in the channel. Also Broken ribs produce higher ratio as compared to continuous ribs due to higher turbulence and recirculation through out the channel in case of broken ribs. The ratios clearly predict that the ratio are high for V-IV broken rib as compared to the other configurations. V rib are the next best configurations with higher in post turn section. Inverted ribs are next to V rib configurations and the IV-V are the worst performer in terms of heat transfer. Similar profiles of Nusselt Number are observed in Fig. 5.13 and 5.14 for Reynolds Number 56,000 and 85,000 except the ratio are slightly less.

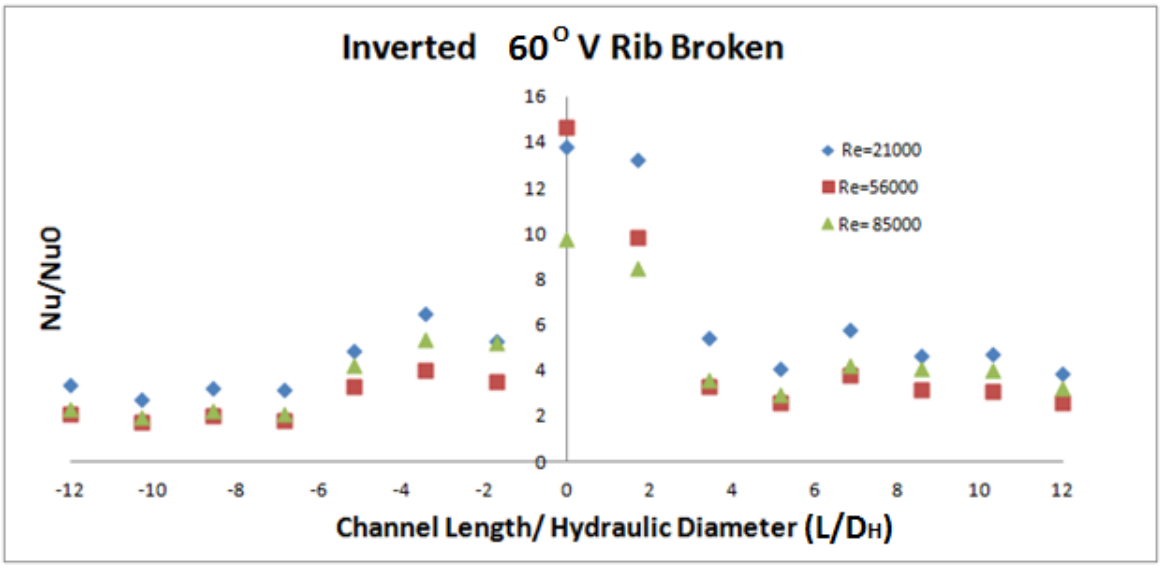

Figure 5.15 Comparision of Inverted 60° broken rib for different Reynolds Number

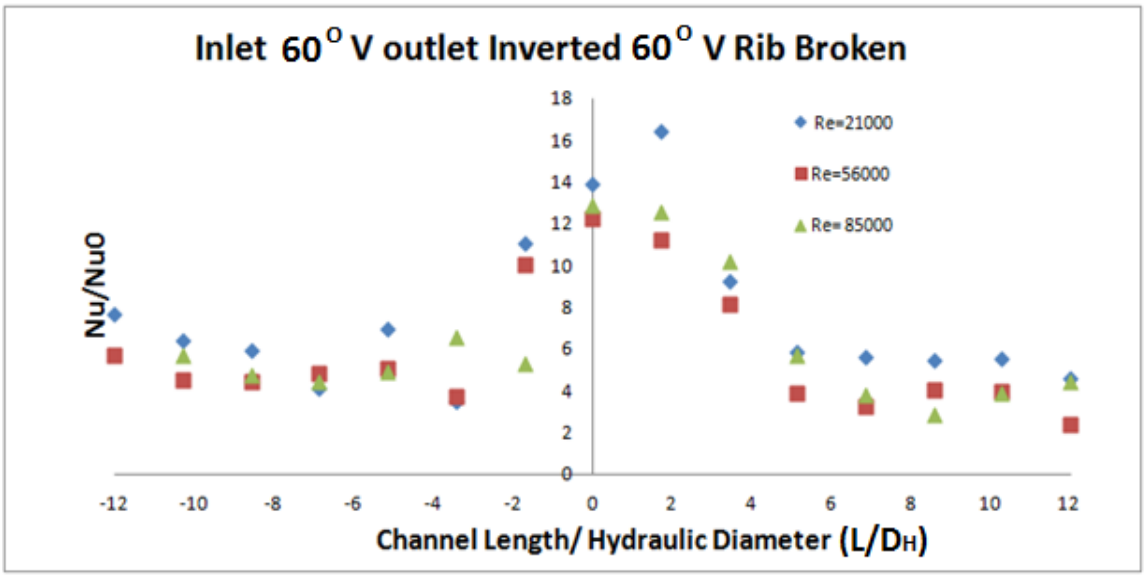

Figure 5.16 Comparison of Inlet 60° V and outlet 60° V Rib broken rib for different Reynolds Number

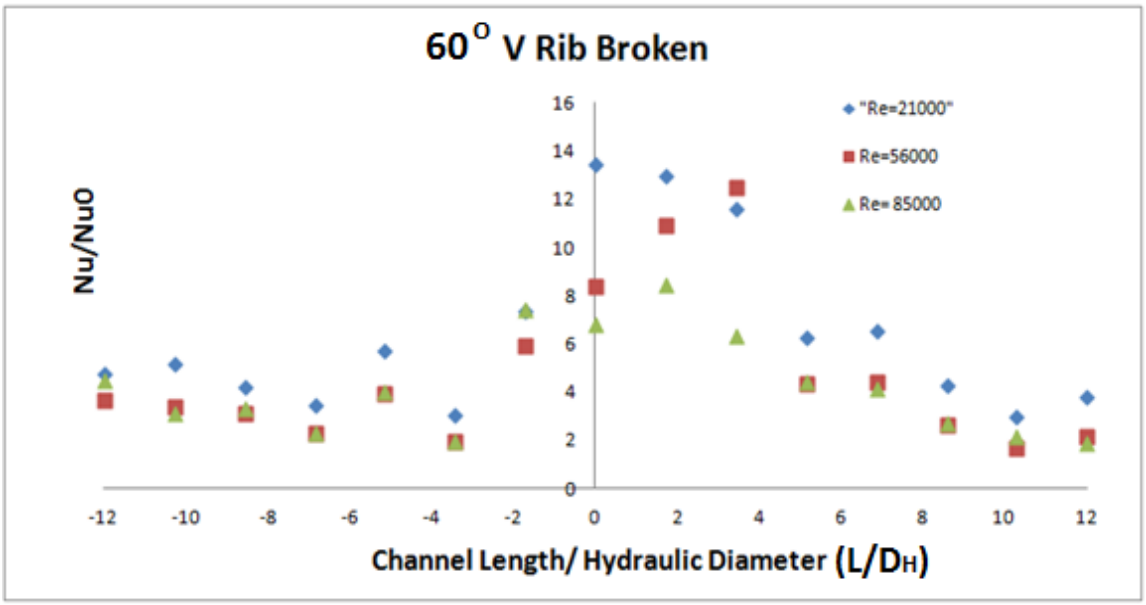

Figure 5.17 Comparison of 60° V Rib broken rib for different Reynolds Number

Figure 5.15 shows comparison of IV continuous rib at different Reynolds number to show the effect of Reynolds Number on heat transfer.

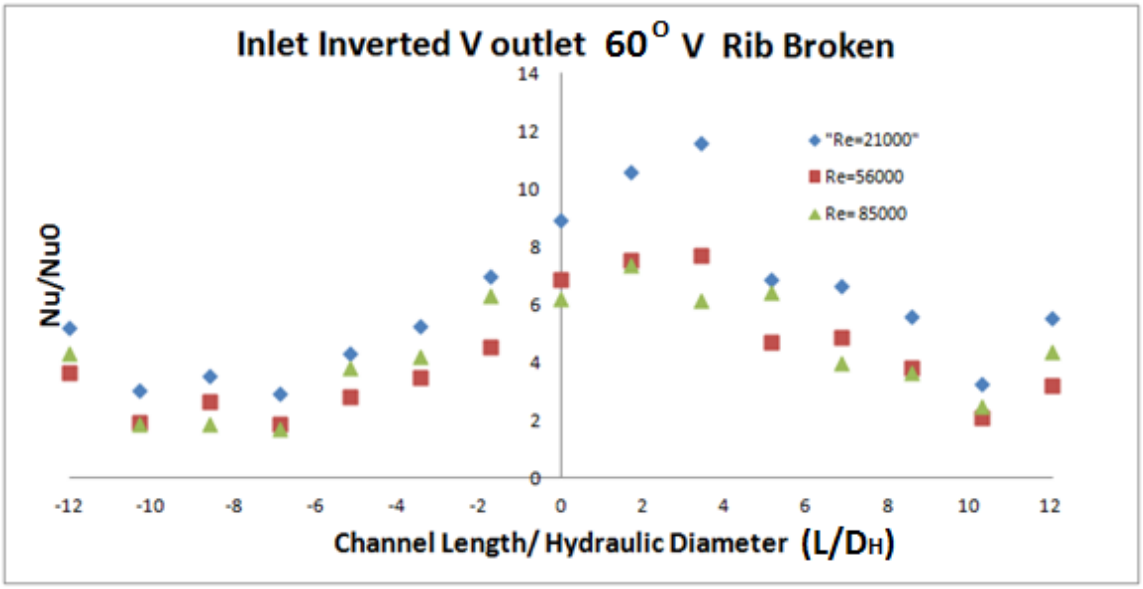

Figure 5.18 Comparison of 60° Inlet Inverted V and Outlet 60° V Rib broken rib for different Reynolds Number

This figure shows how throughout channel Nusselt Number ratio decreases with increase in Reynolds Number. The same nature of profile can be seen in the Fig. 5.16 for V-IV, Fig. 5.17 for V and Fig. 5.18 for IV-V. Overall the best configuration is V-IV and the worst being the IV-V. The important conclusion being V pointing towards the upstream always enhances the heat transfer. For this reason V-IV is the best profile.

Broken and Continuous Combined Results:

Figure 5.19 shows comparison of IV continuous and broken rib at different Reynolds number. It shows that as the Reynolds number increases the ratio decreases. It again shows and reiterates that as the Reynolds Number increases then the ratio decreases for both cases. Also with broken ribs the ratio are on the higher side for all the cases. Similar profile pattern are for other ribs as well seen in Fig. 5.17 for V-IV, Fig. 5.18 for V and

Fig. 5.19 for IV-V. Comparisons clearly show that the broken ribs are better performing in terms of heat transfer.

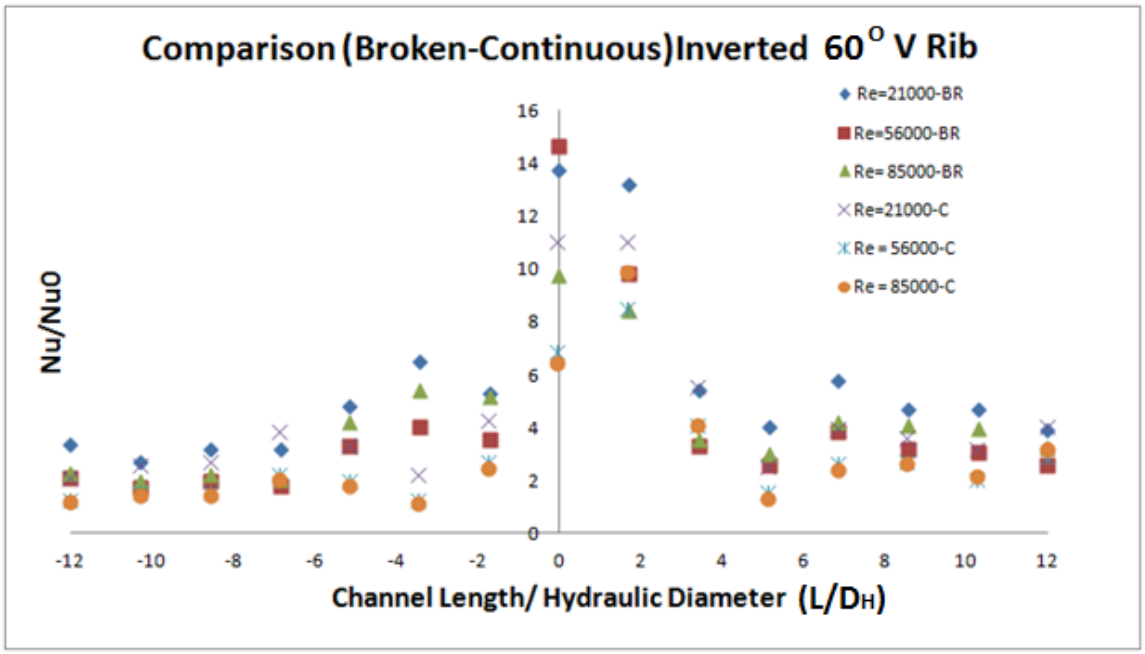

Figure 5.19 Comparison of Inverted V for Broken and Continuous ribs at different Reynolds Number

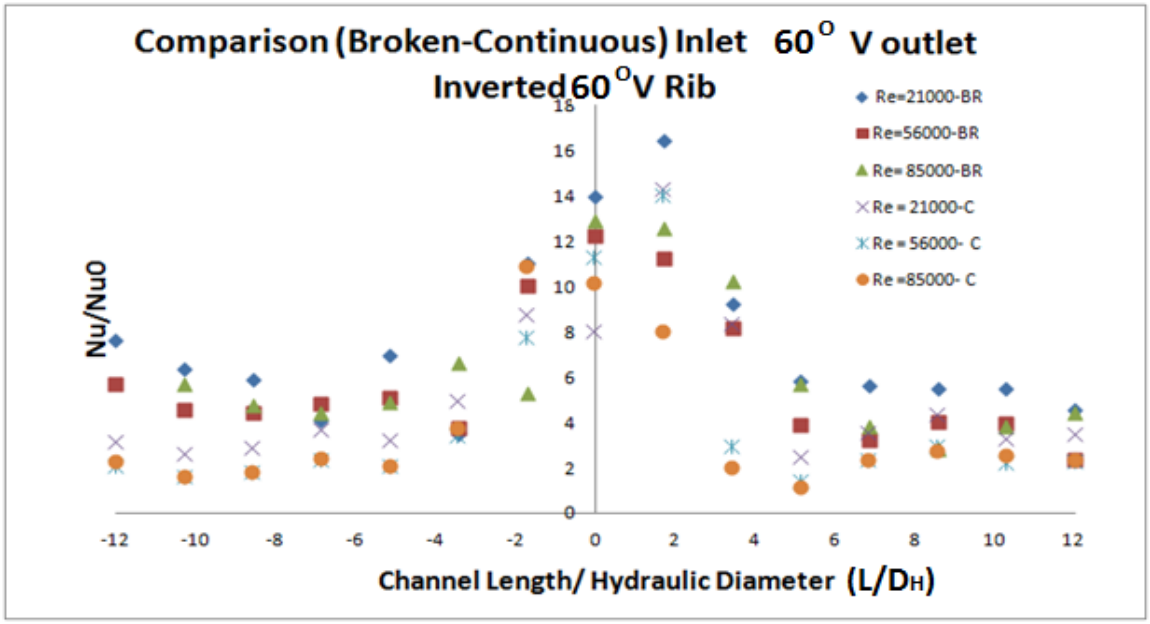

Figure 5.20 Comparison of Inlet V and outlet Inverted V for Broken and Continuous ribs at different Reynolds Number

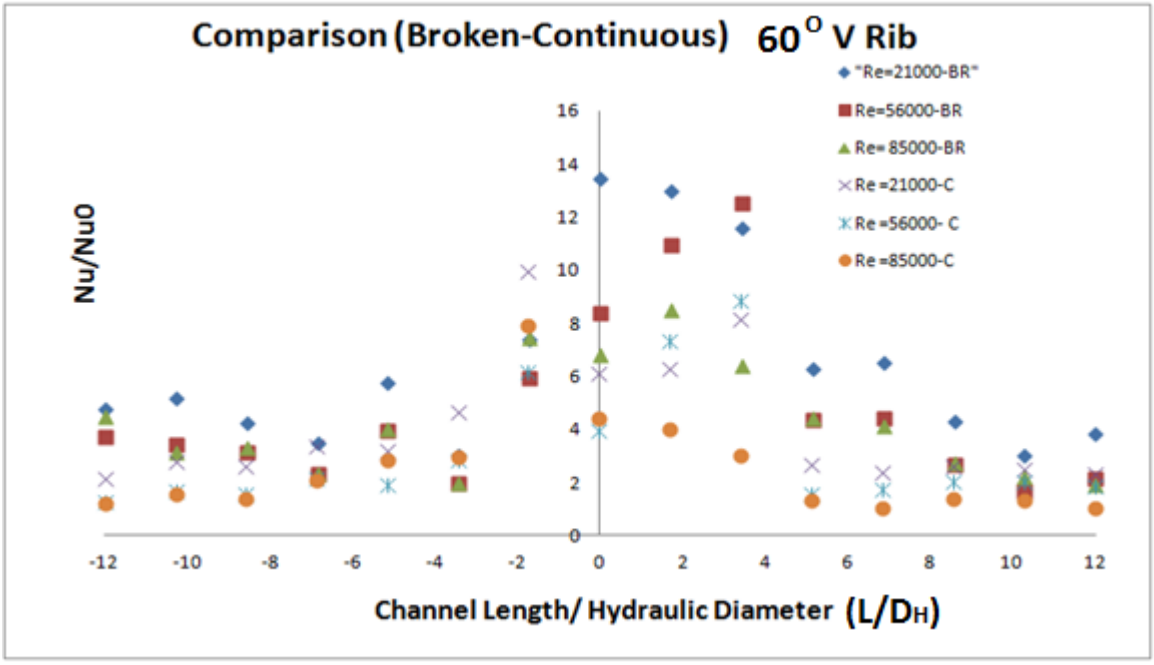

Figure 5.21 Comparison of V Ribs for Broken and Continuous ribs at different Reynolds Number

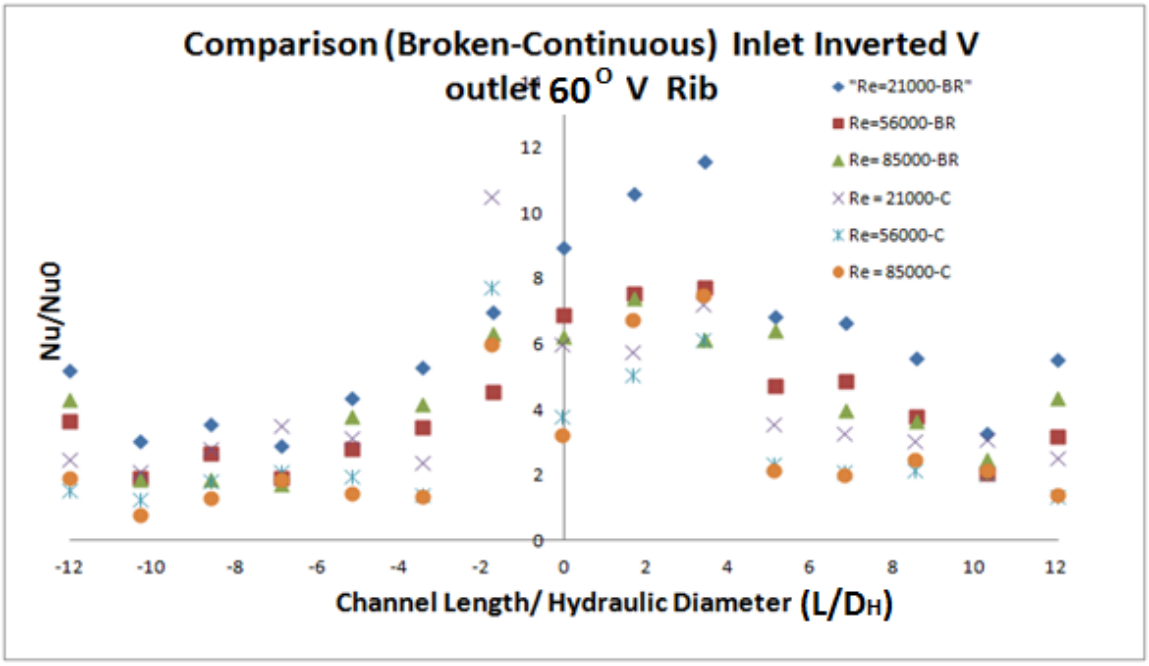

Figure 5.22 Comparison of Inlet Inverted V and Outlet V Ribs for Broken and Continuous ribs at different Reynolds Number

Overall seeing the above comparision of all the cases for Nusselts Number it can be clearly predicted that the broken ribs V-IV is the best configuration considered. In case for continuous case again V-IV is the best. V pointing towards the flow always enhances the heat transfer which are because of the flow being diverted through V channel in addition to recirculation and secondary flow development due to ribs. These explanation will be explained in the numerical analysis section in more detail.

5.5 Uncertainty Analysis:

As discussed in the previous section uncertainty analysis is done based on the equations used for calculating the ratio.

$$\frac{Nu}{Nu_0} = \left(\frac{D_H}{k}\right)\left(\frac{Q_{net}}{A(T_s - T_{bx})}\right)\left(\frac{1}{0.023 * Re^{\frac{4}{5}} * Pr^{.4}}\right)$$

The uncertainty of each variable is estimated that is

Steps Involved for the analysis of uncertainty were as:

1. For each parameter such as heat flux, area, Reynolds Number and temperature of surface which affects the Nusselt Number calculation, standard deviation are calculated.

2. The uncertainty of individual parameters is calculated based on 95% confidence level.

3. Upper and lower limit of combined results are also calculated based on 95% confidence limit.

Heat Transfer Area (A): ± 1.25%

Hydraulic Diameter (D_H): ± 1.12%

Reynolds Number (Re):± 1.51 % (Re= 21000), ± 2.95 % (Re= 56000), ± 4.21 % (Re= 85000).

Temperature (T): ± 0.46%

Net Heat Input (Q_{net}): ± 1.73%

Overall Nusselt Number: ± 3.3% for Re= 21000

± 3.9% for Re= 56000

± 4.6% for Re= 85000

Air Conductivity (k_T), Prandtl Number (Pr), Density (ρ) is considered to be constant during the uncertainty analysis.

Using the combined effect of all the parameters affecting the Nusselt Number ratio an overall uncertainty is calculated. From the uncertainty analysis it can be clearly predicted that it is mostly influenced by the temperature measured, heat input and velocity measurement.

CHAPTER 6: HEAT TRANSFER RESULTS AND DISCUSSION- NUMERICAL

6.1 General Description of Physical Models:

The geometrical models selected to compare the results of the numerical simulations are same as in the experimental study (which are discussed in the sections 4.4 and 5.2). The two-pass channels have the square cross-section of 5.08E-02 m, where each pass is 6.096 E-01 m long with L/D_H as 12. The rib height to channel width is (e/D_H) is 0.125 and rib pitch to height ratio is (P/e) is 10. A 90^o rib was placed along the divider wall in the middle of the 180^o turn for all ribbed channel. Detailed dimensions of the model selected for numerical analysis are shown in chapter 5.

Experimental studies till date have generally used typical rib height of approximately 5% to 12% of channel hydraulic diameter and P/e ratio varying from 7-15. Research has also indicated that for high Reynolds Number, a P/e ratio of 10 has produced good results, leading to the idea of this geometrical model. The rib configuration for one pass in case of 60^o V was done and produced good results. In my set up, I have not only extended the study to two pass; but have also looked at multiple different arrangements of 60^o V ribs. Extension of this work led to studying of broken V channels as well. These results bring us closer to the possibility of future parametric studies varying pitch length and aspect ratios.

The location of flow separation, reattachment and secondary flow can be identified from the detailed heat transfer phenomenon. In the present study, Reynolds numbers of 21000, 56000 and 85000 are used for numerical simulation. The idea is to develop a method to predict heat transfer using the turbulence model selected.

6.2 Computational Details:

6.2.1 Overview:

To investigate the three-dimensional turbulent flow field and temperature variations in a rectangular two-pass channel with V rib turbulators for continuous and broken cases , *k*-ω SST and RSM turbulence models are employed for the numerical simulation. In real life situations, LES and DNS require large computing resources and hence *k*-ω SST and RSM turbulence model are considered for a detailed analysis of all the cases. The grids were generated using the ANSYS mesher. The governing equation of fluid flow and heat transfer are solved numerically using appropriate boundary conditions to achieve the results.

6.2.2 Governing Equations:

The governing equations for different variables can be expressed as follows:

Navier-Strokes Equation:

Mass conservation equation:

$$\frac{\partial \rho u_i}{\partial x_i} = 0 \tag{6.1}$$

Momentum equation:

$$\frac{\partial \rho u_i u_j}{\partial x_j} = -\frac{\partial p}{\partial x_i} + \frac{\partial}{\partial x_j}\left[\mu\left(\frac{\partial u_i}{\partial x_j} + \frac{\partial u_j}{\partial x_i}\right) - \rho\overline{u_i' u_j'}\right] \tag{6.2}$$

Energy equation:

$$\frac{\partial \rho u_j T}{\partial x_j} = \frac{\partial}{\partial x_j}\left[\frac{\mu}{\mathrm{Pr}}\frac{\partial T}{\partial x_j} - \rho\overline{u_j' T'}\right] \tag{6.3}$$

6.2.3 Boundary Conditions:

For this paper, the major requirement is the analysis and simulation of continuous and broken rib turbulators. The boundary conditions are assumed as the experimental conditions to validate the results. All the two pass square channel walls are assumed to be of constant heat flux. No-slip velocity conditions are applied at all walls. The inlet velocity is considered to be based on the Reynolds number. A uniform velocity and temperature of the air are set at the inlet and a pressure outflow condition is chosen at outlet.

Table 6.1: Inlet and Boundary conditions used for Simulation

Inlet Velocity	Reynolds Number=21000, 56000 and 85000
Inlet Temperature	300K
Cooling Channel Wall Heat Flux	2087.6 W/m^2
Outlet Wall	Pressure Outlet
Fluid Used	AIR

Table 6.2: Fluid properties

Density(kg/m^3)	1.225
Viscosity(kg/m-s)	1.789E-5
Thermal Conductivity(W/m-K)	0.0242

Table 6.3: Inlet Turbulent Specification Method

Re= 21000	Turbulent Intensity (%) I	4.61
	Hydraulic Diameter (D_H, m)	5.08E+02
Re= 56000	Turbulent Intensity (%) I	4.08
	Hydraulic Diameter (D_H, m)	5.08E+02
Re= 85000	Turbulent Intensity (%) I	3.88
	Hydraulic Diameter (D_H, m)	5.08E+02

Table 6.4: Inlet Reynolds-Stress Specification Method

Re=21000	Dimensionless Reynold Stress $\frac{\overline{uu}}{(U_{in})^2}$	0.0021
	Dimensionless Reynold Stress $\frac{\overline{vv}}{(U_{in})^2}$	0.0021
	Dimensionless Reynold Stress $\frac{\overline{ww}}{(U_{in})^2}$	0.0021
Re=56000	Dimensionless Reynold Stress $\frac{\overline{uu}}{(U_{in})^2}$	0.0016

	Dimensionless Reynold Stress $\frac{\overline{vv}}{(U_{in})^2}$	0.0016
	Dimensionless Reynold Stress $\frac{\overline{ww}}{(U_{in})^2}$	0.0016
Re=85000	Dimensionless Reynold Stress $\frac{\overline{uu}}{(U_{in})^2}$	0.0015
	Dimensionless Reynold Stress $\frac{\overline{vv}}{(U_{in})^2}$	0.0015
	Dimensionless Reynold Stress $\frac{\overline{ww}}{(U_{in})^2}$	0.0015

Fluid is assumed to be incompressible with constant thermal physical properties and the flow is assumed to be three dimensional, turbulent, steady and non-rotating. The working fluid is dry air. In this study, enhanced wall treatment is used in RSM model for near wall treatment. The convergence criterions for continuity, momentum, RSM, *k*-ω SST equations are 10E-4 with 10E-6 for the energy equation. The detailed boundary conditions are given in tables 6.1 to 6.4.

6.2.4 Grid Dependence Tests:

The grids were generated using structured cut cells in Ansys mesher. For uniformity of mesh, same types of grid meshing formulations were used for all types of rib turbulators.

Reynolds Number 21000 was used for grid independence study and the parameter used was velocity in the turning region. To ensure the accuracy and validity of the numerical results, a careful check of the grid independence has been carried out. y+ values in case of *k*-ω *SST* as well as RSM are maintained below 1 for accurate prediction of the results. Figure 6.1 shows the grid independence test results. 5.5M cells were considered. Figure 6.2 shows y+ map along the first grid point for Reynolds Number of 21,000. The different grids selected can be seen in Fig. 6.3 and Fig. 6.4. The number of elements considered for all different ribs were around 5.5 Million. The structural mesh was specifically considered to achieve better results. Table 6.5 shows the resources used for both simulation models.

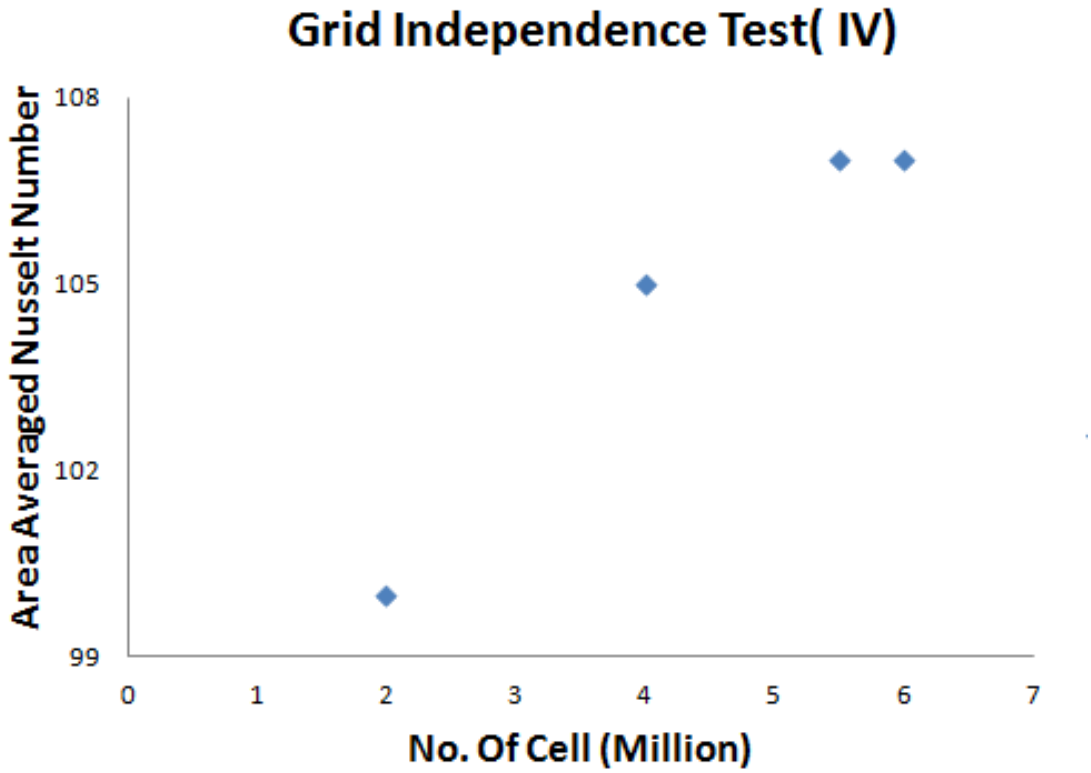

Figure 6.1: Grid Independent test results

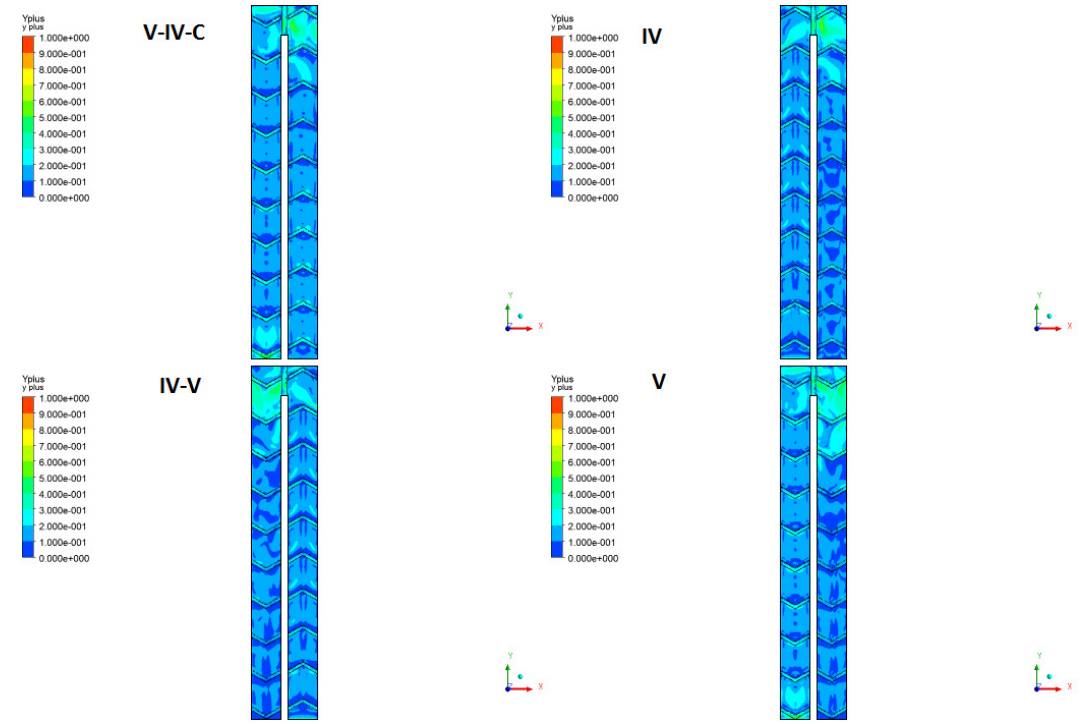

(a)

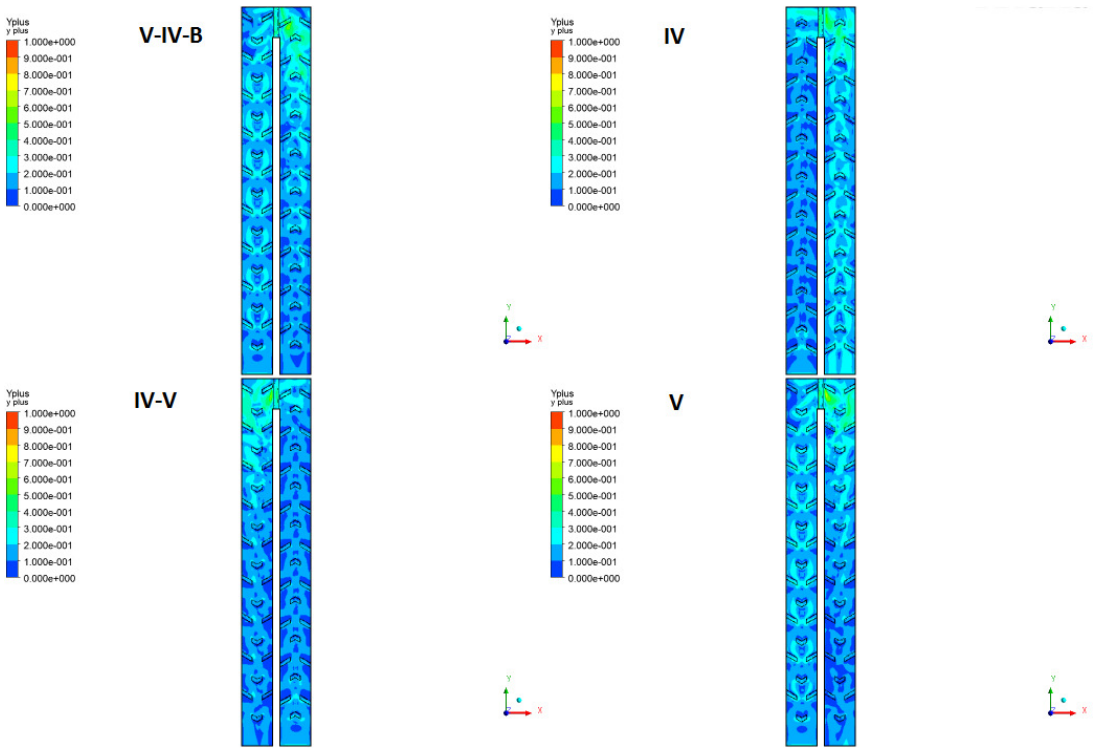

(b)

Figure 6.2: y+ value for the grid selected a) Continuous b) Broken

Table 6.5: Resource usage summary

SST k-omega	RSM
CPU time : 3.91E04 sec.	CPU time : 2.11E05 sec.
Max Memory : 1.10E04MB	Max Memory : 1.25E04MB
Max Swap :1.18E04 MB	Max Swap : 1.33E04 MB
Max Processes :17	Max Processes : 17
Max Threads : 30	Max Threads : 26

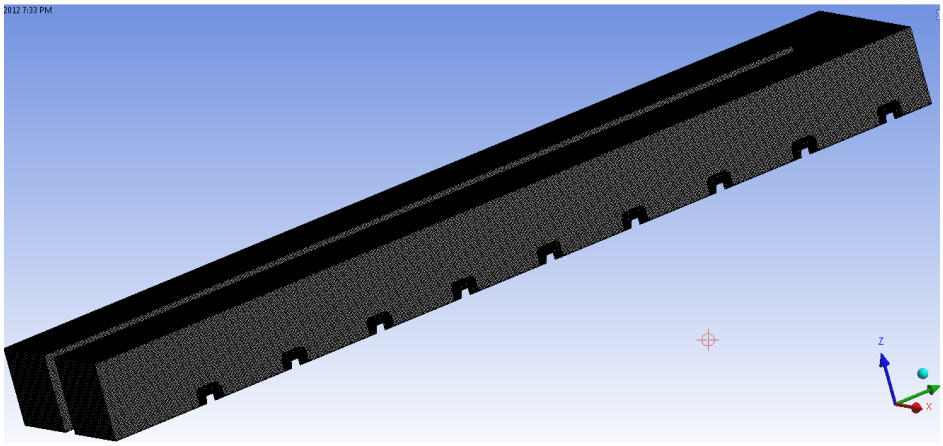

(a)

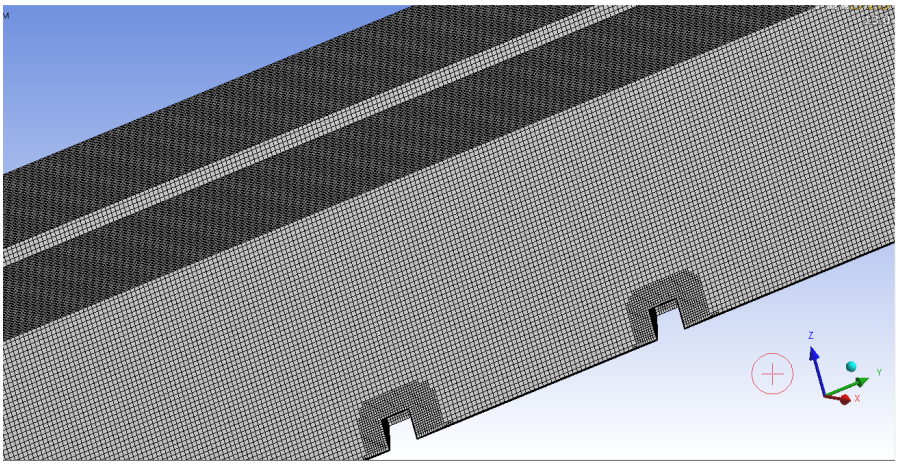

(b)

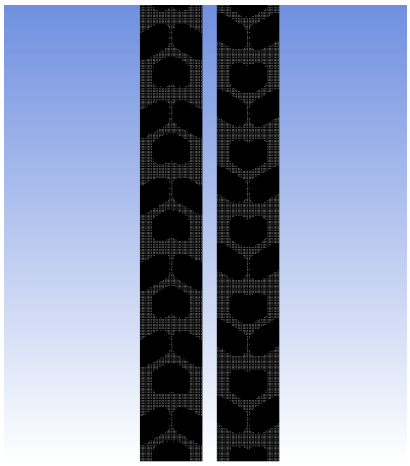

(c)

Figure 6.3: Mesh considered for Broken V-IV rib and IV-V (a) Complete channel View (b) Zoomed View of mesh from side (c)Mesh from Back view of channel

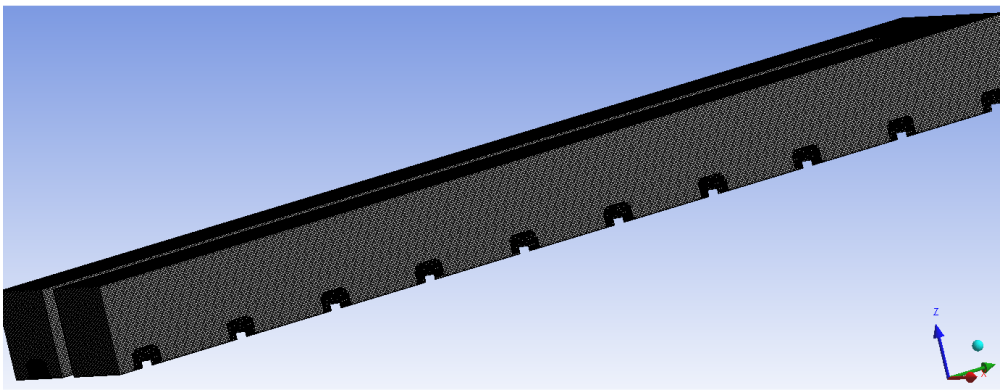

(a)

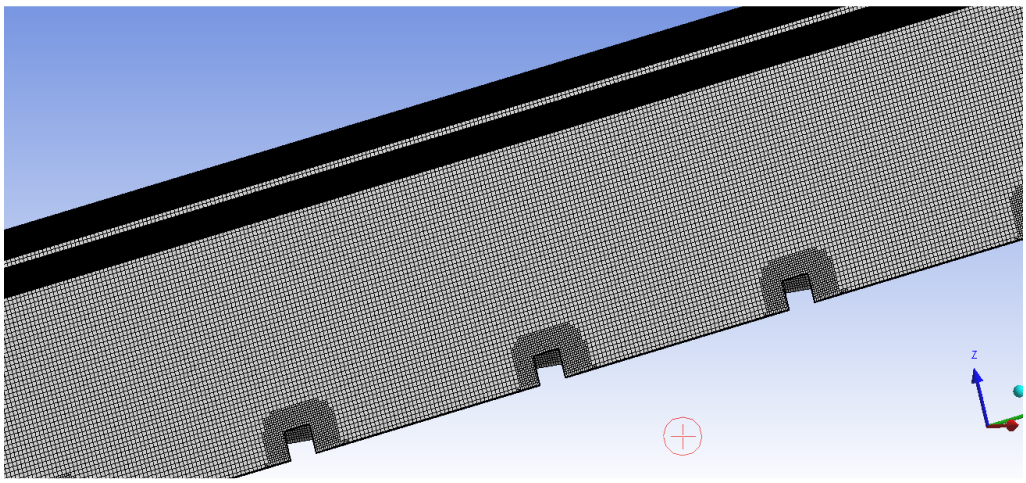

(b)

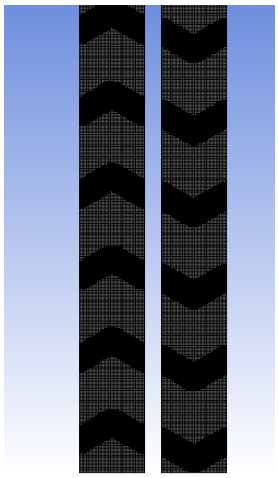

(c)

Figure 6.4: Mesh considered for Continuous V-IV rib and IV-V (a) Complete channel View (b) Zoomed View of mesh from side (c)Mesh from Back view of channel

The mesh is for all the configurations considered, for Continuous as well as Broken V. The view shown in these figures are (a) Complete channel View (b) Zoomed View of mesh from side (c) Mesh from Back view of channel. The mesh clearly shows how structured mesh are considered for simulation with very dense mesh near the wall to capture the near wall effect.

6.3 Heat Transfer Models:

Nusselt number can be calculated as

$$Nu = \frac{hD_h}{k_T} \tag{6.4}$$

Where, D_h is the hydraulic diameter and k_T is the thermal conductivity of the fluid (air in this case). This was done using five different locations at inlet, turn and outlet of the two pass channel. In the vicinity of the rib turbulator, high turbulence levels cause

sudden local increase in velocity magnitude. This increase in velocity and turbulence causes secondary flow and better mixing of the fluid in this area which results in very high Nusselt number. As the numerical data cannot have such high resolutions, the Nusselt number trends were observed rather that the actual distribution. For comparison, Nusselt number was normalized with the Dittus-Boelter relation

$$Nu_o = 0.023 \mathrm{Re}_D^{4/5} \mathrm{Pr}^{0.4}$$

(6.5)

Comparisons of Nusselt Number ratios for all different rib turbulators considered for Reynolds 21000, 56000 and 85000 using the shear stress model for k-ω SST and RSM model are shown in results and discussion.

6.4 Results and Discussion:

Nusselt Number Ratio:

For a complete analysis of the results, the heat transfer comparison of all Reynolds numbers considered for all different ribs are shown in the figure below. The results are shown for surface Nusselt number and Nusselt Number ratio.

A. Continuous Ribs:

Figure 6.5 (a) shows surface Nusselt Number and 6.5 (b) shows surface Nusselt number ratio for k-ω SST (Re = 21,000). In these figures, the cases are compared to each other for better understanding of Nusselt Number profile along the wall. Nusselt Number ratios as well as surface Nusselt Number have higher values for the case of V-IV continuous rib and low values for the IV-V ribs. The overall Nusselt Number is higher in

the mid section and on the rib due to recirculation in that region. Just after the ribs, the values are lower because of this being the separation region.

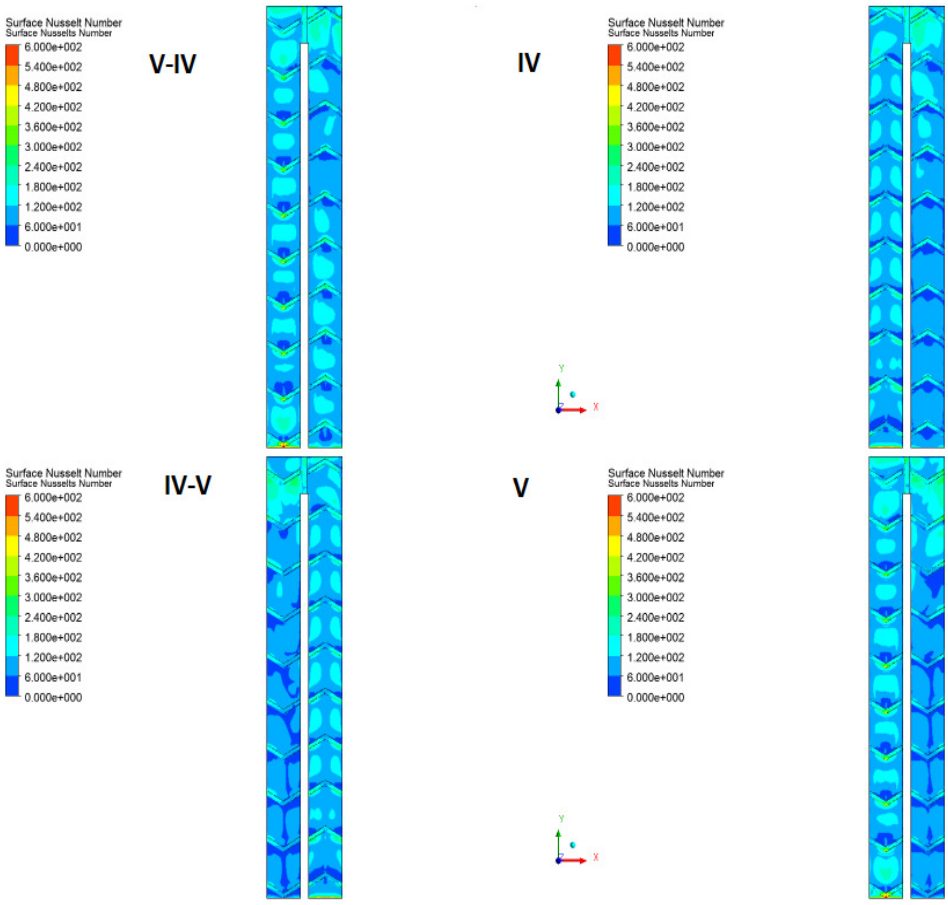

(a)

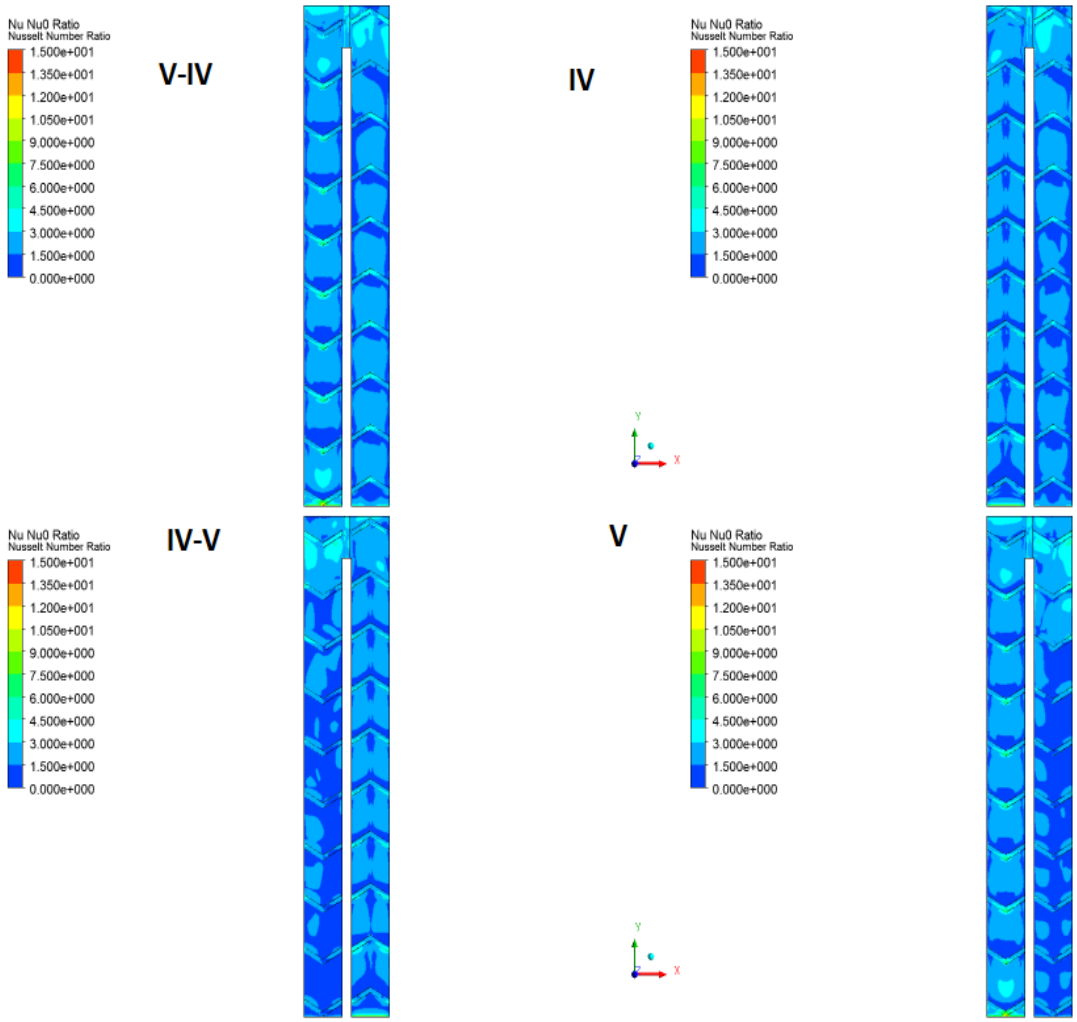

(b)

Figure 6.5: Continuous Rib (Re=21000, *k*-ω SST) (a) Surface Nusselt Number along wall (b) Surface Nusselt Number Ratio

B. Broken Ribs:

Figure 6.6(a) shows surface Nusselt Number and 6.6(b) shows surface Nusselt number ratio for *k*-ω SST (Re = 21,000).The cases are compared to each other for a better understanding of Nusselt Number profile along the wall. Nusselt Number ratios as well as surface Nusselt Number have higher values in the case of V-IV continuous ribs and lower values for the IV-V ribs. In case of broken ribs, there is an increase in surface Nusselt

Number and Nusselt Number ratio as compared to continuous ribs. These enhancements are due to shape of broken ribs and flow trips on them. On the V portion of the rib, flow bifurcates and secondary flow is developed.

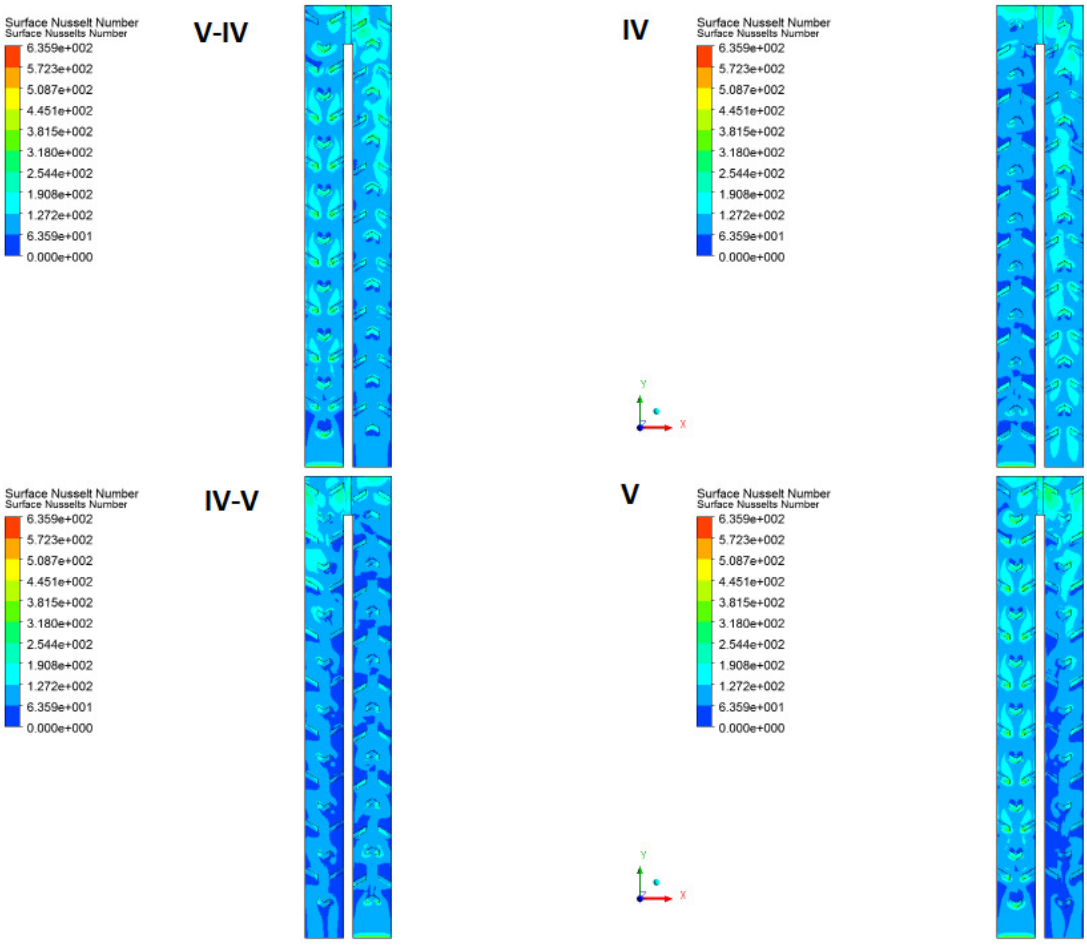

(a)

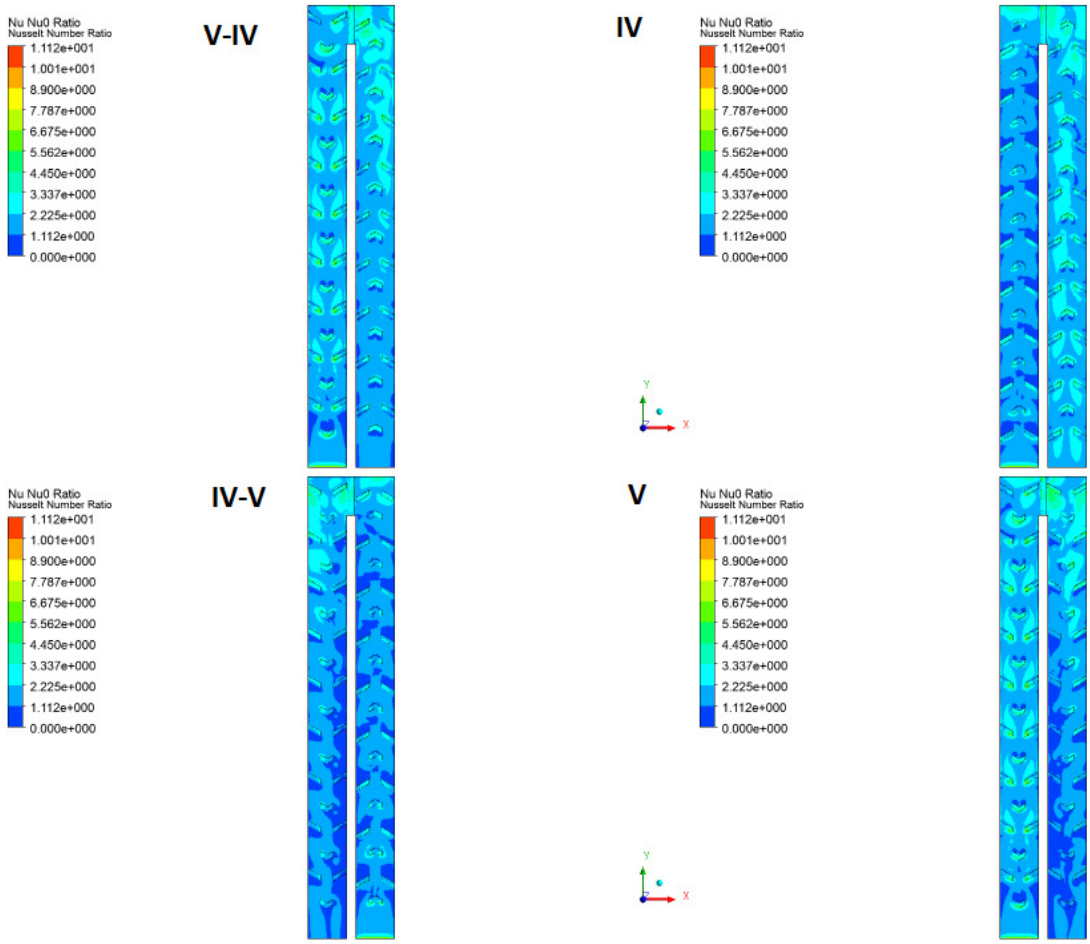

(b)

Figure 6.6: Broken Rib (Re=21000, *k*-ω SST) (a) Surface Nusselt Number along wall (b) Surface Nusselt Number Ratio

Velocity and Temperature Fields:

In order to provide a better understanding of enhanced heat transfer over the rib turbulators and to get the nature of the flow, velocity vectors and turbulent kinetic energy can be used. Nusselt number ratio is highest on top of the rib. Two secondary flow structures are generated at the tip of V and the Nusselt number ratios between the

ribs are uniform. Due to this mixing of fluid, the Nusselt number is enhanced. Downstream to the rib tip, there is low heat transfer because of flow separation. In the after turn region, Nusselt number ratios are higher near outer wall and low near the divider wall. This is due to centrifugal forces at the turn.

The two circulating regions occur at the first-pass channel corner and the second-pass corner. As the fluid flows through the 180-deg turn, centrifugal forces arising from the curvature and pressure differences (low pressure at inner wall while high pressure at outer wall) produce a pair of counter-rotating vortices in the turn. When the air travels through the 180-deg turn of the two-pass channels, areas of impingement, separation and recirculation are created.

Figures 6.7 and 6.8 show the turbulent kinetic energy profile for center location for inlet and outlet two pass channel. Because of the recirculation and separation region near the rib surface, there is high TKE (turbulent kinetic energy) which enhances heat transfer in the region. Only when the V pointed is upstream, TKE is higher near the surface. In the case of V pointing downstream, there is high TKE away from the surface which detoriates performance.

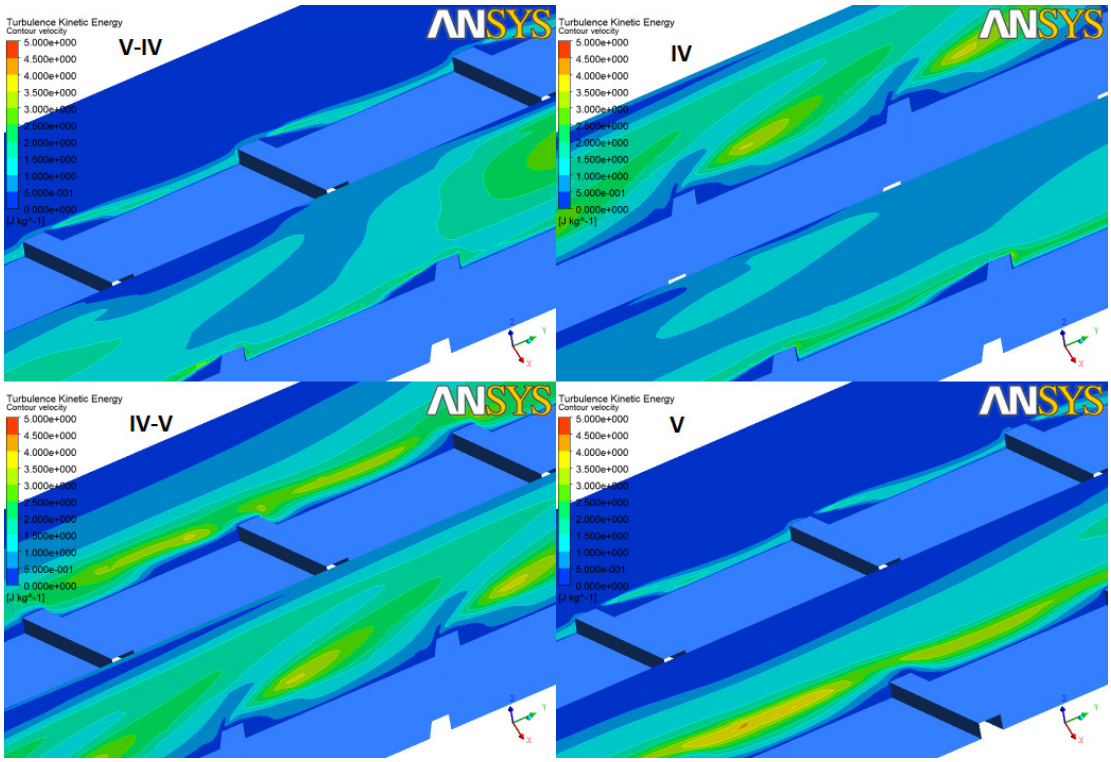

Figure 6.7: Continuous Rib Turbulent Kinetic Energy @ x = 0.5Dh, @ x= 1.75Dh

(Re=21000, *k*-ω SST)

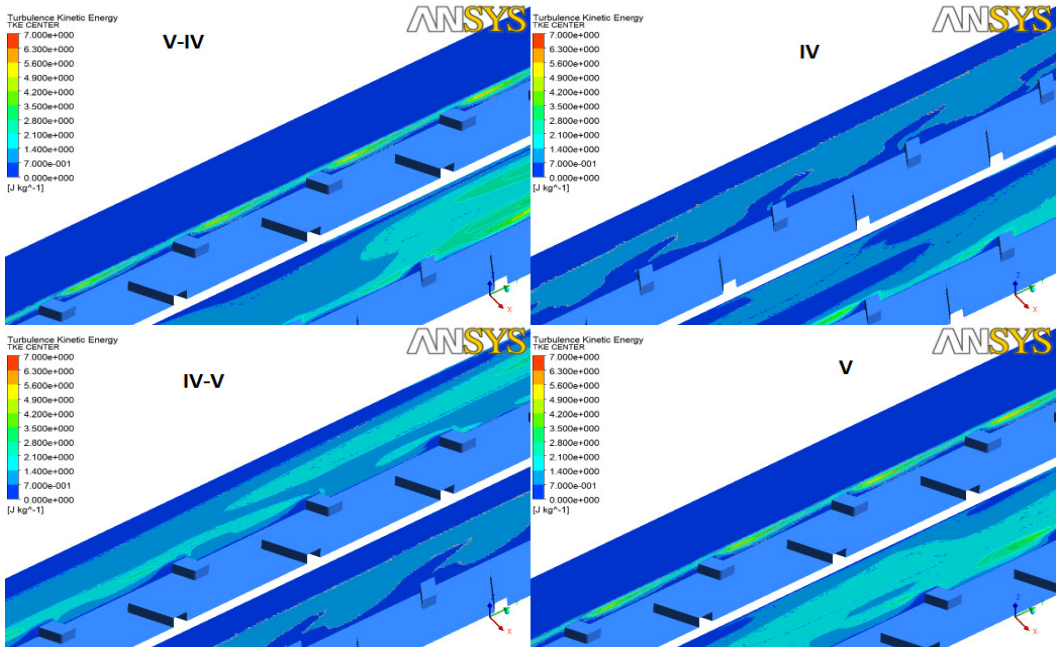

Figure 6.8: Broken Rib Turbulent Kinetic Energy @ x = 0.5Dh, @ x= 1.75Dh

(Re=21000, *k*-ω SST)

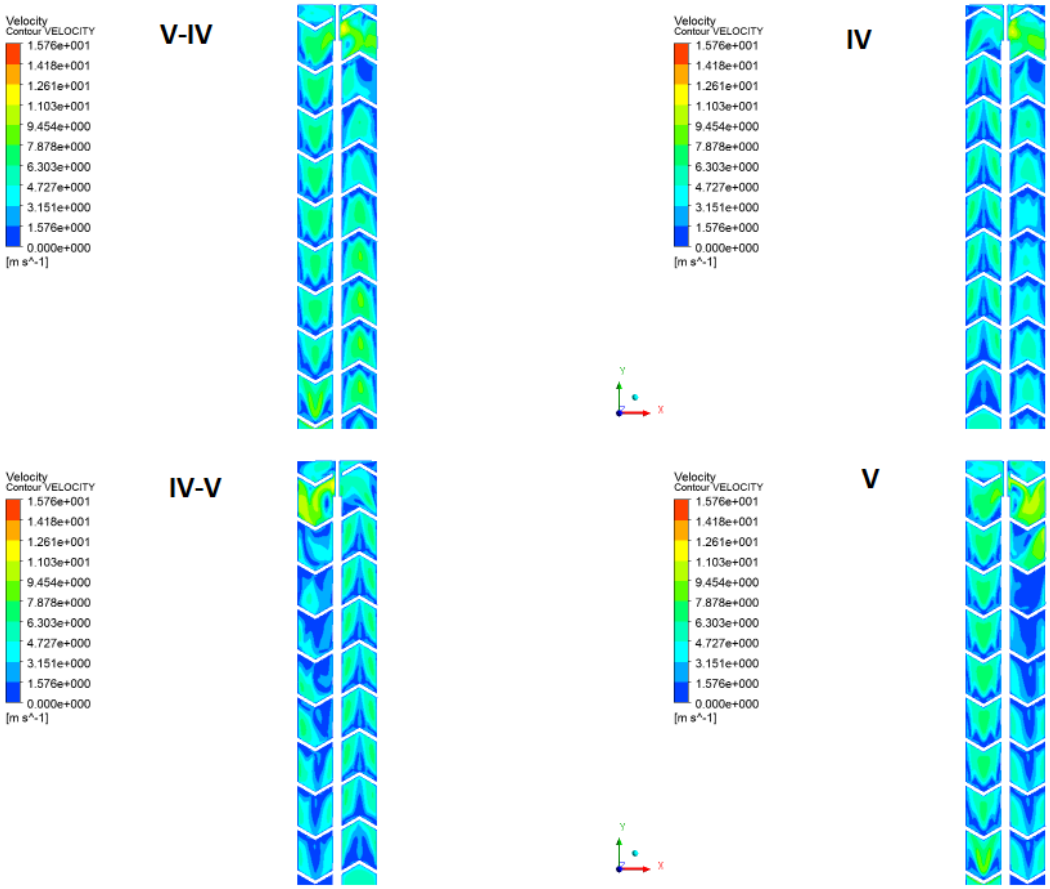

Figure 6.9: Continuous Rib Turbulent Kinetic Energy @ z = 0.01Dh, (Re=21000, *k*-ω SST)

Figures 6.9 and 6.10 show the turbulent kinetic energy profile for location Z= 0.01Dh for inlet and outlet of two pass channel. As can be seen, TKE is high for V-IV for both continuous and broken case throughout. TKE is high in V upstream channel as compared to other cases because of the mainstream flow through the V profile of the ribs. When the V is pointed upstream, the TKE is higher near the surface, contrary to the case where V is pointed downstream. In the latter, there is high TKE away from surface which detoriates the performance. High TKE means higher turbulence which correlates with high heat transfer.

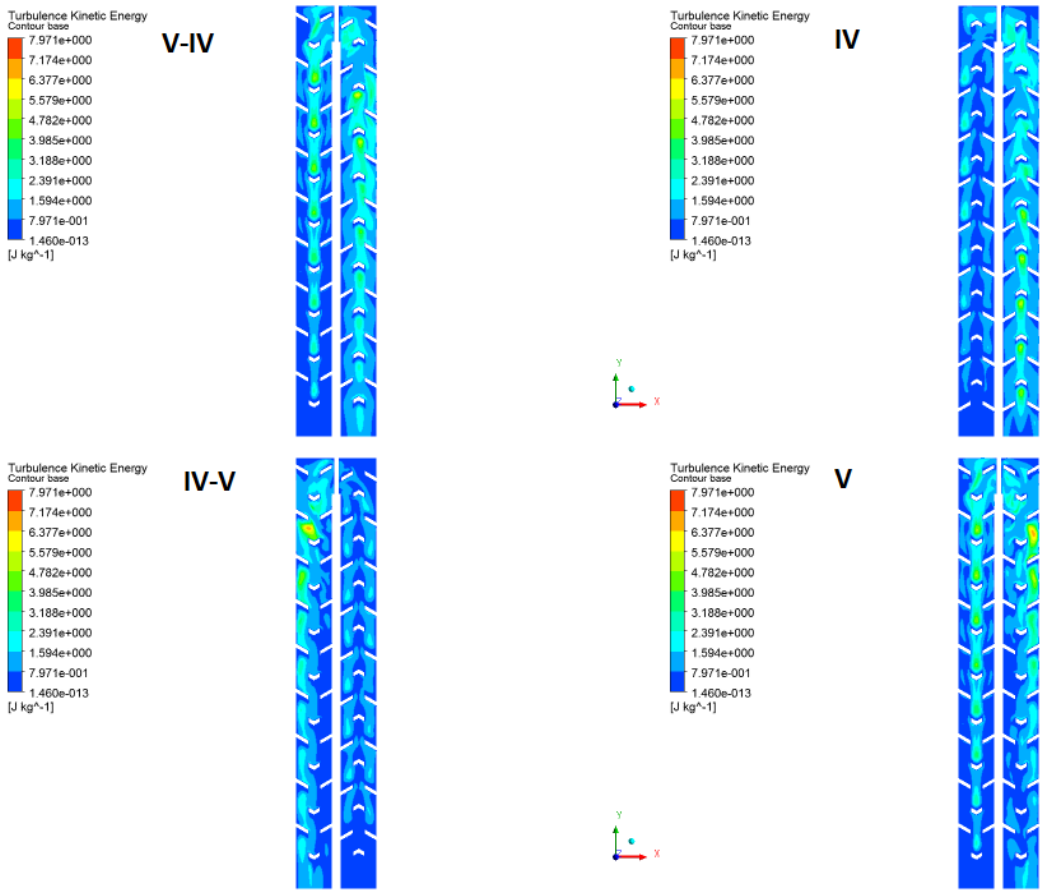

Figure 6.10: Broken Rib Turbulent Kinetic Energy @ z = 0.01Dh, (Re=21000, *k*-ω SST)

Heat Transfer and Nusselt Number distribution

The span wise regionally averaged local Nusselt number for all different types of V rib arrangements is calculated. The averaged Nusselt number for all Reynolds numbers considered are summarized in appendix B for both $k\omega$-SST and RSM models. These figures provide the averaged Nusselt number as normalized by the corresponding values for fully developed turbulent flow and heat transfer based on inlet channel conditions (identical Reynolds numbers). The values for Nu_0 of fully developed channel flow are

obtained from Dittus-Boelter relation. Both models produce approximately identical results for heat transfer. Similar to the experimental results, V-IV gives good results for both continuous as well as broken ribs.

Numerical Results

	KWSST-C		
IV	**Re_D**	**delP (Pa)**	**Area AV Nu**
	21000	1.36E+02	1.07E+02
	56000	9.13E+02	2.33E+02
	85000	2.02E+03	3.17E+02
IV-V	**Re_D**	**delP**	
	21000	1.37E+02	1.03E+02
	56000	9.50E+02	2.18E+02
	85000	2.19E+03	3.08E+02
V	**Re_D**	**delP**	
	21000	1.52E+02	1.10E+02
	56000	1.06E+03	2.34E+02
	85000	2.39E+03	3.23E+02
V-IV	**Re_D**	**delP**	
	21000	1.60E+02	1.18E+02
	56000	1.15E+03	2.55E+02
	85000	2.56E+03	3.49E+02

	RSM-C		
IV	**Re_D**	**delP (Pa)**	**Area AV Nu**
	21000	1.40E+02	1.10E+02
	56000	9.36E+02	2.22E+02
	85000	2.09E+03	3.08E+02
IV-V	**Re_D**	**delP**	
	21000	1.37E+02	1.04E+02
	56000	9.10E+02	2.08E+02
	85000	2.01E+03	2.89E+02
V	**Re_D**	**delP**	
	21000	1.51E+02	1.14E+02
	56000	1.06E+03	2.19E+02
	85000	2.43E+03	3.00E+02
V-IV	**Re_D**	**delP**	
	21000	1.58E+02	1.18E+02
	56000	1.07E+03	2.25E+02
	85000	2.38E+03	3.48E+02

Figure 6.11: Numerical Results for continuous Rib using *k-ω* SST and RSM for all the rib arrangement

Numerical Results

KWSST-BR			
IV	Re_D	delP (Pa)	Area AV Nu
	21000	1.16E+02	2.33E+02
	56000	7.50E+02	4.55E+02
	85000	1.68E+03	6.40E+02
IV-V	Re_D	delP	
	21000	1.03E+02	1.96E+02
	56000	6.63E+02	4.17E+02
	85000	1.46E+03	5.75E+02
V	Re_D	delP	
	21000	1.24E+02	2.42E+02
	56000	8.57E+02	5.10E+02
	85000	1.94E+03	7.03E+02
V-IV	Re_D	delP	
	21000	1.38E+02	2.63E+02
	56000	9.71E+02	5.54E+02
	85000	2.04E+03	7.40E+02

RSM-BR			
IV	Re_D	delP (Pa)	Area AV Nu
	21000	1.05E+02	2.09E+02
	56000	7.55E+02	4.44E+02
	85000	1.66E+03	6.18E+02
IV-V	Re_D	delP	
	21000	1.04E+02	2.09E+02
	56000	7.59E+02	4.23E+02
	85000	1.67E+03	5.83E+02
V	Re_D	delP	
	21000	1.25E+02	2.46E+02
	56000	8.82E+02	5.14E+02
	85000	2.14E+03	6.93E+02
V-IV	Re_D	delP	
	21000	1.25E+02	2.50E+02
	56000	9.15E+02	5.40E+02
	85000	2.14E+03	7.47E+02

Figure 6.12: Numerical Results for broken Rib using *k-ω* SST and RSM for all the rib arrangement

This figure contains the overall averaged Nusselt Number ratio throughout the channel along with the pressure loss for different velocities. It clearly depicts increase in the Nusselt Number with increasing velocity, with the overall best configuration being V-IV.

C. Comparison with Experimental Results:

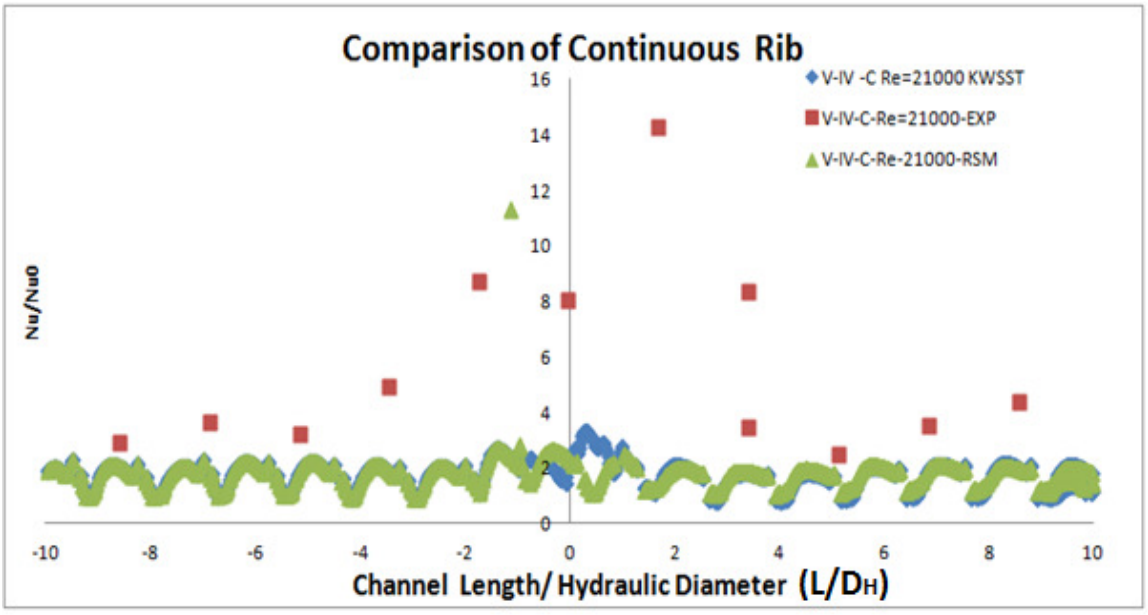

Figure 6.13: V-IV Continuous Comparison with Experimental Results

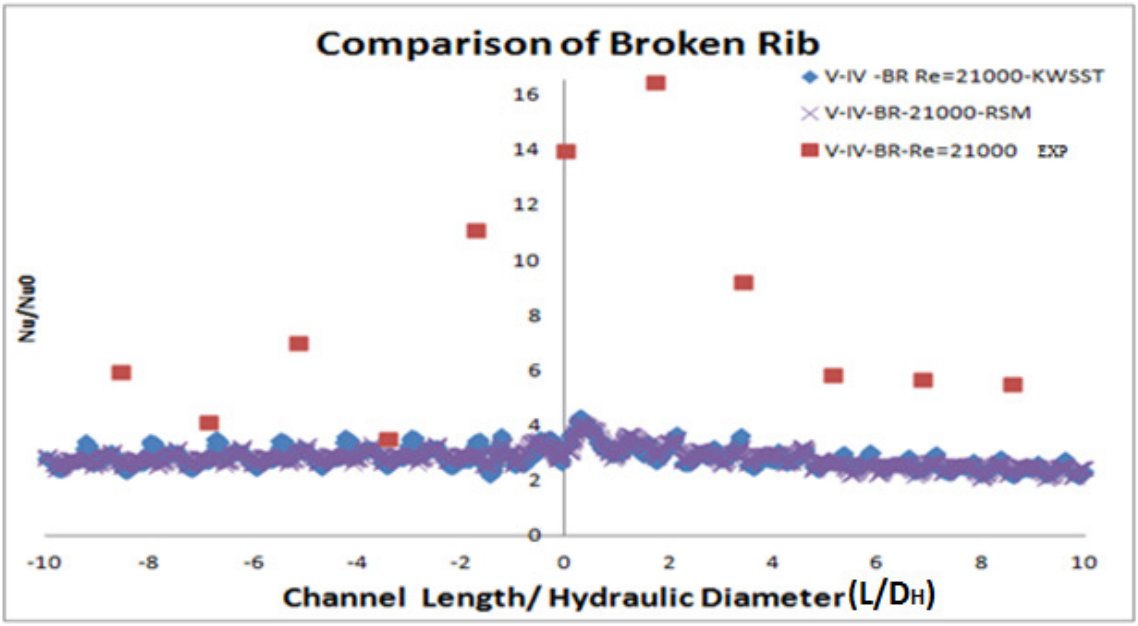

Figure 6.14: V-IV Continuous Comparison with Experimental Results

Figures 6.13 and 6.14 show comparison of broken and continuous ribs for Reynolds Number of 21,000 for V-IV. The experimental results profile is similar to the numerical results, except in the turn region where there is a very high spike. It is important to note that the result pattern obtained using numerical simulation and experimental work is similar.

CHAPTER 7: LARGE EDDY SIMULATIONS

7.1 Introduction:

Large-eddy simulation (LES) is an unsteady, three-dimensional simulation methodology where the Navier–Stokes equations are spatially filtered, the resolved scales of motion are directly computed, and the influence of the filtered scales on the resolved scales is modeled. LES lies between Direct Numerical simulations (DNS) and turbulence closure schemes. Turbulent flows are characterized by eddies with varying length and time scales. The largest eddies being comparable in size to characteristic length of mean flow. LES is used to compute both the mean flow and large, energy containing eddies accurately. The premise of LES is based on the fact that energy tends to travel down the energy cascade to small scale, and not in reverse direction. Since DNS is not feasible for most of the practical engineering problems which involve high Reynolds Number flow there is a need to increase usage of LES. DNS is a method in which the Navier-strokes equations are solved numerically without any turbulence model. This means that whole range of spatial and temporal scales of the turbulence must be resolved. The number of mesh points and time step in case of DNS is very large and hence the computational cost associated with DNS is very high even at low Reynolds Number. The main reason for using LES is that it avoids the need to resolve all the large eddies using turbulence closure models. Large eddies dominate the transport of mass, momentum and energy in flow. Being the future of CFD simulations, LES is implemented for both 60^{o} continuous V rib and broken V rib.

7.2 Governing Equations:

Large Eddy Simulations are transient and 3D in nature in which large scales are solved directly and small scales are modeled. The equations are obtained by box filtering (Volume averaging). The turbulent stress tensors are represented as subgrid scale stresses as the smaller eddies are self-similar. Self similarity: For very high Re, the statistics of components in the equilibrium range, being independent of the larger scales, is universally and uniquely determined by the viscosity and the rate of energy dissipation.

Sub Grid Scale Model:

Kolmogorov's theory of self similarity is that the large eddies of the flow are dependent on the geometry while smaller scales are more universal. Smaller eddies are accounted by using sub grid-scale-model (SGS Model). The important part of LES is to introduce the idea of filtering of velocity. Mathematically, velocity field can be separated into resolved part and sub grid part. Resolved parts of the field represent the large eddies while sub grid part of the velocity represents the small scales. One may think of a new function G, Filtering kernel [70]

$$\overline{u_i}(\vec{x}) = \int G(\vec{x} - \vec{\varepsilon})u(\vec{\varepsilon})d\vec{\varepsilon} \tag{7.1}$$

resulting in

$$u_i = \overline{u_i} + u_i'' \tag{7.2}$$

where,

$\overline{u_i}$ is resolvable scale part

u_i'' is the sub grid scale part

$\bar{u}_i$ is resolvable scale part in LES after filtering, it does not represent the mean motion but the sum of mean motion plus the large scale in turbulence. u_i'' is the sub grid scale part velocity. The main difference between these quantities and Reynolds averaging are

$\bar{\bar{u}}_i \neq \bar{u}_i$(Reynold Averaged Value) and $\overline{u_i''} \neq 0$ [73]

For almost all of the practical implementations, LES uses the grid itself as the filter and perform no explicit filtering. In explicit filtering, an LES filter is applied to the discretized Navier-Stokes equations, providing a well-defined filter shape and reducing the truncation error. However, explicit filtering requires a finer grid than implicit filtering leading to increase in computational cost. The equations shown in this section is for incompressible fluids. The fluid in this study is assumed incompressible as the maximum temperature during experiments reached 120 ^{o}F. Variation in density at this temperature was only around 5% and hence it was safely assumed to be incompressible. The filtered equations are developed from the incompressible Navier- Stokes equations of motion. [70]

$$\frac{\partial u_i}{\partial t} + u_j \frac{\partial u_i}{\partial x_j} = -\frac{1}{\rho}\frac{\partial p}{\partial x_i} + \frac{\partial}{\partial x_j}\left(\nu \frac{\partial u_i}{\partial x_j}\right) \tag{7.3}$$

Substituting in the decomposition

$$u_i = \bar{u}_i + u_i'' \tag{7.4}$$

$$p = \bar{p} + p'' \tag{7.5}$$

then filtering the resulting equation gives the equation of motion for the resolved field.

$$\frac{\partial \bar{u}_i}{\partial t} + \bar{u}_j \frac{\partial \bar{u}_i}{\partial x_j} = -\frac{1}{\rho}\frac{\partial \bar{p}}{\partial x_i} + \frac{\partial}{\partial x_j}\left(\nu \frac{\partial \bar{u}_i}{\partial x_j}\right) + \frac{1}{\rho}\frac{\partial \tau_{ij}{}^{r}}{\partial x_j} \tag{7.6}$$

The extra term $\frac{\partial \tau_{ij}{}^{r}}{\partial x_j}$ arises from the non linear advection terms, due to the fact that

$$\overline{u_j}\frac{\partial \overline{u_i}}{\partial x_j} = \overline{u_j\frac{\partial u_i}{\partial x_j}} \tag{7.7}$$

and hence $$\tau_{ij}{}^{r} = \overline{u_i}\,\overline{u_j} - \overline{u_i u_j} \tag{7.8}$$

This shear stress is the subgrid stress which is analogous to Reynolds averaged momentum equation. These stresses are introduced because of filtering of Navier strokes equations. Similar equations can be derived for subgrid-scale field. The subgrid scale turbulent models employ Boussinesq hypothesis to calculate the deviatoric part of stresses from

$$\tau_{ij}{}^{r} - \frac{1}{3}\tau_{kk}\delta_{ij} = -2\mu_t\overline{s_{ij}} \tag{7.9}$$

Where μ_t is subgrid scale turbulent viscosity [71].

$\overline{s_{ij}}$ is rate of strain tensor

$$\overline{s_{ij}} = 1/2\left(\frac{\partial \overline{u_i}}{\partial x_j} + \frac{\partial \overline{u_{ji}}}{\partial x_i}\right) \tag{7.10}$$

There are different models for subgrid scale turbulent viscosity namely Smagorinsky-Lilly model, the dynamic Smagorinsky-Lilly model, the Wall Adapting Local Eddy Viscosity (WALE) model. In this study WALE model is implemented for simulation.

Wall Adapting Local Eddy Viscosity Model:

In Wale model eddy viscosity is modeled by

$$\mu_t = \rho L_S^2 \frac{\left(s_{ij}^d s_{ij}^d\right)^{3/2}}{\left(\overline{s_{ij}}\,\overline{s_{ij}}\right)^{5/2} + \left(s_{ij}^d s_{ij}^d\right)^{5/4}} \tag{7.11}$$

$$L_S = \min(k'd, C_W V^{1/3}) \tag{7.12}$$

$$s_{ij}^d = 1/2\left(\overline{g}_{ij}^2 + \overline{g}_{ji}^2\right) - 1/3\delta_{ij}\overline{g}_{kk}^2 \tag{7.13}$$

$$\overline{g}_{ij} = \frac{\partial \overline{u_i}}{\partial x_j} \tag{7.14}$$

where L_S is mixing length for subgrid scales

k is von karman constant

d is the distance to the closest wall

Default WALE constant C_W is 0.325 and has been found to yield satisfactory results for a wide range of flow [70]. Advantage of WALE model is that it returns a zero turbulent viscosity for laminar shear flows. This allows the correct treatment of laminar zones in the domain. WALE model is designed to return the correct wall asymptotic behavior for wall bounded flows. The WALE model is therefore preferable compared to the Smagorinsky-Lilly model as it produces non-zero turbulent viscosity.

7.3 Computational Model:

LES model is carried out for the best configuration on the surface of the test section. These two configurations are analyzed for the Reynolds Number of 56000. LES is selected to analyze the channel flow more accurately and to understand the flow pattern. The main advantages of using LES over RANS are reliability, repeatability and universality. The objective of LES study is to examine flow pattern effect due to V and broken ribs and the effect of main and secondary flows, turbulence and the heat transfer inside the duct.

Channels Selected for LES:

A) Continuous V ribs:

Case 1: 60^o V rib at inlet and 60^o inverted V rib at outlet (V-IV-C)

B) Broken V ribs:

Case 2: 60^o Broken V rib at inlet and 60^o Broken inverted V rib at outlet (V-IV-B)

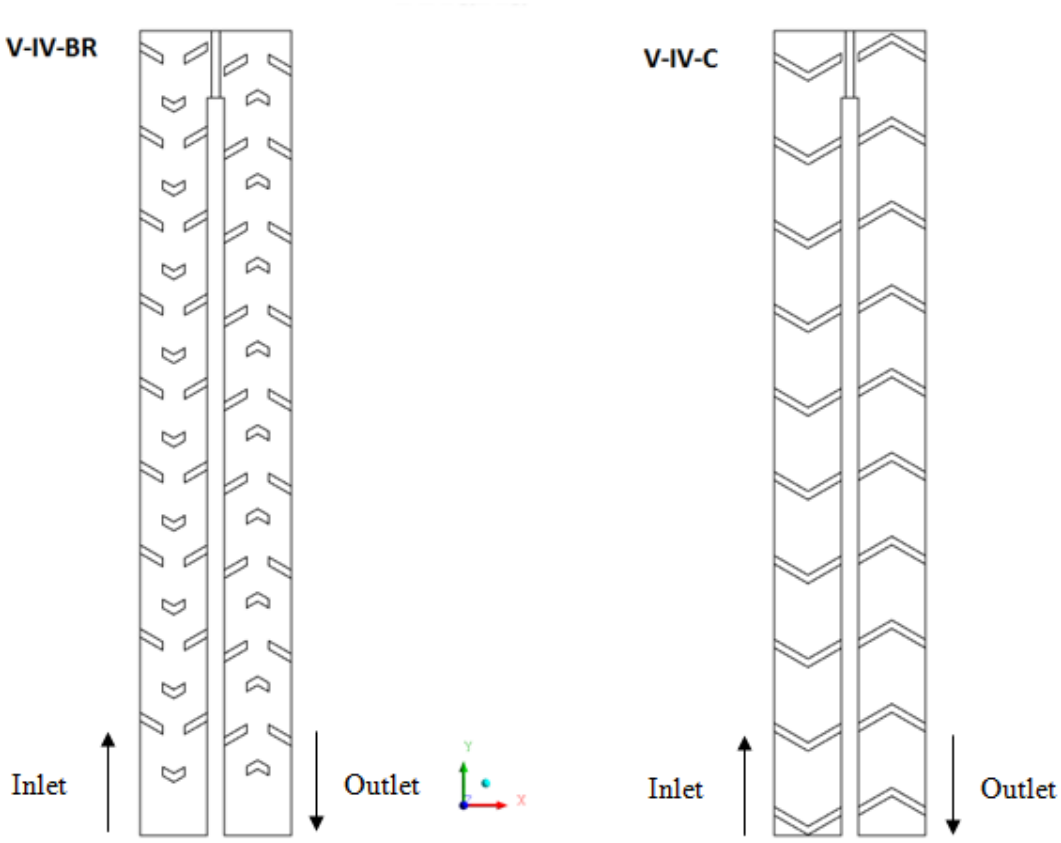

Figure 7.1: Inlet V and Outlet Inverted V 60^{o} Continuous and Broken rib turbulators top View

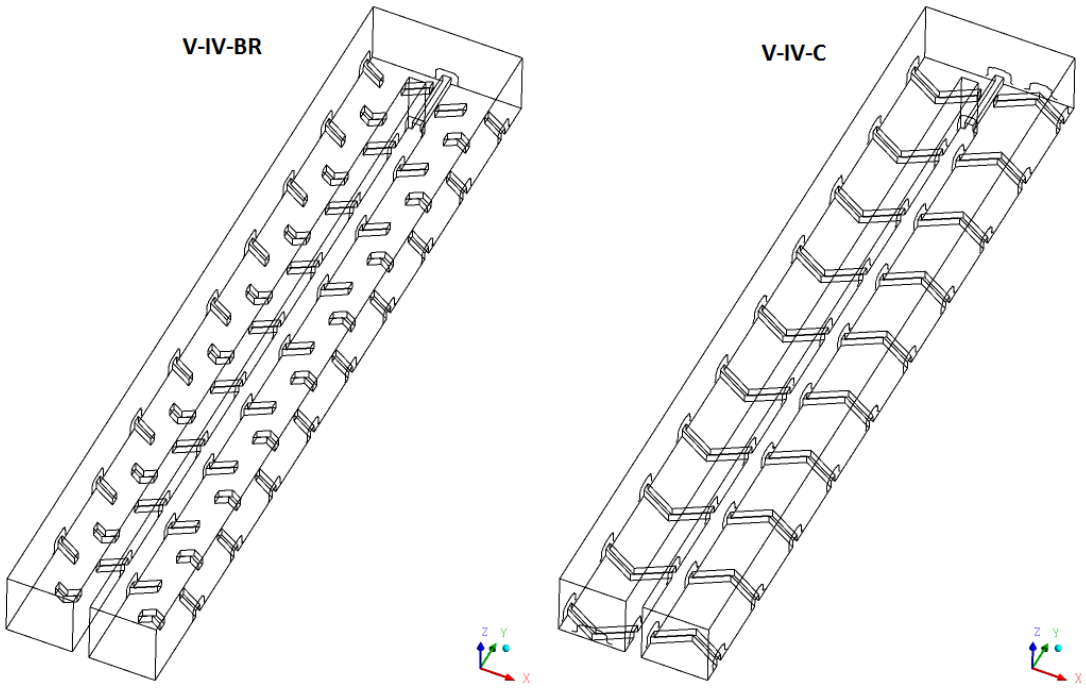

Figure 7.2: Inlet V and Outlet Inverted V 60^{o} Continuous and Broken rib turbulators isometric view

7.4 Numerical Method:

For Large Eddy simulation Ansys Fluent software is used in both cases. The numerical models setting for both continuous and broken V-IV are shown in Tables 7.1, 7.2 and 7.3. A three dimensional, unsteady, second order Implicit Large Eddy simulation is used for simulation. This model uses WALE subgrid scale model. Pressure Velocity coupling method is used as Semi Implicit Method for Pressure Linked Equations (SIMPLE). Table 7.3 shows unsteady calculation parameters.

Ensemble Averaging (Phase averaging): Averaging method for a time dependent flow which requires one to perform the experiment repeatedly for N times, then averaging is taken over the entire range of experiment over N, Number of experiments. It includes

short time Reynolds average and potentially more general. It is difficult to produce because it requires N experiments.

Table 7.1: Numerical case model setting

Model	Settings
Space	3D
Time	Unsteady, 2nd order Implicit
Viscous	Large Eddy Simulations
Sub-Grid Scale Model	WALE
Pressure-Velocity Coupling	SIMPLE
Equations Solved	Flow, Energy

Table 7.2: Discretization Scheme

Pressure	Standard
Momentum	Bounded Central Differencing
Energy	First Order Upwind

Table 7.3: Unsteady Calculation Parameters

Time Step (s)	3.175E-04
Max. Iterations Per Time Step	20
Total Time (s)	3.175 E-01

7.5 Computational Detail:

The computational domain consists of complete two pass cooling channel with 60^{o} V-IV broken and continuous ribs placed on the surface. In LES, the grid requirement in stream wise should be approximately 100, wall-normal to be 1 and spanwise should be 30 respectively. The number of grids used for LES is around 8M. The grids were generated

using structured cutcell in Ansys mesher. For uniformity of mesh, same types of grid meshing formulations were used for both configurations.

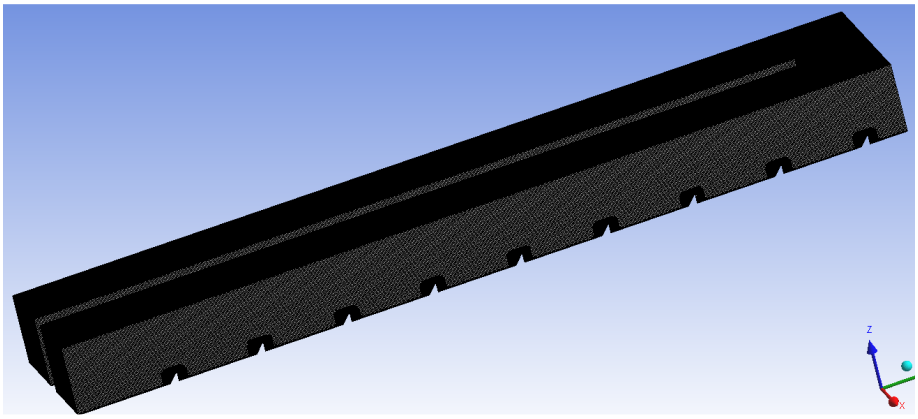

(a)

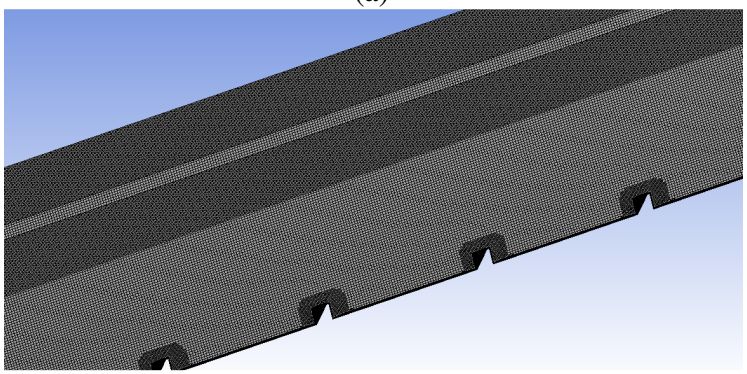

(b)

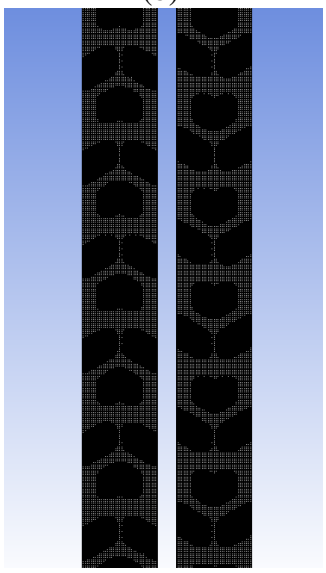

(c)

Figure 7.3: Mesh considered for Broken V-IV (a) Complete channel View (b) Zoomed View of mesh from side (c)Mesh from Back view of channel

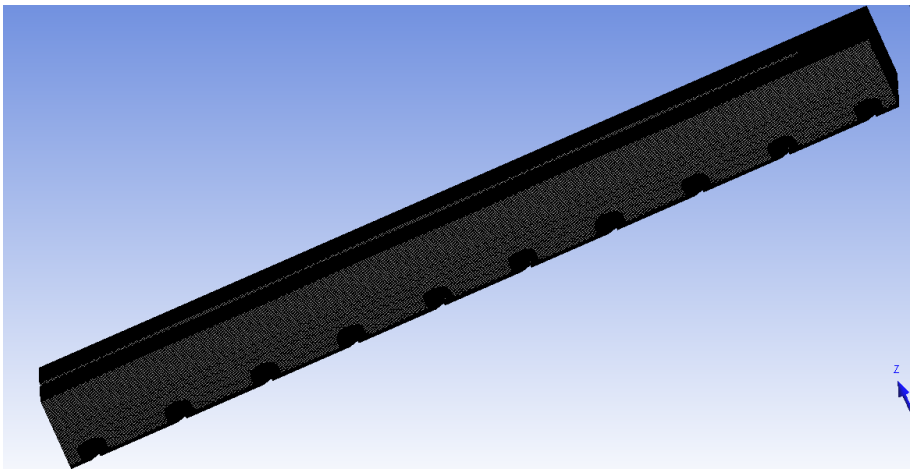

(a)

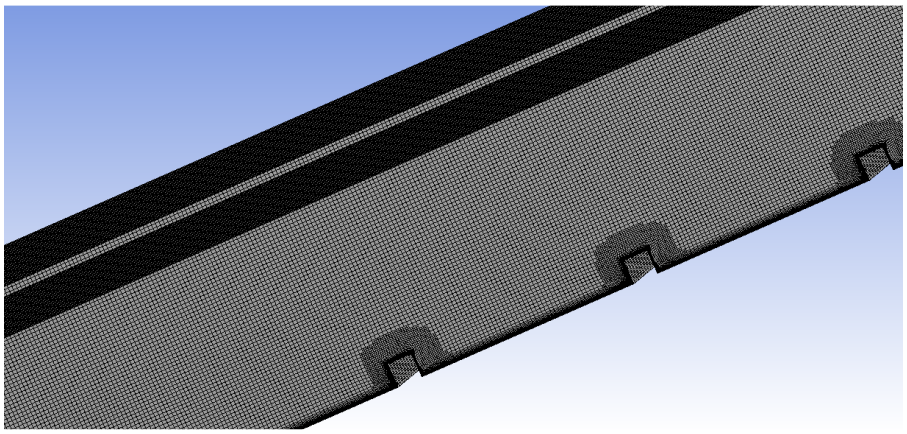

(b)

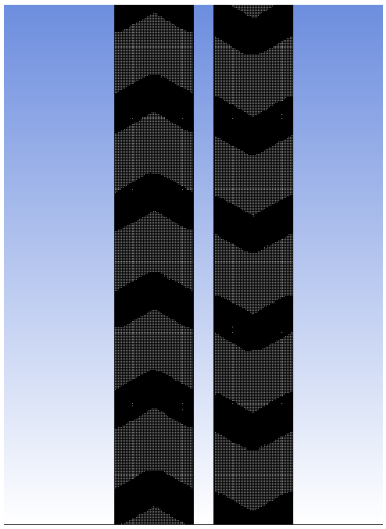

(c)

Figure 7.4: Mesh considered for Continuous V-IV (a) Complete channel View (b) Zoomed View of mesh from side (c)Mesh from Back view of channel

Figures 7.3 and 7.4 show the complete channel view, zoomed view of mesh and the back view of mesh used for LES calculation for broken and continuous ribs.

7.6 Boundary Conditions:

In this section, all the required parameters and boundary conditions used for simulation are described. As discussed in the section 7.7 the steps followed for LES simulations, firstly a steady state RANS model is run and then LES is carried out for better results. In Table 7.4 all the fluid properties selected for simulation are tabulated. Table 7.5 provides a complete list of boundary condition used for the simulations. Also the inlet boundary conditions used during simulation are important parameter for understanding the flow pattern which can be seen in the Table 7.6, which provides the Turbulence Intensity and Inlet Reynolds stresses. The LES model was run on HPC and the details of timing and memory are listed in the Table 7.7. Hence it is clearly seen that LES modeling are very computer intensive.

Table 7.4: Numerical case Fluid Properties

Material	**Air**
Density (kg/m^3)	1.225
Specific Heat (J/kg-K)	1006
Thermal Conductivity (W/m-K)	0.0242
Viscosity (kg/m-s)	1.789E-05

Table 7.5: Inlet and Boundary conditions used for Simulation

Inlet Velocity	Reynolds Number=56000
Inlet Temperature	300K
Cooling Channel Wall Heat Flux	2087.6 W/m^2
Outlet Wall	Pressure Outlet
Fluid Used	AIR

Table 7.6: Reynolds-Stress Specification Method

Re=56000	Turbulent Intensity (%) I	4.08
	Hydraulic Diameter (D_H, m)	5.08E-02
	Dimensionless Reynold Stress $\frac{\overline{uu}}{(U_{in})^2}$	0.0016
	Dimensionless Reynold Stress $\frac{\overline{vv}}{(U_{in})^2}$	0.0016
	Dimensionless Reynold Stress $\frac{\overline{ww}}{(U_{in})^2}$	0.0016

Table 7.7: Resource usage summary for LES Modeling

LES-C	LES-BR
CPU time : 1.78E+06 s	CPU time : 1.76 E+06 s
Max Memory :1.81E+04 MB	Max Memory : 17250 MB
Max Swap : 1.89E+04MB	Max Swap : 1.80E+04MB
Max Processes :17	Max Processes : 17
Max Threads : 26	Max Threads : 26

7.7 Steps Involved for

As Large Eddy simulation involves running a transient solution from initial condition on fine mesh having appropriate time step size. The solution must run long enough to become independent of the initial condition and to enable the statistics of flow field to be determined. [70]

1. Starting point of LES model should be any Reynolds averaged steady turbulence model which is reasonably converged. Instantaneous velocity field should be generated out of steady field RANS model. In this thesis, RSM model was run before starting LES model.

2. When LES model is activated, unsteady solver is activated. Second order implicit formulation is selected. The bounded central differencing spatial discretization is activated for momentum equations.

3. The duration of the simulation can be determined beforehand by estimating the mean flow residence time in the solution domain (L/U, where L is the characteristic length of the solution domain and U is a characteristic mean flow velocity). The simulation should run for at least some mean flow residence time.

7.8 Results and Discussions:

Continuous and broken V-IV ribs are selected for further analysis which can provide insight in the flow pattern and turbulence enhancement. There are very few studies done using LES for complete two pass channel. There are some data considering periodic zones for analysis. [54, 55, 64, 66]. To author's knowledge, this is the first study using two pass channel for broken and continuous V-IV ribs.

Velocity and Temperature Field:

The geometry of the ribs greatly affects the flow field and in turn temperature in the channel. Figs. 7.5 and 7.6 show the surface Nusselt Number and ratio of Nusselt Number for Reynolds Number of 56,000. Broken V-IV produces better heat transfer as compared to continuous V-IV. The figure clearly shows that the Nusselt Number is high in the first pass and further increases in the second pass. This continued increase in the second pass is because of the turning effect and Coriolis Effect in the turn region. Fig. 7.7 shows surface locations on which streamline and velocity profiles will be discussed in this section.

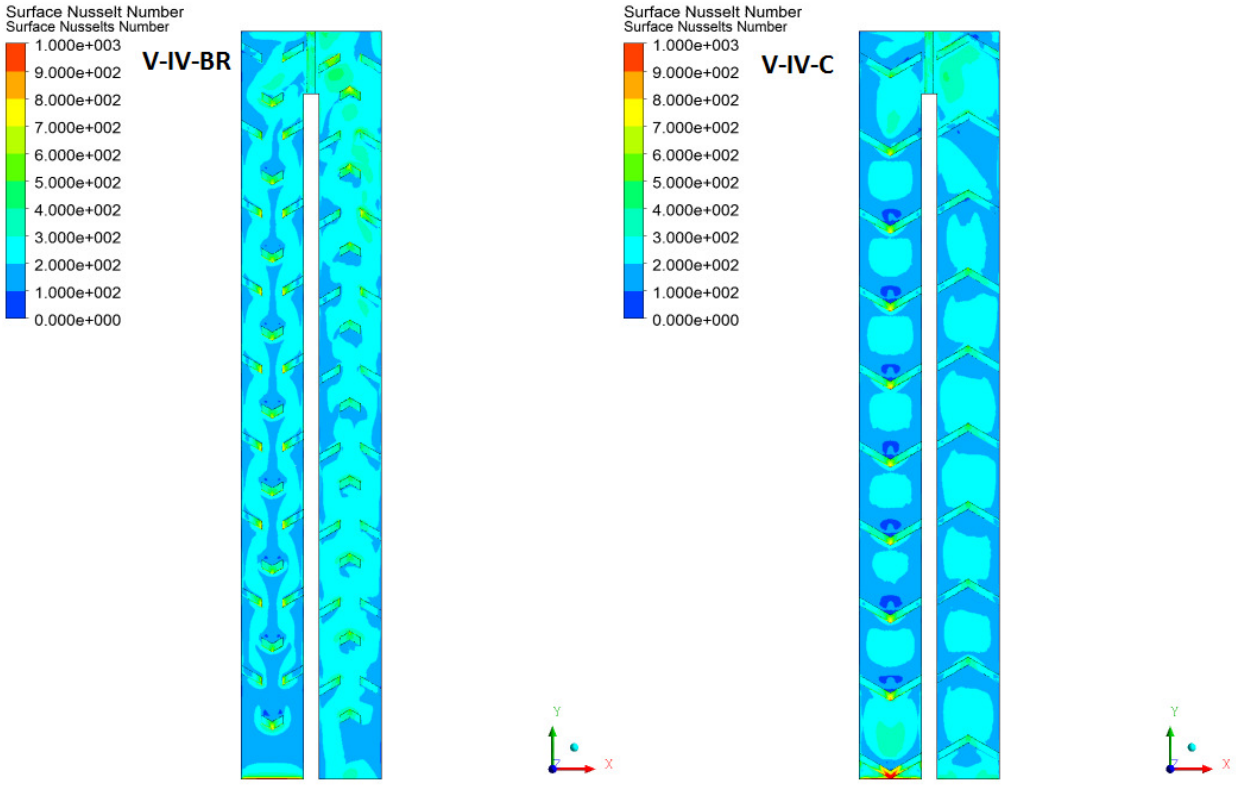

Figure 7.5: Surface Nusselt Number for bottom wall (Re= 56000)

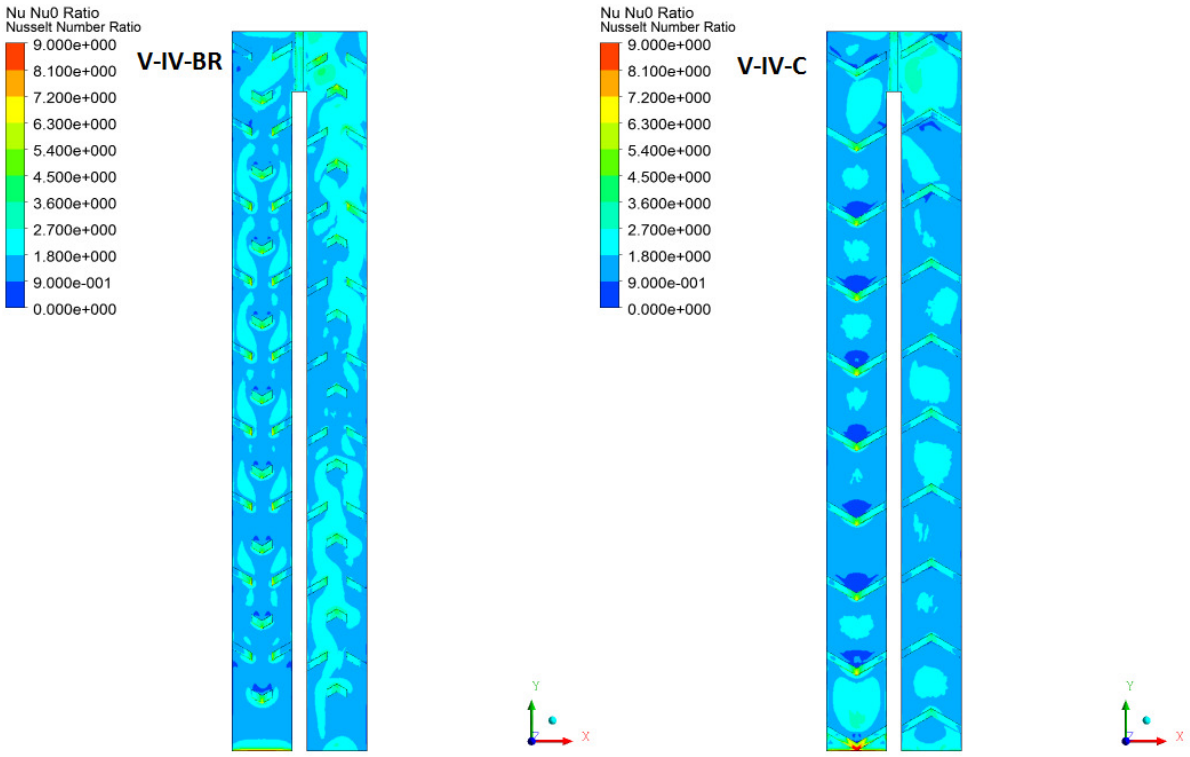

Figure 7.6: Surface Nusselt Number ratio for bottom wall (Re= 56000)

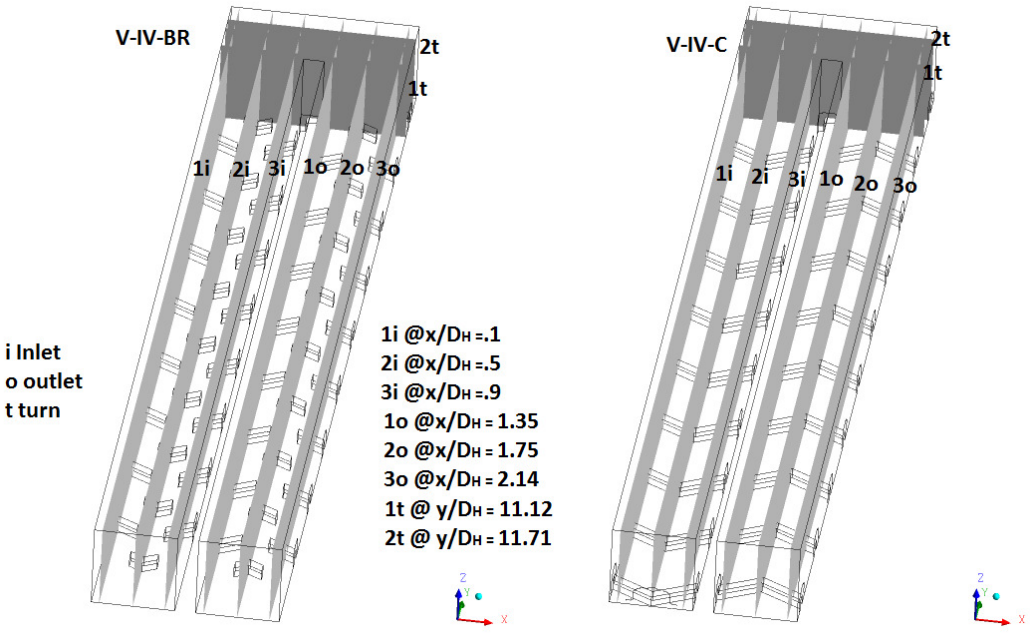

Figure 7.7: location of velocity profile and Streamlines produced

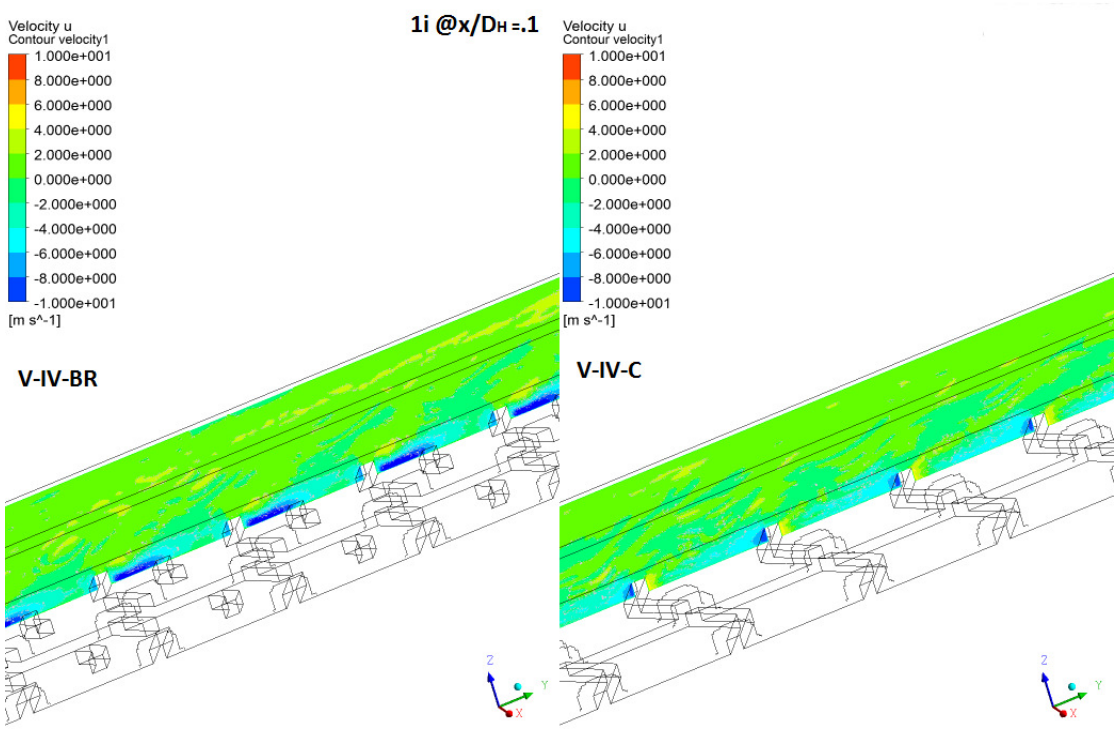
1i @x/DH =.1
Velocity u
Contour velocity1
1.000e+001
8.000e+000
6.000e+000
4.000e+000
2.000e+000
0.000e+000
-2.000e+000
-4.000e+000
-6.000e+000
-8.000e+000
-1.000e+001
[m s^-1]
V-IV-BR
V-IV-C

(a)

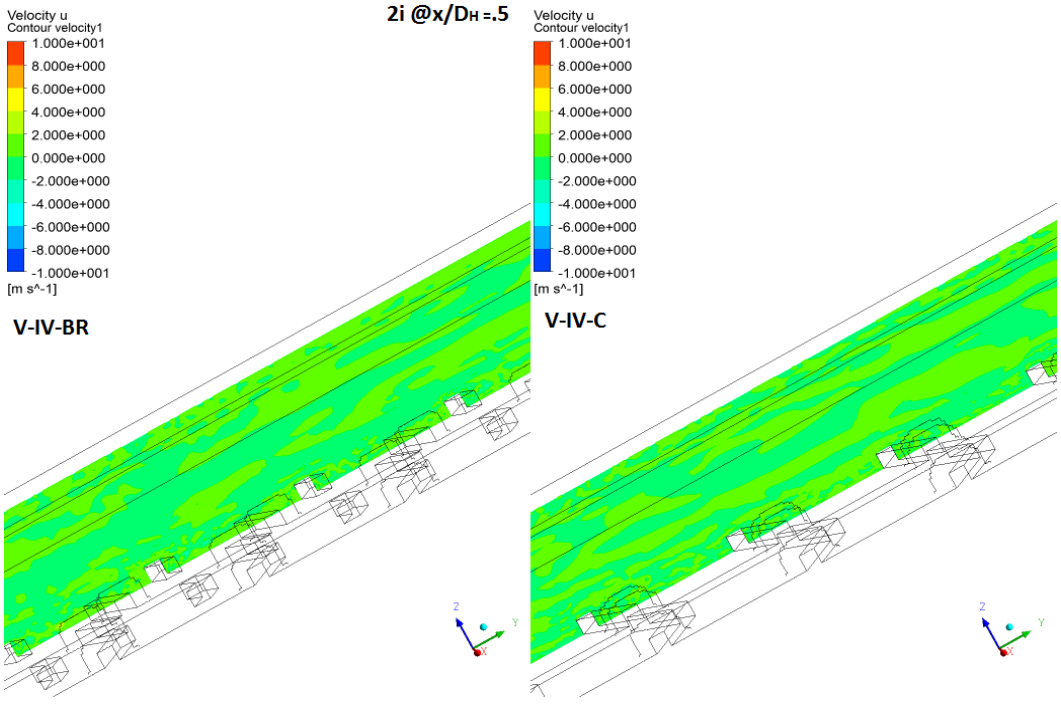
2i @x/DH =.5
Velocity u
Contour velocity1
1.000e+001
8.000e+000
6.000e+000
4.000e+000
2.000e+000
0.000e+000
-2.000e+000
-4.000e+000
-6.000e+000
-8.000e+000
-1.000e+001
[m s^-1]
V-IV-BR
V-IV-C

(b)

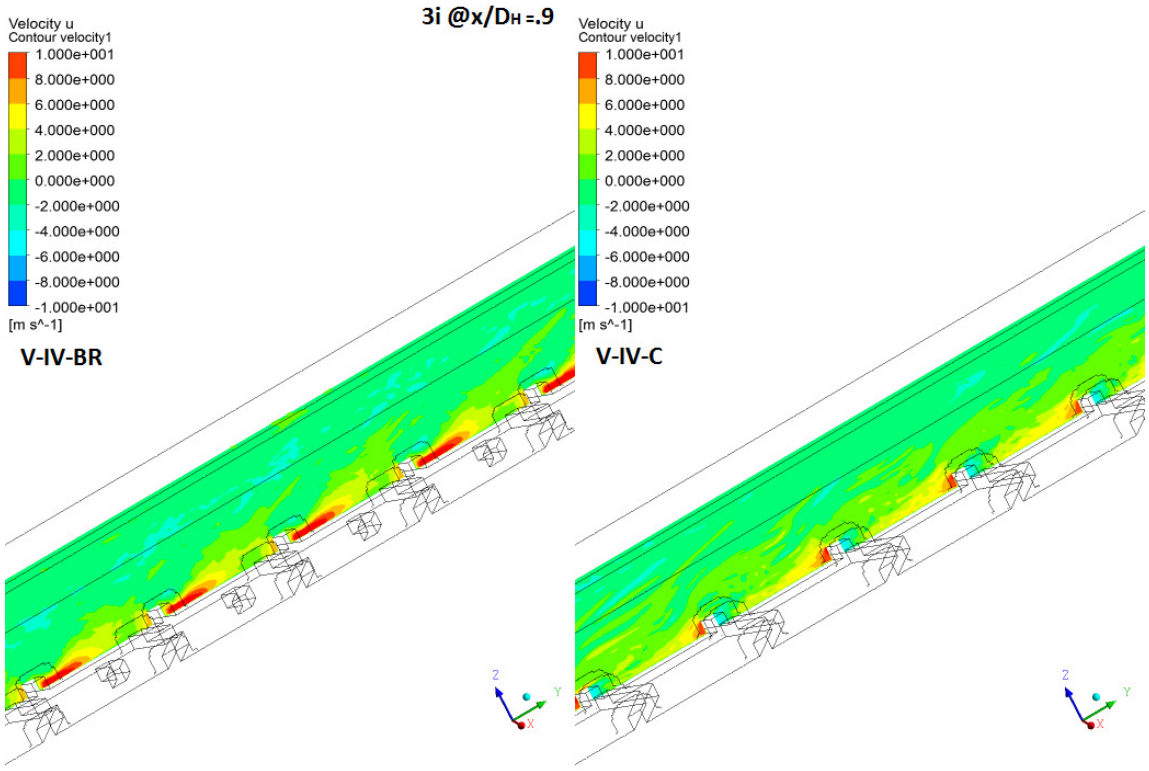

(c)

Figure 7.8: Spanwise velocity contours for inlet for Broken and Continuous ribs

(a) $x/D_H = 0.1$ (b) $x/D_H = 0.5$ (c) $x/D_H = 0.9$

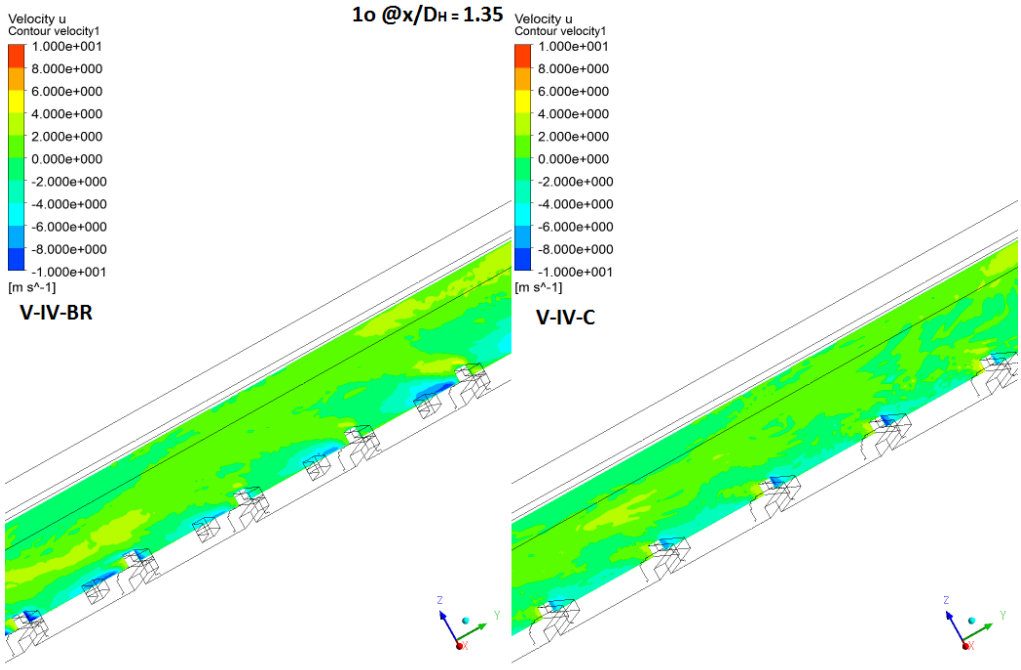

(a)

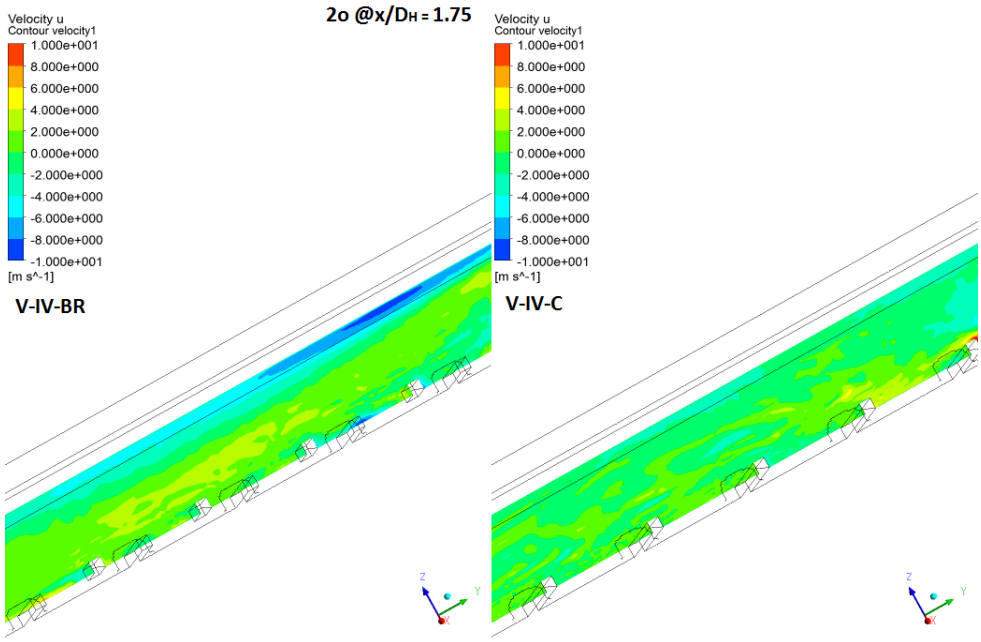

(b)

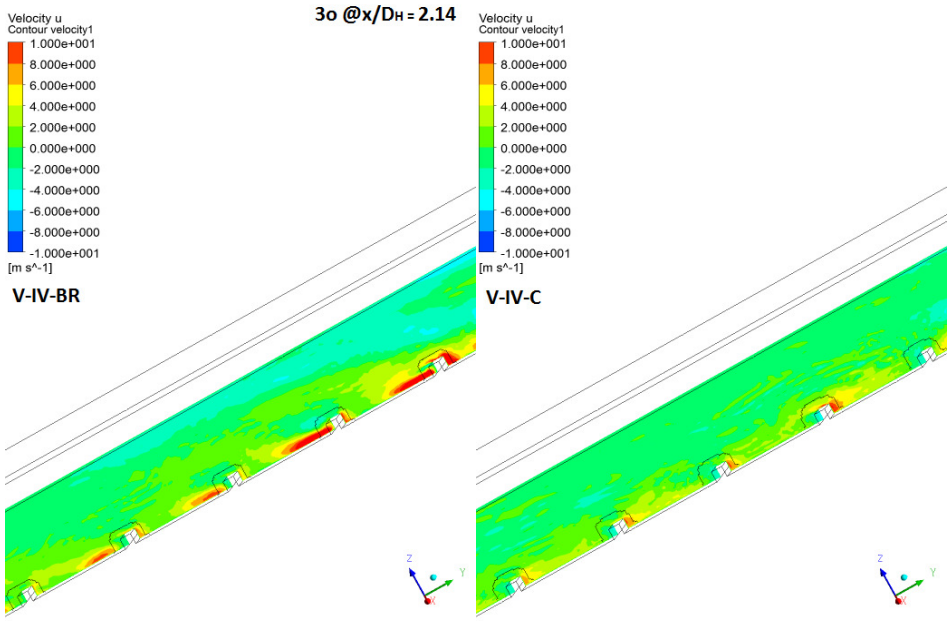

(c)

Figure 7.9: Spanwise velocity contours for outlet for Broken and Continuous ribs

(a) x/D_H =1.35 (b) x/D_H= 1.75 (c) x/D_H= 2.14

Figures 7.8 and 7.9 show spanwise velocity contours for broken and continuous ribs for Reynolds Number of 56,000. Fig. 7.8 shows the inlet location from outer to inner side while Fig. 7.9 shows the outlet locations from inner to outer side. The important observation to be made from the figures is that in the inlet section, as we move towards the inner surface, Spanwise velocity magnitude increases for both Broken and Continuous ribs; with the magnitude and amount being higher for broken ribs, which may explain the high heat transfer in the inner surface of the ribs. Similarly, fig. 7.9 clearly shows increase in velocity as one moves towards towards the outer surface, thus increase in Nusselt Number in outer section.

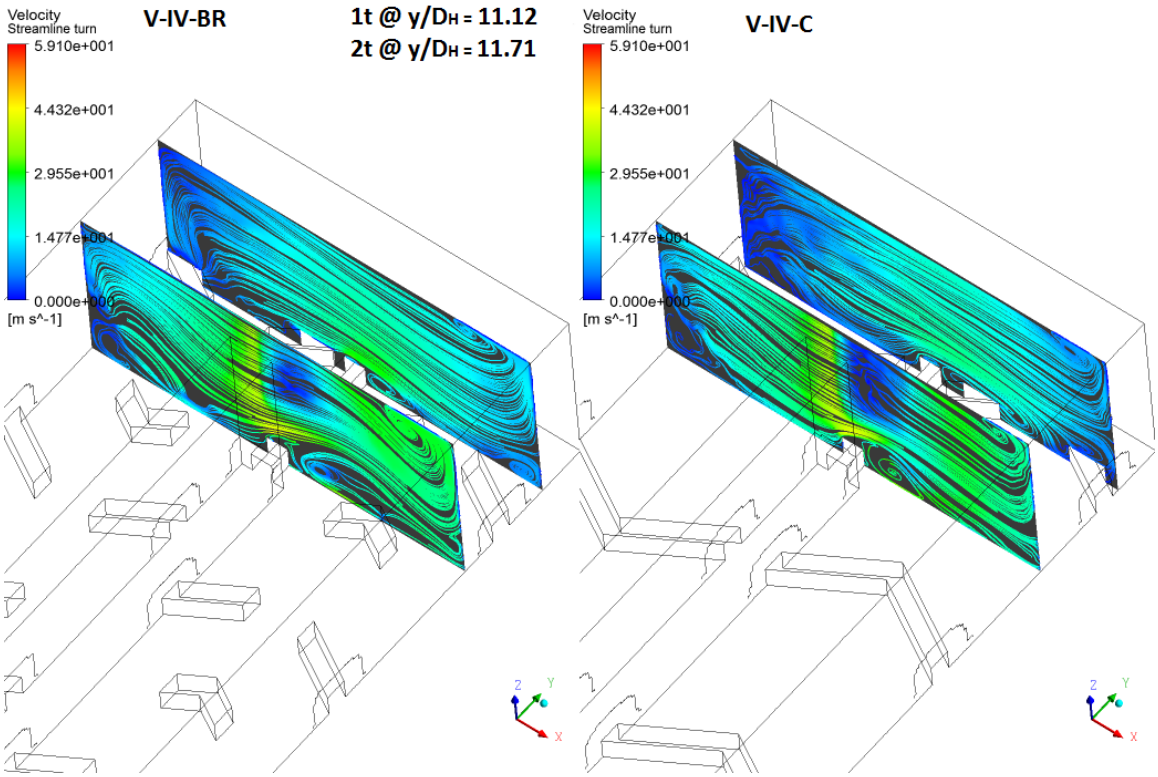

Figure 7.10: Streamlines for turn for Broken and Continuous ribs

at y/D_H =11.12 and y/D_H= 11.71

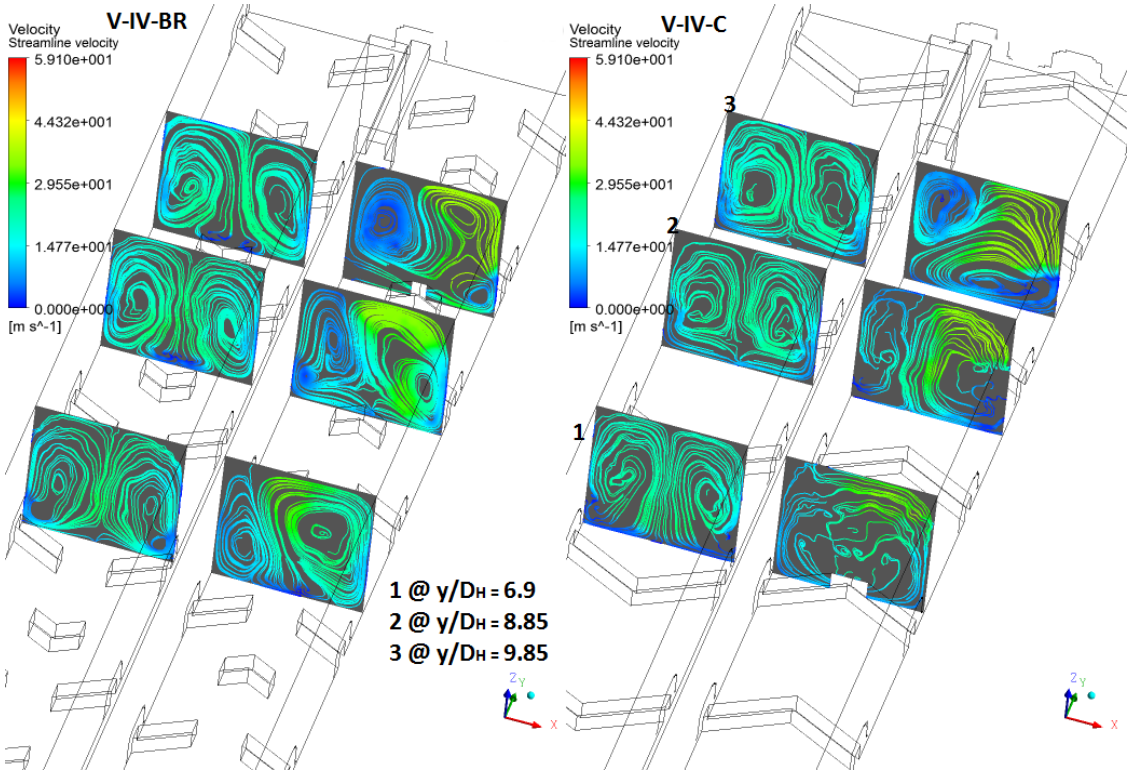

Figure 7.11: Streamlines for Inlet and Outlet for Broken and Continuous ribs

Figure 7.10 shows streamlines for turn section for broken and continuous ribs depicting velocity recirculation in the turn section leading to increase in the heat transfer. In broken rib case, secondary flow is predominant at y/D_H =11.12 in the inlet section as compared to continuous ribs. Right after the turn region, there is a recirculation zone in case of broken ribs. As the flow turns, it impinges on the surface and heat transfer enhancement takes place.From these streamlines, it can also be suggested that overall recirculation is more in case of broken ribs leading to greater heat transfer.

Figure 7.11 shows streamlines developed for broken and continuous ribs at different locations as it is clearly evident that the recirculation regions in case of broken ribs are more prominent as compared to continuous ribs therefore, higher heat transfer takes place in the case of broken ribs. Post turn regions have higher recirculation zones because of

the turning effect of the flow as it impinges on the outer surface and flow is channeled in second pass. As seen in Fig. 7.6, heat transfer is higher in areas where secondary flow develops .As seen in Fig. 7.12, in case of broken ribs, velocity in bottom surface contours is very high leading to increase in heat transfer.

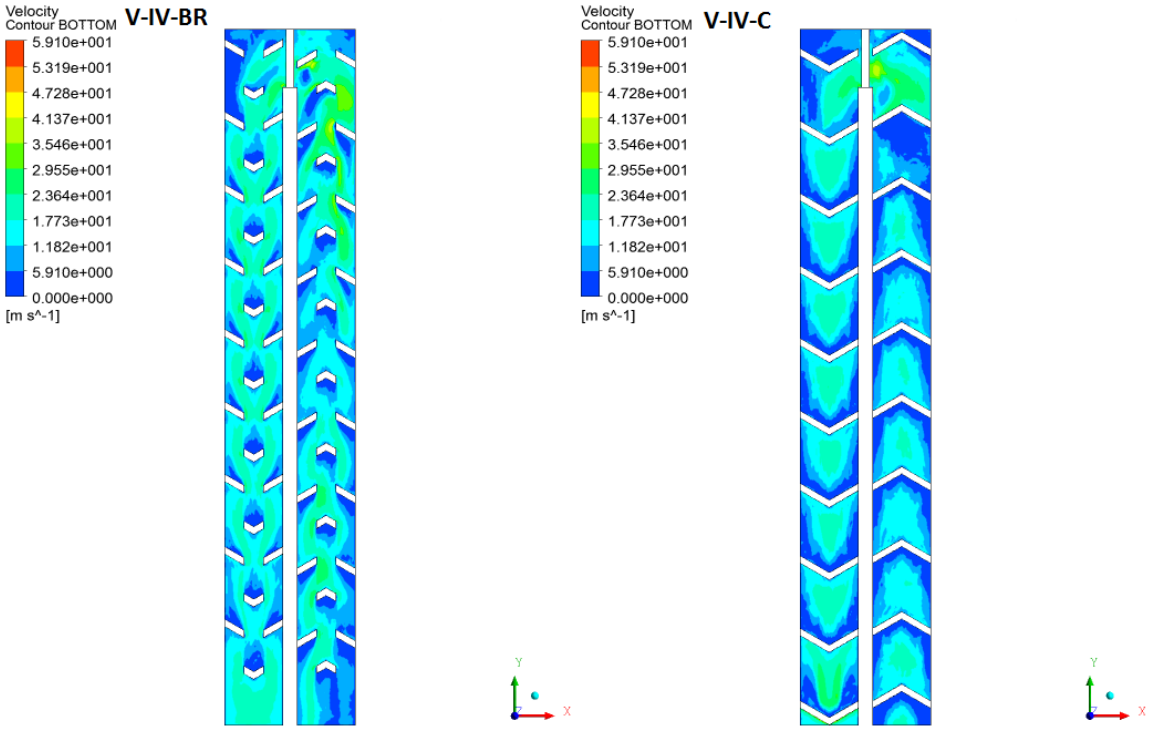

Figure 7.12: Velocity Contours @ z= $0.01D_H$ for Inlet and Outlet for Broken and Continuous rib

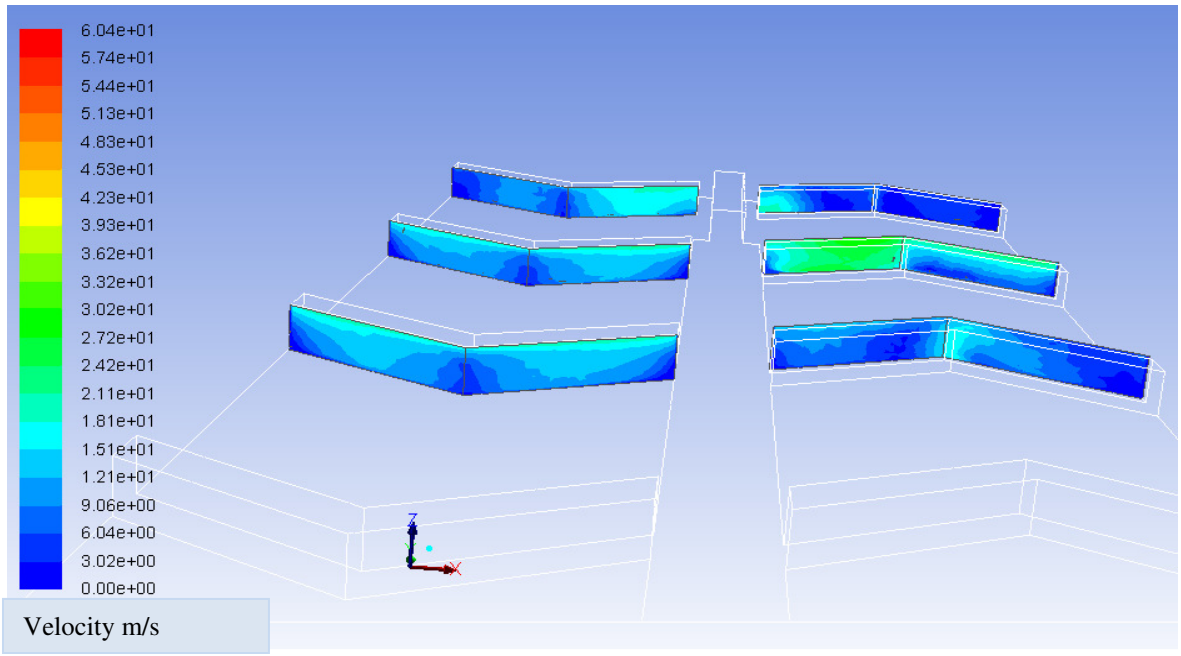

(a)

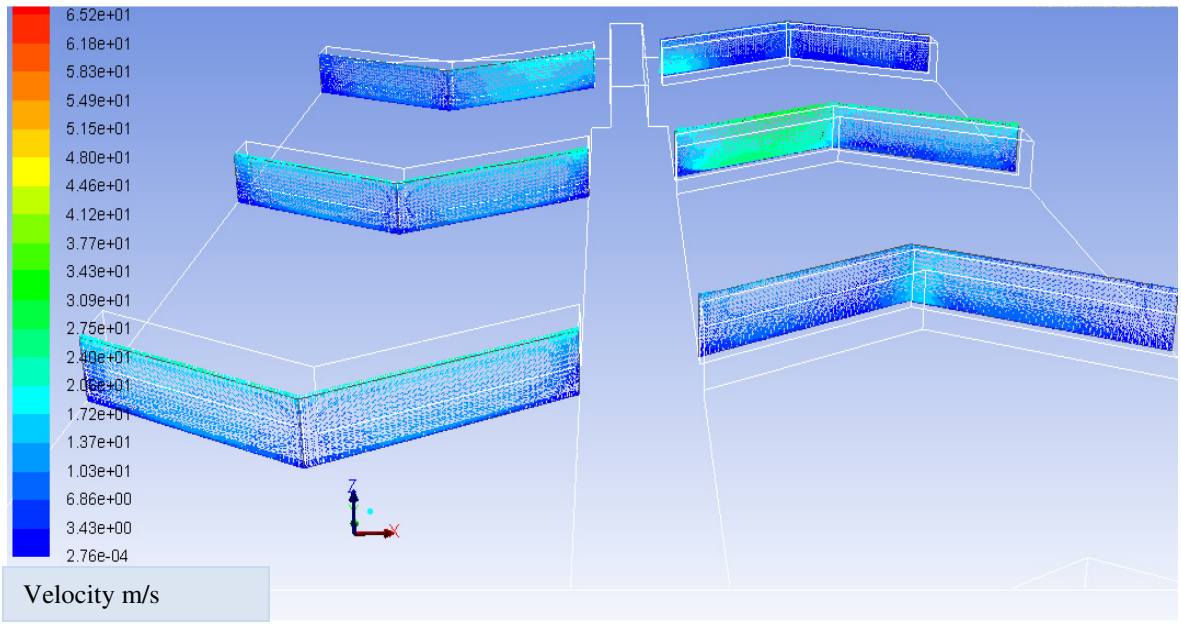

(b)

Figure 7.13: a) Velocity Contours b) Velocity Vectors for Continuous V-IV ribs

Figure 7.13 shows velocity contours and vectors just before the ribs (for continuous ribs) in first as well as second pass. As compared to IV, it can be seen that the flow bifurcates

through the V ribs increasing heat transfer throughout the region. This outward flow along the V pointed upstream enhances mixing of flow, creating secondary flow and turbulence. Fig. 7.14 shows velocity vectors and recirculation zones for V-IV continuous ribs. These recirculation zones are created because of V upstream in the first pass, which are enhanced in the second pass because of additional turning effect. Velocity vectors in the inlet and outlet section are shown in Fig. 7.15 (a) for continuous ribs and in Fig. 7.15 (b) for broken ribs. There is greater recirculation in case of broken ribs as compared to continuous ribs in both first and second pass. This increase is because of the placement of broken ribs in the middle of normal pitch ribs. These broken ribs bifurcate flow in the center in addition to the other rib areas and hence, high mixing of flow occurs.

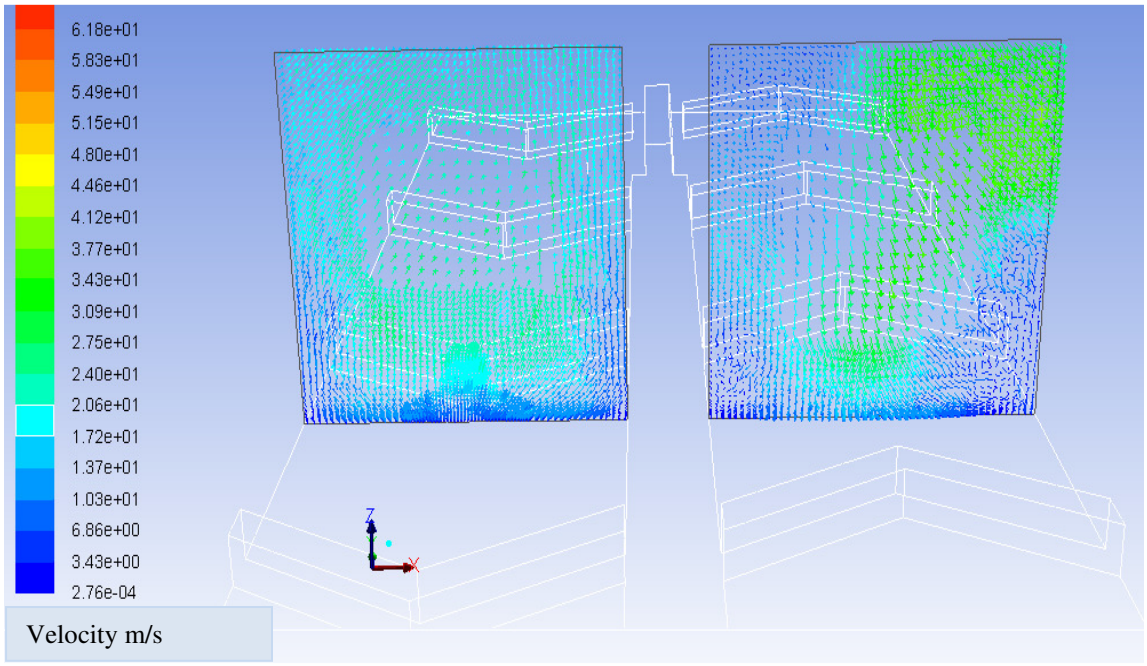

(a)

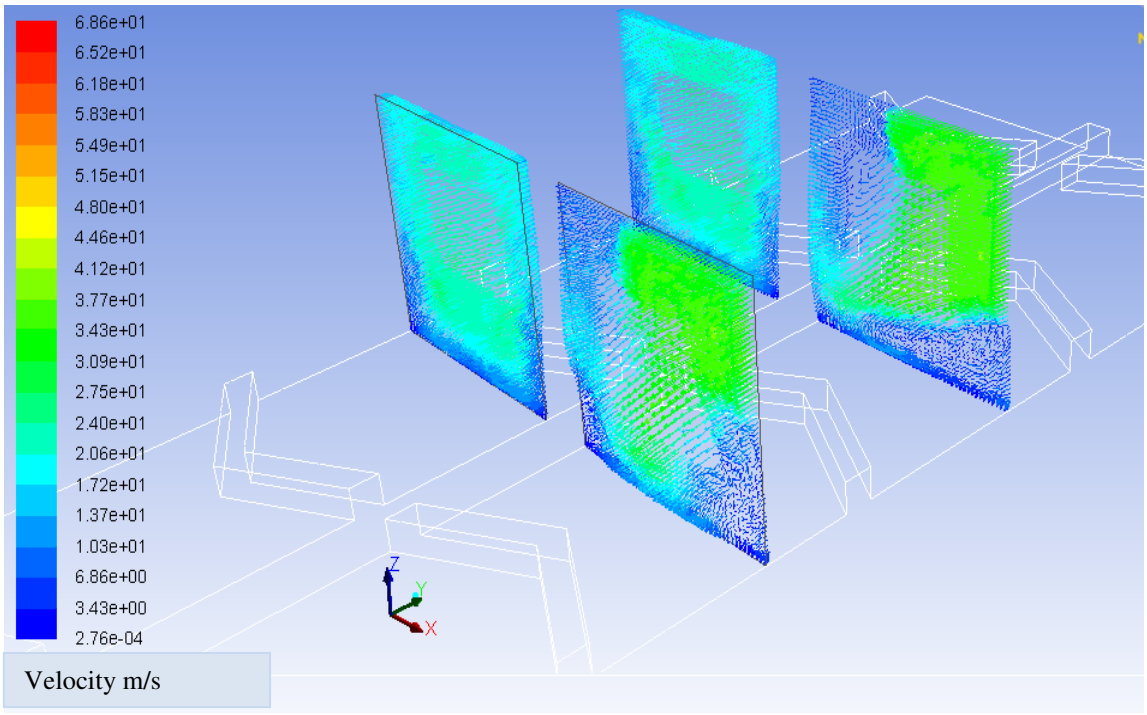

(b)

Figure 7.14: a) Velocity Vector Front View b) Velocity Vectors for Continuous V-IV ribs

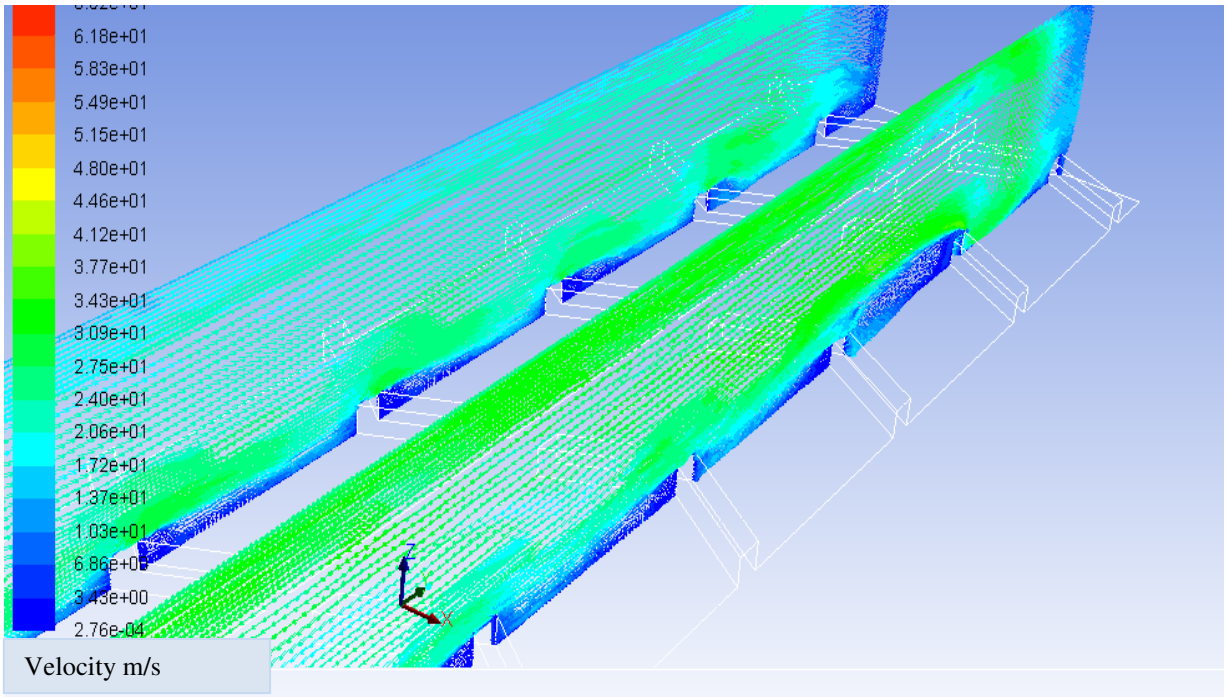

(a)

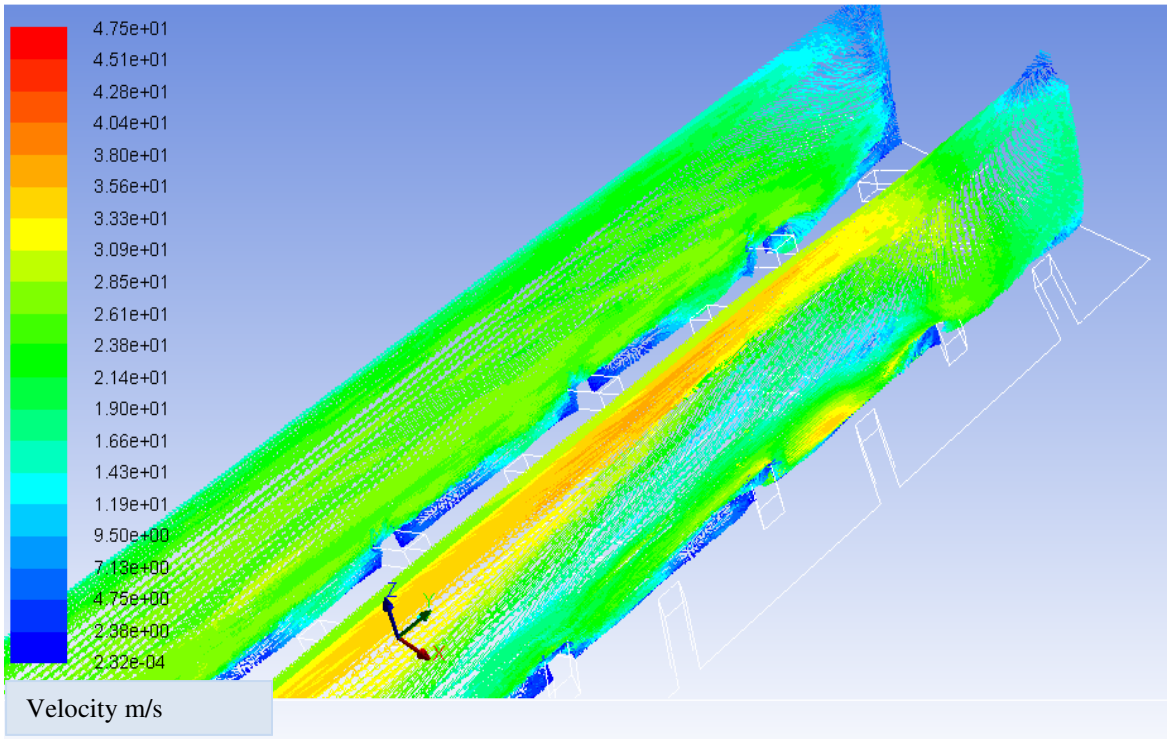

(b)

Figure 7.15: a) Velocity Vector for Continuous b) Velocity Vectors for broken @ x = $0.5D_H$ and x = $1.75D_H$

Fig. 7.16 shows velocity vectors and recirculation zones for V-IV broken ribs. In the first pass, these recirculation zones are created because of V upstream, again, enhanced in the second pass because of turning effect. The recirculation and secondary flow is relatively more dominant in this case as compared to continuous ribs, causing increased heat transfer. Figure 7.17 shows velocity contours and vectors for broken ribs just before the ribs for first pass well as second pass. The flow bifurcates along the two arms of the V ribs. This effect occurs twice in case of broken V ribs causing higher heat transfer throughout the region as compared other cases.

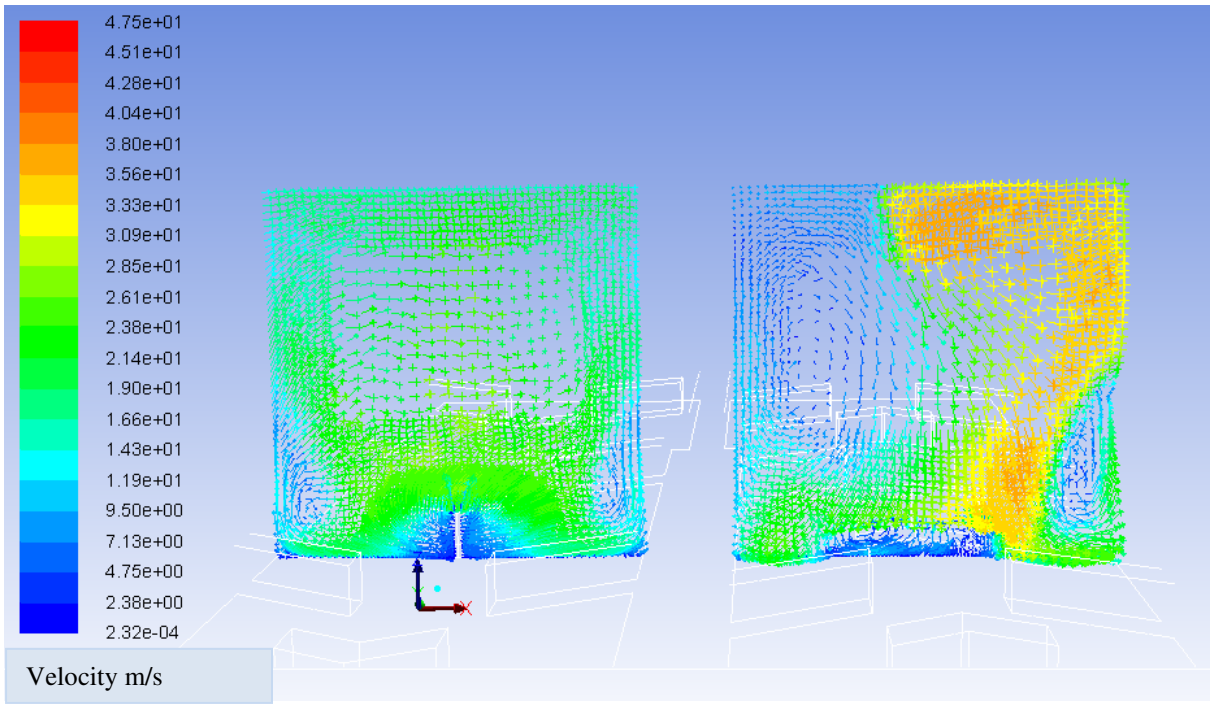

(a)

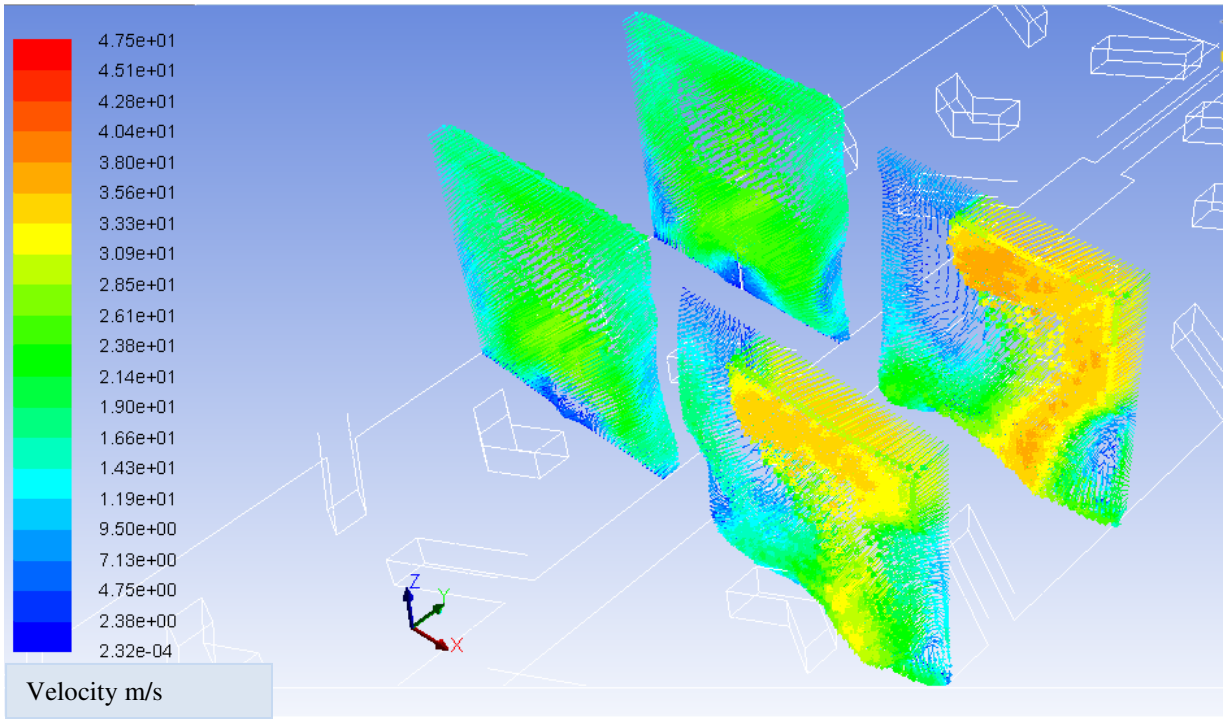

(b)

Figure 7.16: a) Velocity Vector Front View b) Velocity Vectors for Broken V-IV ribs

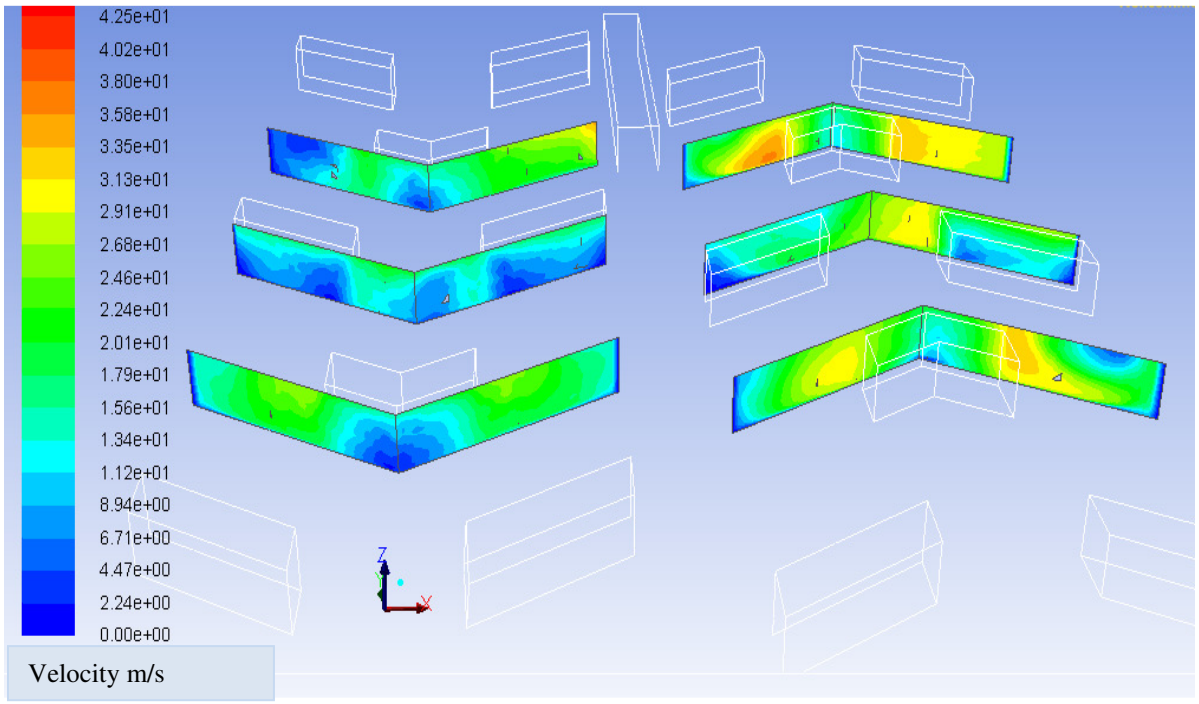

(a)

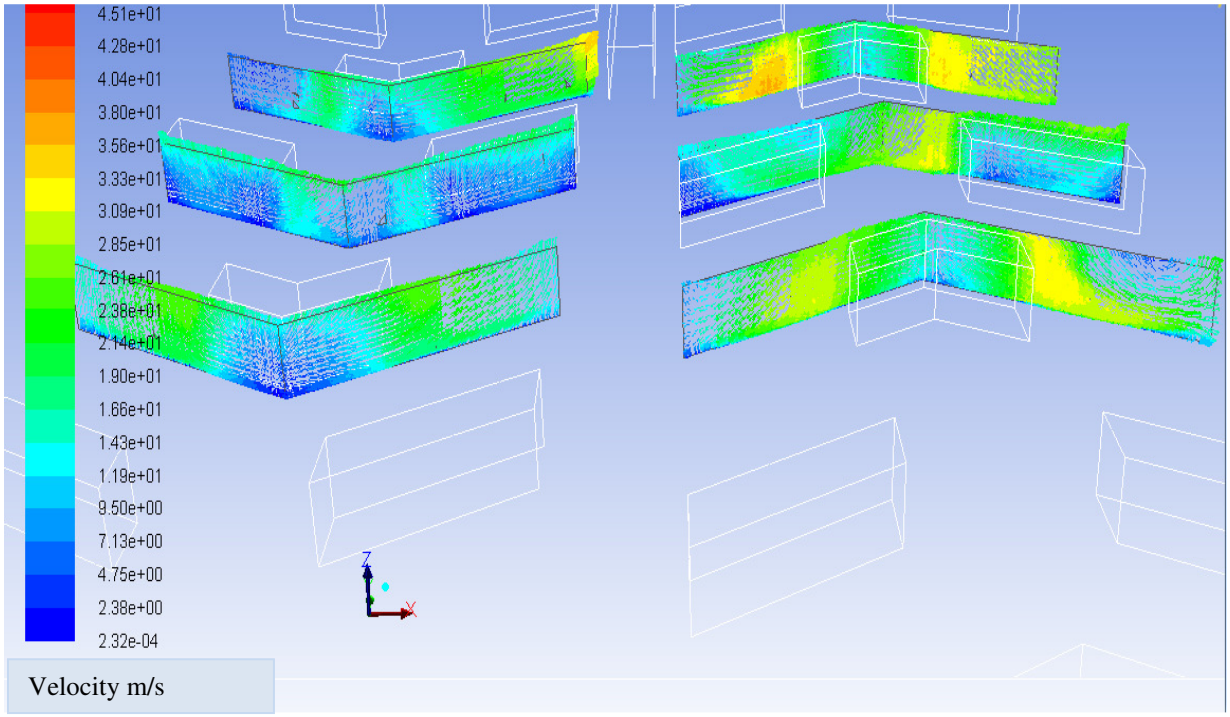

(b)

Figure 7.17: a) Velocity Contours b) Velocity Vectors for Broken V-IV ribs

Iso surfaces :

To fully understand the flow around the ribs in case of continuous and broken V ribs, detailed analyses of isosurfaces of different parameters are done. The parameters used are vorticity, helicity, swirling strength, lamda 2 function and Q criterion.

Vorticity is a vector that describes local spinning of a fluid around a specific point. Mathematically, vorticity of a flow is vector field equal to curl of velocity field.

Helicity is dot product of vorticiy vector and velocity vector. It is the extent to which helix like motion occurs. If a fluid is moving and rotating on an axis parallel to the direction of motion, it will have helicity. Swirling strength is the imaginary part of complex eigenvalues of velocity gradient tensor. It is a measure of local swirling rate inside the vortex. It is positive only if the discriminant is positive and its values represent the strength of swirling motion around local centers.

Q-Criterion identifies vortices as flow regions with positive second invariant of velocity gradient tensor

$$Q = \frac{1}{2}(\Omega_{IJ}\Omega_{IJ} - S_{IJ}S_{IJ}) \tag{7.15}$$

where Ω_{IJ} and S_{IJ} are the anti symmetric and the symmetric parts of velocity gradient tensor. Q criterion is the applied criterion to visualize coherent structures embebbed in the instantaneous field.

Lambda 2 Criterion is the negative value of the second eigenvalue of the symmetry square of velocity gradient tensor which is used as vortex identification method.

Vorticity dominated regions can be determined using these parameters and these vortex core detection methods can provide insight into the wake generation due to ribs. Figs. 7.18 to 7.28 show different isosurface parameters and all these are compared for broken

and continuous ribs cases. Fig. 7.18 shows absolute helicity isosurface for a value of 47063 s^{-2}, it can be seen that there is larger helicity generated area in case of broken rib as compared to continuous rib. In the broken rib case, helicity is present just before and on the rib as compared to only on the rib in case of continuous ribs. The values shown in the figure below are actual values for ease of comparison.

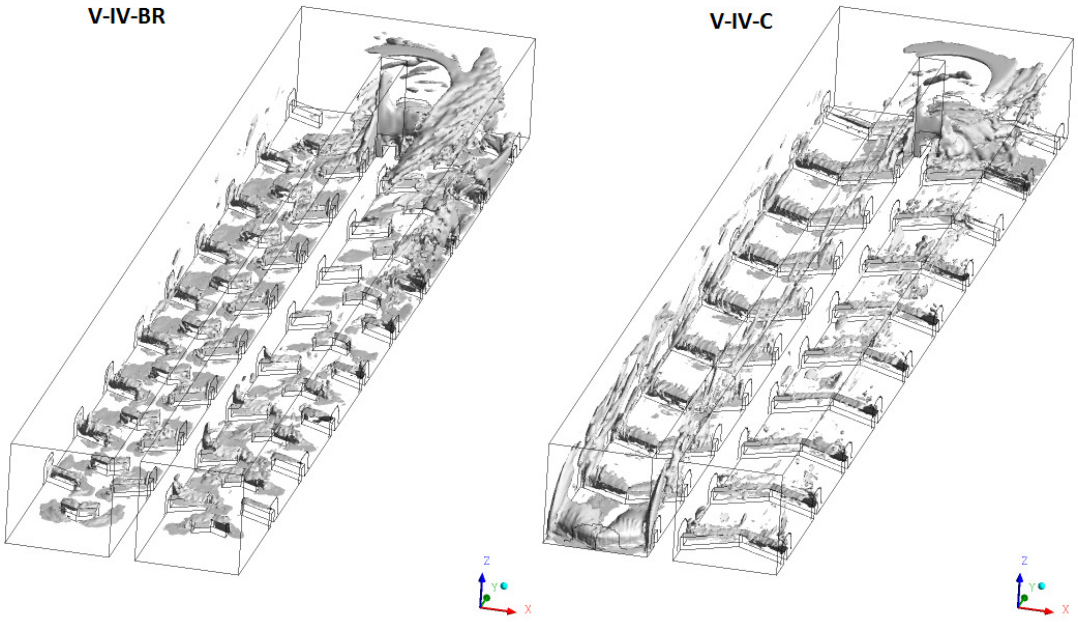

Figure 7.18: Isosurface for absolute Helicity: 4.706E+04 s^{-2} (Re= 56000)

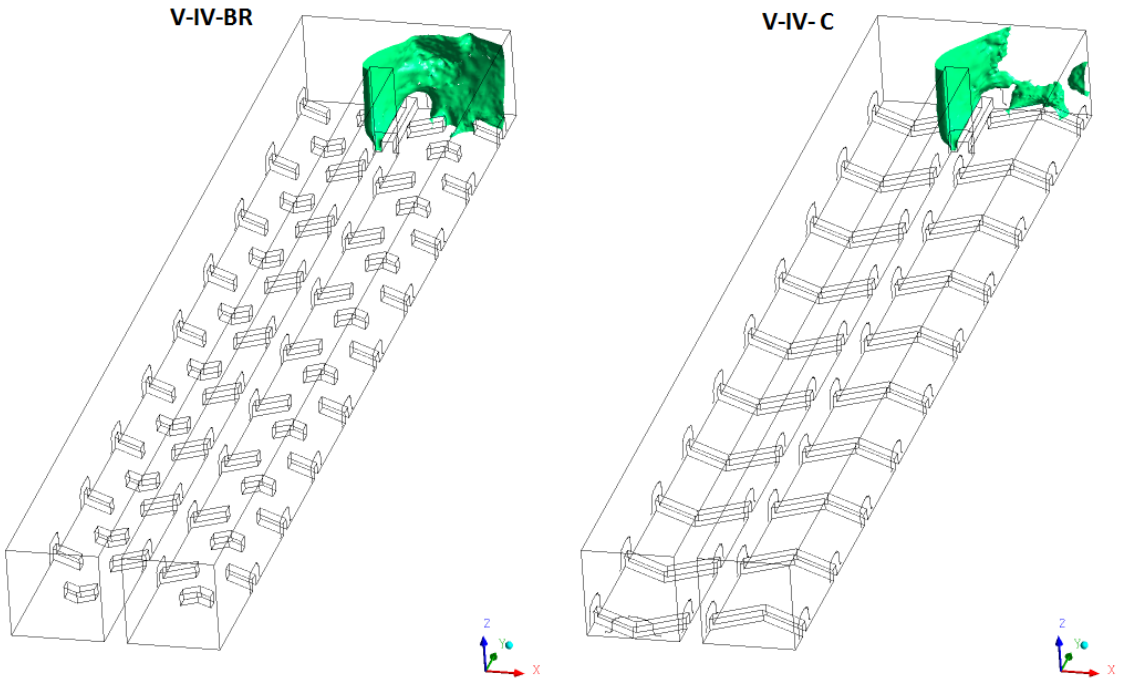

Figure 7.19: Isosurface for absolute Pressure: 1.079E+05 Pa (Re= 56000)

Figure 7.19 shows pressure isosurface which is high in case of broken ribs . Figure 7.20 shows eddy viscosity for both the cases discussed,it can seen from the figure that it is also higher for broken case in terms of eddy viscosity. Figure 7.21 shows swirling strength isosurface, which again clearly shows that broken ribs produce more swirling strength as compared to continuous ribs and the flow is more turbulent near the rib surface leading to generation of secondary flow which helps in the development of the heat transfer. It is seen in the figure that in case of broken ribs , the swirling strengh is enhanced and streched along the ribs. Figure 7.22 (a,b) shows spanwise velocity isosurface . In the figure, because of V upstream, the velocity is expanding near the inner surface in the inlet section and just the opposite in the outlet section. Fig. 7.22 (b) shows isosurface of Spanwise velocity is higher in case of broken ribs.This phenomenon is seen just after the

broken rib and continues till the subsequent broken rib. We donot see this in case of continuous ribs. This is because the vortex being streched in V upstream. Figs. 7.23 and 7.24 show the velocity and vorticity isosurface which again is higher for broken ribs.

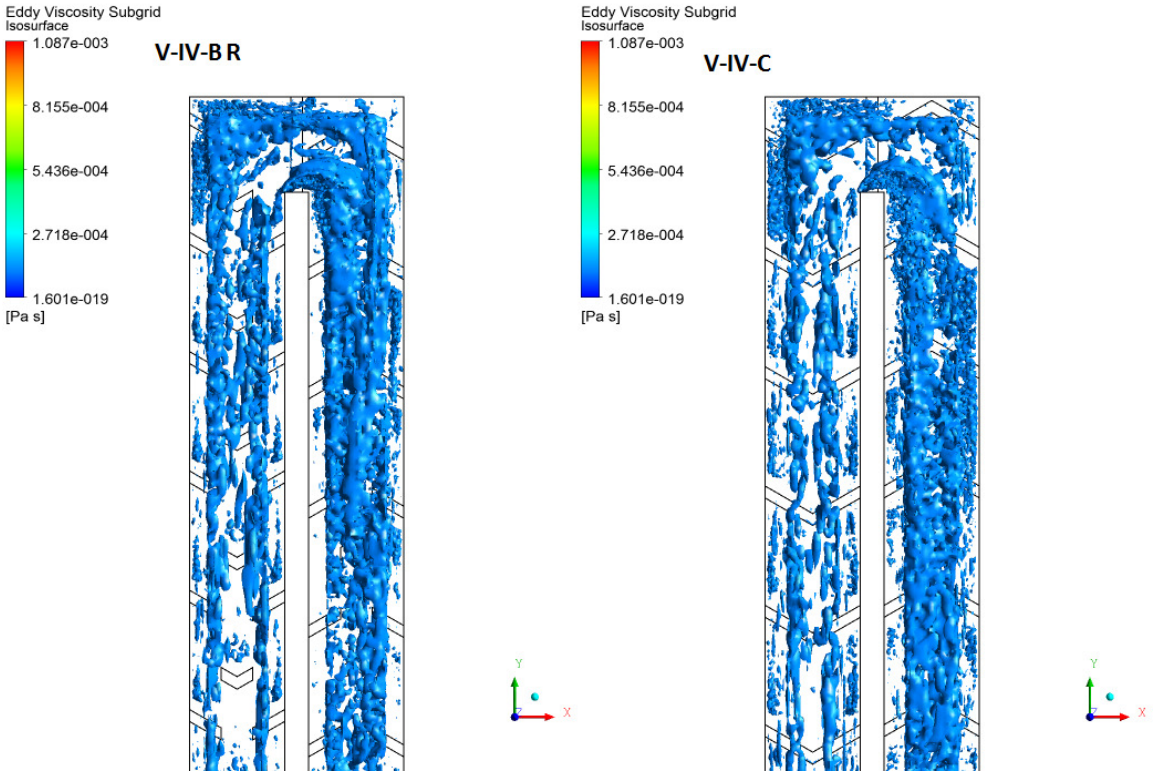

Figure 7.20: Isosurface for Eddy Viscosity: 1.098E-04 Pa-s (Re= 56000)

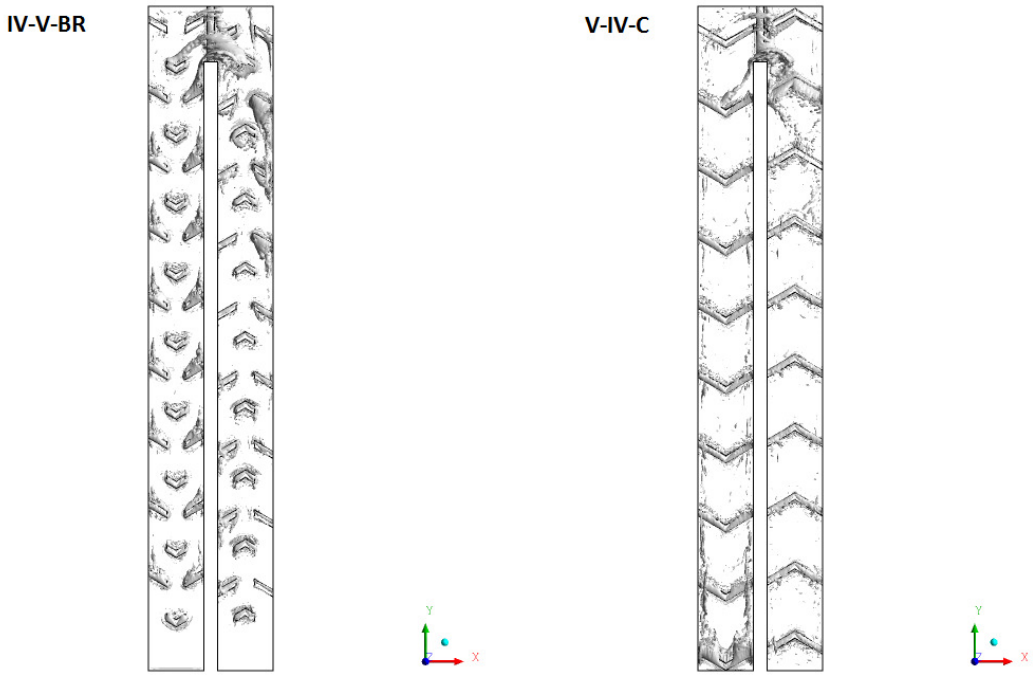

Figure 7.21: Isosurface for Swirling Strength: 1719 s $^{-1}$Re= 56000)

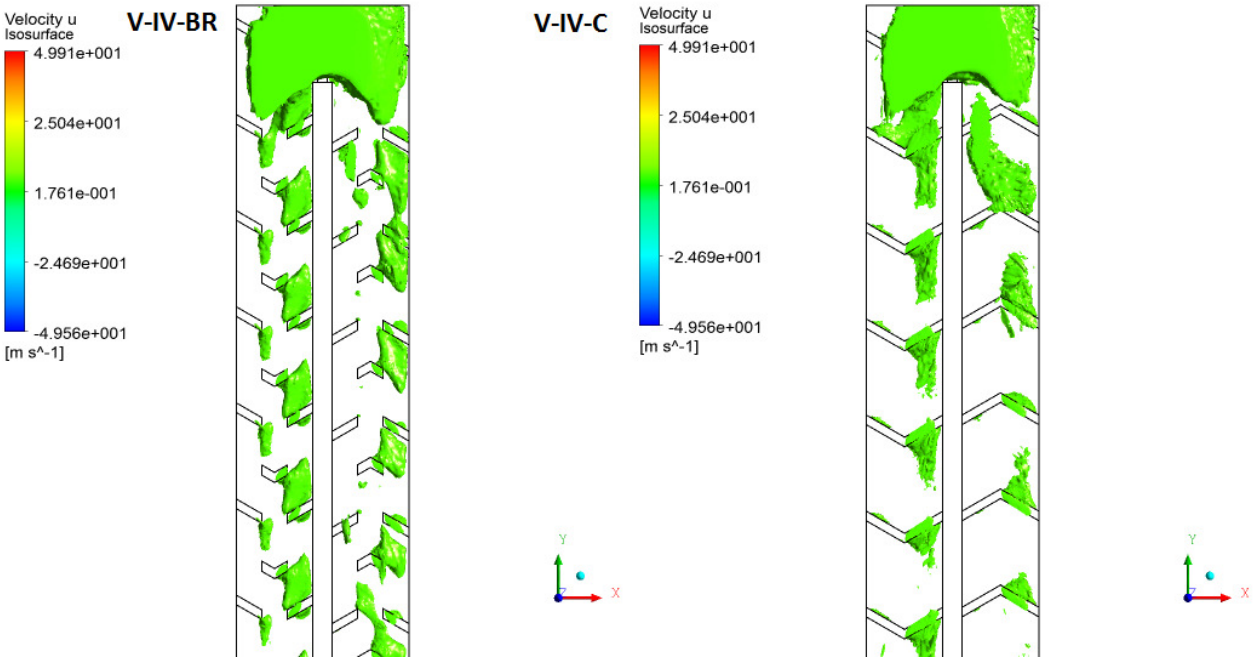

(a)

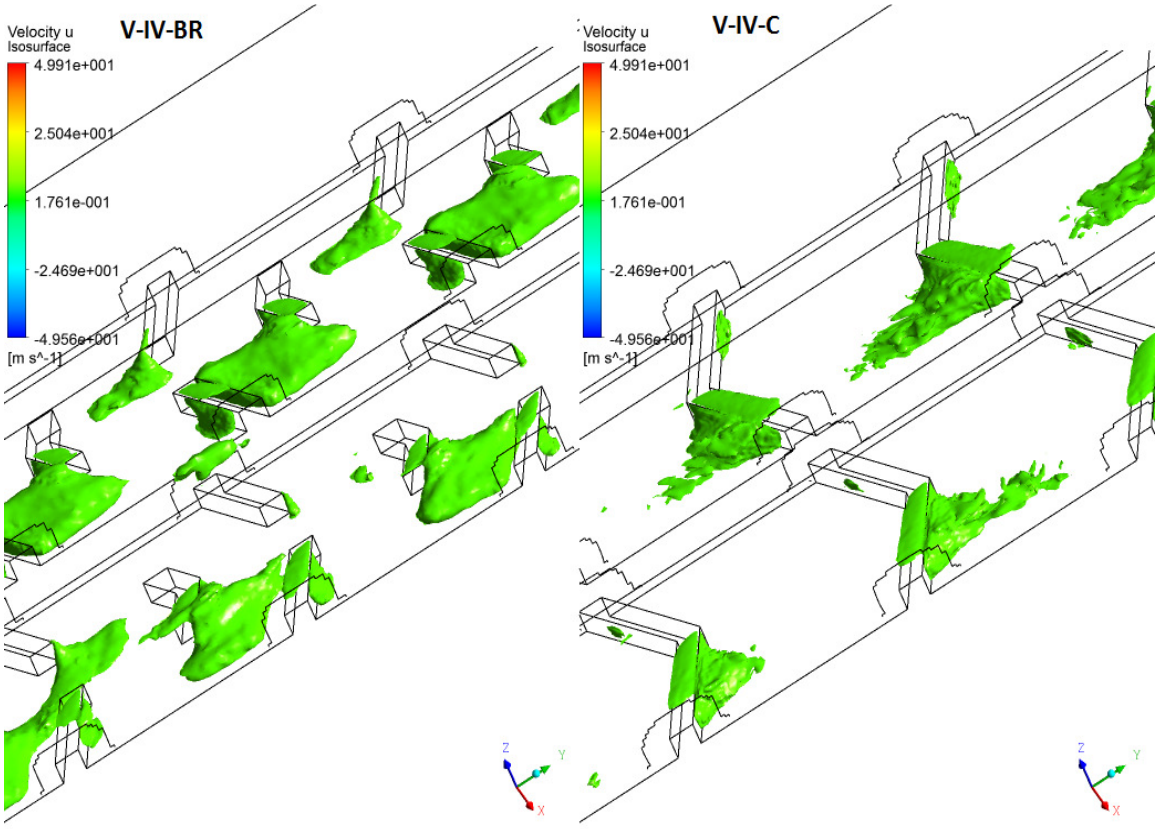

(b)

Figure 7.22: Isosurface for u Velocity: 4.55 m/s (Re= 56000)

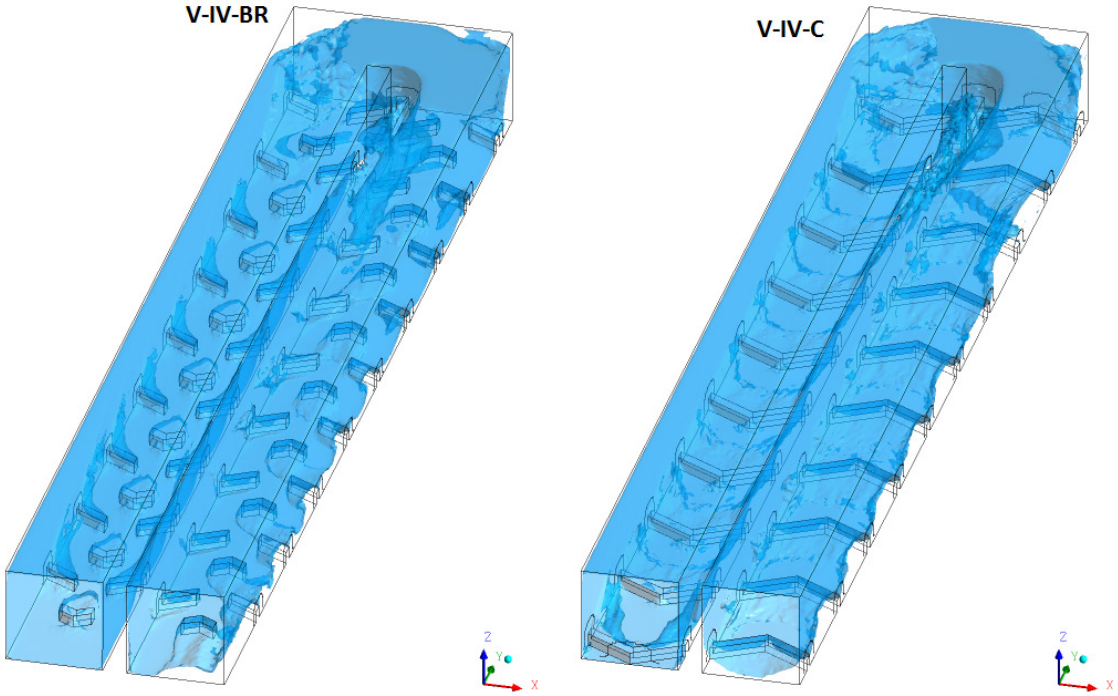

Figure 7.23: Isosurface for Velocity: 8.2 m/s (Re= 56000)

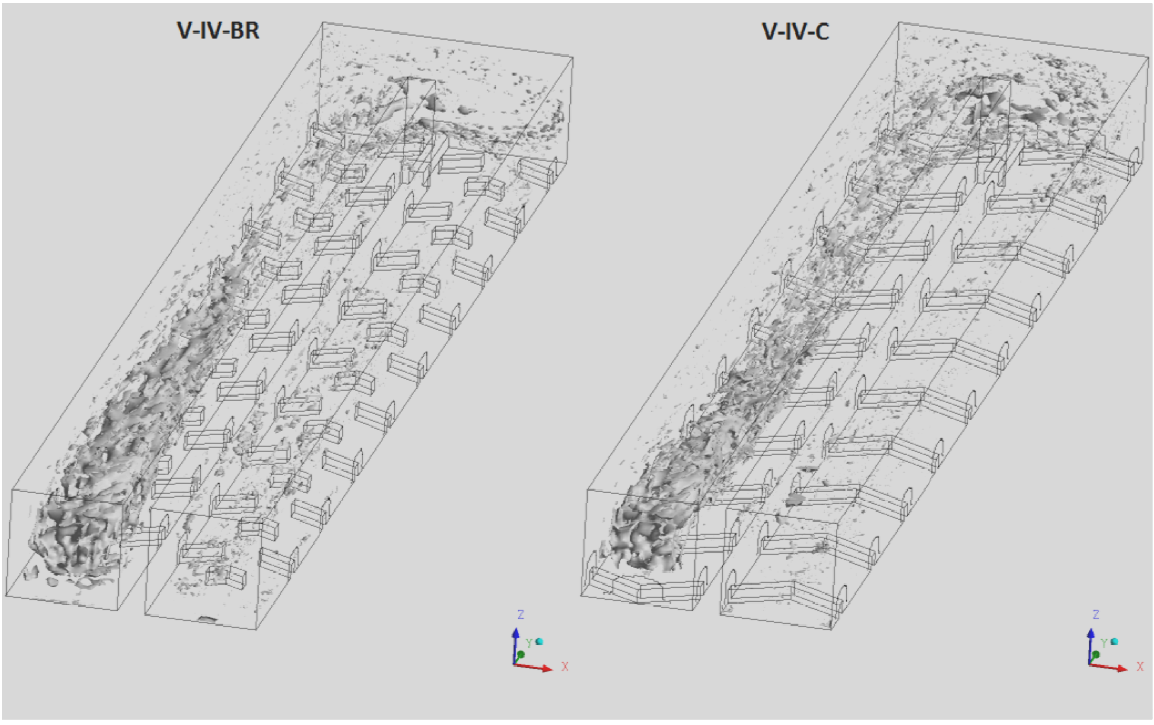

Figure 7.24: Isosurface for Vorticity: 379 s^{-1} (Re= 56000)

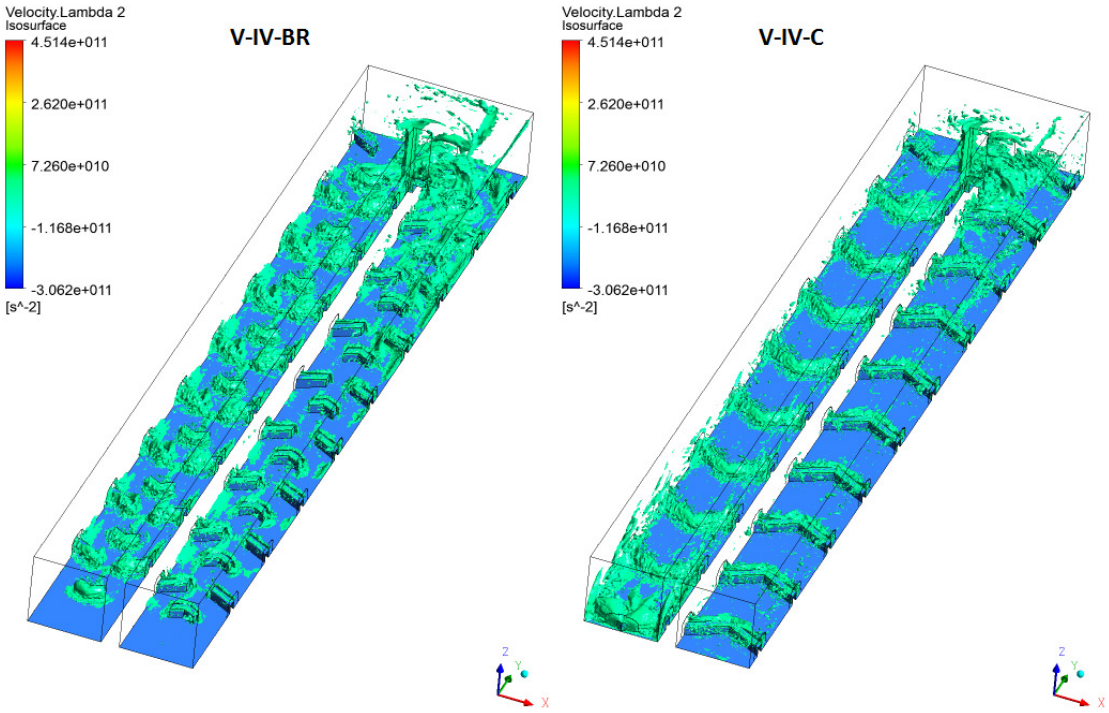

Figure 7.25: Isosurface for Velocity Lambda 2: 1.269E+06 s^{-2} (Re= 56000)

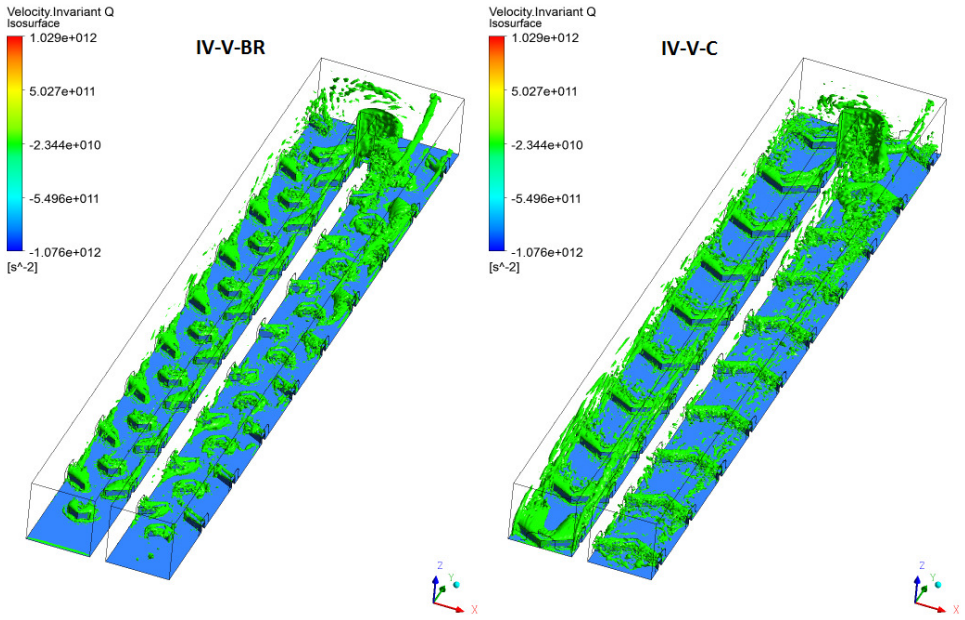

Figure 7.26: Isosurface for Velocity Invariant Q: 1.269E+06 s^{-2} (Re= 56000)

Figs 7.25 and 7.26 show comparison of velocity lambda 2 and Invariant Q which are robust tools to illustrate coherent structure. It can be speculated that turbulent regimes are established by the ribs and these ribs produce structures. This development of Invariant Q and lambda 2 along the surface of the ribs can be seen in both broken and continuous cases. These show perturbation created by the ribs and this flow phenomenon becomes completely three dimensional near the ribs. Figure 7.27 shows Velocity swirling strength for 1000 s^{-1} and fig. 7.28 shows vorticity isosurface. Both of these isosurfaces show how the turbulence is enhanced because of V ribs. Comparison between these two geometries is done based on the difference in the location of swirling or vorticity generation.

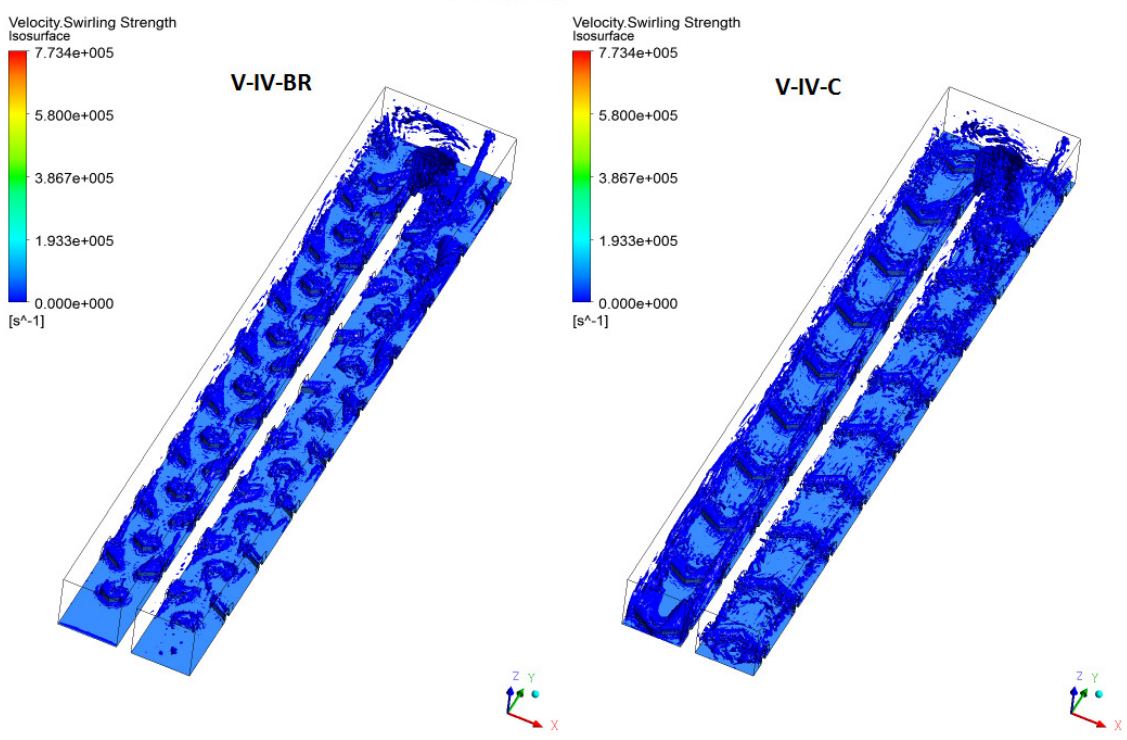

Figure 7.27: Isosurface for Velocity Swirling Strength: 1000 s^{-1} (Re= 56000)

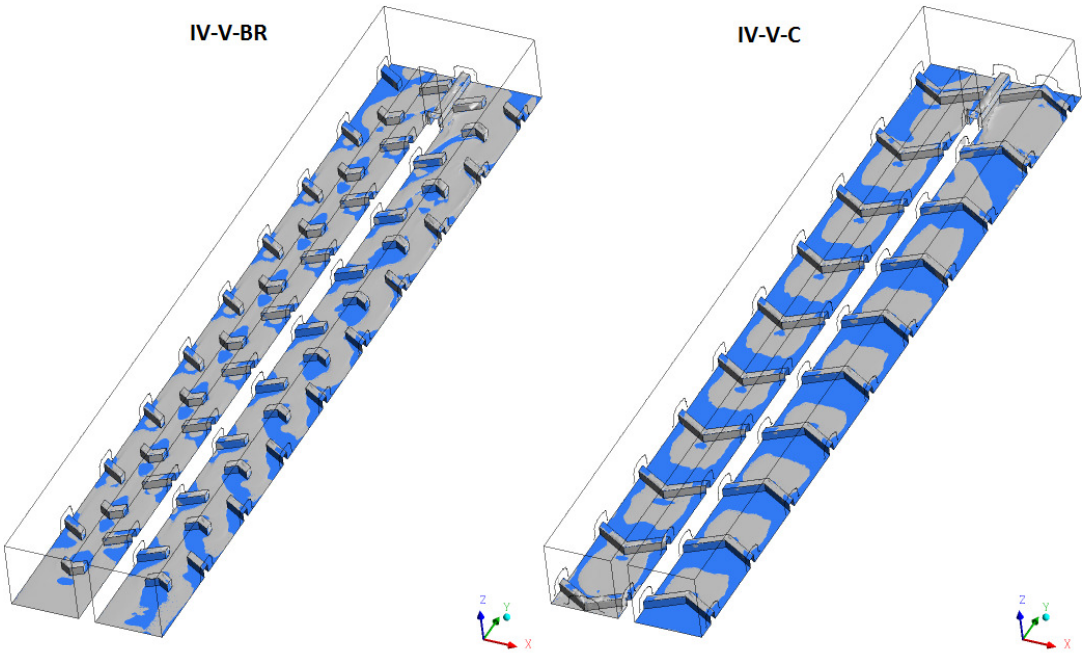

Figure 7.28: Isosurface for Vorticity: 3.516E+04 s^{-1} (Re= 56000)

.

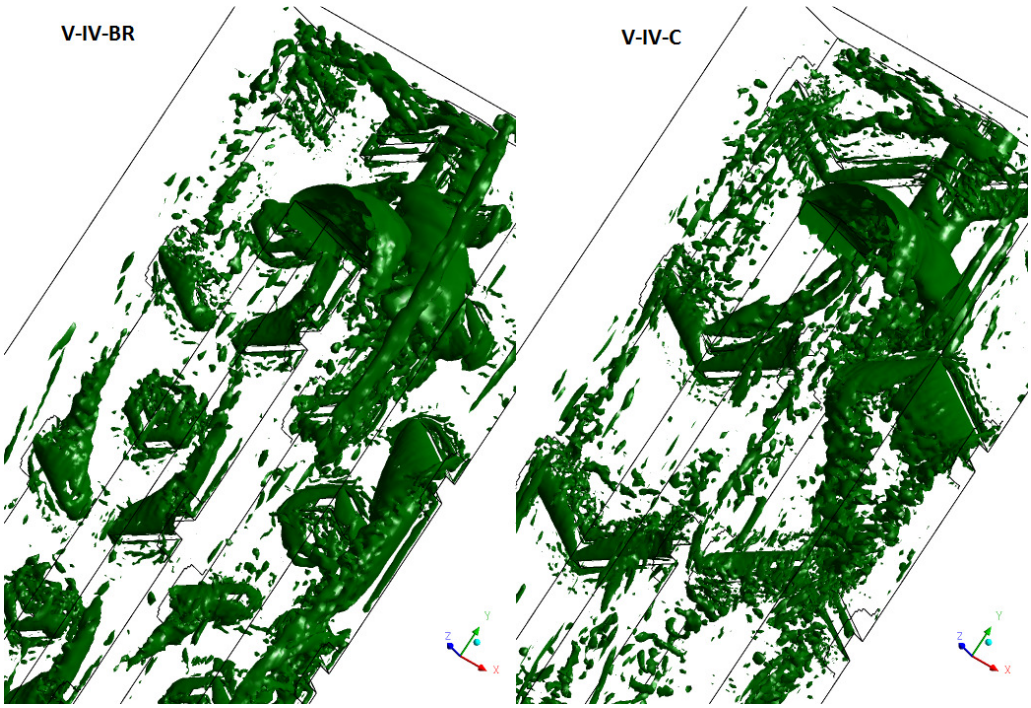

(a)

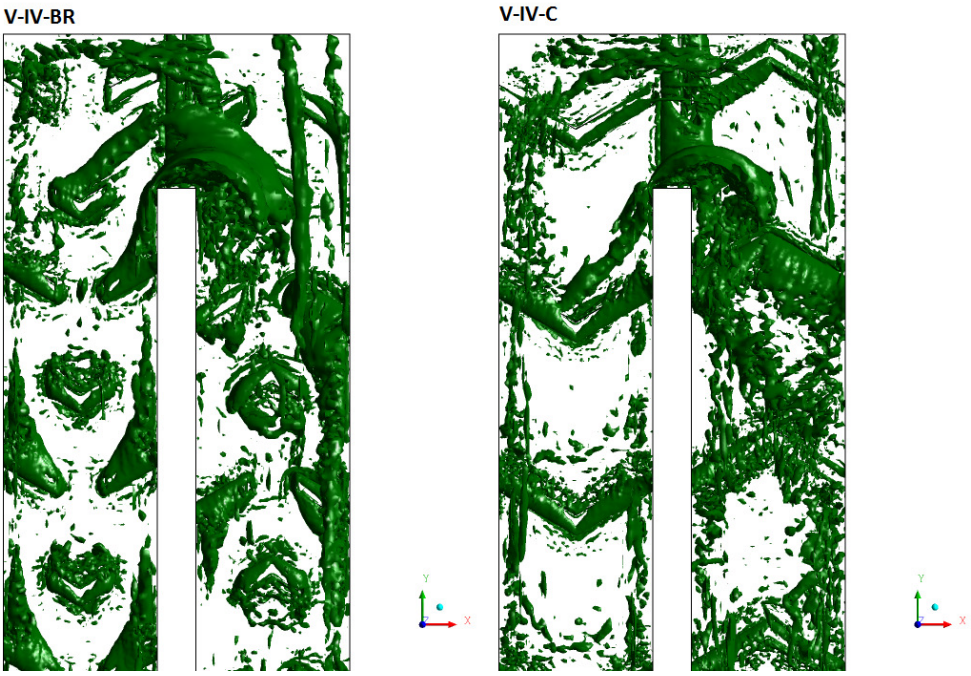

(b)

Figure 7.29: Isosurface for Q Criterion: 1.201E+06 s^{-2} (Re= 56000)

All vortex core parameters such as Vorticity, Helicity, Q criterion and Lambda 2 criterion are compared for both cases and were found to be higher in case of Broken V rib. To understand the physics of the vortex generation around a rib, a detailed discussion follows.

In Fig. 7.25, Lambda 2 criteria are shown for both types of ribs. Vortex field near the leading edge of the ribs is considerably stronger than that on the trailing edge which causes destabilization of flow field near the leading edge resulting in shear layer separation. High Nusselt Number at the leading edge is a clear indication of this phenomenon. Vortical structures near either side of the rib walls can be seen in Fig. 7.25, these are generated due to wall turbulence in the form of hairpin getting influenced by separating shear layers. Since the area of flow cross-section is decreasing, it causes flow

to accelerate locally and these vortical structures are carried downstream by the main flow.

In Fig. 7.29, Q criterion is shown for both types of ribs. Fig 7.29 (a) is an isometric view of the vortices generated around the turn region and 7.29 (b) is the top view of the ribs. Vortex field near the leading edge of the ribs is considerably stronger. Compared to continuous ribs, after the generation of vortices along the leading side, these vortices are convected more rapidly in case of Broken V. This is because of the high stream wise flow in the central region of broken ribs increasing vortices along inner and outer wall. In case of continuous V, the vortices are generated but are reduced along the flow because of velocity reduction. In case of broken ribs, there is a broken pointed V in upstream direction which causes re separation and hence greater heat transfer.

Figure 7.30 shows Streamlines for broken ribs with Nusselt Number for Inlet section as well as outlet section. Similarly Fig. 7.31 shows Streamlines for continuous ribs with Nusselt Number for Inlet section as well as outlet section. The higher heat transfer coefficient or Nusselt Number enhancement for upstream can be explained by vortex line streching. As observed in the figure, vortex generated is amplified by the velocity gradient along the ribs. In case of broken ribs, the vortex generation is amplified becouse of presence of additional arms between two V shaped ribs. Further thinning of boundary layer takes place resulting in higher heat transfer.

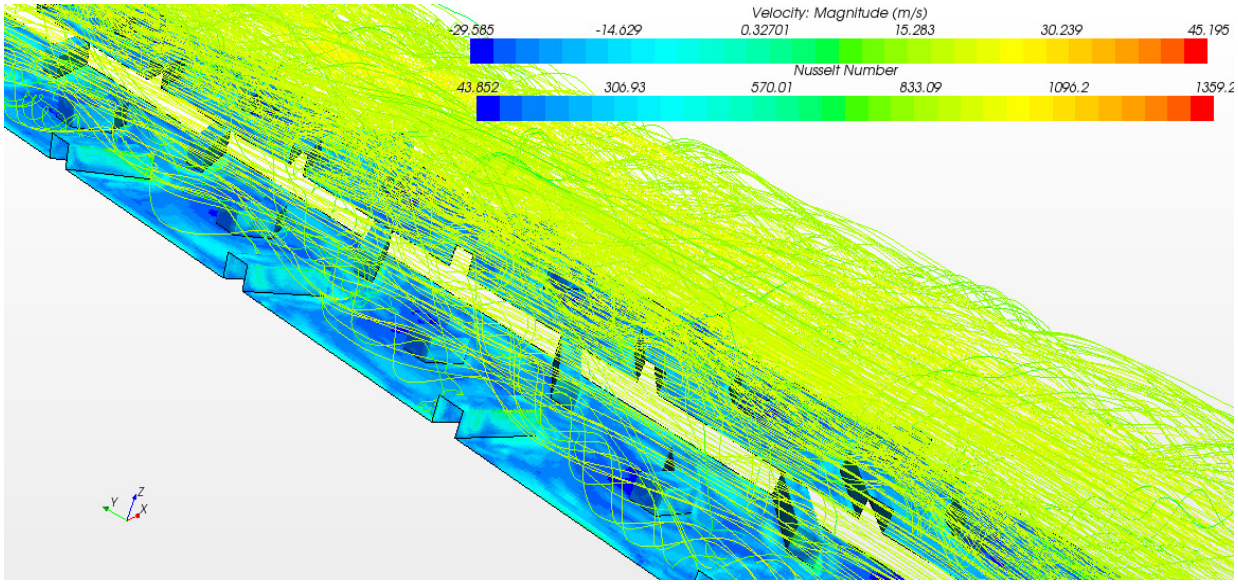

(a)

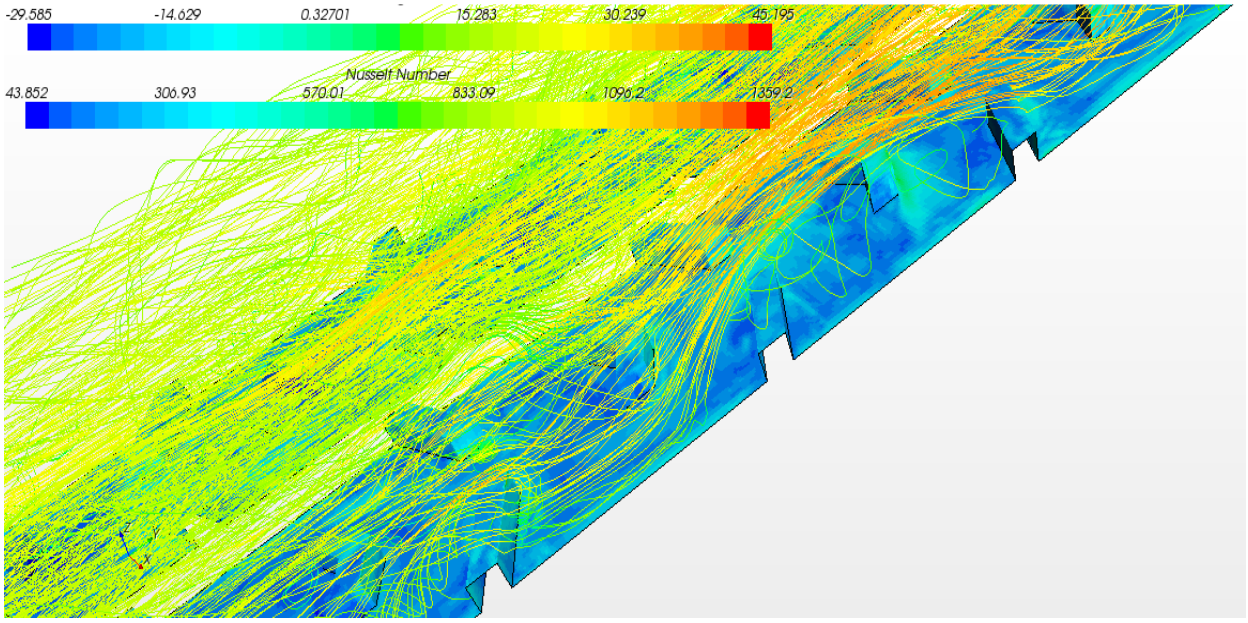

(b)

Figure 7.30: Streamlines for Broken ribs with Nusselt Number a) Inlet Section b) Outlet Section (Re =56,000)

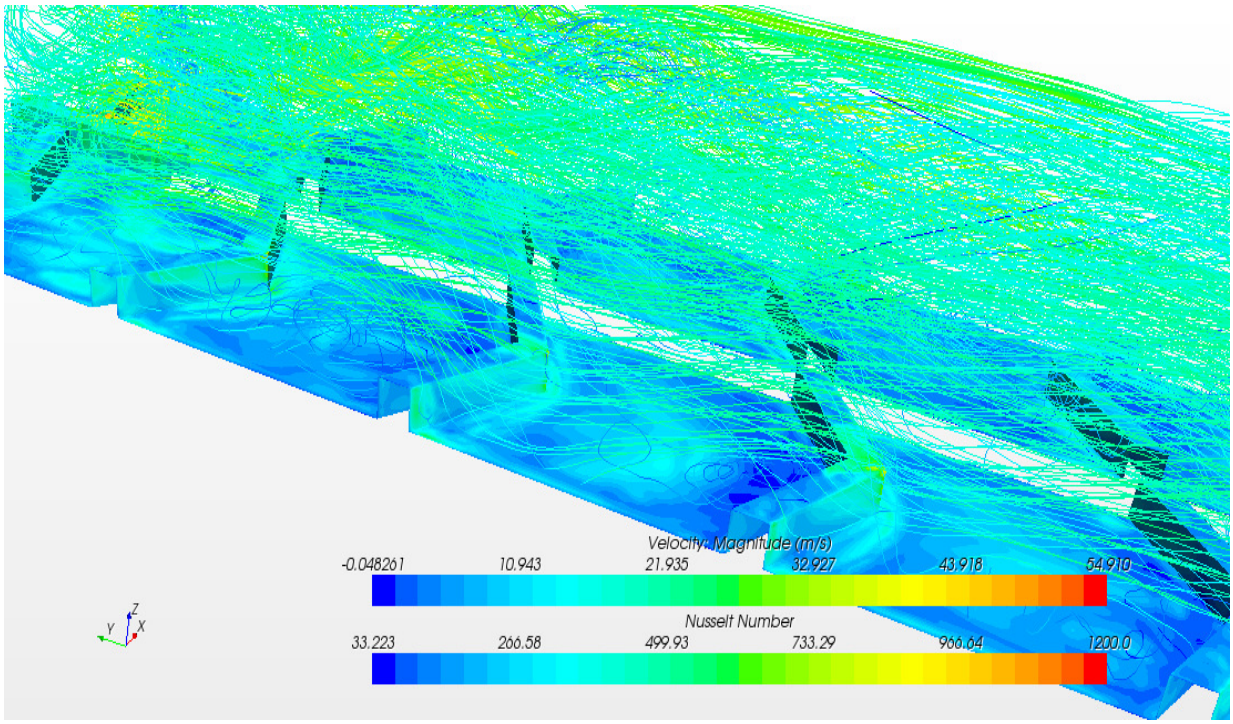

(a)

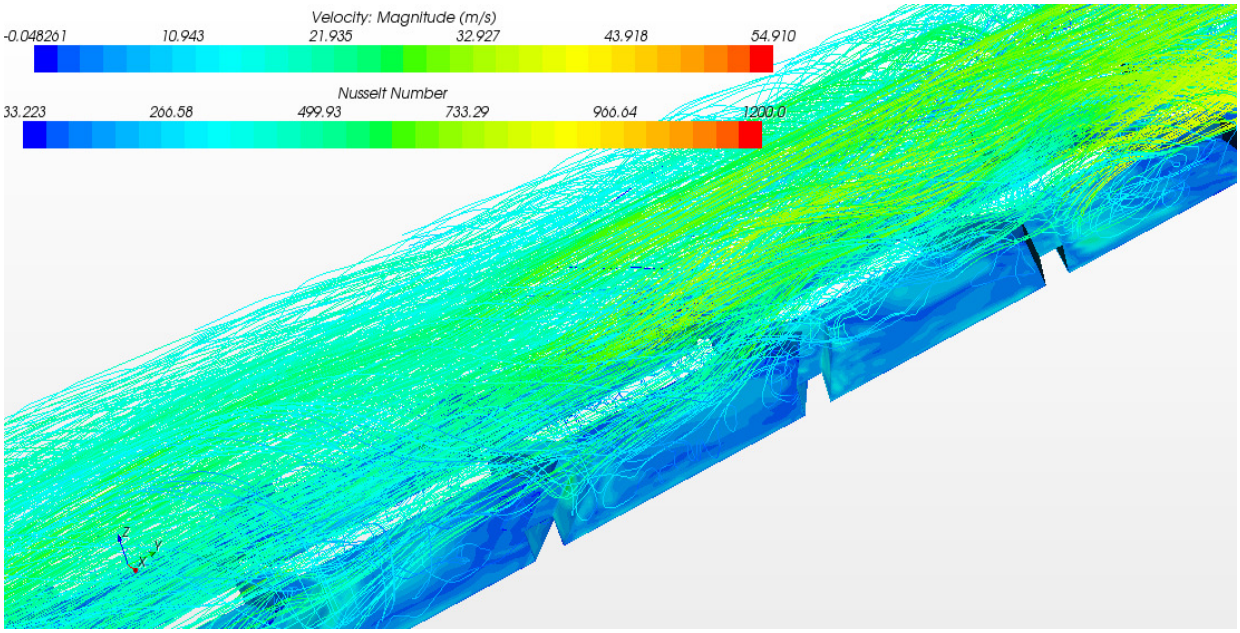

(b)

Figure 7.31: Streamlines for Continuous ribs with Nusselt Number a) Inlet Section b) Outlet Section (Re =56,000)

CHAPTER 8: HYBRID LES/RANS MODELING WITH ASM

8.1 Introduction:

Large-Eddy Simulation (LES) methods directly calculate large-scale turbulent structures and reserve modeling only for the smallest scales. In outer region, grid resolution is dependent on larger turbulent scales instead of near wall turbulent scale. Reynolds's stress model (RSM) is a higher level turbulence model called as Second Order Closure. In RSM, the eddy viscosity approach is not used and the Reynolds stresses are directly computed. The exact Reynolds stress transport equation accounts for the directional effects of the Reynolds stress fields. One example of Hybrid LES-RANS is Detached Eddy Simulation (DES). DES is a mix of LES and URANS. The aim is to treat the boundary layer with RANS and capture the outer detached eddies with LES.

LES provides accurate velocity, velocity gradient value because it directly calculates the large scale structures and RSM provides Reynolds stresses. The main objective of this work is to use a Hybrid LES/RANS model with Algebraic Stress Model (ASM) to modify Reynolds stresses and calculate heat transfer. These modified Reynolds stresses are used to predict heat transfer in cooling channel. ASM is used because of its simplicity and accuracy to predict the near wall effect. It can be implemented in the latter stage for post processing of results.

8.2 Algebraic Stress Model (ASM):

The main problem in predicting turbulent flow is to determine the Reynolds stresses. Algebraic Stress model is an economical way of accounting for the anisotropy of Reynolds Stresses without going into full length of solving the Reynolds stress transport

equations. Algebraic equation can be obtained for these Reynolds stress by relating to mean velocity gradient. Rodi [75] proposed that if convective and diffusive transport terms are removed or modeled then the Reynolds stress equation can be reduced to a set of algebraic equations.

To solve a turbulent flow with RSM turbulence model, eleven turbulent transport equations that includes six for Reynolds stress, two for *k* and ε and three in $\overline{u_\iota \theta}$ need to solved . It becomes very costly to solve these eleven transport equations. The idea is to use the Reynolds stress equation convective and diffusive terms and express in terms of *k,* as *k* equations are already being solved.

Assuming $\overline{u_\iota u_J} \sim k$, with some mathematical manipulation we can get algebraic stress equations as

$$\frac{\overline{u_i u_j}}{k} - \frac{2}{3}\delta_{ij} = \lambda\left(\frac{P_{ij}}{\epsilon} - \frac{2}{3}\delta_{ij}\right) \tag{8.1}$$

where

$$\lambda = \frac{1 - C_{\emptyset 2}}{\frac{P_k}{\epsilon} - 1 + C_{\emptyset 1}} \tag{8.2}$$

8.3 LES/RANS Modeling with ASM:

As suggested in the previous sections, ASM model have few advantages as it's a cheap method for Reynolds stress anisotropy. It potentially combines the generality of the approach of the RSM with the economy of *k*-ε model. It has been successfully applied to isothermal and buoyant thin shear layers. Meroney [76] used an algebraic stress model for stratified turbulent shear flows. Till now there has been some LES modeling which uses RANS model in the near wall zone like LES-URANS.

In the present study LES model and RSM model are used to modify Reynolds stresses. Modification of Reynolds stresses are done using ASM and then these modified Reynolds stresses are used for heat transfer measurement. The main reasoning is to use ASM model coupling together with the LES model. The use of modified Reynolds stress using these equations provides better results.

Reynolds Stress Production Term:

$$P_{ij} = -\left(\overline{u_l u_m}\frac{\partial U_j}{\partial x_m} + \overline{u_j u_m}\frac{\partial U_i}{\partial x_m}\right) \tag{8.3}$$

Equation 8.3 is the Reynolds stress production term of Reynolds stress transport equations. All the Reynolds stress production terms are expanded as shown in Eq. 8.4 to Eq. 8.9.

Expansion of Reynolds Stress Production Term used in ASM Reynolds stress calculation:

$$P_{11} = -2\left(\overline{uu}\frac{\partial U}{\partial x} + \overline{uv}\frac{\partial U}{\partial y} + \overline{uw}\frac{\partial U}{\partial z}\right) \tag{8.4}$$

$$P_{12} = -\left(\overline{uu}\frac{\partial V}{\partial x} + \overline{uv}\frac{\partial V}{\partial y} + \overline{uw}\frac{\partial V}{\partial z} + \overline{uv}\frac{\partial U}{\partial x} + \overline{vv}\frac{\partial U}{\partial y} + \overline{vw}\frac{\partial U}{\partial z}\right) \tag{8.5}$$

$$P_{13} = -\left(\overline{uu}\frac{\partial W}{\partial x} + \overline{uv}\frac{\partial W}{\partial y} + \overline{uw}\frac{\partial W}{\partial z} + \overline{uw}\frac{\partial U}{\partial x} + \overline{vw}\frac{\partial U}{\partial y} + \overline{ww}\frac{\partial U}{\partial z}\right) \tag{8.6}$$

$$P_{22} = -2\left(\overline{uv}\frac{\partial V}{\partial x} + \overline{vv}\frac{\partial V}{\partial y} + \overline{vw}\frac{\partial V}{\partial z}\right) \tag{8.7}$$

$$P_{23} = -\left(\overline{uv}\frac{\partial W}{\partial x} + \overline{vv}\frac{\partial W}{\partial y} + \overline{vw}\frac{\partial W}{\partial z} + \overline{uw}\frac{\partial V}{\partial x} + \overline{vw}\frac{\partial V}{\partial y} + \overline{ww}\frac{\partial V}{\partial z}\right) \tag{8.8}$$

$$P_{33} = -2\left(\overline{uw}\frac{\partial W}{\partial x} + \overline{vw}\frac{\partial W}{\partial y} + \overline{ww}\frac{\partial W}{\partial z}\right) \tag{8.9}$$

All the production terms consist of Reynolds stresses and gradient of velocity. The idea was to obtain all the gradient of velocity terms from LES model and the Reynolds stress terms from RSM model. Using these values, modified Reynolds stress terms were calculated. The whole rationale was to use ASM and get the results which provide better numerical results prediction as discussed in the next section.

Reynolds Stresses of ASM:

$$\overline{uu} = \left[\lambda\left(\frac{P_{11}}{\epsilon} - \frac{2}{3}\right) + \frac{2}{3}\right] k \tag{8.10}$$

$$\overline{uv} = \left[\lambda\left(\frac{P_{12}}{\epsilon}\right)\right] k \tag{8.11}$$

$$\overline{uw} = \left[\lambda\left(\frac{P_{13}}{\epsilon}\right)\right] k \tag{8.12}$$

$$\overline{vv} = \left[\lambda\left(\frac{P_{22}}{\epsilon} - \frac{2}{3}\right) + \frac{2}{3}\right] k \tag{8.13}$$

$$\overline{vw} = \left[\lambda\left(\frac{P_{23}}{\epsilon}\right)\right] k \tag{8.14}$$

$$\overline{ww} = \left[\lambda\left(\frac{P_{33}}{\epsilon} - \frac{2}{3}\right) + \frac{2}{3}\right] k \tag{8.15}$$

All the Reynolds stresses from ASM are shown in Eq. 8.10 to Eq. 8.15. These equations are expansion of all the six Reynolds stresses used for modification and for the final calculation of heat transfer enhancements.

Steps involved in Hybrid LES/RANS modeling with ASM (For heat transfer calculation):

1. All velocity gradient terms are obtained from LES model.

2. Reynolds stresses are obtained by solving the RSM model.

3. Modified Reynolds stresses are obtained from the ASM.

4. Turbulent kinetic energy calculated using modified Reynolds stress from ASM.

The interlinkage between the near wall variation in temperature and local wall heat flux is given by [77]

$$\frac{c_{p*k_p^{0.5}*\rho}}{h} = \left(\frac{U_p * k_p^{0.5}}{\tau_w/\rho} + \mathbf{\Lambda}\right) \tag{8.16}$$

Where **Λ** is **Λ** Function given by Jayatilleke [78]

$$\mathbf{\Lambda} = 9.24\left[\left(\mathrm{Pr}/\mathrm{Pr}_T\right)^{0.75} - 1\right]\left[1 + 0.28\exp\left(\frac{-0.007\mathrm{Pr}}{\mathrm{Pr}_T}\right)\right] \tag{8.17}$$

Once heat transfer coefficient is calculated using the Eq. 8.16 then, Nusselt number ratio can be formulated.

8.4 Rib arrangement:

Hybrid LES/RANS modeling with ASM model is carried out for the best configuration for a Reynolds Number of 56,000. The ribs selected for continuous as well as broken ribs are Inlet V and Outlet Inverted V. The results are shown for these two best configurations and it shows great agreement with experimental results.

A) Continuous V ribs:

Case 1: 60^o V rib at inlet and 60^o inverted V rib at outlet (V-IV_C)

B) Broken V ribs:

Case 2: 60^o Broken V rib at inlet and 60^o Broken inverted V rib at outlet (V-IV_B)

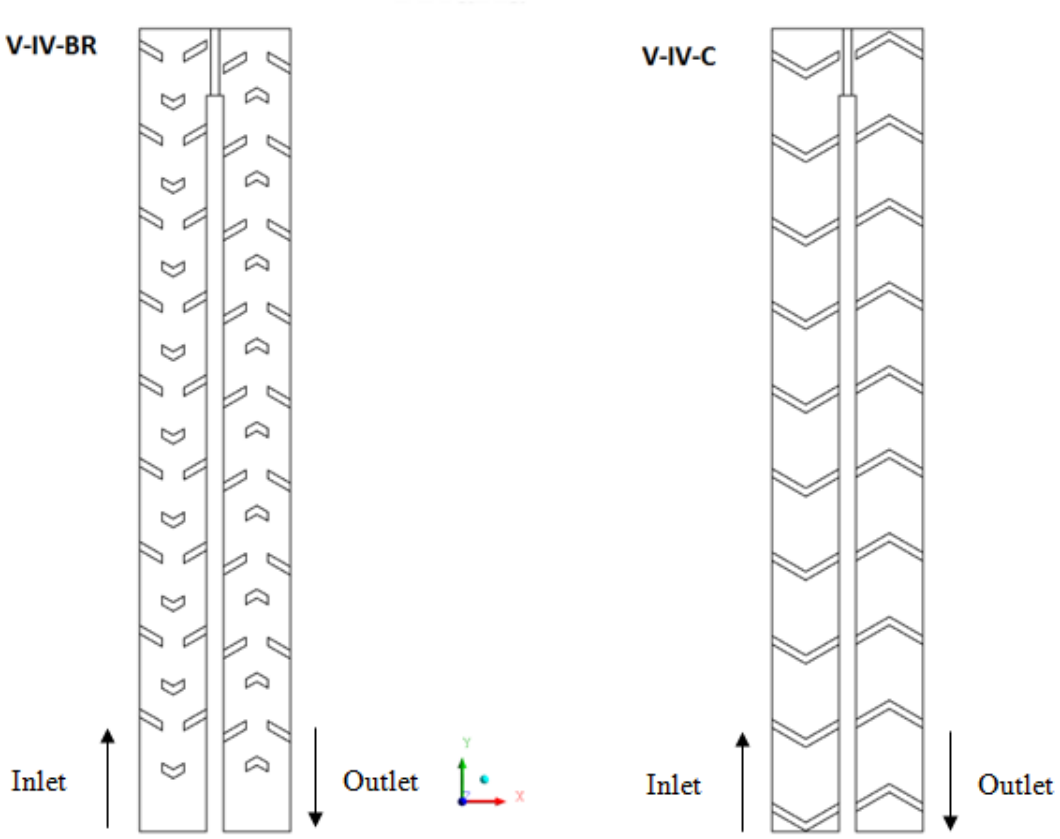

Figure 8.1: Inlet V and Outlet Inverted V 60^{o} Continuous and Broken rib turbulators top View

Figures 8.1 and 8.2 show the rib configuration selected for analysis. Fig. 8.1 shows top view of the ribs and the fig. 8.2 shows isometric views of the ribs considered.

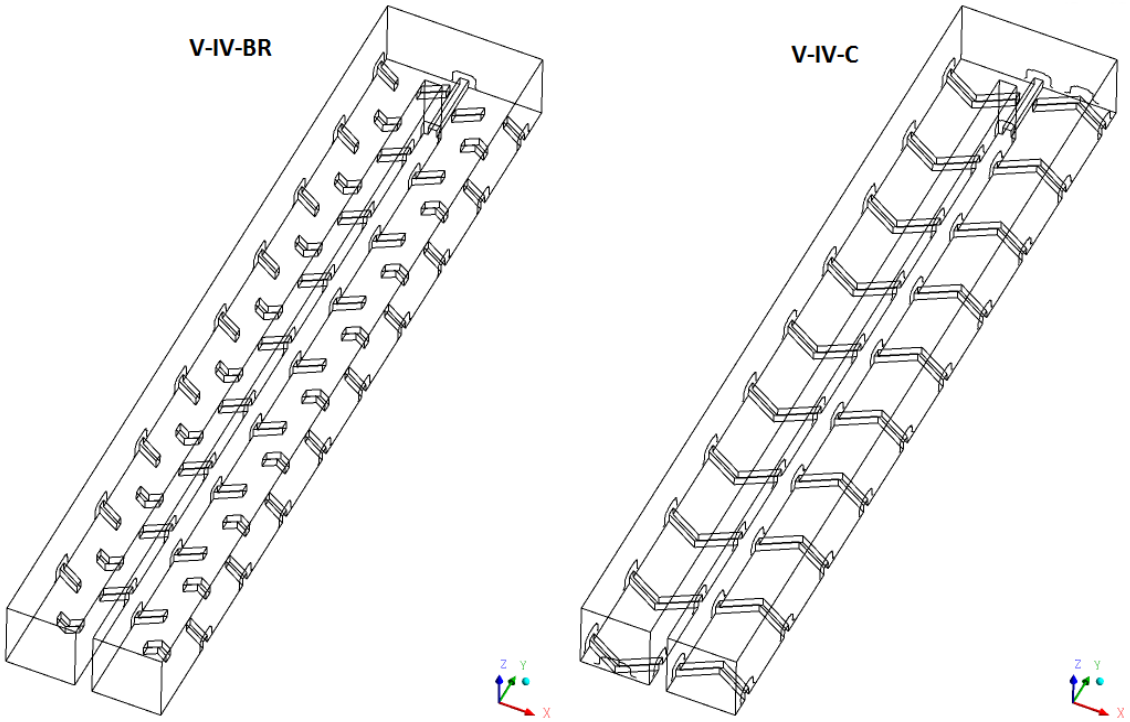

Figure 8.2: Inlet V and Outlet Inverted V 60^{o} Continuous and Broken rib turbulators isometric view

8.5 Results and Discussions:

Nusselt Number Ratio:

Figures 8.3 and 8.4 show comparison of Nusselts Number ratio of Inlet V and Outlet Inverter V Broken and Continuous rib channel. The comparision of Hybrid LES/RANS with ASM is done with RSM , LES and Experimental Results. From the figures, it can be clearly concluded that Hybrid model predicts heat transfer rate in channel more accurately as compared to other model. Comparision was done for Reynolds Number of 56,000 as LES simulation is done for those cases. The results show that from inlet to outlet, there is increase in Nusselt Number ratio. In turn there is a peak, which is because of the turn effect and Coriolis effect of the flow. The results are used as post processing

this particular case but it greatly signifies that LES/ASM model can be used as a substitute to LES/RANS model presently by significantly reducing the computer resource.

Table 8.1: Resource usage summary comparison

LES-C	RSM
CPU time : 1.78 E+06 s	CPU time : 2.11E+05 s
Max Memory :1.81E+04 MB	Max Memory : 1.25E+04 MB
Max Swap : 1.89E+04 MB	Max Swap :1.33E+04MB
Max Processes :17	Max Processes : 17
Max Threads : 26	Max Threads : 26

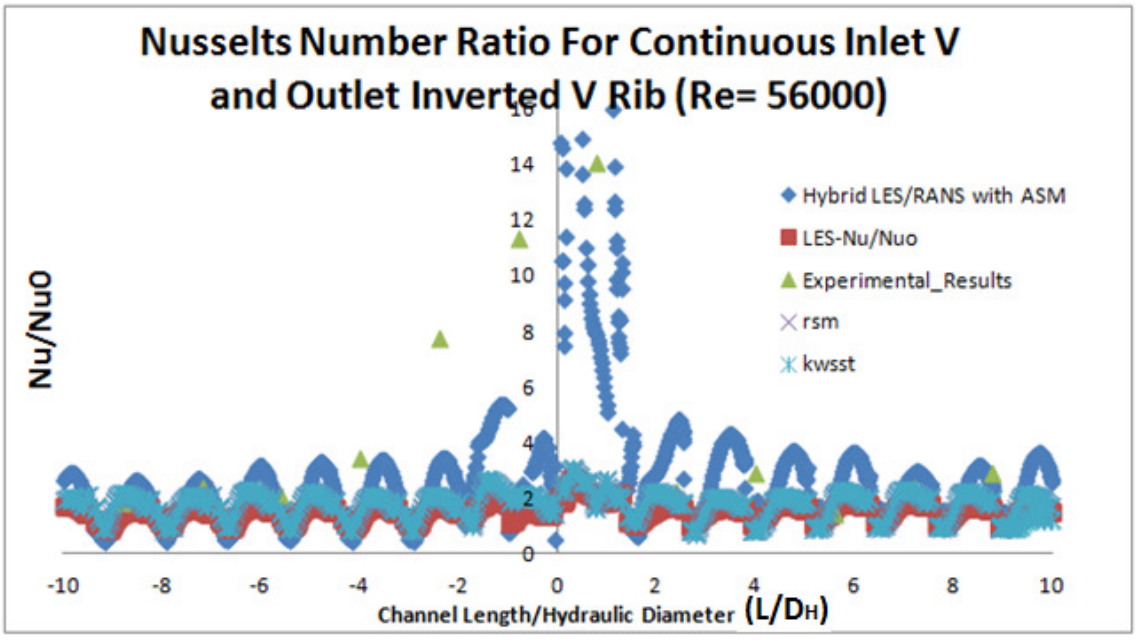

Figure 8.3 Inlet V and Outlet Inverted Continuous V Rib

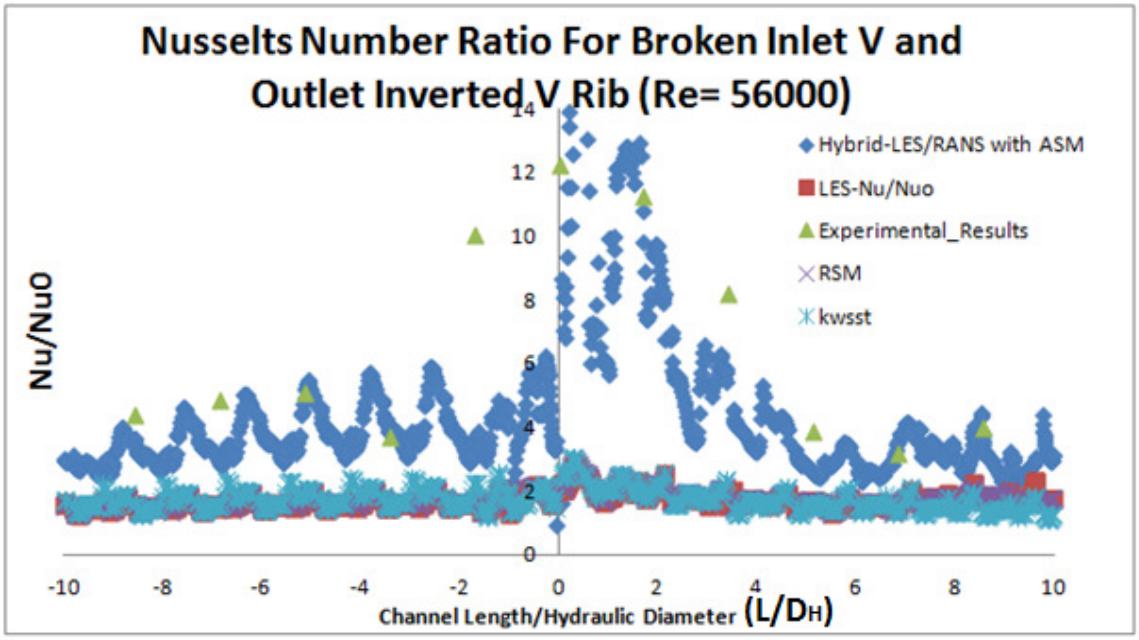

Figure 8.4 Inlet V and Outlet Inverted Broken V Rib

Reynolds Stress Comparision:

In Figs. 7.5 and 7.6 Reynold stress are compared for both RSM and Hybrid LES/RANS models with ASM .The values of Reynolds stresses vary slightly with less fluctuations. This clearly demonstrates that with less expensive ASM model, Reynolds stresses can be predicted more accurately. The main aim was to a technique which provides accurate heat transfer results. This shows that LES-ASM coupling can be done to accurate results with less expense.

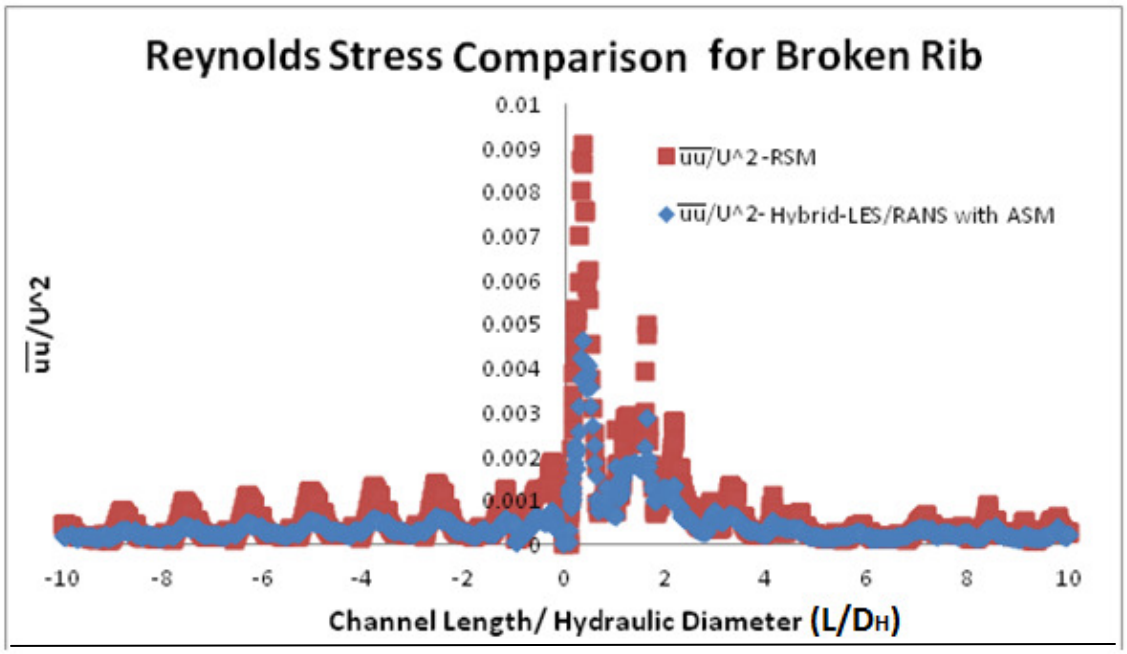

Figure 8.5(a)

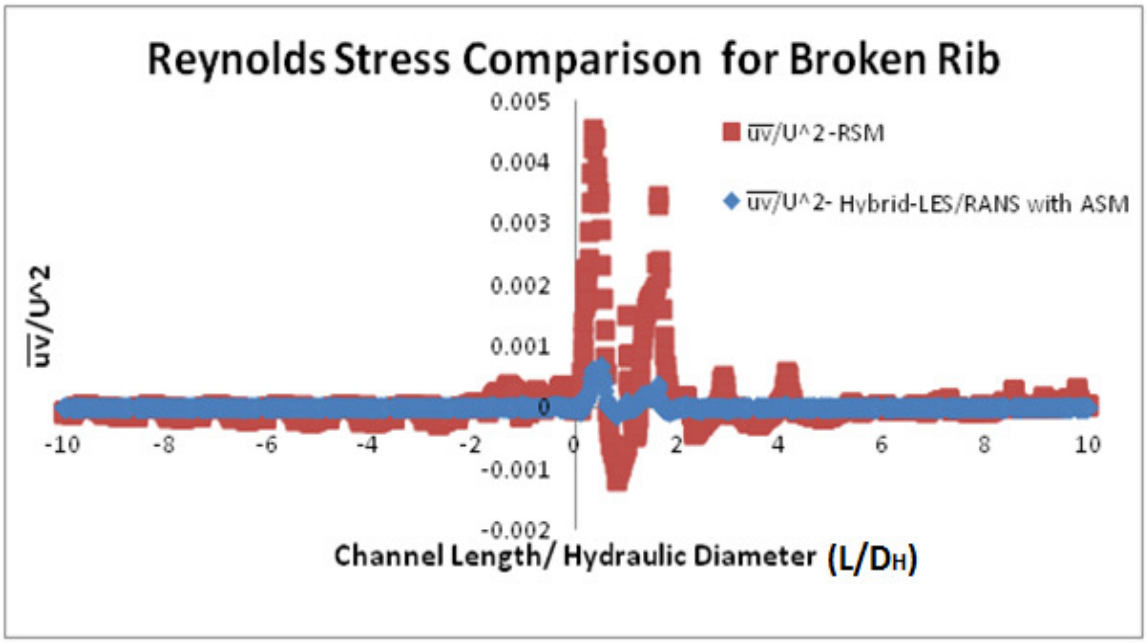

Figure 8.5(b)

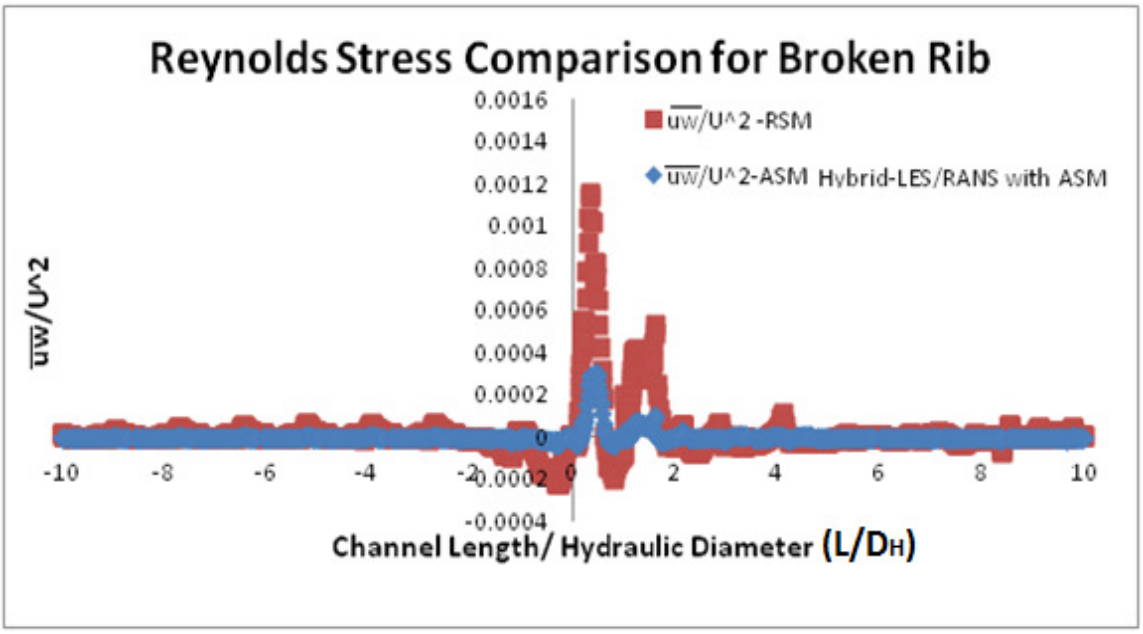

Figure 8.5(c)

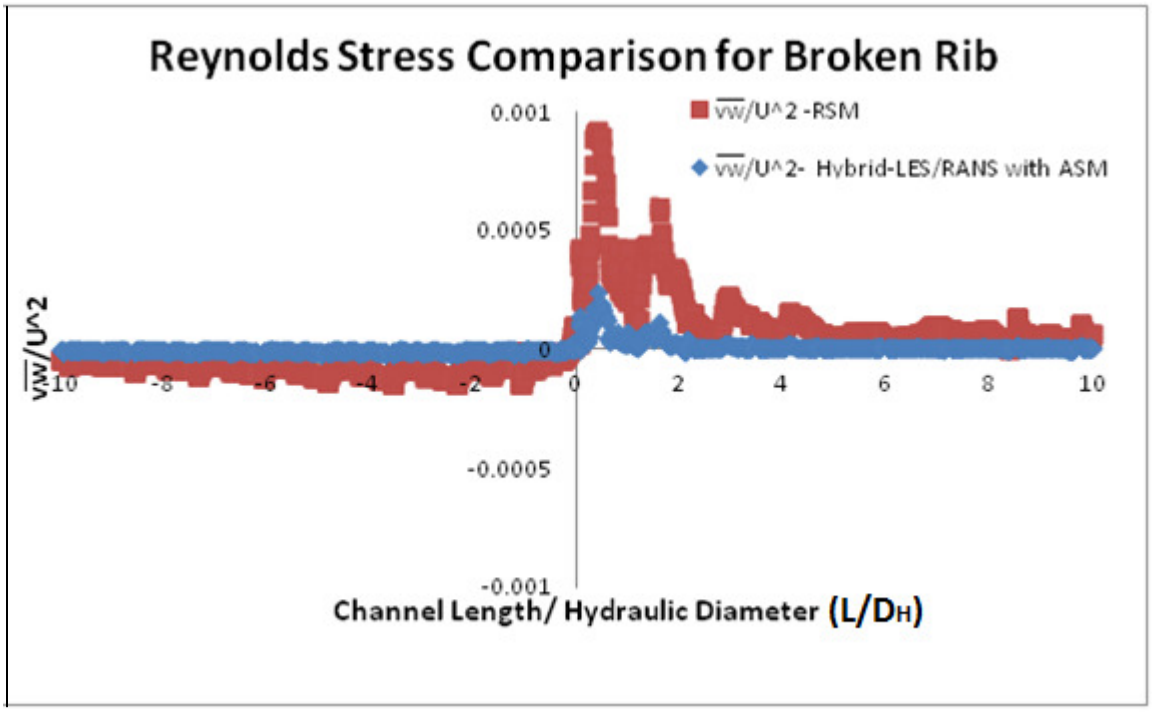

Figure 8.5(d)

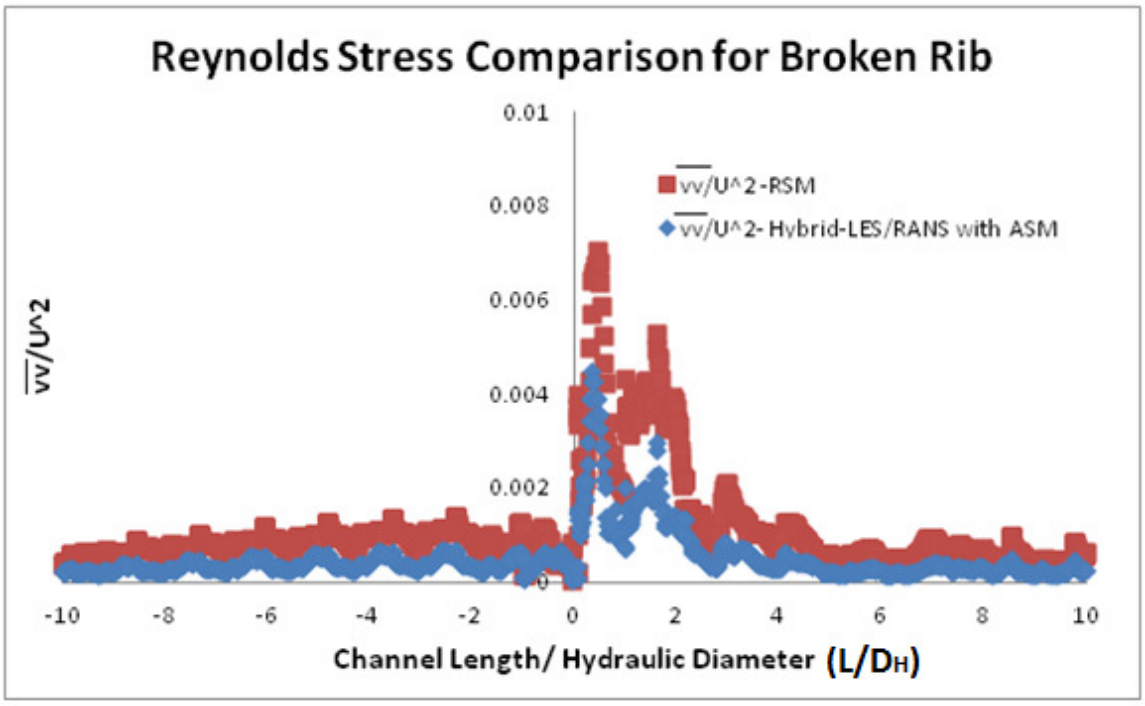

Figure 8.5(e)

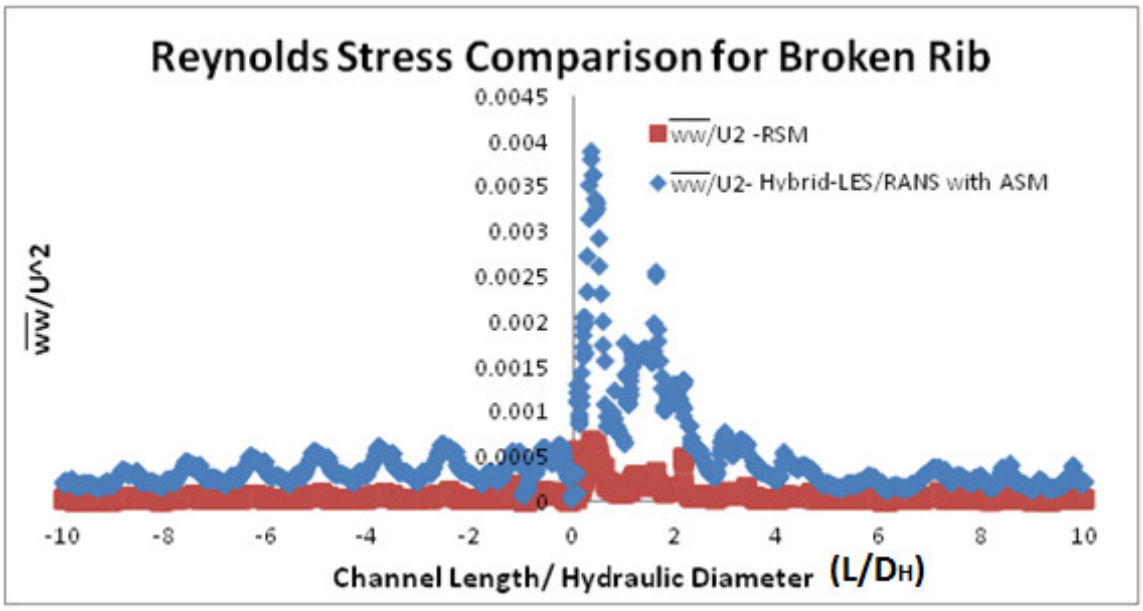

Figure 8.5(f)

Figure 8.5 Reynolds stress comparison of RSM with ASM Inlet V and Outlet Inverted Broken V Rib

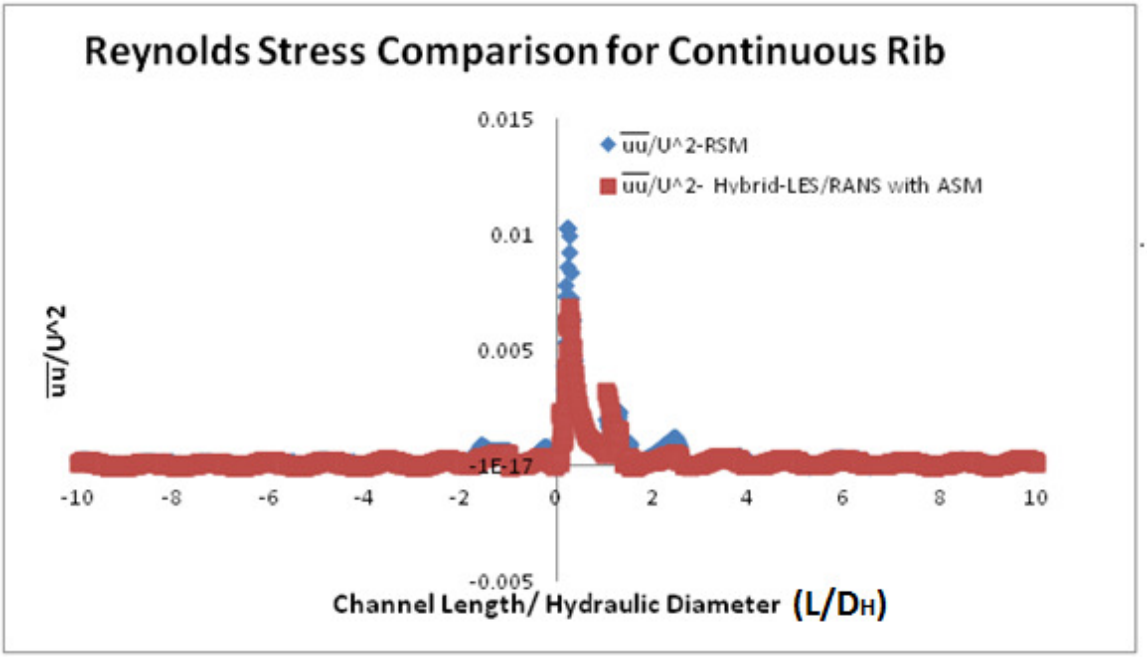

Figure 8.6(a)

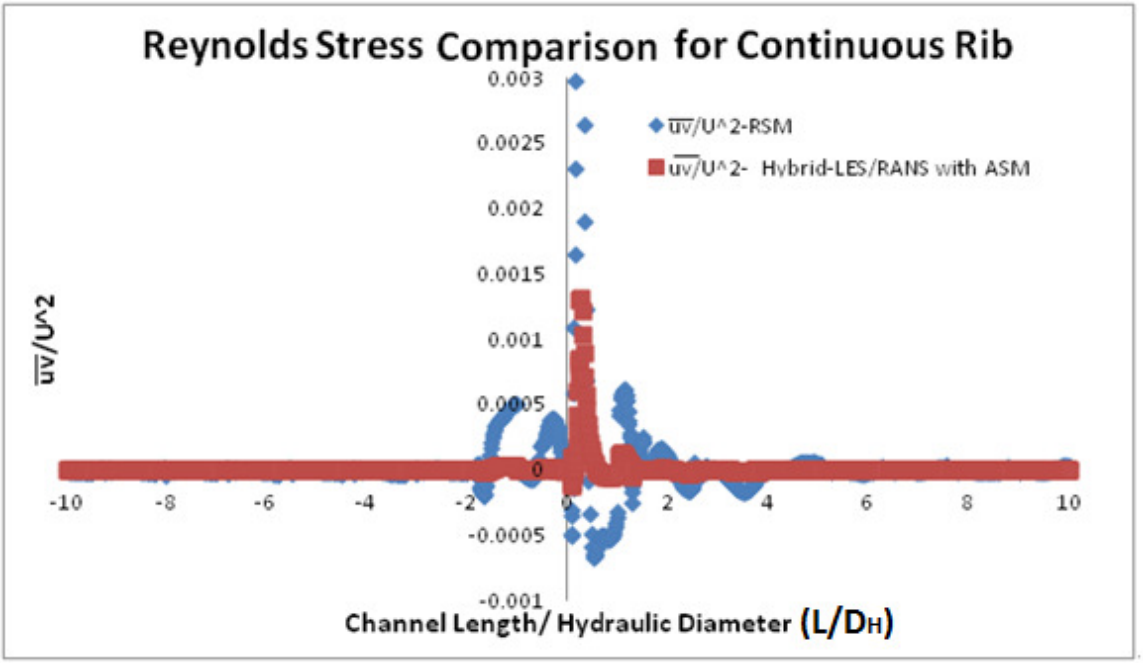

Figure 8.6(b)

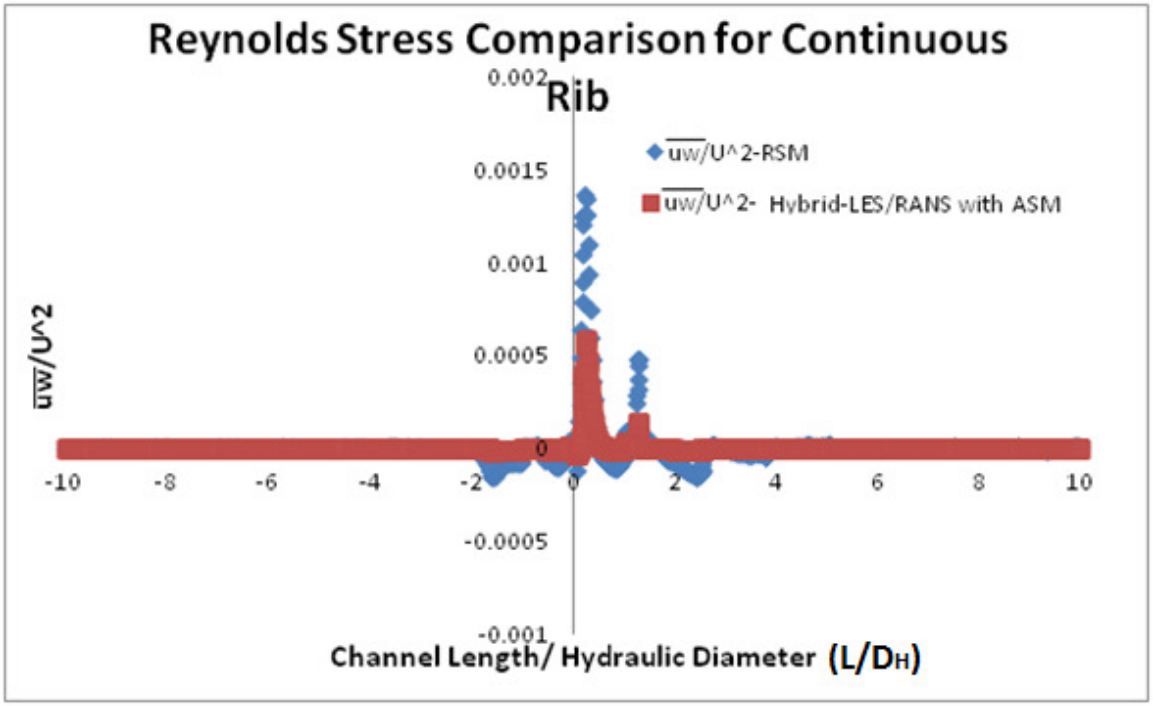

Figure 8.6(c)

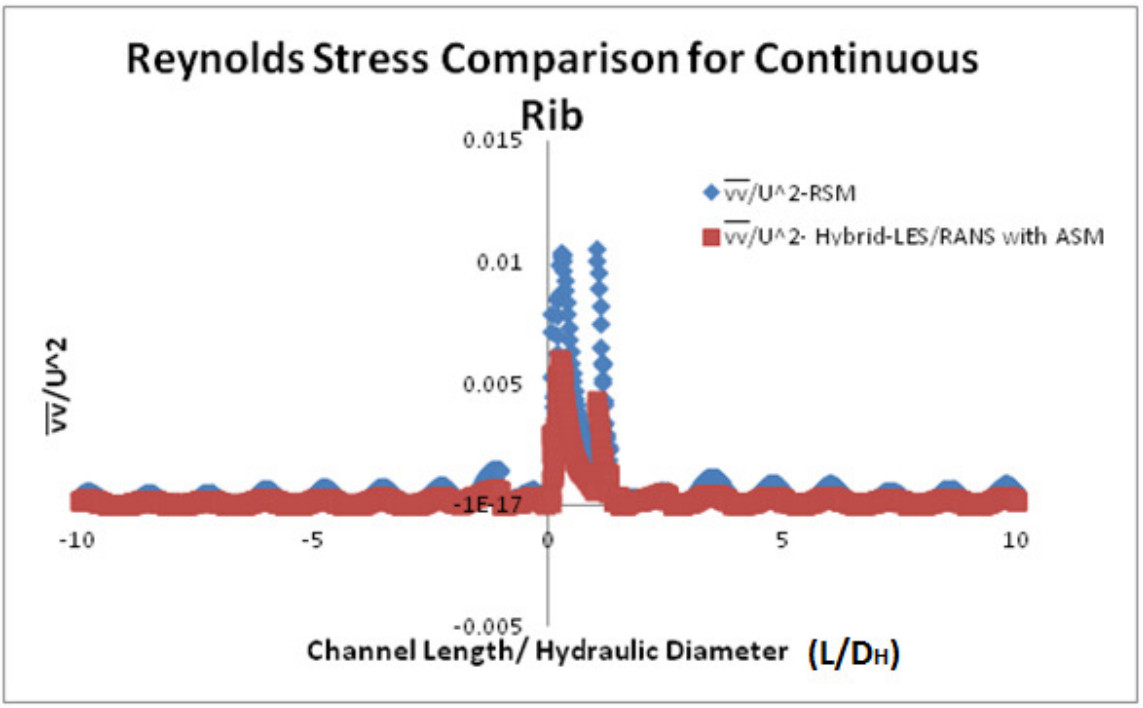

Figure 8.6(d)

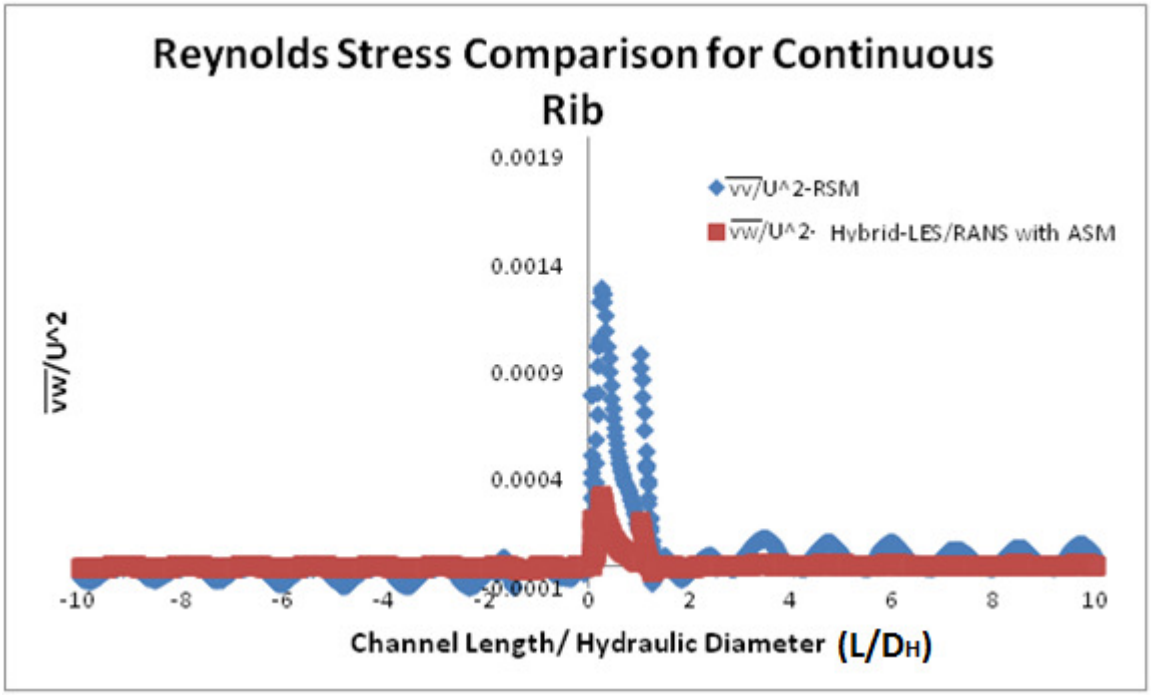

Figure 8.6(e)

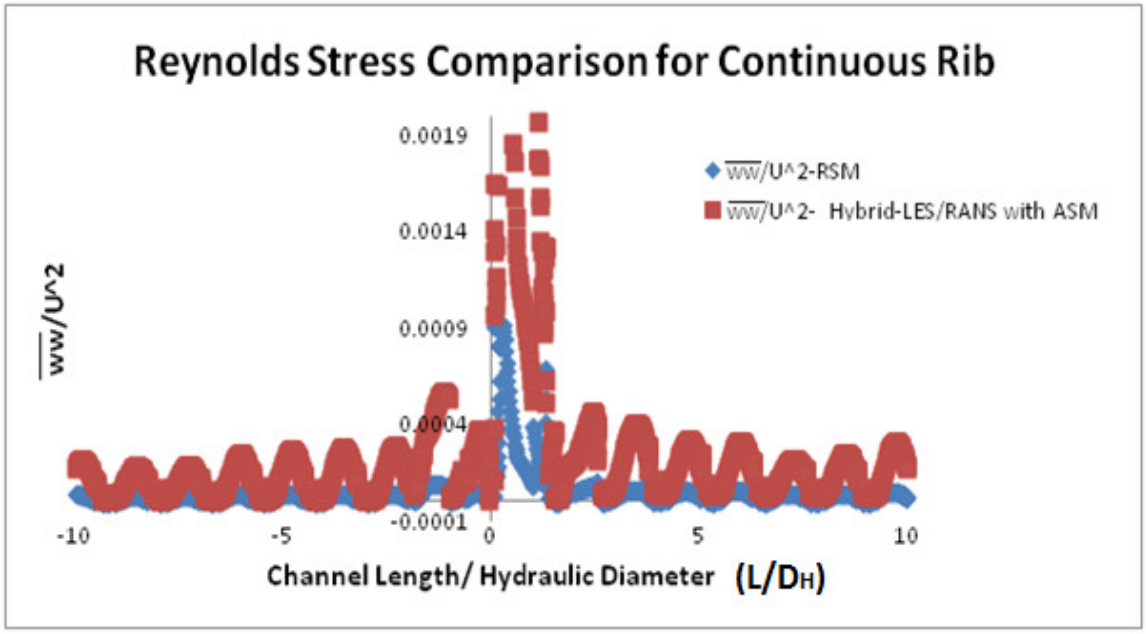

Figure 8.6(f)

Figure 8.6 Reynolds stress comparison of RSM with ASM Inlet V and Outlet Inverted Continuous V Rib

Hybrid LES/RANS modeling with ASM produces very accurate validation with experimental results because it takes the best predicted parameters from LES (velocity and velocity gradient) and RANS (Reynolds stresses) and uses ASM model to calculate the modified Reynolds stresses. These modified Reynolds stresses are used to calculate the kinetic energy at the first grid point. These modified kinetic energy, velocity and wall shear stress from the LES model produce accurate results. Kinetic energy is dependent on modified Reynolds stress from ASM. Figures 8.5(f) and 8.6(f) show $\overline{ww}$ Reynolds stress components for Inlet V and Outlet Inverted Broken V Rib and Inlet V and Outlet Inverted continuous V Rib respectively. The results clearly depict a predominance in $\overline{ww}$ for ASM which leads to higher Nusselt Number.

CHAPTER 9: CONCLUSIONS

This study provides a variety of heat transfer results in gas turbine blade two pass internal cooling channels. There are eight different rib configurations for 60^o V ribs which were extensively studied. In this study, a detailed analysis starting from experimental set up to advanced LES modeling was carried out.

9.1 Conclusions:

At the end of this research work, following observations and detailed conclusion were reached:

1. Experimental results:

a) In the experimental work, all the rib configurations namely, 1. Inverted V ribs 2. V ribs 3. Inlet V and outlet Inverted V and 4. Inlet Inverted V and outlet V for continuous 60^o and broken 60^o were studied. Comparing all the heat transfer results produced V-IV as the best profile for both broken as well as continuous ribs followed by V ribs and then IV. The worst performer in terms of heat transfer is IV-V.

b) Comparing the broken and continuous ribs, the heat transfer enhancement was 1.5 times higher in broken vs. continuous ribs. There was a spike in Nusselt Number ratio in the turn region because of turn effect.

c) As the Reynolds Number increases, the Nusselt Number ratio decreases for all the cases considered.

2. Numerical Simulations:

a) Numerical simulations for all the cases using k-ω SST and RSM turbulence models are carried out. It shows that with increase in Reynolds Number, Nusselt Number decreases.

b) Nusselt Number ratio and Surface Nusselt Number comparison shows highest values in case of V-IV for broken as well as continuous ribs. As Nusselt Number is heat transfer predictors, it shows that this configuration is the best.

c) The flow patterns can be visualized using both the turbulence models which provided guidance to understand that recirculation and reattachment takes place just after the ribs. Secondary flow are generated which enhances heat transfer.

d) Comparison with experimental results showed the same effect but there were some variation in the turn region. Overall both the models were able to predict the physics and the heat transfer in the ribs considered.

3. Large Eddy Simulations:

a) Large Eddy simulations of Broken and Continuous ribs were performed for V-IV rib as these were the best available ribs. A great amount of flow phenomenon was studied along the two pass channel.

b) These results showed that the ribs are inherently responsible for vortex generation. Towards inner wall, high heat transfer rate was observed because of vortex line stretching. In case of upstream V ribs, there is bifurcation of flow and hence a high turbulence is generated in the region.

c) Vortex core parameters such as Vorticity, Helicity, Q criterion are studied in detail and results were analyzed for vortex generation. Broken ribs show higher vorticity than continuous ribs.

4. Hybrid LES/RANS Modeling with ASM:

a) This method is devised to post process the results of heat transfer where results of LES and RANS models are used to produce a modified Reynolds stress using ASM.

b) This model produced better results which were validated with experimental results.

c) This idea reiterates that a new turbulence approach can be used where LES/ASM are used for simulation.

9.2 Recommendations:

The importance and objective of this study was to develop an experimental set up for testing stationary internal passage cooling channels with different configurations of 60 ^{o} continuous V and 60 ^{o} broken V. In addition to that, validation with two equation turbulence models was carried out. Also, Large Eddy Simulation which are very effective and high fidelity numerical simulation methods were performed in this work.

A new technique for Reynolds stress improvement using Hybrid LES/RANS Modeling with ASM was implemented.

Few recommendations for future research in this area:

1. Rotating Channel:

To accurately predict the flow phenomenon, a rotating test rigs should be made and tested. This will account for centrifugal force as well as buoyancy effect which are critical for rotating turbine blade.

2. Parameters Variation:

A more detailed analysis can be done with varying different parameters like rib height, aspect ratio and U bend.

3. Post Processing:

In terms of post processing for experimental work, full surface temperature measurement will be more useful. This should be attempted for numerical analysis as well.

4. Advanced Ribs to be tested:

With the above study it was demonstrated that if the V ribs are pointing upstream in the channel along the flow, then heat transfer is enhanced. Figures 9.1 and 9.2 are suggestions for rib turbulators arrangements to be used in future cooling channels.

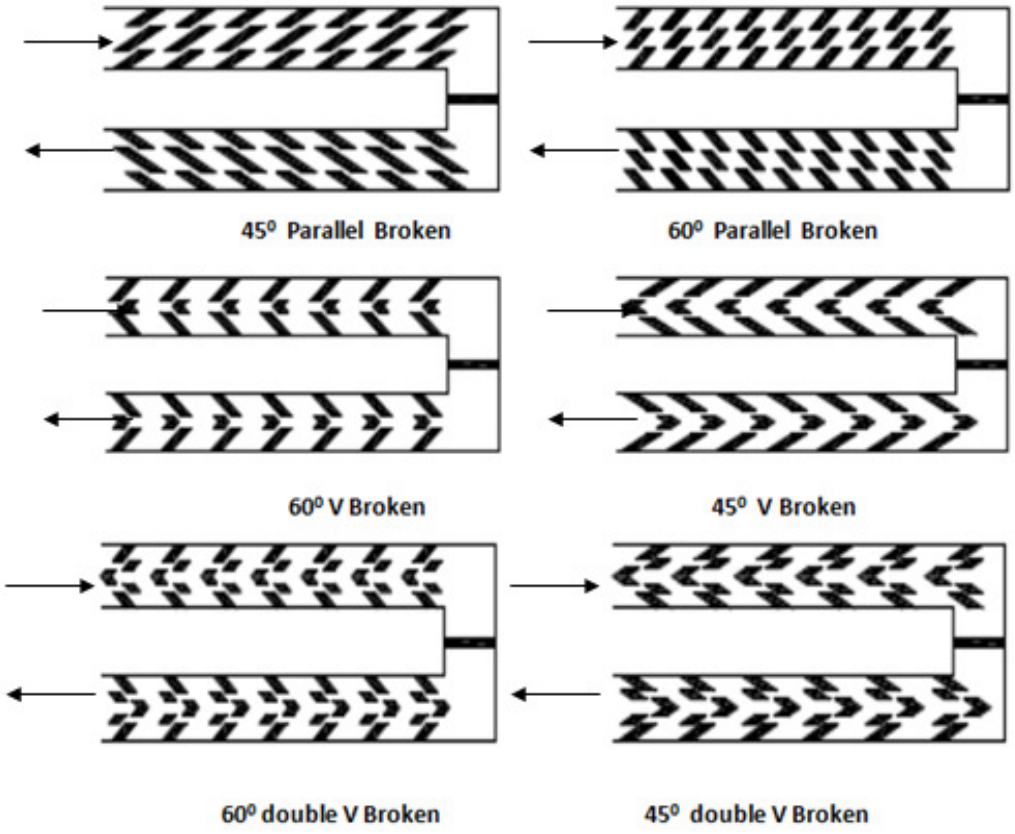

Figure 9.1: High performance Rib turbulator for Internal blade cooling

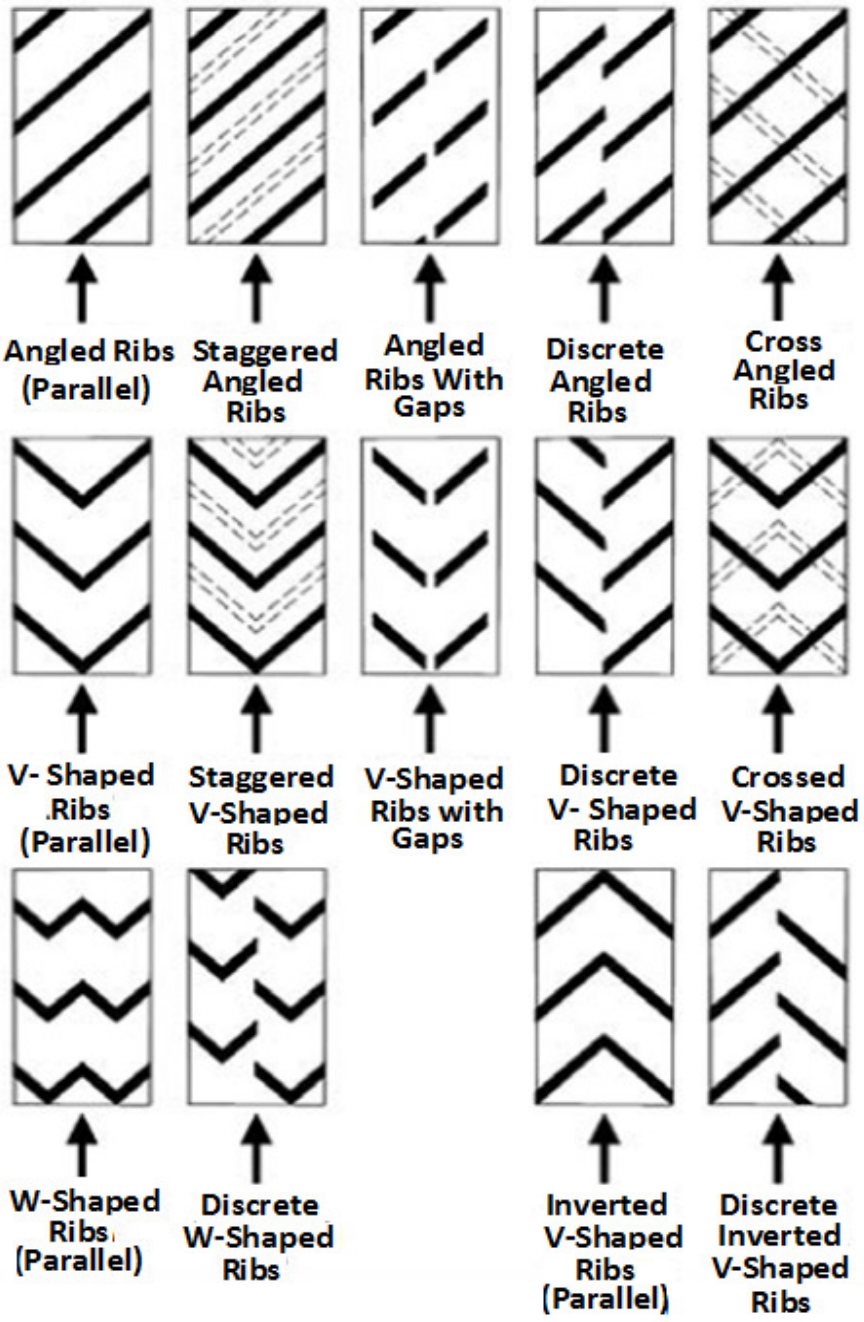

Figure 9.2: Advanced rib configuration in cooling channels

REFERENCES:

[1] Gas Turbine Handbook, NETL, 2006

[2] D.E. Metzger, L.W. Florschuetz, D.I. Takeuchi, R.D. Behee, and R.A. Berry, "Heat Transfer Characteristics for Inline and Staggered Arrays of Circular Jets with Cross flow of Spent Air" ASME Journal of Heat Transfer, 101 (1979): 526-531.

[3] L.W. Florschuetz, R.A. Berry, and D.E. Metzger, "Periodic Streamwise Variations of Heat Transfer Coefficients for Inline and Staggered Arrays of Circular Jets with Crossflow of Spent Air" ASME Journal of Heat Transfer 102 (1980): 132-137.

[4] R.N. Koopman and E.M. Sparrow, "Local and Average Transfer Coefficients Due to an Impinging Row of Jets" International Journal of Heat and Mass Transfer 92 (1976): 73-82.

[5] D.M. Kercher and W. Tabakoff, "Heat Transfer by a Square Array of Round Air Jets Impinging Perpendicular to a Flat Surface Including the Effect of Spent Air" ASME Journal of Engineering for Power, Vol. 92 (1970): 73-82.

[6] L.W. Florschuetz, C.R. Truman, and D.E. Metzger, "Streamwise Flow and Heat Transfer Distributions for Jet Array Impingement with Cross flow" ASME Journal of Heat Transfer 103 (1981): 337-342.

[7] R.E. Chupp, H.E. Helms, P.W. McFadden, and T.R. Brown, "Evaluation of Internal Heat Transfer Coefficients for Impingement Cooled Turbine Airfoils" AIAA Journal of Aircraft. 6 (1969): 203-208.

[8] R.S Bunker and D.E. Metzger, "Local Heat Transfer in Internally Cooled Turbine Airfoil Leading Edge Regions. Part I:Impingement Cooling Without Film Coolant Extraction" ASME Journal of Turbo machinery 112 (1990): 451-458.

[9] D.E. Metzger and R.S. Bunker, “Local Heat Transfer in Internally Cooled Turbine Airfoil Leading Edge Regions. Part II: Impingement Cooling with Film Coolant Extraction” ASME Journal of Turbo machinery. 112 (1990): 459-466.

[10] D.E. Metzger, R.A. Berry, and J.P. Bronson, “Developing Heat Transfer in Rectangular Ducts With Staggered Arrays of Short Pin Fins” ASME Journal of Heat Transfer 104 (1982): 700-706.

[11] M.K. Chyu, Y.C. Hsing, T.I.P. Shih, and V. Natarajan, “Heat Transfer Contributions of Pins and Endwall in Pin-Fin Arrays: Effects of Thermal Boundary Condition Modeling” ASME Paper No. 98-GT-175 (1998).

[12] Vanfossen, G.J., 1982, “Heat-Transfer Coefficients for Staggered Arrays of Short Pin Fins” ASME Journal of Engineering for Power, Vol. 104, pp. 268-274.

[13] D.E. Metzger, W.B. Shephard, and S.W. Haley, “Row Resolved Heat Transfer Variations in Pin-Fin Arrays Including Effects of Non-Uniform Arrays and Flow Convergence” ASME Paper No. 86-GT-132 (1986).

[14] T.K. Kumaran, J.C. Han, and S.C. Lau, “Augmented Heat Transfer in a Pin Fin Channel with Short or Long Ejection Holes” International Journal of Heat Mass Transfer, 34 no. 10 (1991): 2617-2628.

[15] M.K. Chyu, Y. Yu, H. Ding, J.P. Downs, and O. Soechting, “Concavity Enhanced Heat Transfer in an Internal Cooling Passage” ASME Paper No. 97-GT-437 (1997).

[16] H.K. Moon, T. O’Connell, and B. Glezer, “Channel Height Effect on Heat Transfer and Friction in a Dimpled Passage” ASME Paper No. 99-GT-163 (1999).

[17] G.I. Mahmood, M.L. Hill, D.L. Nelson, P.M. Ligrani, H.K. Moon, and B. Glezer,, "Local Heat Transfer and Flow Structure on and above a Dimpled Surface in a Channel" ASME Journal of Turbo machinery 123 (2001): 115-123.

[18]S.W. Moon, and S.C. Lau, "Turbulent Heat Transfer Measurements on a Wall with Concave and Cylindrical Dimples in a Square Channel" ASME Paper No.GT-2002-30208 (2002).

[19] R.S. Bunker and K.F. Donnellan, "Heat Transfer and Friction Factors for Flows Inside Circular Tubes with Concavity Surfaces" ASME Paper No. GT-2003-38053 (2003).

[20] Webb, R.L, Eckert, E.R.G., and Goldstein, R.J., "Heat Transfer and Friction in tubes with repeated-rib roughness" Int. Journal of heat and mass transfer, Vol. 14, pp. 601-617, 1971.

[21] Burggraf, F., "Experimental Heat Transfer and pressure drop with two dimensional turbulence promoter applied to two opposite walls of square tube in Augmentation of convective heat and mass transfer", Eds. Bergles and Webb, ASME pp 70-79,1979.

[22]Han, J.C., Glicksman, L.R., and Rohsenow, W.M.,"An investigation of heat transfer and friction for rib roughened surface.", Int. Journal of heat and mass transfer, Vol.21, pp 1143-1156,1978.

[23]. J.C. Han, L.R. Glicksman, and W.M. Rohsenow, "An Investigation of Heat Transfer and Friction for Rib-Roughened Surfaces", International Journal of Heat and Mass Transfer 21 (1978): 1143-1156.

[24] J.C. Han, J.S. Park, and C.K. Lei, “Heat Transfer Enhancement in Channels with Turbulence Promoters” , ASME Journal of Engineering for Gas Turbines and Power 107 (1985): 628-635.

[25] J.C. Han, “Heat Transfer and Friction Characteristics in Rectangular Channels with Rib Turbulators”, ASME Journal of Heat Transfer 110 (1988): 321-328.

[26] J.C. Han and J.S. Park, “Developing Heat Transfer in Rectangular Channels with Rib Turbulators” , International Journal of Heat and Mass Transfer 31(1988): 183-195.

[27] J.C. Han, "Recent studies in turbine blade cooling", International journal of rotating machinery 10 (2004): 443-457.

[28] J.C. Han, Y.M. Zhang, and C.P. Lee, “Augmented Heat Transfer in Square Channels with Parallel, Crossed, and V-shaped Angled Ribs” , Journal of Heat Transfer, Transactions ASME 113 (1991): 590-596.

[29] J.C. Han and Y.M. Zhang, “High Performance Heat Transfer Ducts with Parallel and V-Shaped Broken Ribs”, International Journal of Heat and Mass Transfer 35 (1992): 513-523.

[30] S.V. Ekkad and J.C. Han, “Detailed Heat Transfer Distributions in Two-Pass Square Channels with Rib Turbulators”, International Journal of Heat and Mass Transfer 40 (1997): 2525-2537.

[31]S.V. Ekkad,Y. Yuang, and J.C. Han, “Detailed Heat Transfer Distributions in Two-Pass Smooth and Turbulated Square Channels with Bleed Holes”, International Journal of Heat and Mass Transfer 41 (1998): 3781-3791.

[32] J.C. Han, J.J. Huang, and C.P. Lee, “Augmented Heat Transfer in Square Channels with Wedge-Shaped and Delta-Shaped Turbulence Promoters”, Journal of Enhanced

Heat Transfer 1 no.1 (1993): 37-52.

[33] R.S Bunker and S.J. Osgood, “The Effect of Turbulator Lean on Heat Transfer and Friction in a Square Channel”, ASME Paper No. GT-2003-38137 (2003).

[34] M.E. Taslim and S.D. Spring, “Effects of Turbulator Profile and Spacing on Heat Transfer and Friction in a Channel”, AIAA Journal of Thermophysics and Heat Transfer 8 no. 3 (1994): 555-562.

[35] J.C. Bailey and R.S. Bunker, “Heat Transfer and Friction in Channels with Very High Blockage 45° Staggered Turbulators”, ASME Paper No. GT-2003-38611(2003).

[36]M.E. Taslim and S.D. Spring, “Experimental Heat Transfer and Friction Factors in Turbulated Cooling Passages of Different Aspect Ratios where Turbulators are Staggered”, AIAA Paper No. 88-3014, 24th Joint Propulsion Conference (1988).

[37] J.R. Shen, Z. Wang, P.T. Ireland, T.V. Jones, and A.R. Byerley, “Heat Transfer Enhancement Within a Turbine Blade Cooling Passage Using Ribs and Combinations of Ribs With Film Cooling Holes”, ASME Journal of Turbomachinery 188 (1996): 428-433.

[38] D. Thurman and P. Poinsette, “Experimental Heat Transfer and Bulk Air Temperature Measurements for a Multipass Internal Cooling Model with Ribs and Bleed”, ASME Paper No. 2000-GT-233 (2000).

[39] J.H. Wagner, B.V. Johnson, and F.C. Kopper, “Heat Transfer in Rotating Serpentine Passages With Smooth Walls”, ASME Journal of Turbo machinery 113 (1991): 321-330.

[40] S. Dutta and J.C. Han, “Rotational Effects on the Turbine Blade Coolant Passage Heat Transfer”, Annual Review of Heat Transfer 9 (1997): 269-314.

[41] J.C. Han, Y.M. Zhang, and K. Kalkuehler, “Uneven Wall Temperature Effect on Local Heat Transfer in a Rotating Two-Pass Square Channel with Smooth Walls”, ASME Journal of Heat Transfer 114 (1993): 850-858.

[42] J.A. Parsons, J.C. Han, and Y.M. Zhang, “Wall Heating Effect on Local Heat Transfer in a Rotating Two-Pass Square Channel with 90-Degree Rib Turbulators”, International Journal of Heat and Mass Transfer 37 no. 9 (1994): 1411-1420.

[43]Y.M. Zhang, J.C. Han, J.A. Parsons, and C.P. Lee, “Surface Heating Effect on Local Heat Transfer in a Rotating Two-Pass Square Channel with 60-Degree Angled Rib Turbulators” ASME Journal of Turbo machinery 117 (1995): 272-278.

[44] S. Acharya, V. Eliades, and D.E. Nikitopoulos, “Heat Transfer Enhancements in Rotating Two-Pass Coolant Channels with Profiled Ribs: Part 1 – Average Results”, ASME Paper No. 2000-GT-0227 (2000).

[45] J.H. Wagner, B.V. Johnson, R.A. Graziani, and F.C. Yeh, “Heat Transfer in Rotating Serpentine Passages With Trips Normal to the Flow”, ASME Journal of Turbomachinery 114 (1992): 847-857.

[46] Jayatilleke, C.L., "The influence of Prandtl Number and Surface Roughness on the Resistance of Laminar Sub-Layer to momentum and Heat Transfer", Progress in Heat and Mass Transfer , Vol. 1, 1969,pp. 193-329.

[47] Kajishima, T., Miyake, Y., 1992, “A Discussion on Eddy Viscosity Models on the Basis of the Large Eddy Simulation of Turbulent Flow in a Square Duct,” Computers Fluids, 21, pp. 151-161.

[48] Choi, D., Prasad, D., Wang, M., Pierce, C., 2000, “Evaulation of an Industrial CFD Code for LES Applications,” Center for Turbulence Research, Proceedings of the Summer Program, pp. 221-228.

[49] Hébrard, J., Métais, O., Slinas-Vasquez, M., 2004, “Large-Eddy Simulation of Turbulent Duct Flow: Heating and Curvature Effects, "International Journal of Heat and Fluid Flow, 25, pp. 569-580.

[50] Pallares, J., Davidson, L., 2000, “Large-Eddy Simulations of Turbulent Flow in a Rotating Square Duct,” Physics of Fluids, 12, pp. 2878-2898.

[51] Pallares, J., Davidson, L., 2002, “Large-Eddy Simulations of Turbulent Heat Transfer in Stationary and Rotating Square Ducts,” Physics of Fluids, 14, pp. 2804-2816.

[52] Yang, K.-S., Ferziger, J.H., 1993, “Large-Eddy Simulation of Turbulent Obstacle Flow Using a Dynamic Subgrid-Scale Model,” AIAA Journal, 31, pp. 1406-1413.

[53] Murata, A., Mochizuki, S., 2000, “Large Eddy Simulation with a Dynamic Subgrid-Scale Model of Turbulent Heat Transfer in an Orthogonally Rotating Rectangular Duct with Transverse Rib Turbulators,” International Journal of Heat and Mass Transfer, 43, pp. 1243-1259.

[54] Murata, A., Mochizuki, S., 2001, “Comparison between Laminar and Turbulent Heat Transfer in a Stationary Square Duct with Transverse or Angled Rib Turbulators,” International Journal of Heat and Mass Transfer, 44, pp. 1127-1141.

[55] Murata, A., Mochizuki, S., 2004, “Large Eddy Simulation of Turbulent Heat Transfer in a Rotating Two-Pass Smooth Square Channel with Sharp 180-deg. Turns,” International Journal of Heat and Mass Transfer, 47, pp. 683-698.

[56] Murata, A., Mochizuki, S., 2004, "Centrifugal Buoyancy Effects on Turbulent Heat Transfer in a Rotating Two-Pass Smooth Square Channel with Sharp 180-deg. Turns," International Journal of Heat and Mass Transfer, 47, pp. 3215-3231.

[57] Murata, A., Mochizuki, S., 2004, "Effect of Rib Orientation and Channel Rotation on Turbulent Heat Transfer in a Two-Pass Square Channel with Sharp 180º Turns Investigated by Using Large Eddy Simulation," International Journal of Heat and Mass Transfer, 47, pp. 2599-2618.

[58]Jordan, S.A., 2003, "The Turbulent Character and Pressure Loss Produced by Periodic Symmetric Ribs in a Circular Duct," International Journal of Heat and Fluid Flow, 24, pp. 795-806.

[59]Xu, H., Pollard, A., 2001, "Large Eddy Simulation of Turbulent Flow in a Square Annular Duct," Physics of Fluids, 13, pp. 3321-3337.

[60] Feiz, A.A., Ould-Rouis, M., Lauriat, G., Large Eddy Simulation of Turbulent Flow in a Rotating Pipe," International Journal of Heat and Fluid Flow, 24, pp. 412-420.

[61] Sugawara, K., Yoshikawa, H., Ota, T., 2004, "LES of Turbulent Separated Flow and Heat Transfer in a Symmetric Expansion Plane Channel," Proceedings of the ASME Heat Transfer/Fluids Engineering Summer Conference, Charlotte, North Carolina, Paper no. HT-FED04-56139.

[62] Braun, H., Neumann, H., Mitra, N.K., 1999, "Experimental and Numerical Investigation of Turbulent Heat Transfer in a Channel with Periodically Arranged Rib Roughness Elements," Experimental Thermal and Fluid Science, 19, pp. 67-76.

[63] Saha, A.K., Acharya, S., 2003, "Flow and Heat Transfer in an Internally Ribbed Duct with Rotation: An Assessment of LES and URANS," Proceedings of the ASME Turbo Expo 2003, Atlanta, Georgia.

[64] Tyagi, M., Acharya, S., 2004, "Large Eddy Simulations of Flow and Heat Transfer in Rotating Ribbed Duct Flows," Proceedings of the ASME Turbo Expo 2004, Vienna, Austria.

[65] Ahn, J., Choi, Haecheon, C., Lee, J.S., 2004,"Large Eddy Simulation of Flow and Heat Transfer in a Channel Roughened by Square or Semicircle Ribs," Proceedings of the ASME Turbo Expo 2004, Vienna, Austria.

[66] Tafti, D.K., 2005, "Evaluating the Role of Subgrid Stress Modeling in a Ribbed Duct for the Internal Cooling of Turbine Blades," International Journal of Heat and Fluid Flow, 26, pp. 92-104.

[67] Abdel-Wahab, S., Tafti, D.K., 2004, "Large Eddy Simulation of Flow and Heat Transfer in a 90º Ribbed Duct with Rotation - Effect of Coriolis Forces," Proceedings of the ASME Turbo Expo 2004, Vienna, Austria, ASME Paper No. GT2004-53796.

[68] Takahashi, T., Watanabe, K., 2004, "Large Eddy Simulation of Flow and Heat Transfer in a Rectangular Channel with Crossed Angled Ribs," Proceedings of the ASME Turbo Expo 2004, Vienna, Austria.

[69] Moffat, R.J., 1982, "Contribution to theory of single sample uncertainty analysis," Comparison of Computation and Experiment, 250/Vol.104.

[70] https://www.sharcnet.ca/Software/Fluent12/index.htm

[71] http://www.cfd-online.com/Wiki/Large_eddy_simulation_ (LES)

[72]https://www.sharcnet.ca/Software/Fluent13/help/flu_th/flu_th_sec_les_sgs_models

[73] Davidson, P.A., "Turbulence An introduction for scientists and engineers"

[74] http://en.wikipedia.org/wiki/Large_eddy_simulation

[75] Versteeg, H.K., Malalasekera, W "An introduction to computational fluid dynamics"

[76] Meroney, R.N., "An Algebraic stress model for stratified turbulent shear flows" Computers and Fluids, 1976,vol 4, 93-107.

[77] Amano. R.S., "Numerical Study of liquid cooling gas turbine blade" 82-GT-116.

[78] Jayatilleke, C.L., "The influence of Prandtl Number and Surface Roughness on the resistance of the Laminar Sub-layer to momentum and Heat transfer," Progress in heat and mass transfer, Vol. 1, 1969, pp. 193-329.

APPENDIX A

This section discusses different equipments used in experimental setup. Figure A.1 is solid model for the test section along with the entry length. Solid modeling was done before the making the actual set up. Figs. A.2 (a) and A.2 (b) show the continuous and broken V rib wrapped in copper foil used for testing.

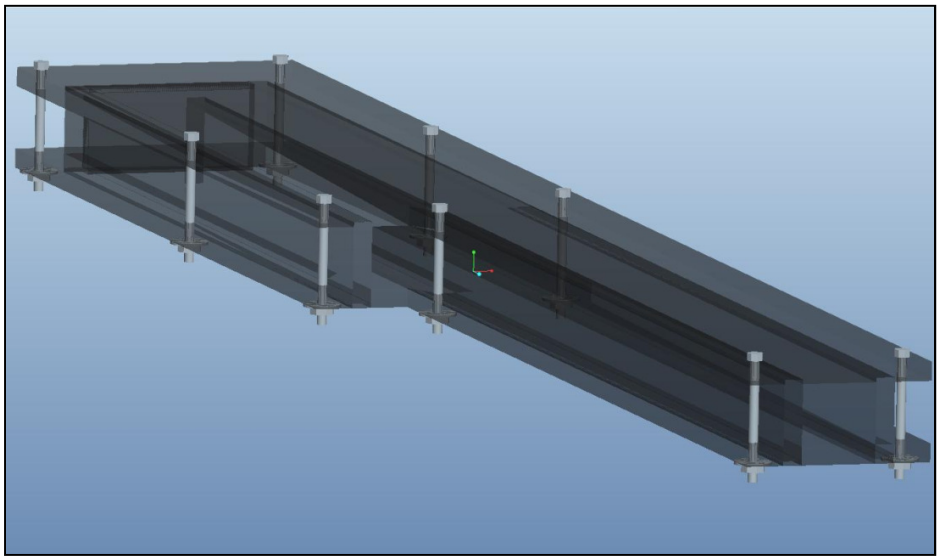

Figure A.1: Gas Turbine Channel with Standard Smooth Base Plate Bolted

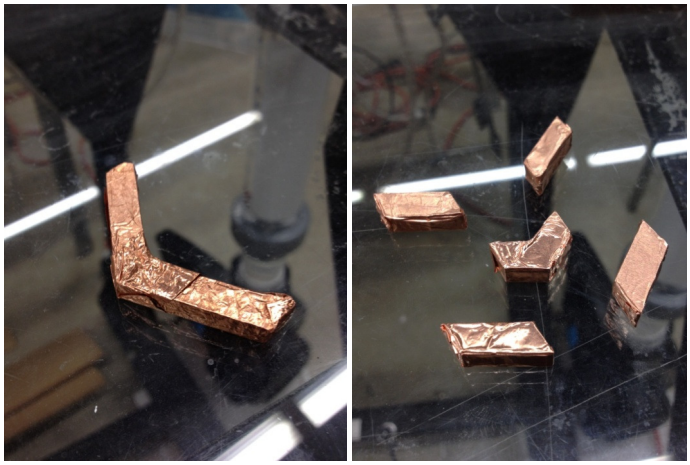

Figure A.2: Ribs used for testing a) Continuous b) Broken

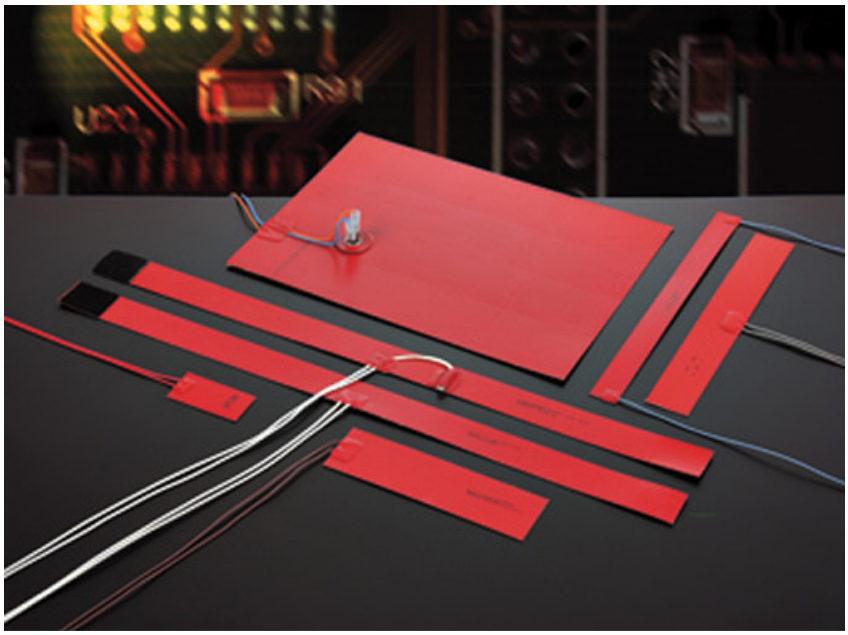

Figure A.3: Heating elements used for the channel heating

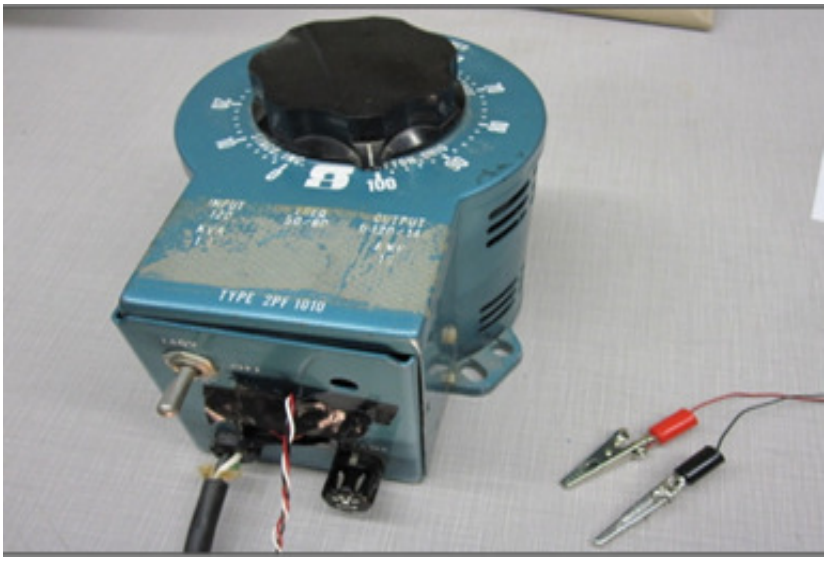

Figure A.4: The AC variac used as a power source for the heating element.

Figure A.3 shows different shapes of heating element. Heating element was selected based on the test section dimensions. Figure A.4 show variac used for power supply to the heating element.

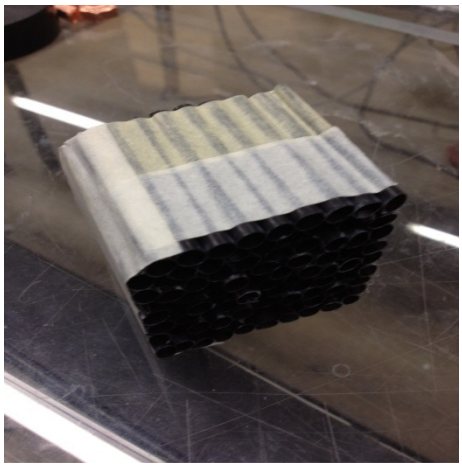

A.5 (a)

A.5 (b)

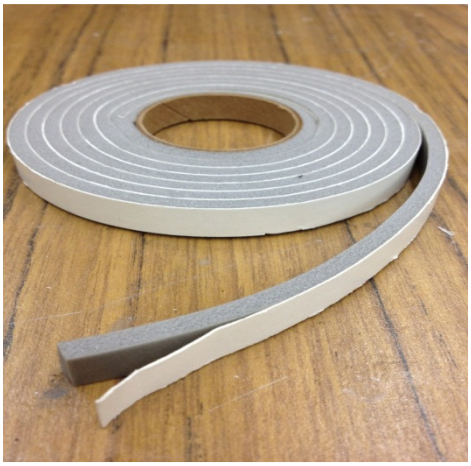

A.5 (c)

Figure A.5: a) Honeycomb b) Insulation c) Weather strip

Figure A.5 (a) shows honeycomb used for making the flow uniform during testing. Figure A.5 (b) is the insulation used to insulate the heat loss during the experiments. Figure A.5 (c) is the weather strip used for sealing the test setup. Figure A.6 is the details of flexible silicone rubber heat sheets and strip used as heating elements. Fig A.7 is the copper foil used for testing.

Figure A.6: Heating elements used for the channel

Figure A.7: Copper sheet used for testing.

Figure A.8 shows 8 channel USB data acquisition module selected for temperature measurement and Fig. A.9 is the Inline sensor used for measuring velocity. Figure A.10 is the differential pressure transmitter to monitor pressure and velocity.

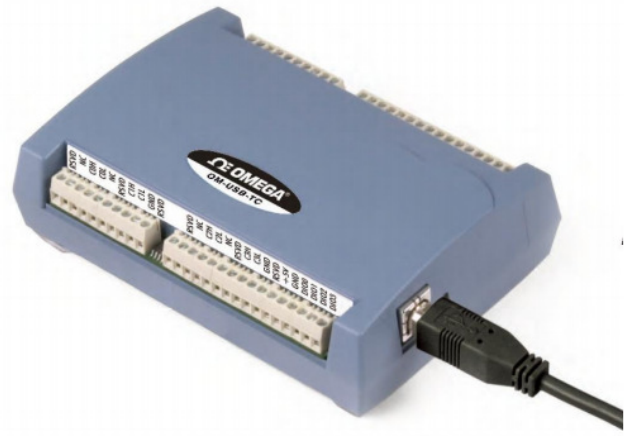

OM-USB-TC
8 Channel Thermocouple Input
USB Data Acquisition Module

Figure A.8: USB Data Acquisition Module

In-Line Flow Sensors

Use with the Dwyer® Differential Pressure Gages or Transmitters

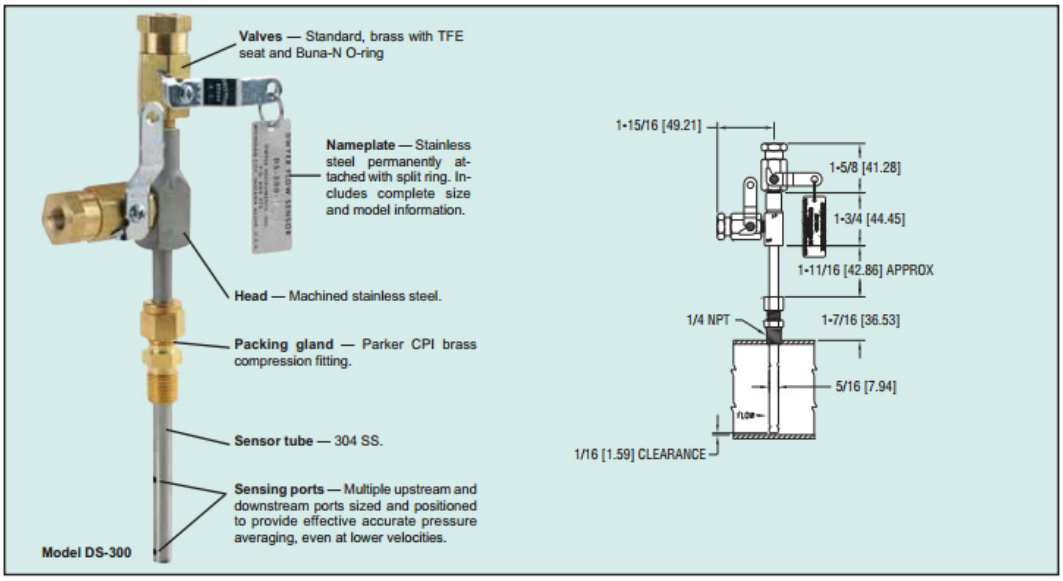

Figure A.9: Inline flow sensor used for measuring velocity and pressure

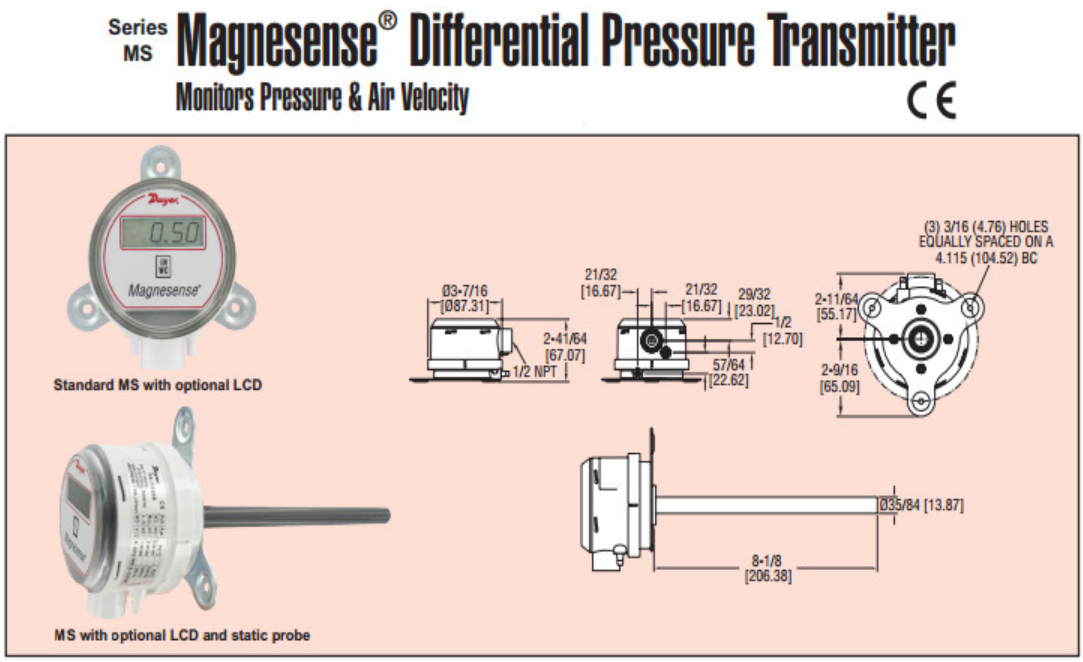

Figure A.10: Differential pressure transmitter to monitor pressure and velocity

Figure A.11 shows the details of software snapshot to calculate pressure drop for the ducting used in experiment. Fig. A.12 shows the fan selected for experiment to produce high velocity with the measured pressure drop. Fig. A.13 shows inlet duct design used for experiments to join the blower and test section. Fig. A.14 is the pressure curve for blower selected for experiment and Fig. A.15 shows slide gate (damper) used on blower.

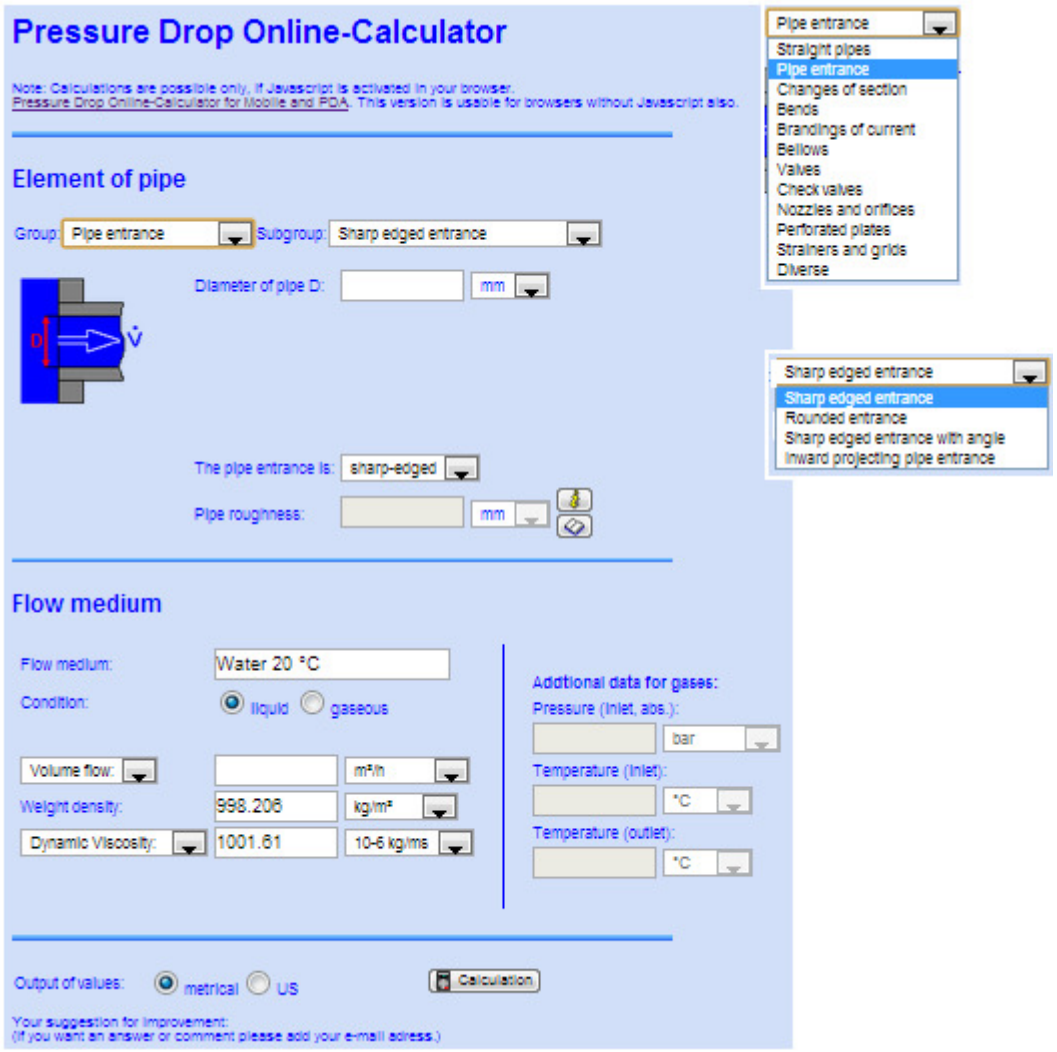

Figure A.11: Pressure Drop Calculation for the ducting used for experiments

Operating Requirements

Volume, ACFM	170
Static Pressure, in. wg	7.0
Density, lb./ft.³	0.075
Operating Temperature, °F	70
AMCA Arrangement No.	4
Motor Frequency, Hz	60
Start-Up Temperature, °F	70

Fan Selection and Specifications

Model	PB-10A		
Fan RPM	3,450		
Wheel Description	Cast Alum. 11 X 3 BC		
Wheel Width, %	100%		
Wheel Diameter, in.	11.00		
Inlet Diameter, in.	6.00		
Outlet Velocity, ft./min.	1,303		
Fan BHP	0.50	Suggested Motor HP:	0.75
Static Efficiency, %	42.5%		
Cold Start BHP	0.50		
Construction Class	N/A		

Figure A.12: Fan selected for experiments

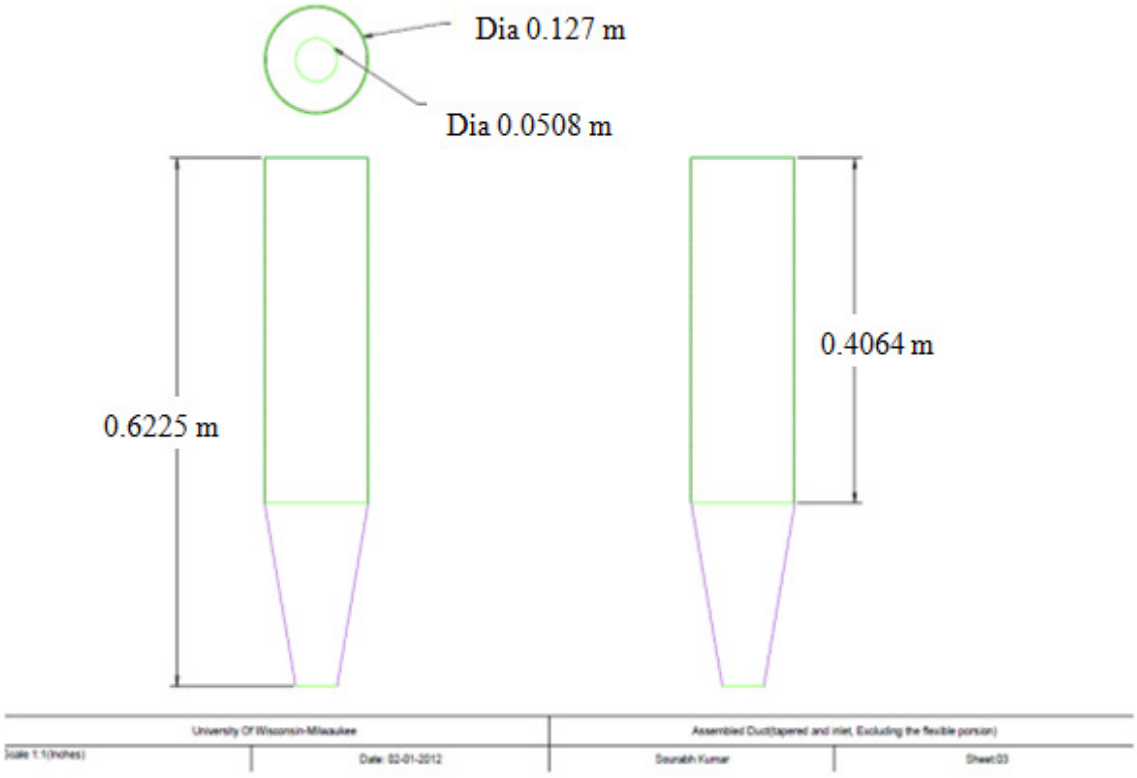

Figure A.13: Inlet Duct Design used for experiments

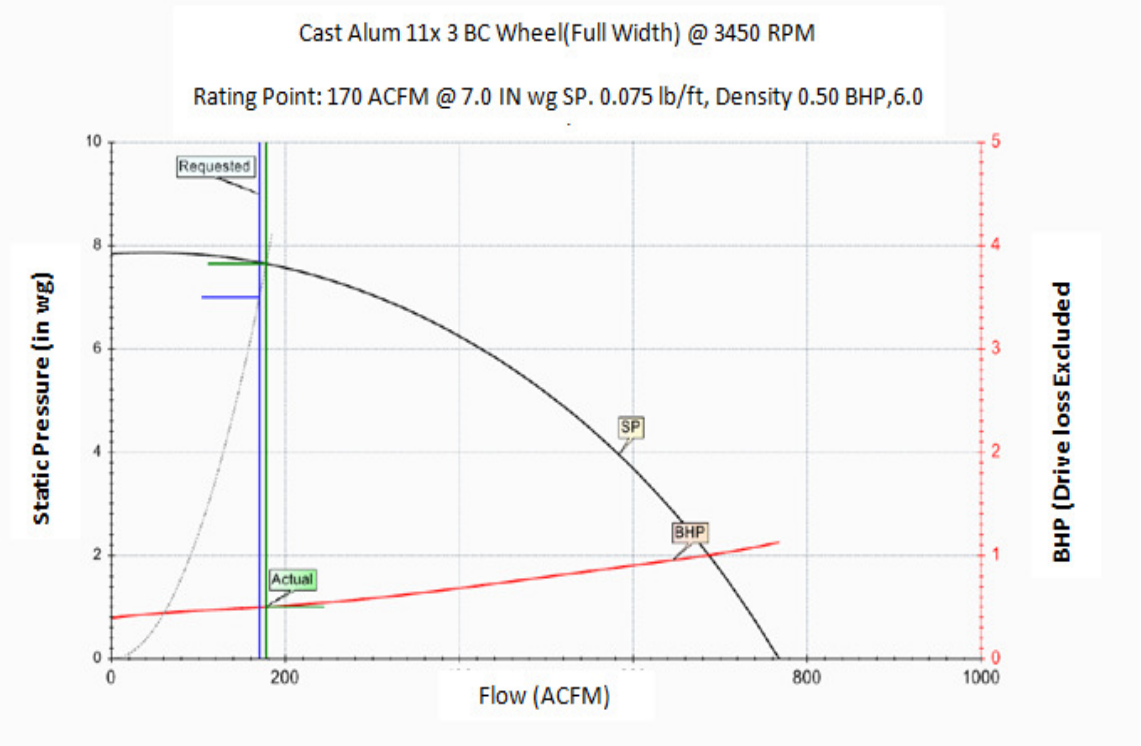

Figure A.14: Fan selected for experiments

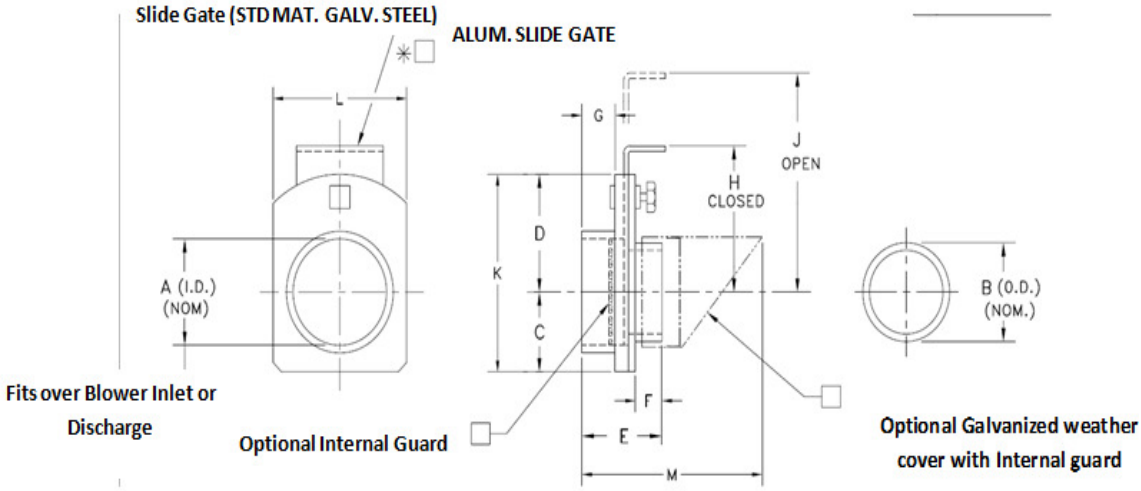

Figure A.15: Slide gate (damper) used on blower

APPENDIX B

This appendix section discusses the RANS (k-ω SST, RMS) model results in detail.

Figures B.1 to B.4 show the mesh considered for broken and continuous ribs.

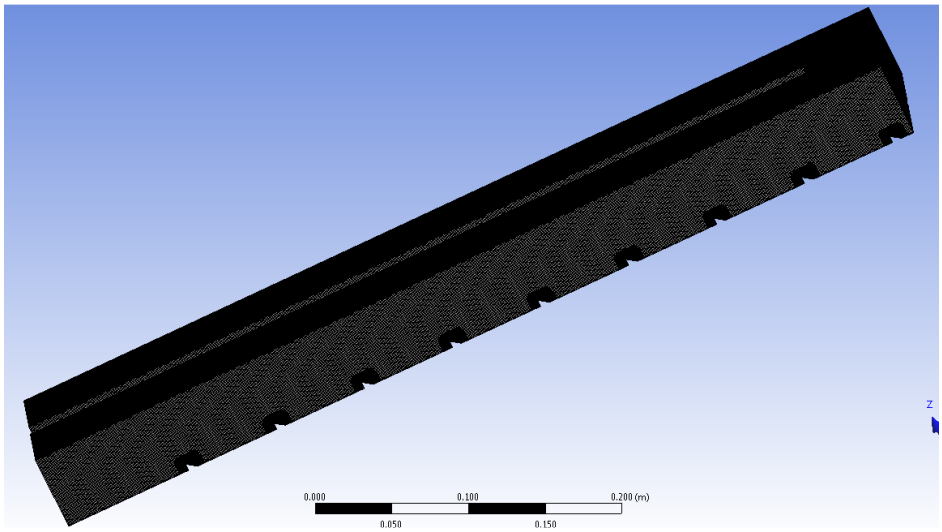

(a)

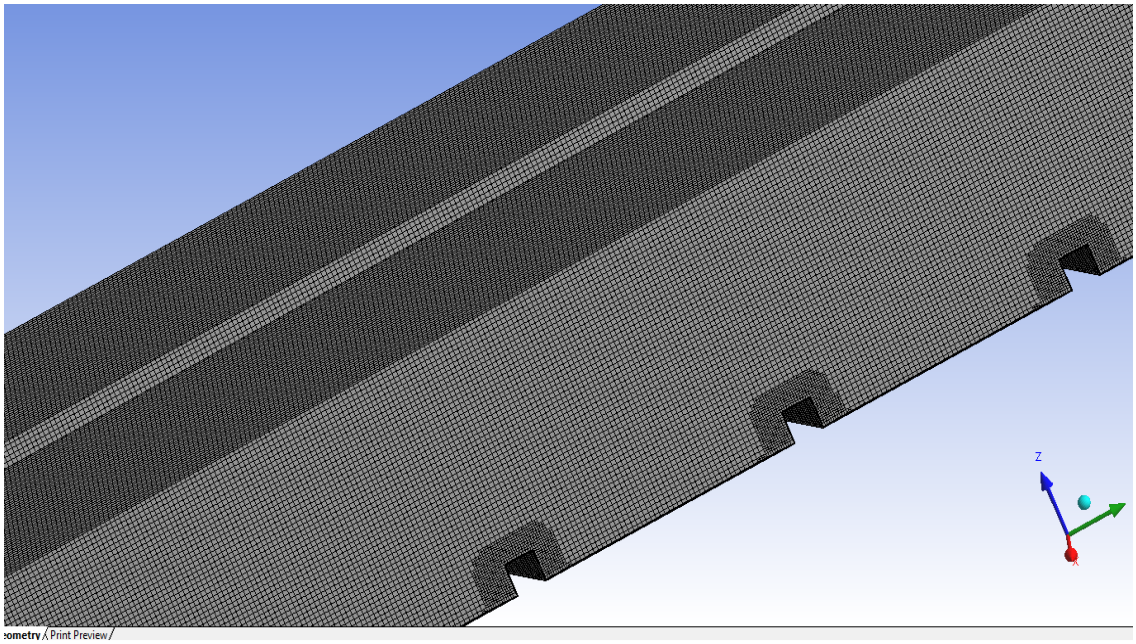

(b)

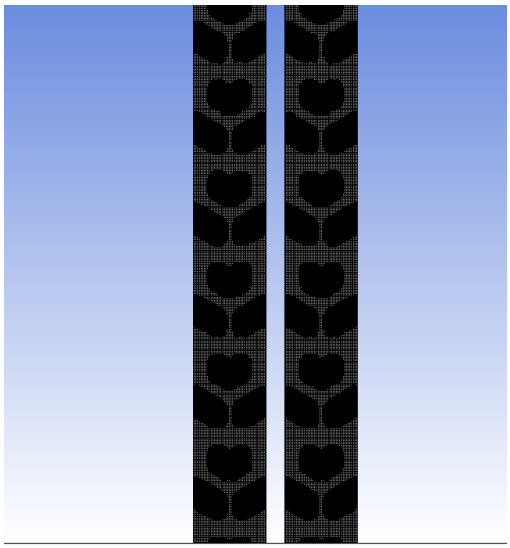

(a)

Figure B.1: Mesh considered for Broken V rib (a) Complete channel View (b) Zoomed View of mesh from side (c)Mesh from Back view of channel

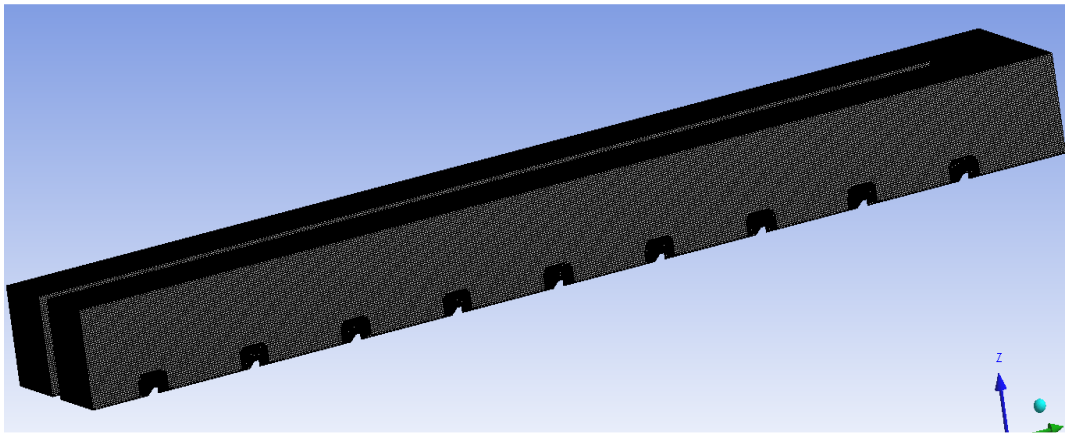

(a)

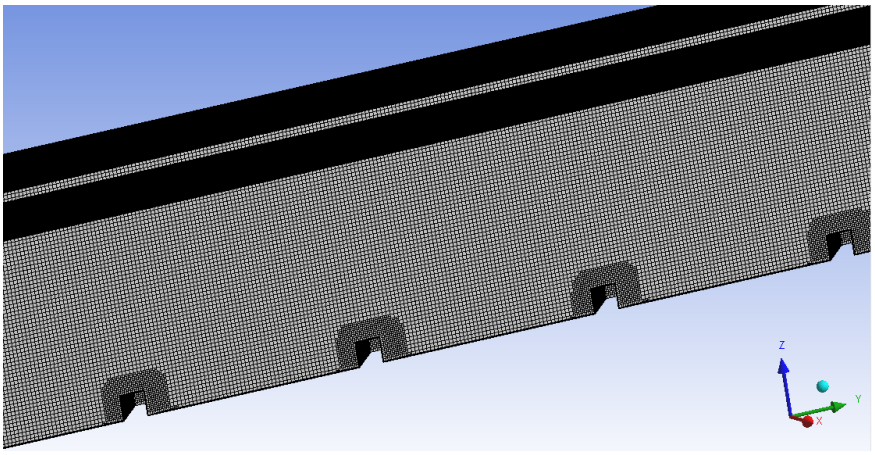

(b)

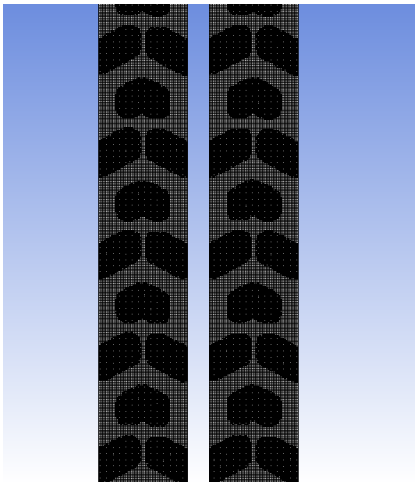

(c)

Figure B.2: Mesh considered for Broken IV rib (a) Complete channel View (b) Zoomed View of mesh from side (c)Mesh from Back view of channel

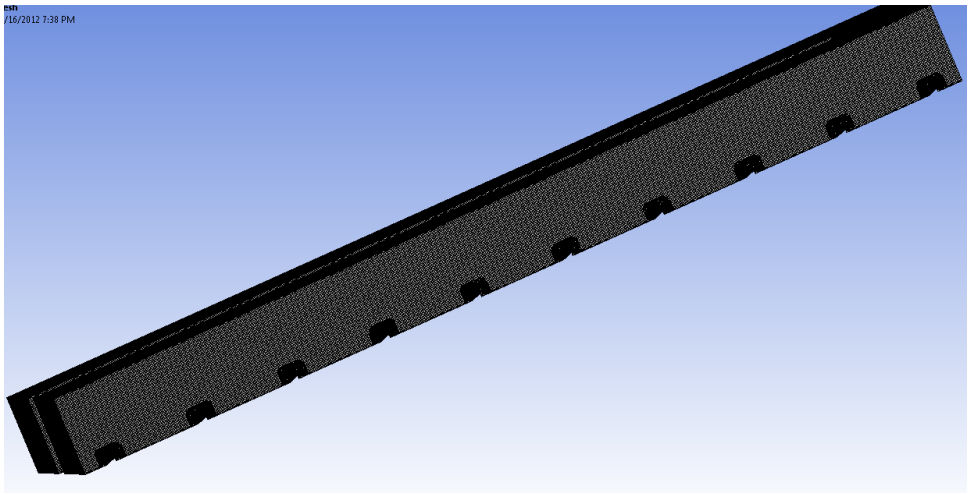

(a)

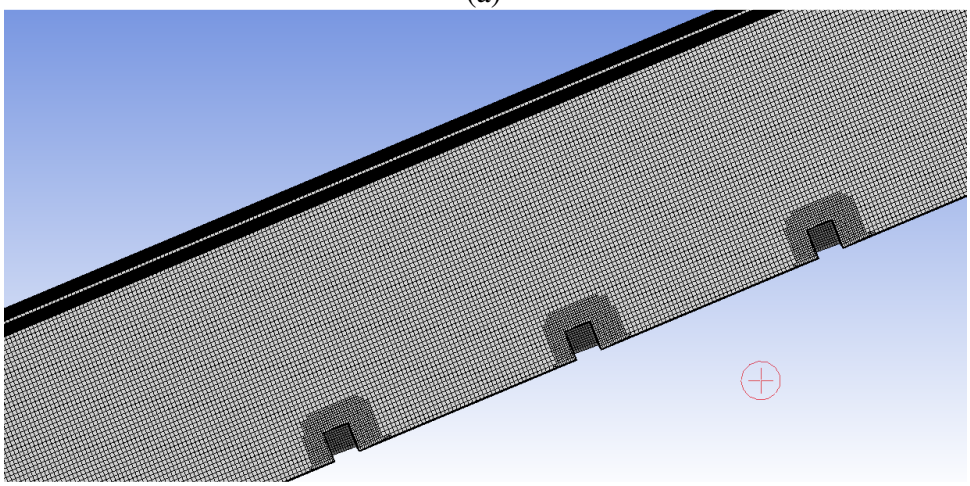

(b)

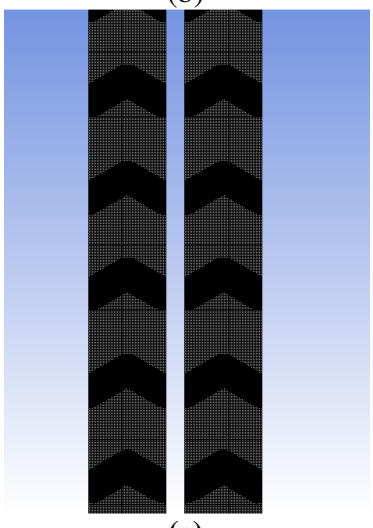

(c)

Figure B.3: Mesh considered for Continuous IV (a) Complete channel View (b) Zoomed View of mesh from side (c)Mesh from Back view of channel

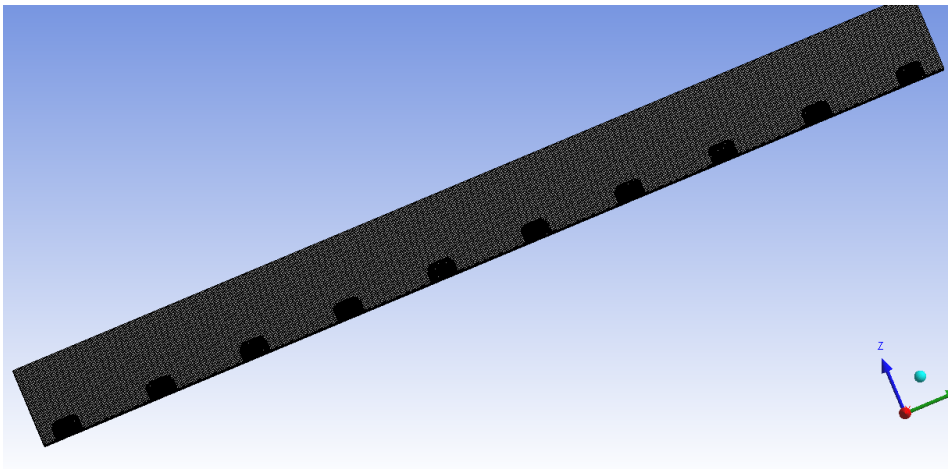

(a)

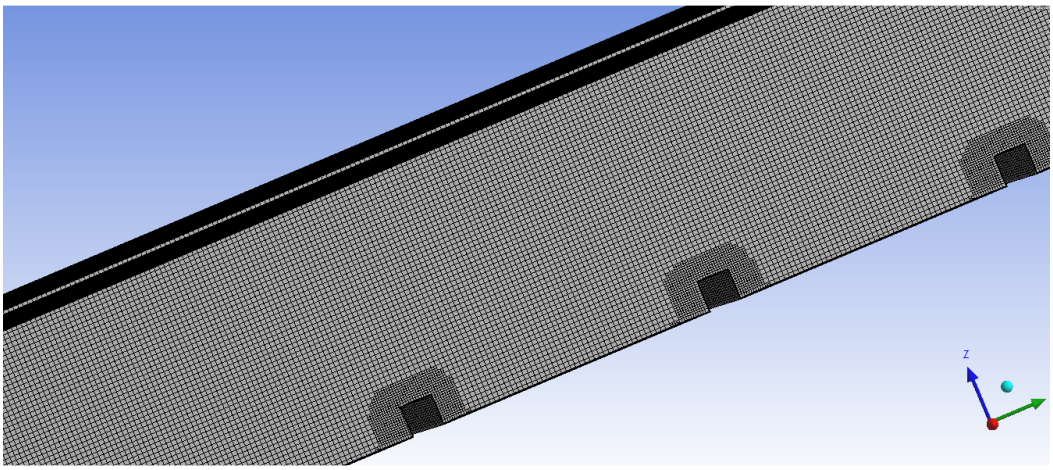

(b)

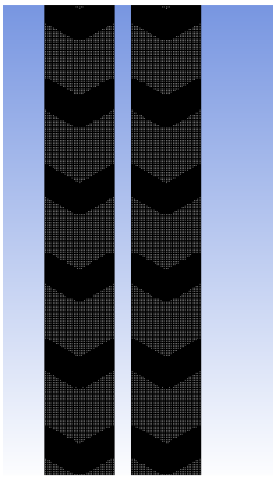

(c)

Figure B.4: Mesh considered for Continuous V (a) Complete channel View (b) Zoomed View of mesh from side (c)Mesh from Back view of channel

B.1: Turbulent Transport Equations

1. Transport Equations for the *k-ω SST* Model

***k*-equation:**

$$\frac{\partial(\rho k)}{\partial t}+\frac{\partial(\rho k u_i)}{\partial x_i}=\frac{\partial}{\partial x_j}\left(\Gamma_k\frac{\partial k}{\partial x_j}\right)+\tilde{G}_K-Y_K+S_K \tag{B.1}$$

ω -Equation:

$$\frac{\partial(\rho\omega)}{\partial t}+\frac{\partial(\rho\omega u_i)}{\partial x_i}=\frac{\partial}{\partial x_j}\left(\Gamma_\omega\frac{\partial\omega}{\partial x_j}\right)+G_\omega-Y_\omega+D_\omega+S_\omega \tag{B.2}$$

$$G_K=-\rho\overline{u_i'u_j'}\frac{\partial u_j}{\partial x_i} \tag{B.3}$$

2. Reynolds Stress Transport Equations

The exact transport equations for the transport of the Reynolds stress

$\rho\overline{u_i'u_j'}$ can be written as follows:

$$\begin{aligned}&\frac{\partial\left(\rho\overline{u_i'u_j'}\right)}{\partial t}+\frac{\partial\left(\rho u_k\overline{u_i'u_j'}\right)}{\partial x_k}=-\frac{\partial\left[\rho\overline{u_i'u_j'u_k'}+p(\overline{\delta_{kj}u_i'+\delta_{ik}u_j'})\right]}{\partial x_k}+\frac{\partial\left[\mu\left(\partial\overline{u_i'u_j'}/\partial x_k\right)\right]}{\partial x_k}\\&-\rho\left(\overline{u_i'u_k'}\frac{\partial u_j}{\partial u_k}+\overline{u_j'u_k'}\frac{\partial u_i}{\partial u_k}\right)-\rho\beta(g_i\overline{u_j'\theta}+g_j\overline{u_i'\theta})+p(\frac{\partial u_i'}{\partial u_j}+\frac{\partial u_j'}{\partial u_i})-2\mu\overline{\frac{\partial u_i'}{\partial u_j}\frac{\partial u_j'}{\partial u_i}}\\&-2\Omega_k\rho\left(\overline{u_j'u_m'}\varepsilon_{ikm}+\overline{u_i'u_m'}\varepsilon_{jkm}\right)+S_{USER}\end{aligned} \tag{B.4}$$

Representation of Reynolds stress model terms:

Local Time Derivative + C_{ij} (Convection) = $D_{T,ij}$(Turbulent Diffusion) + $D_{L,ij}$(Molecular Diffusion) + P_{ij} (Stress Production) + $G_{,ij}$ (Buoyancy Production) + φ_{ij} (Pressure Strain)

+ $\varepsilon_{L,\ ij}$ (Dissipation) + $F_{\ ij}$ (Production by system rotation)+S_{USER} (User Defined Source Term).

Of all the terms in the Reynolds stress model $C_{\ ij}$,$D_{L,\ ij}$, P_{ij} , F_{ij} do not require modeling however $D_{T,\ ij}$, G_{ij}, $\Phi_{\ ij}$, $\varepsilon_{L,\ ij}$ require modeling assumptions to close the equation sets.

B.2: Results and Discussion: Nusselt Number

A. Continuous Ribs:

Figure B.5 (a) shows surface Nusselt Number and B.5 (b) shows surface Nusselt number ratio for *k*-ω SST (Re = 56,000). Figure B.6 (a) shows surface Nusselt Number and B.6 (b) shows surface Nusselt number ratio for *k*-ω SST (Re = 85,000). In each of the figures, all the cases are compared to each other for better understanding of Nusselt Number profile along the wall. Nusselt Number ratios as well as surface Nusselt Number have higher values for the case of V-IV continuous rib and low values for the IV-V ribs. The overall Nusselt Number is higher in the mid section and on the rib due to recirculation in that region. Just after the ribs, the values are lower because of this being the separation region.

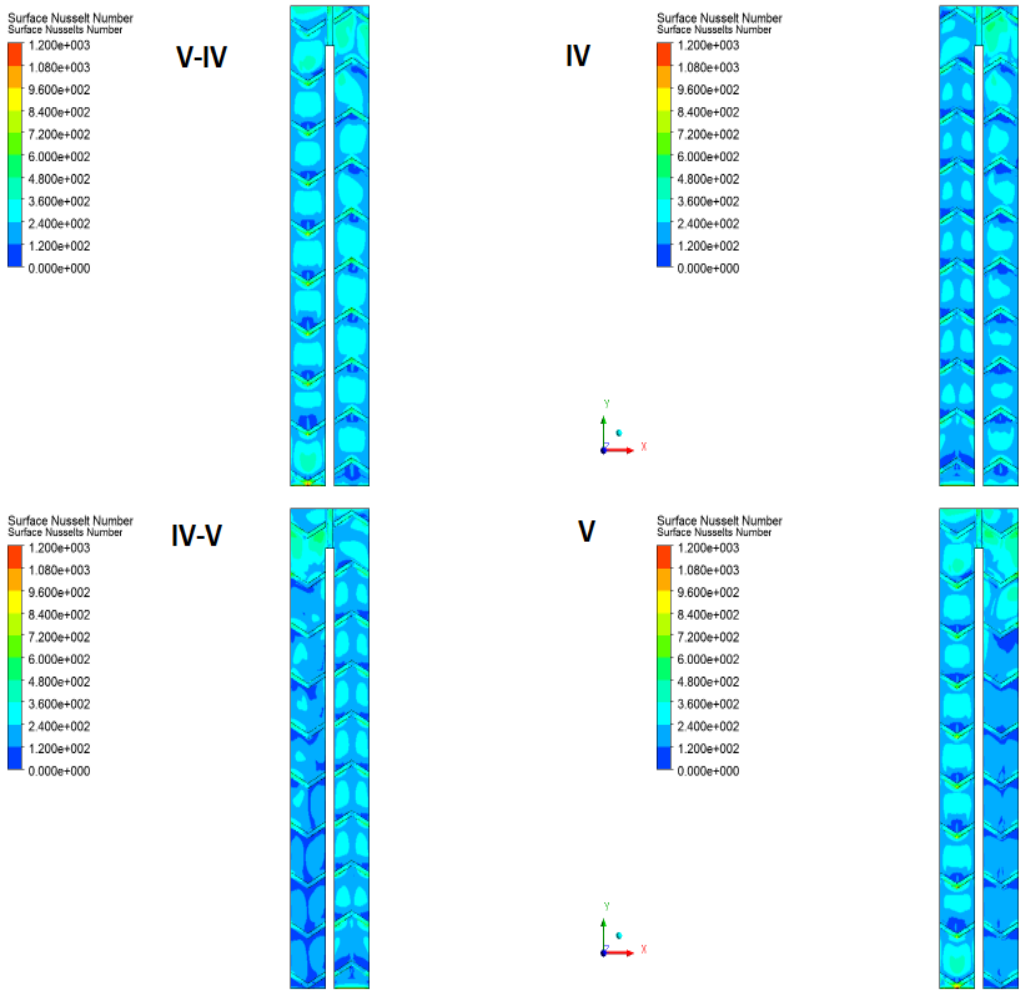
Surface Nusselt Number
Surface Nusselts Number
1.200e+003
1.080e+003
9.600e+002
8.400e+002
7.200e+002
6.000e+002
4.800e+002
3.600e+002
2.400e+002
1.200e+002
0.000e+000
V-IV
IV
IV-V
V

(a)

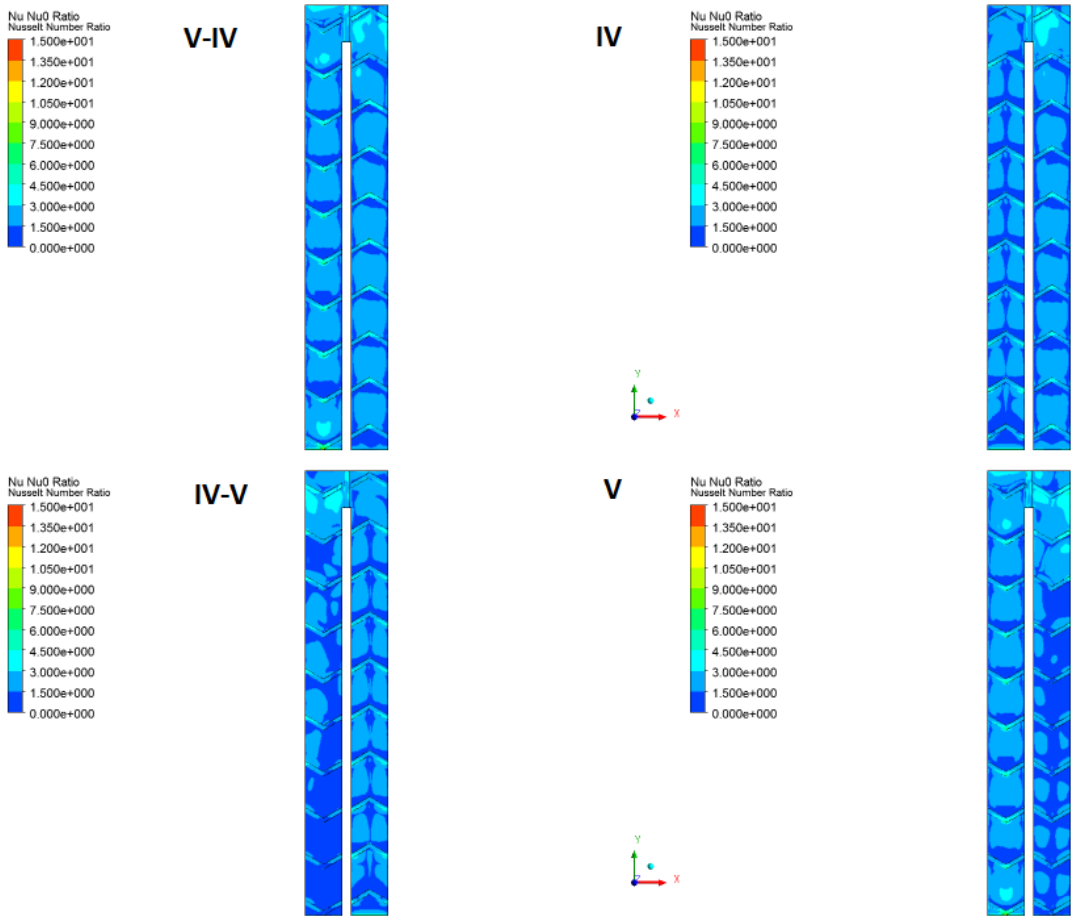

(b)

Figure B.5: Continuous Rib (Re=56000, *k*-ω SST) (a) Surface Nusselt Number along wall (b) Surface Nusselt Number Ratio

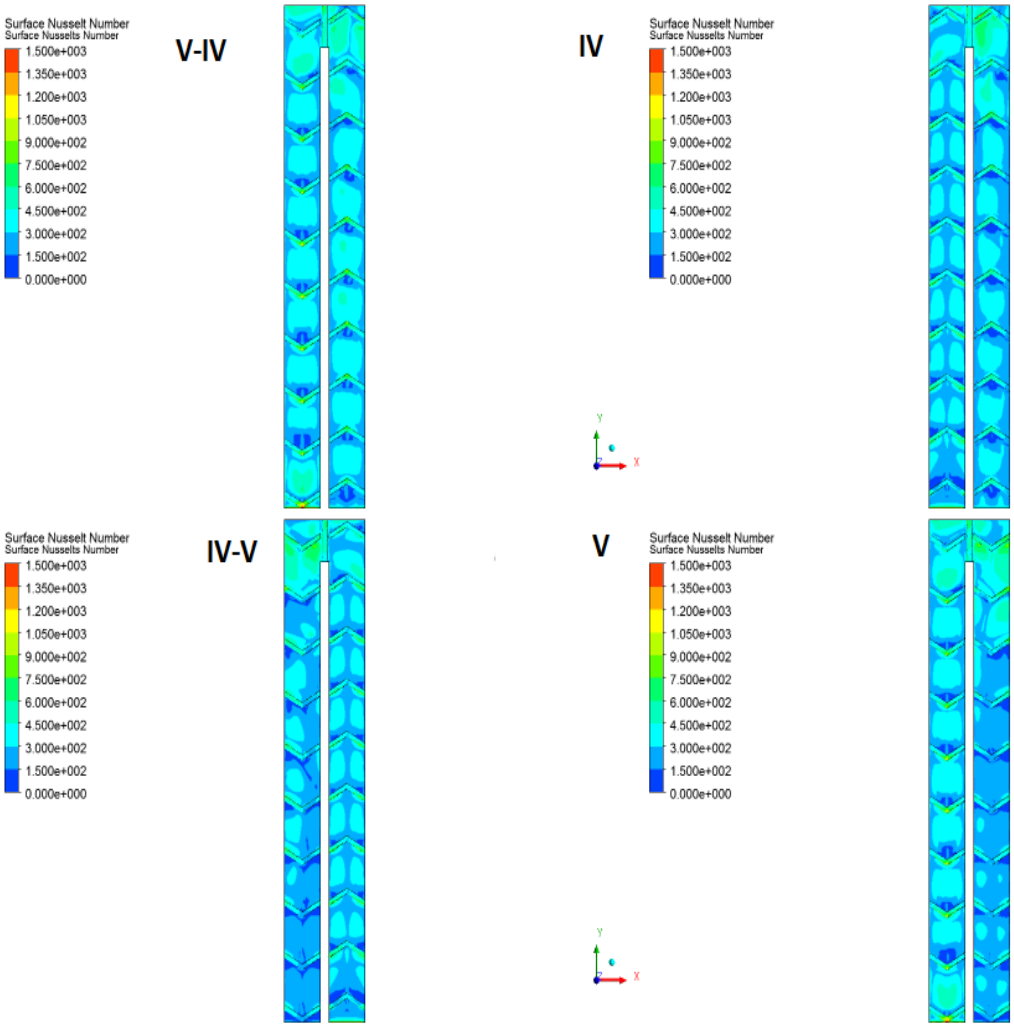
Surface Nusselt Number
Surface Nusselts Number
1.500e+003
1.350e+003
1.200e+003
1.050e+003
9.000e+002
7.500e+002
6.000e+002
4.500e+002
3.000e+002
1.500e+002
0.000e+000
V-IV
IV
IV-V
V

(a)

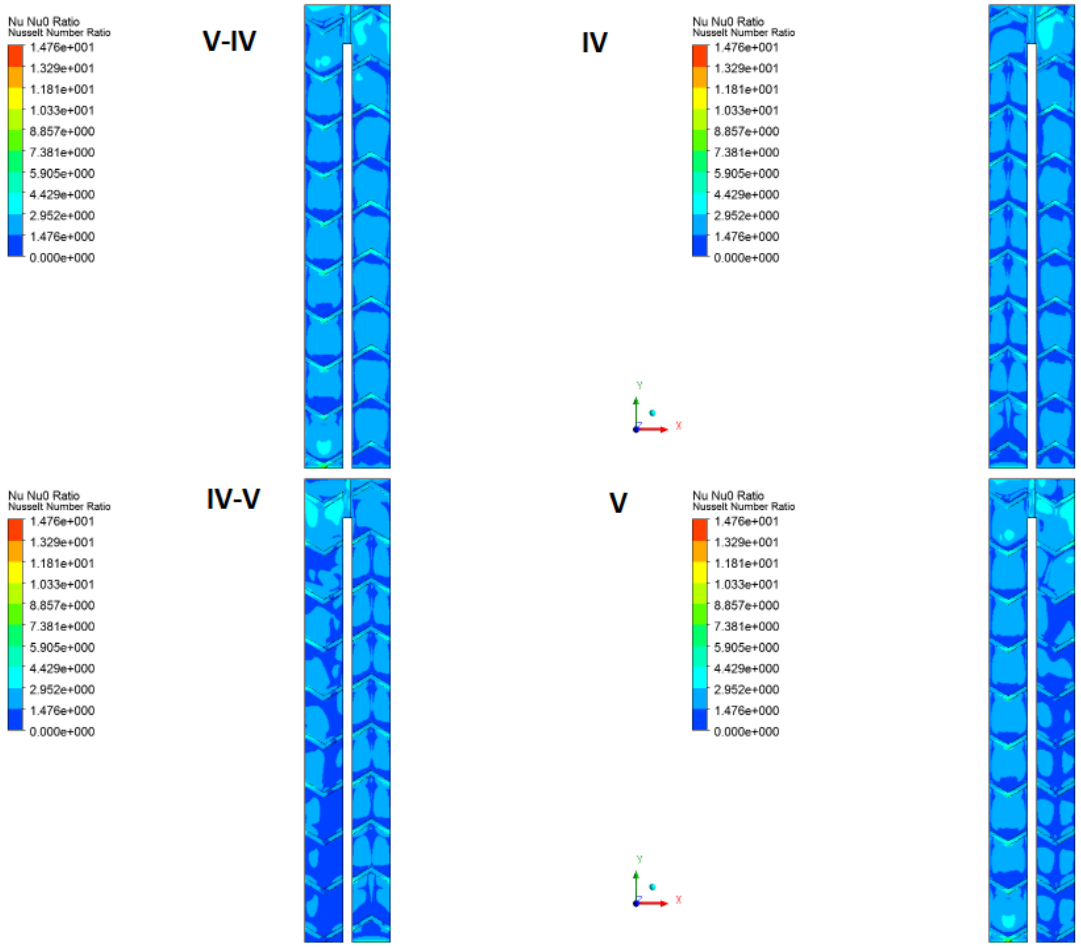

(b)

Figure B.6: Continuous Rib (Re=85000, *k*-ω SST) (a) Surface Nusselt Number along wall (b) Surface Nusselt Number Ratio

Figure B.7 (a) shows surface Nusselt Number and B.7 (b) shows surface Nusselt number ratio for RSM (Re = 21,000) . Figure B.8 (a) shows surface Nusselt Number and B.8 (b) shows surface Nusselt number ratio for RSM (Re = 56,000). Figure B.9 (a) shows surface Nusselt Number and B.9 (b) shows surface Nusselt number ratio for RSM (Re = 85,000). All the cases are compared to each other for better understanding of Nusselt Number

profile along the wall. In the case of V-IV continuous ribs, Nusselt Number ratio as well as Nusselt Number is higher than the values for the IV-V ribs. RSM model also provides similar profiles for these parameters which gives us the insight that the two models behave similarly for this particular problem. Just after the ribs, the values are on the lower side because of it being the separation region as compared to the recirculation observed in the mid section leading to higher values.

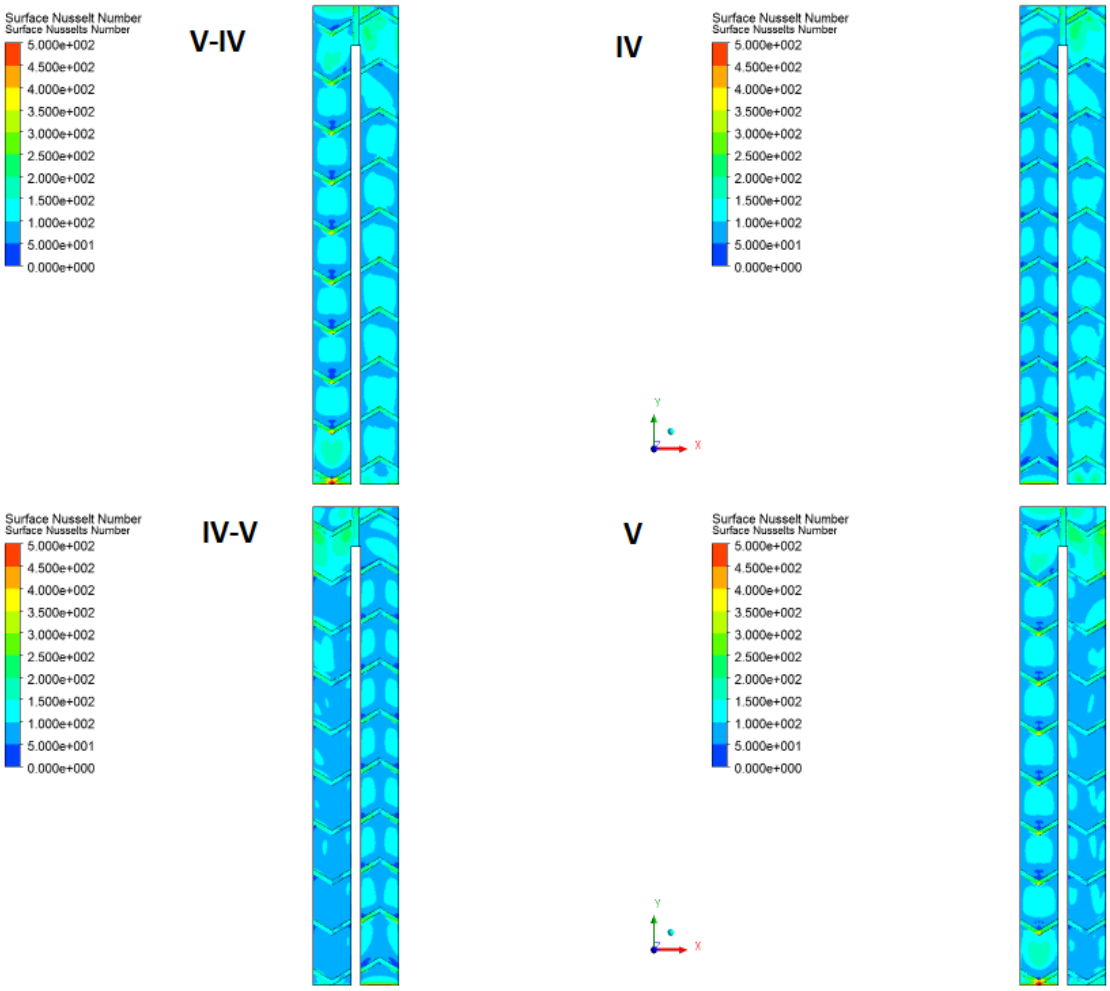

(a)

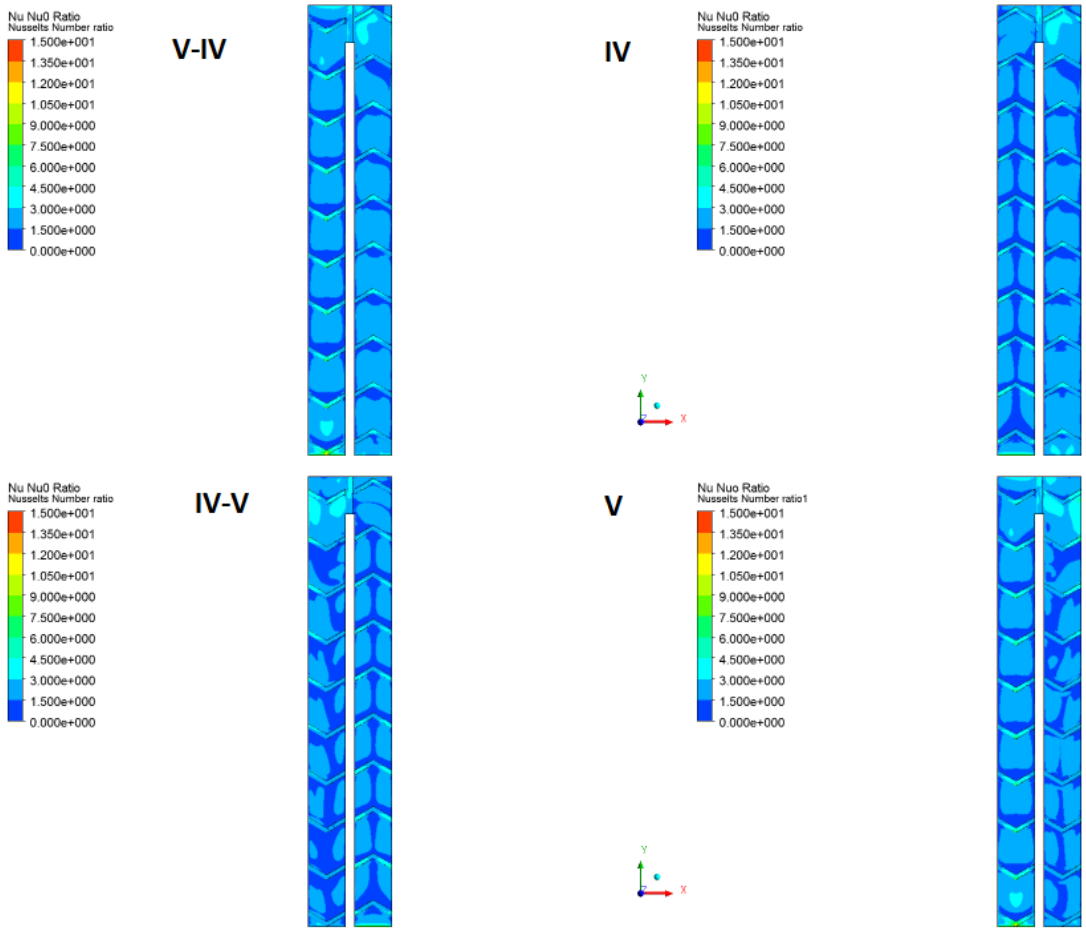

(b)

Figure B.7: Continuous Rib (Re=21000, RSM) (a) Surface Nusselt Number along wall

(b) Surface Nusselt Number Ratio

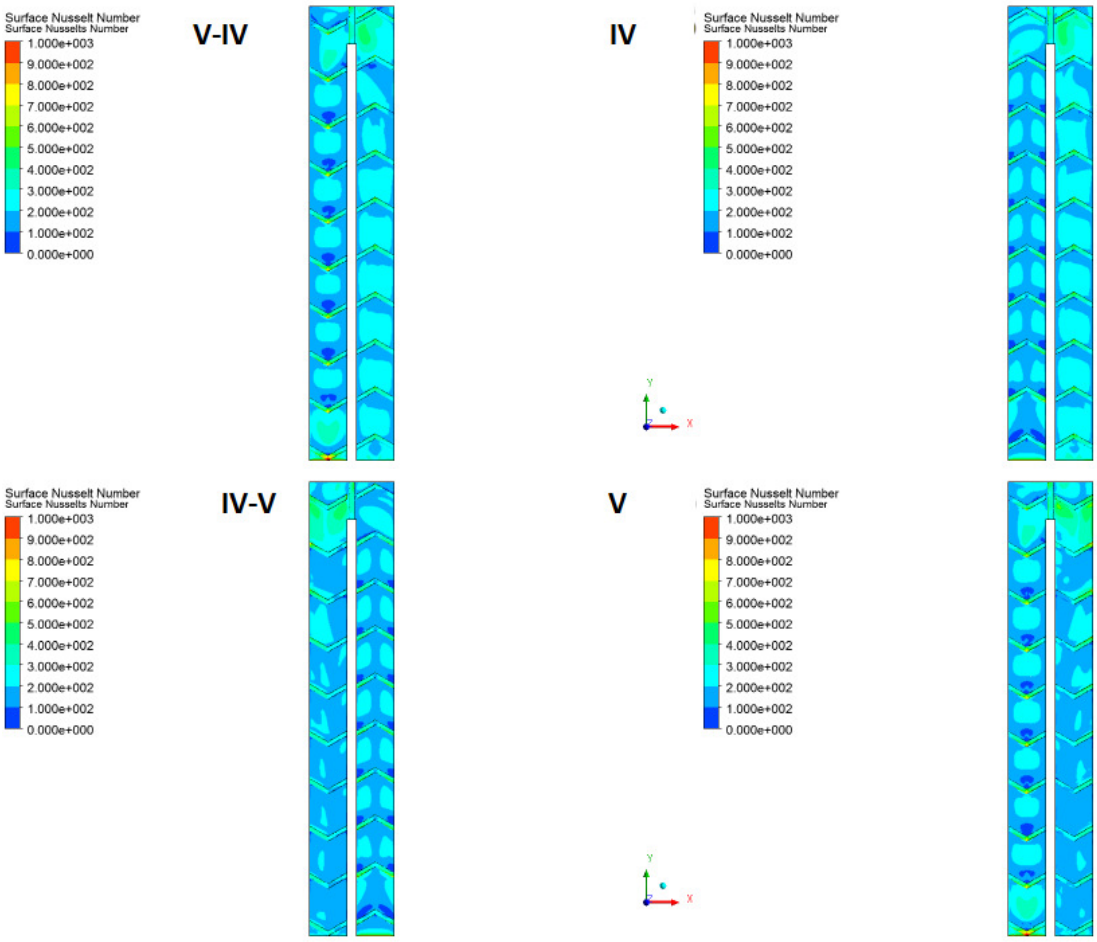
Surface Nusselt Number
Surface Nusselts Number
1.000e+003
9.000e+002
8.000e+002
7.000e+002
6.000e+002
5.000e+002
4.000e+002
3.000e+002
2.000e+002
1.000e+002
0.000e+000
V-IV
IV
IV-V
V
Y
X

(a)

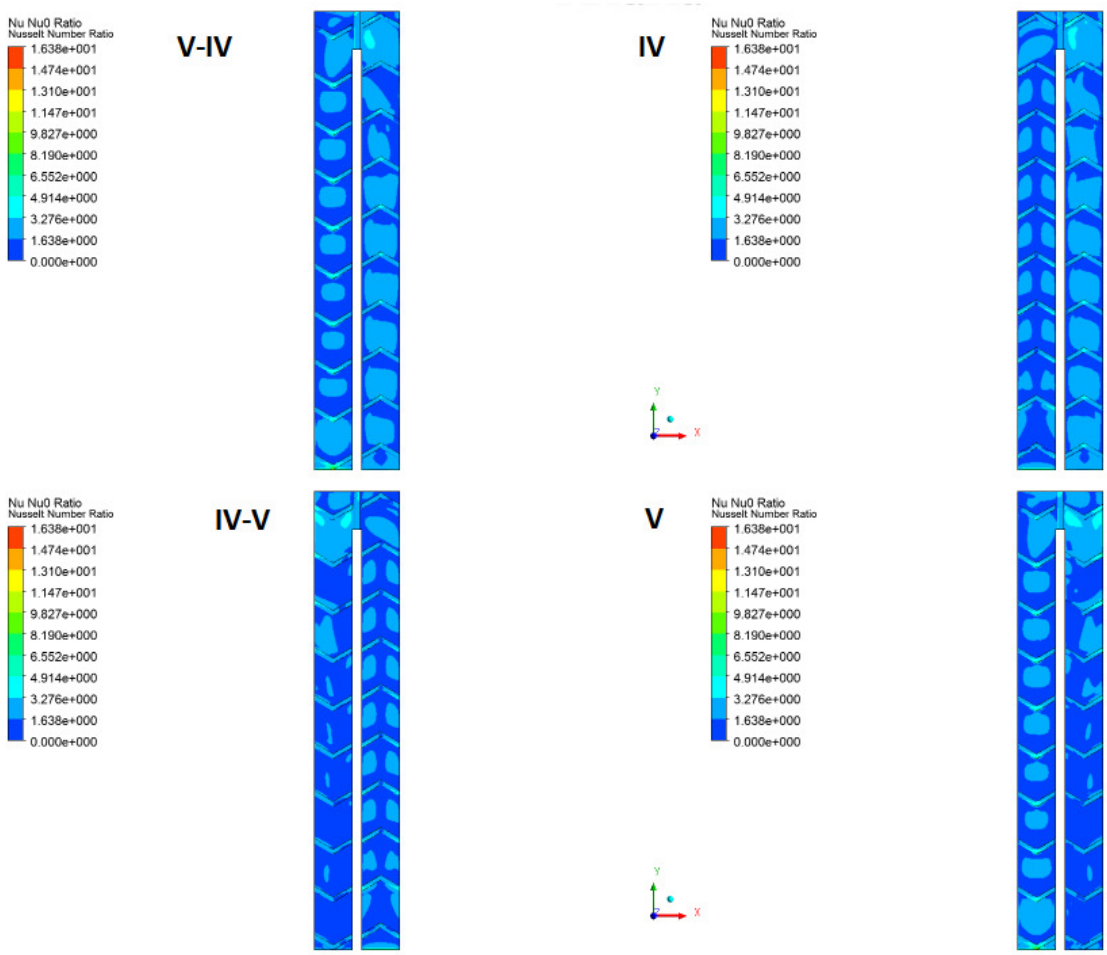

(b)

Figure B.8: Continuous Rib (Re=56000, RSM) (a) Surface Nusselt Number along wall

(b) Surface Nusselt Number Ratio

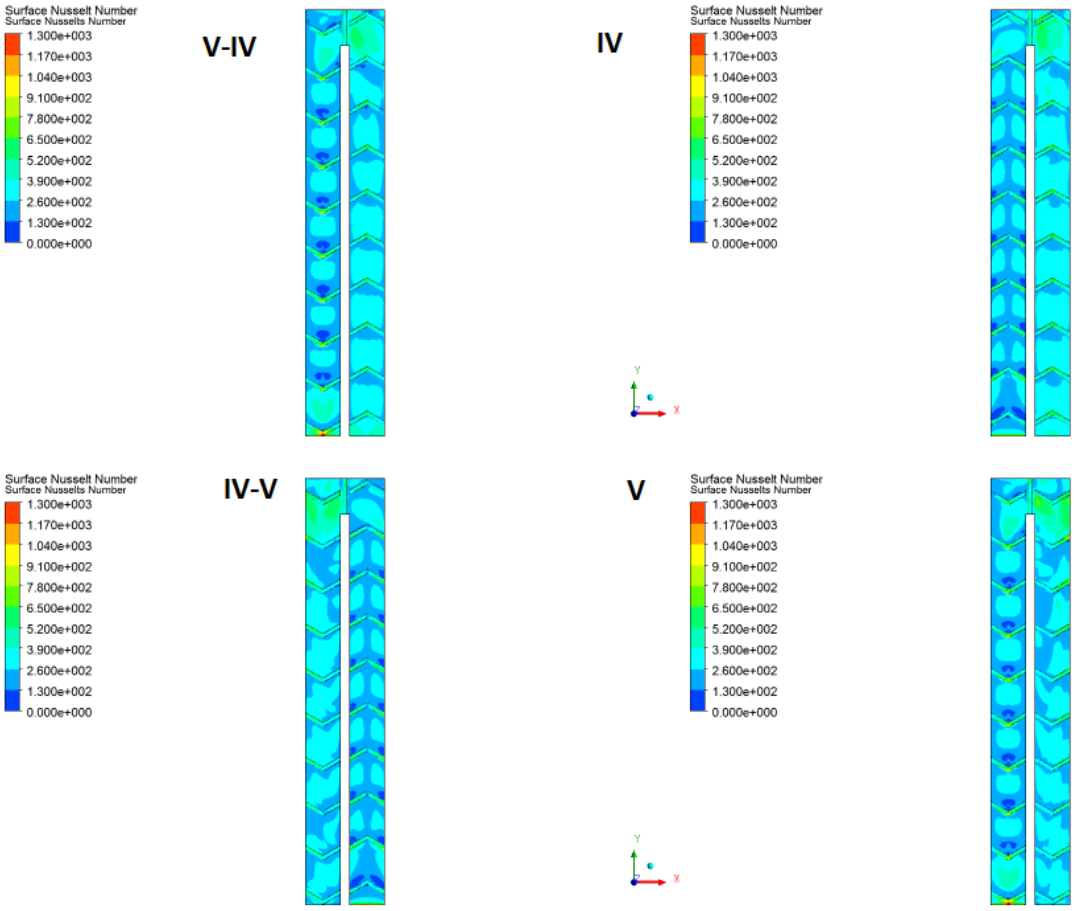
Surface Nusselt Number
Surface Nusselts Number
1.300e+003
1.170e+003
1.040e+003
9.100e+002
7.800e+002
6.500e+002
5.200e+002
3.900e+002
2.600e+002
1.300e+002
0.000e+000
V-IV
IV
IV-V
V

(a)

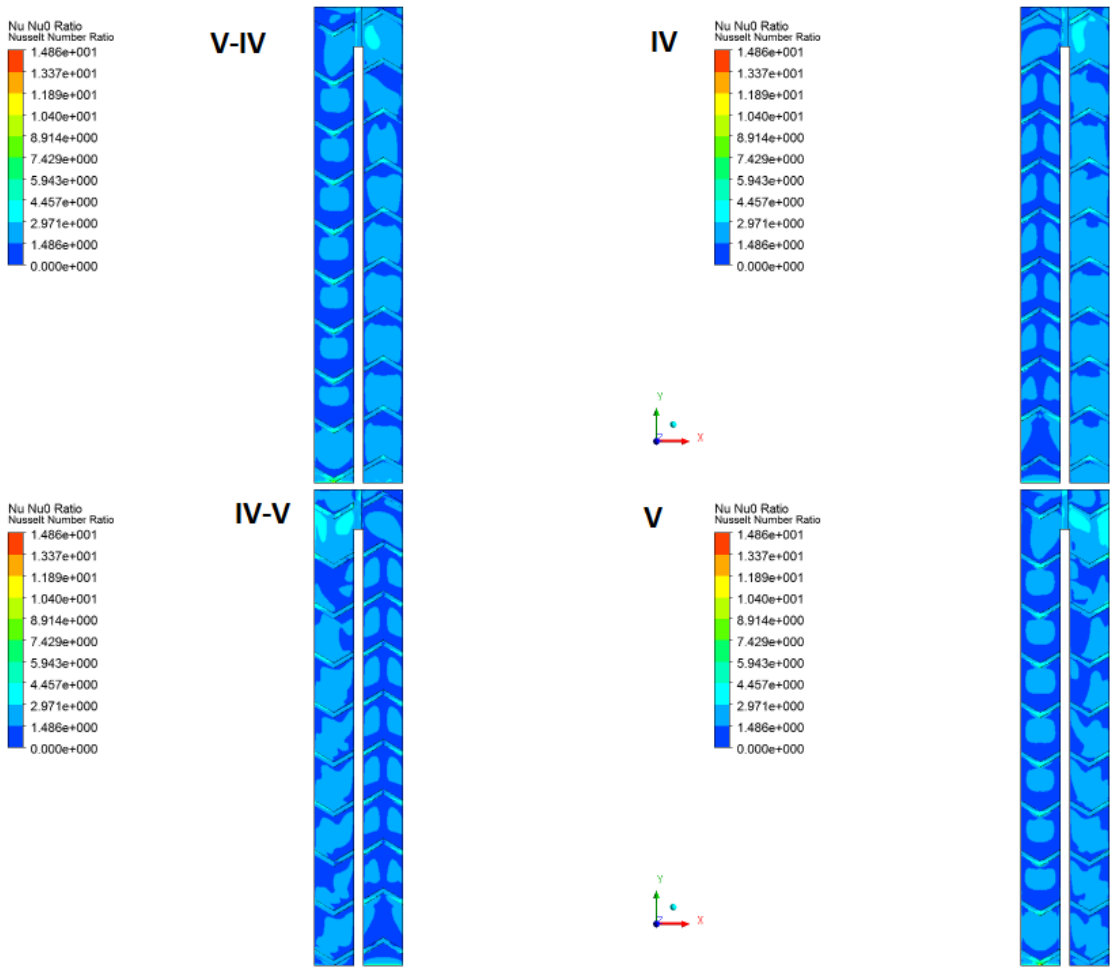

(b)

Figure B.9: Continuous Rib (Re=85000, RSM) (a) Surface Nusselt Number along wall (b) Surface Nusselt Number Ratio

B. Broken Ribs:

Figure B.10 (a) shows surface Nusselt Number and B.10 (b) shows surface Nusselt number ratio for *k*-ω SST (Re = 56,000). Figure B.11 (a) shows surface Nusselt Number and B.11 (b) shows surface Nusselt number ratio for *k*-ω SST (Re = 85,000). In each of the figures, all the cases are compared to each other for a better understanding of Nusselt Number profile along the wall. Nusselt Number ratios as well as surface Nusselt

Number have higher values in the case of V-IV continuous ribs and lower values for the IV-V ribs. In case of broken ribs, there is an increase in surface Nusselt Number and Nusselt Number as compared to continuous ribs. These enhancements are because of the broken ribs, flow trips on broken ribs and then again on the V portion of the rib it bifurcates and the secondary flow are developed.

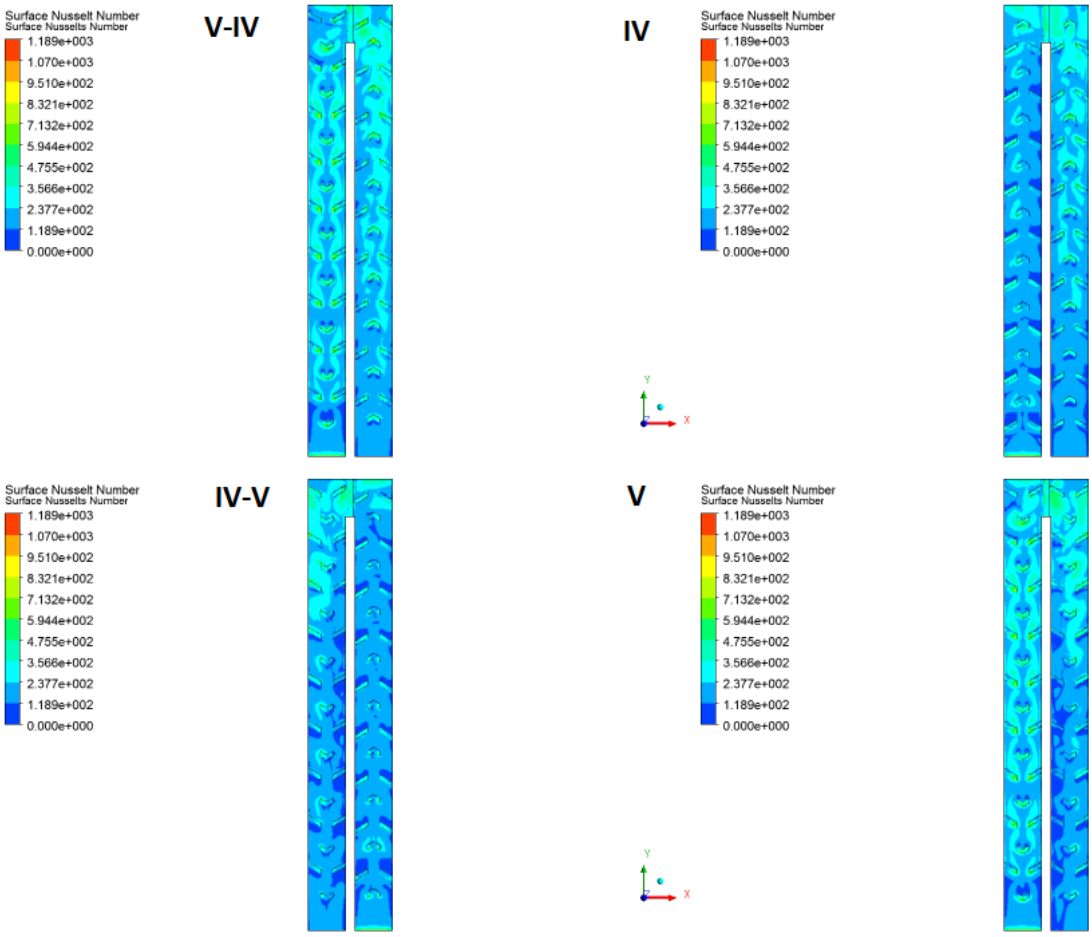

(a)

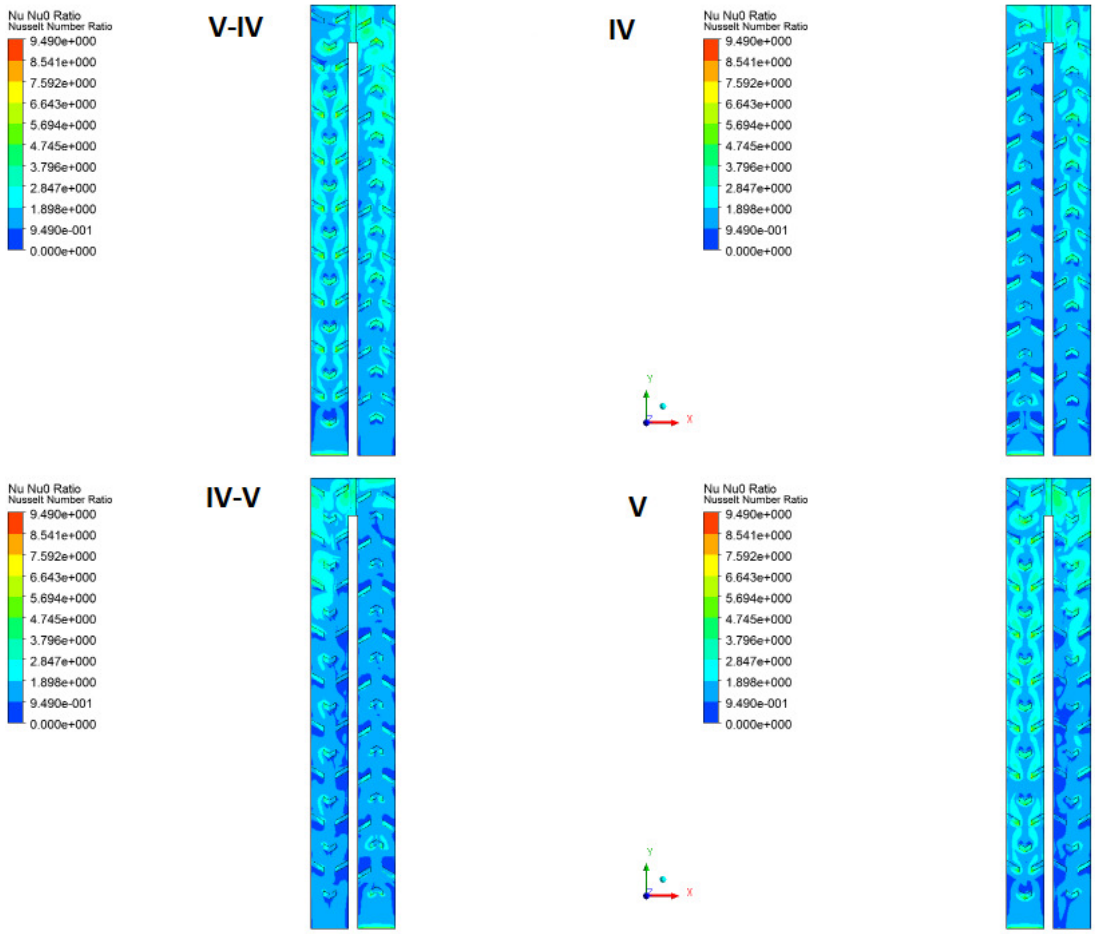

(b)

Figure B.10: Broken Rib (Re=56000, *k*-ω SST) (a) Surface Nusselt Number along wall

(b) Surface Nusselt Number Ratio

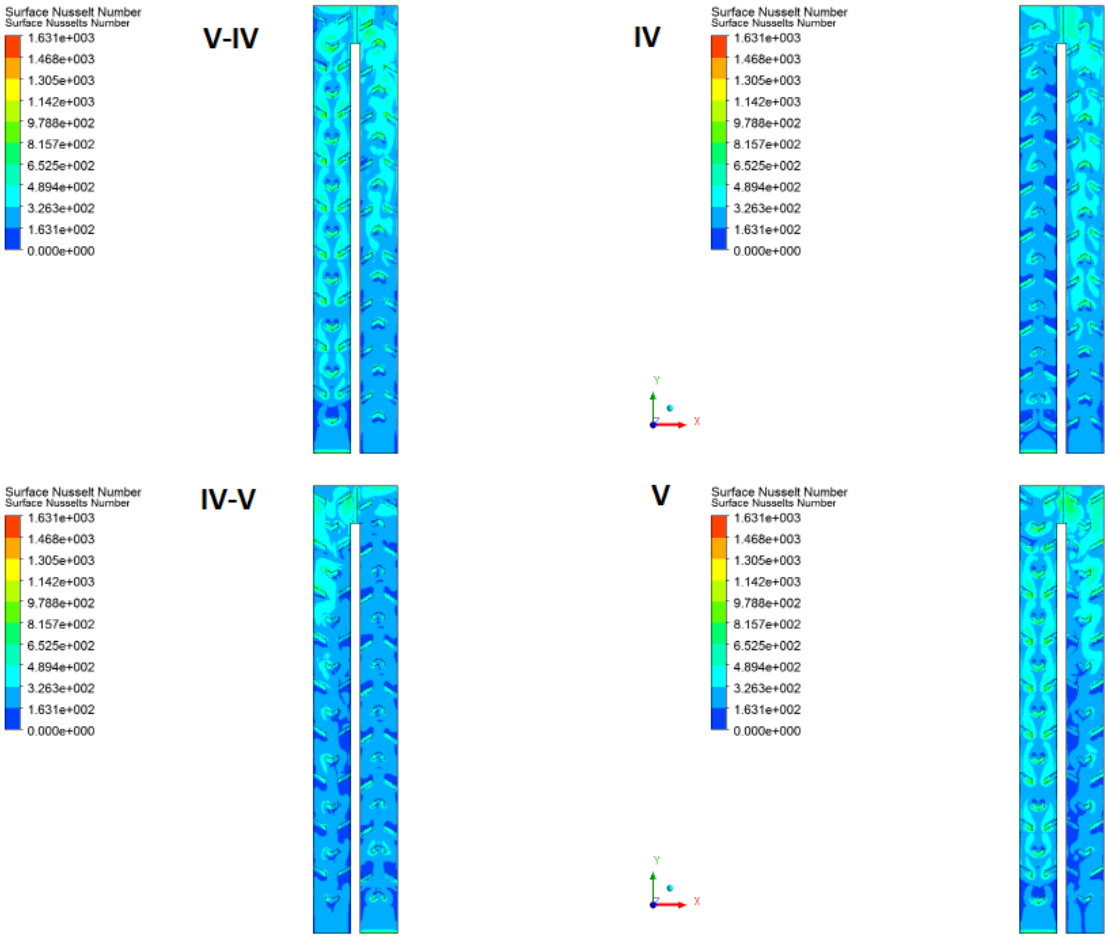
Surface Nusselt Number
Surface Nusselts Number
1.631e+003
1.468e+003
1.305e+003
1.142e+003
9.788e+002
8.157e+002
6.525e+002
4.894e+002
3.263e+002
1.631e+002
0.000e+000
V-IV
IV
IV-V
V

(a)

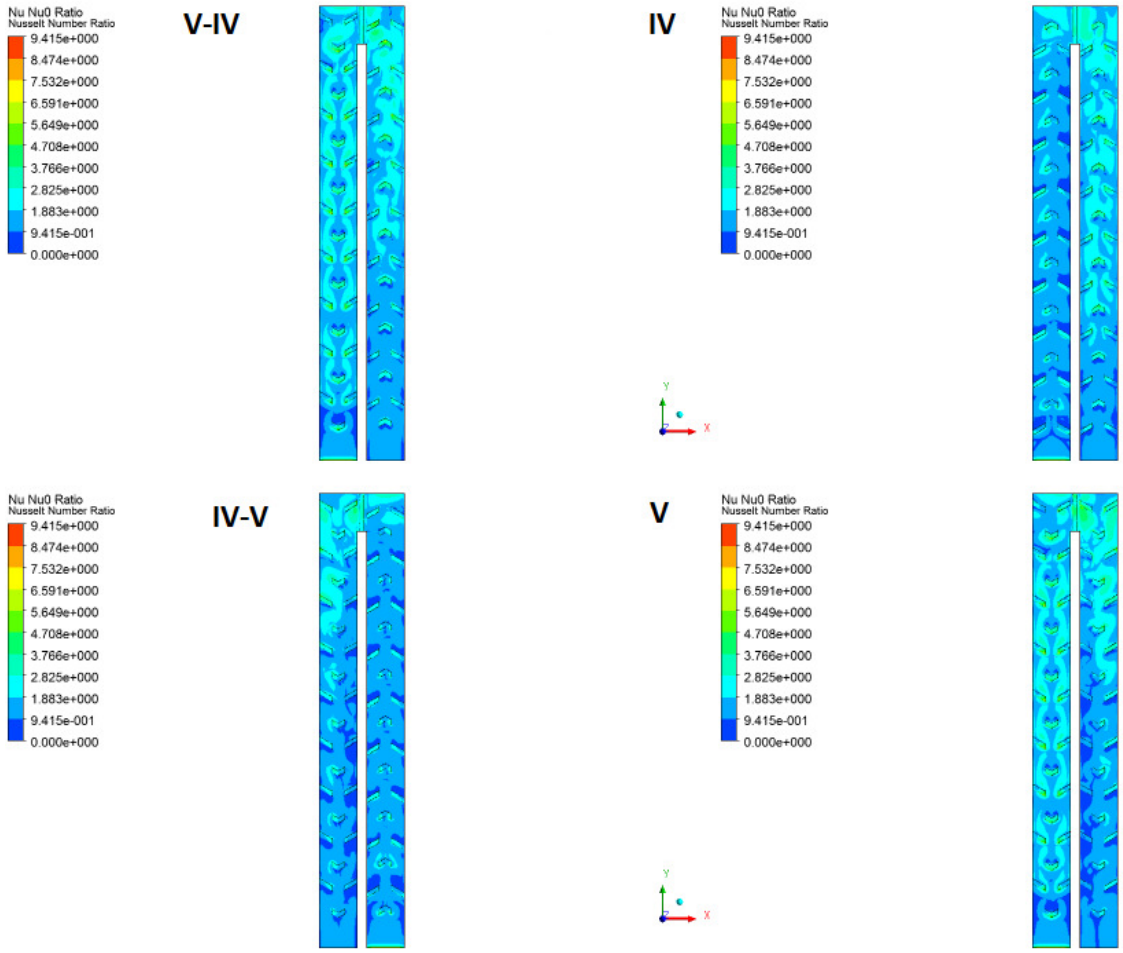

(b)

Figure B.11: Broken Rib (Re=85000, *k*-ω SST) (a) Surface Nusselt Number along wall (b) Surface Nusselt Number Ratio

Figure B.12 (a) shows surface Nusselt Number and B.12 (b) shows surface Nusselt number ratio for RSM (Re = 21,000) . Figure B.13 (a) shows surface Nusselt Number and B.13 (b) shows surface Nusselt number ratio for RSM (Re = 56,000). Figure B.14 (a) shows surface Nusselt Number and B.14 (b) shows surface Nusselt number ratio for RSM (Re = 85,000).

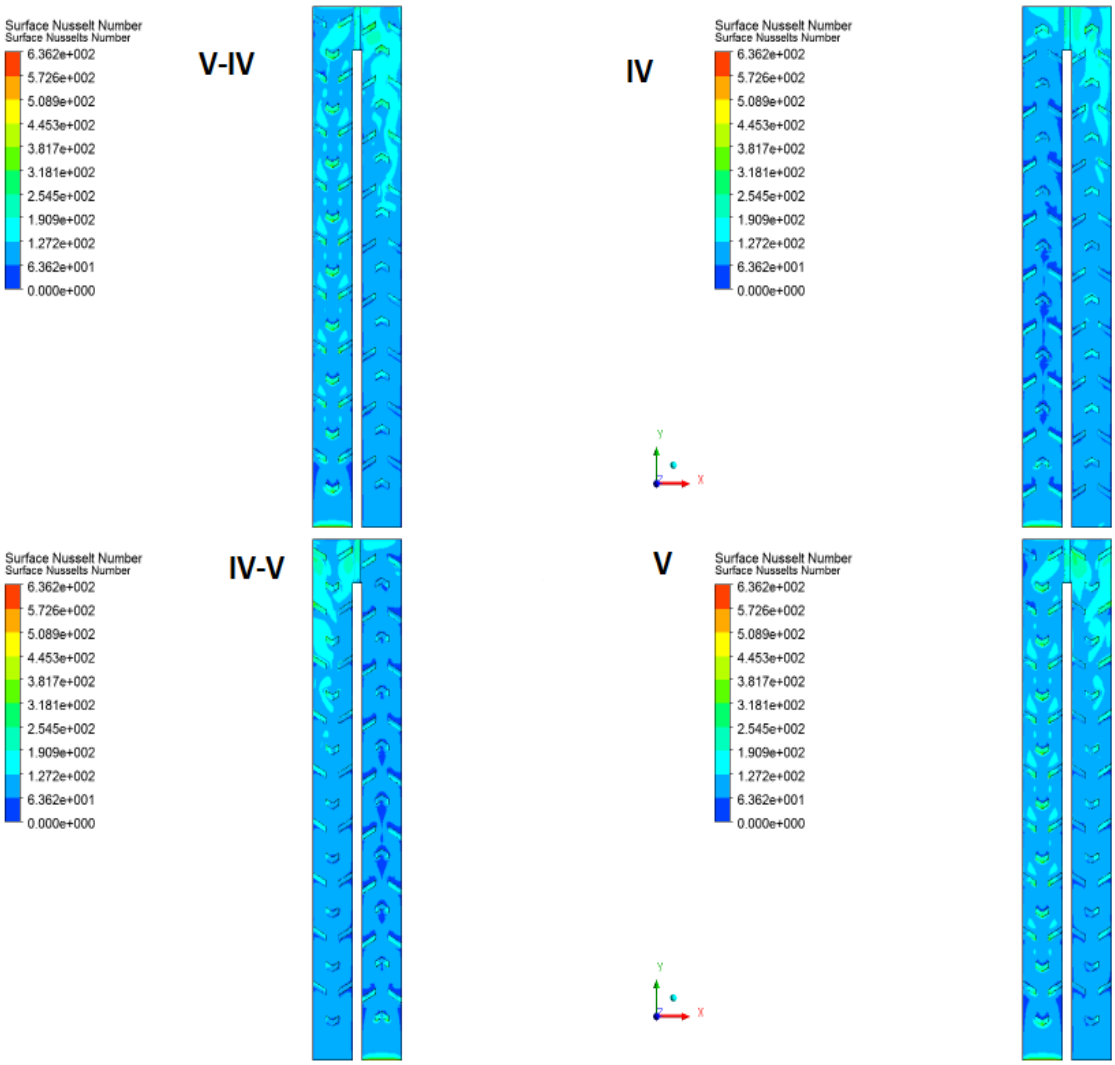
Surface Nusselt Number
Surface Nusselts Number
6.362e+002
5.726e+002
5.089e+002
4.453e+002
3.817e+002
3.181e+002
2.545e+002
1.909e+002
1.272e+002
6.362e+001
0.000e+000
V-IV
IV
IV-V
V

(a)

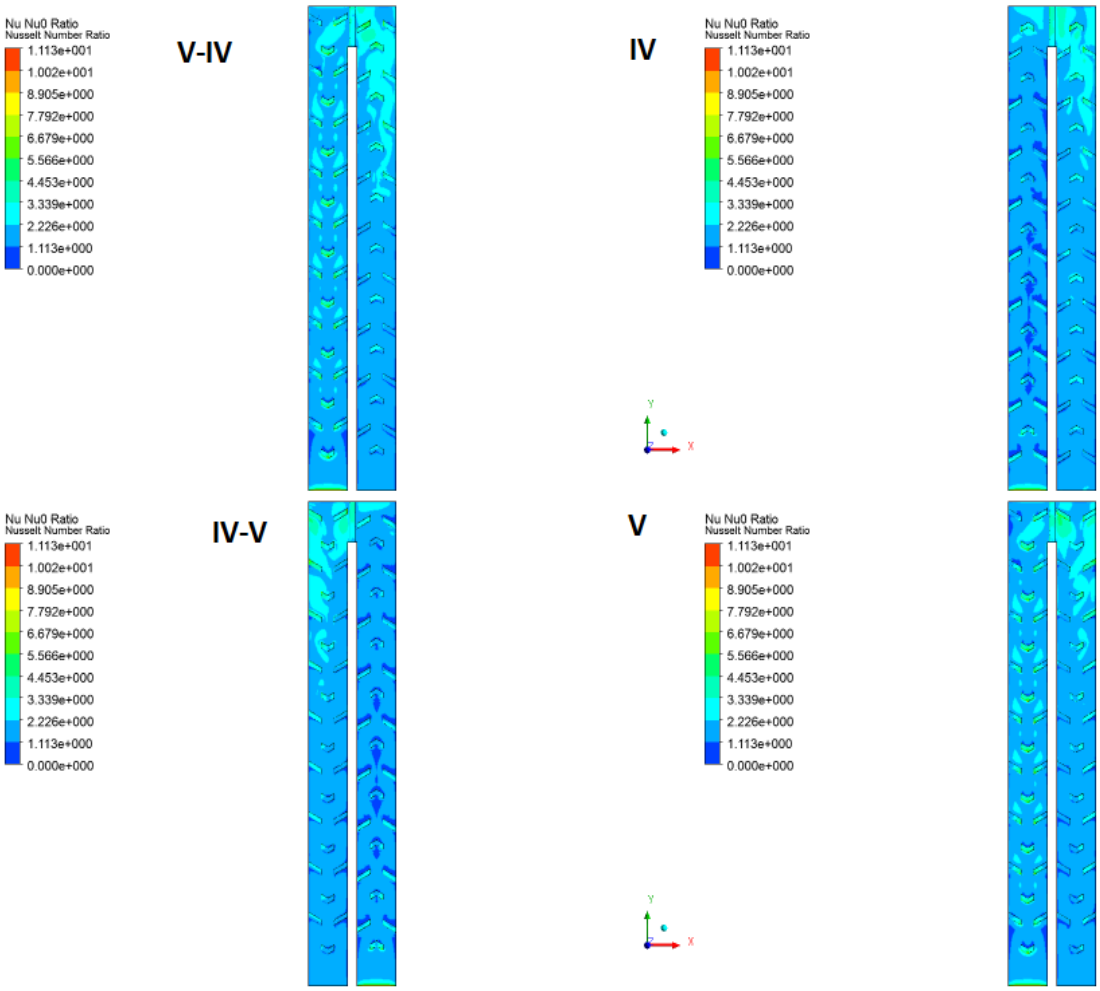

(b)

Figure B.12: Broken Rib (Re=21000, RSM) (a) Surface Nusselt Number along wall (b) Surface Nusselt Number Ratio

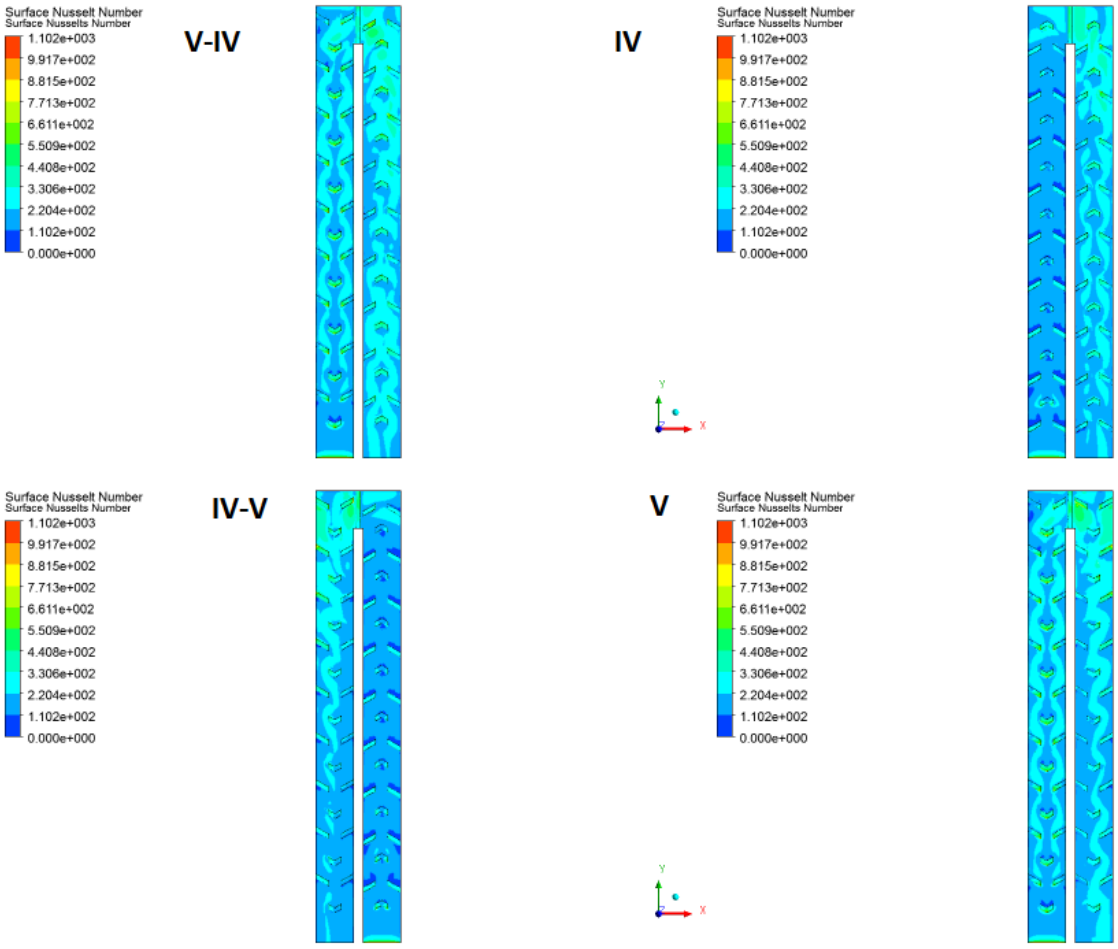
Surface Nusselt Number
Surface Nusselts Number
1.102e+003
9.917e+002
8.815e+002
7.713e+002
6.611e+002
5.509e+002
4.408e+002
3.306e+002
2.204e+002
1.102e+002
0.000e+000
V-IV
IV
IV-V
V

(a)

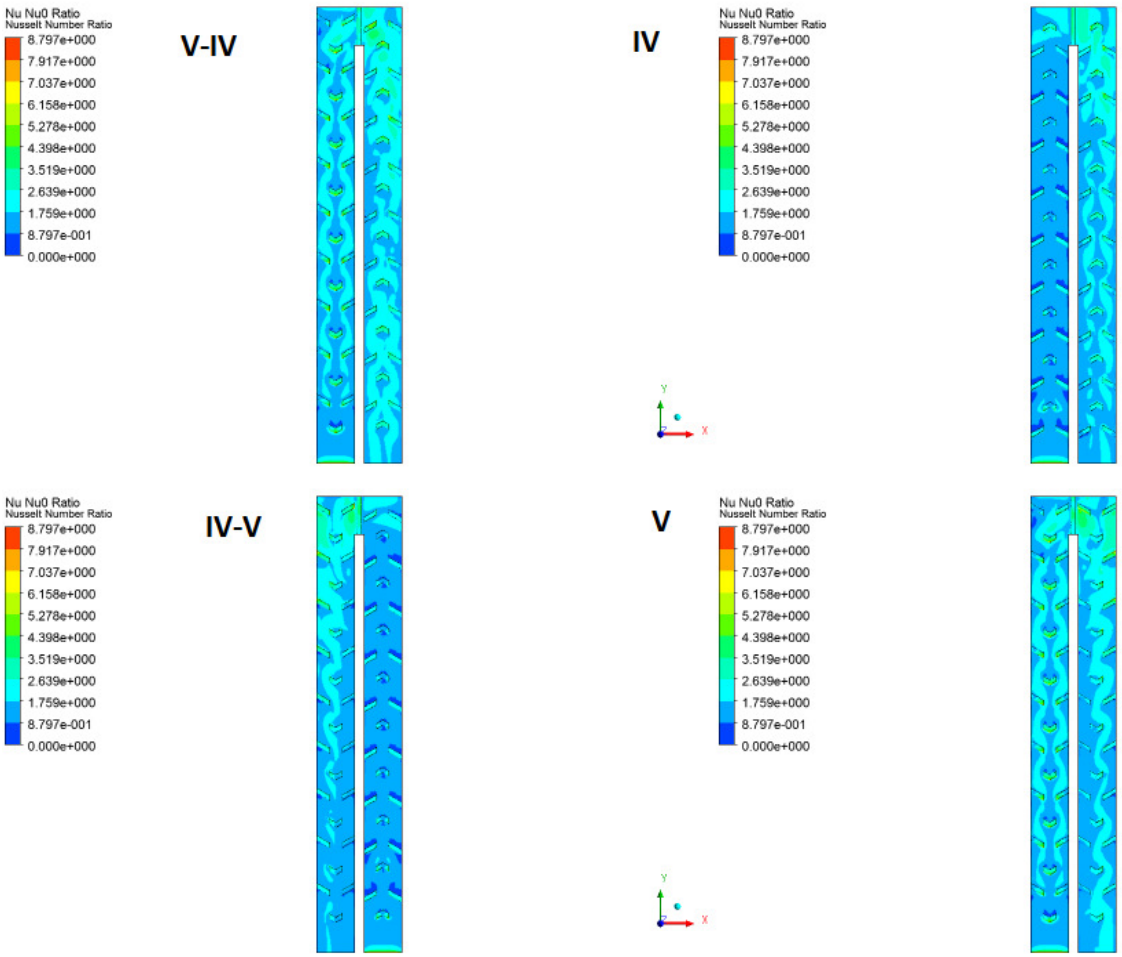

(b)

Figure B.13: Broken Rib (Re=56000, RSM) (a) Surface Nusselt Number along wall (b) Surface Nusselt Number Ratio

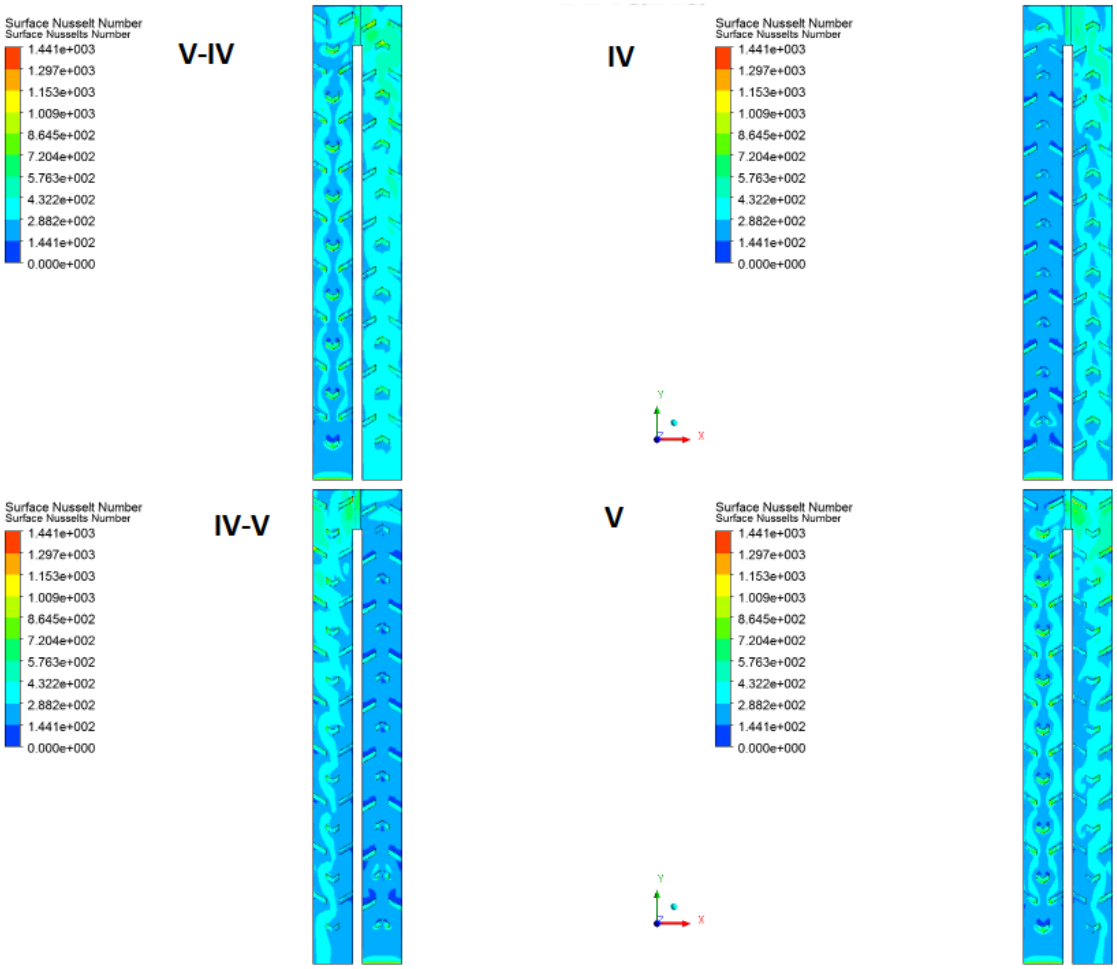
Surface Nusselt Number
Surface Nusselts Number
1.441e+003
1.297e+003
1.153e+003
1.009e+003
8.645e+002
7.204e+002
5.763e+002
4.322e+002
2.882e+002
1.441e+002
0.000e+000
V-IV
IV
IV-V
V

(a)

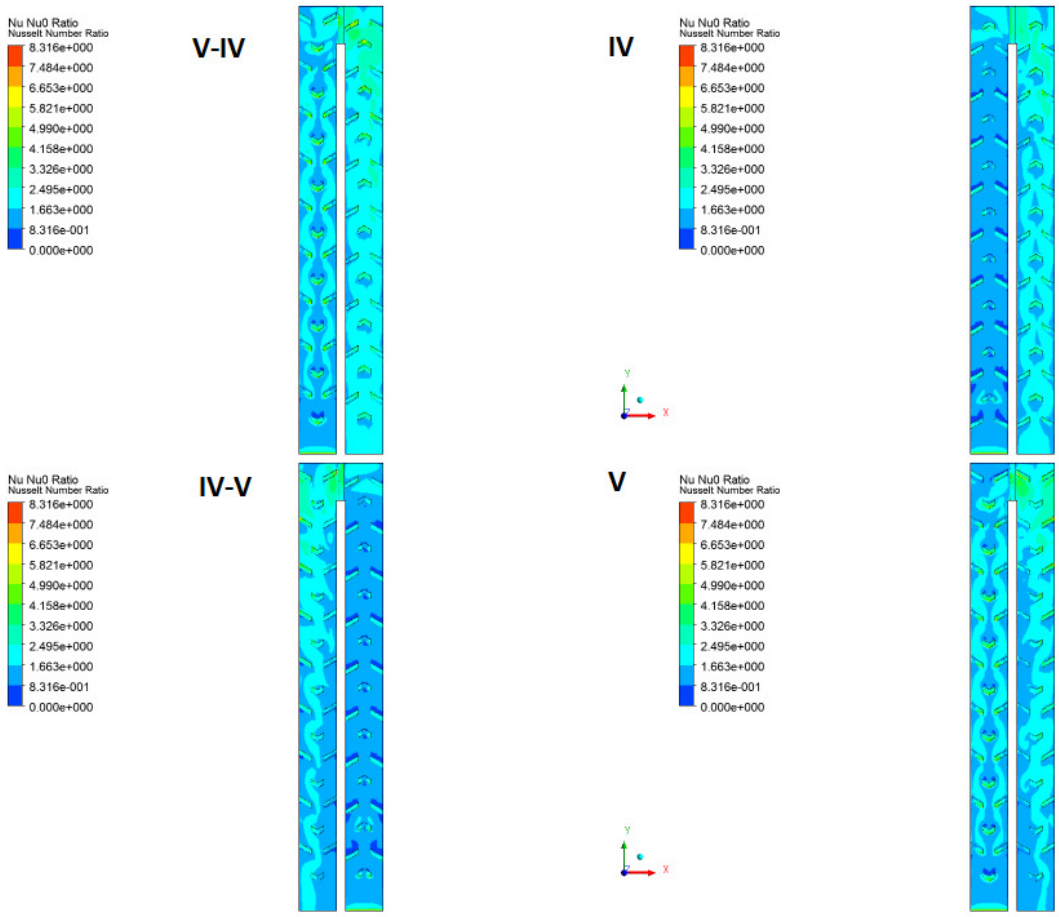

(b)

Figure B.14: Broken Rib (Re=85000, RSM) (a) Surface Nusselt Number along wall (b) Surface Nusselt Number Ratio

Once all the figures are analyzed, conclusion can be clearly drawn that for all the cases and for both the models. The surface Nusselt numbers are higher in the case when the V is pointing upstream. This is because of the secondary flow developed due to V ribs. Again in the turn section for all the cases, because of turning effect and very large swirling of flow, there is an increase in Nusselt Number. It can also be seen that surface Nusselt number increases as the Reynolds number increases. The figure below shows a complete demonstration for all the Broken and Continuous rib results for different

Reynolds Number. The main aim to demonstrate that for all the cases considered, the V-IV for both Continuous as well as Broken produces best heat transfer.

B.3: Results and Discussion: Nusselt Number ratio

A. Broken Ribs:

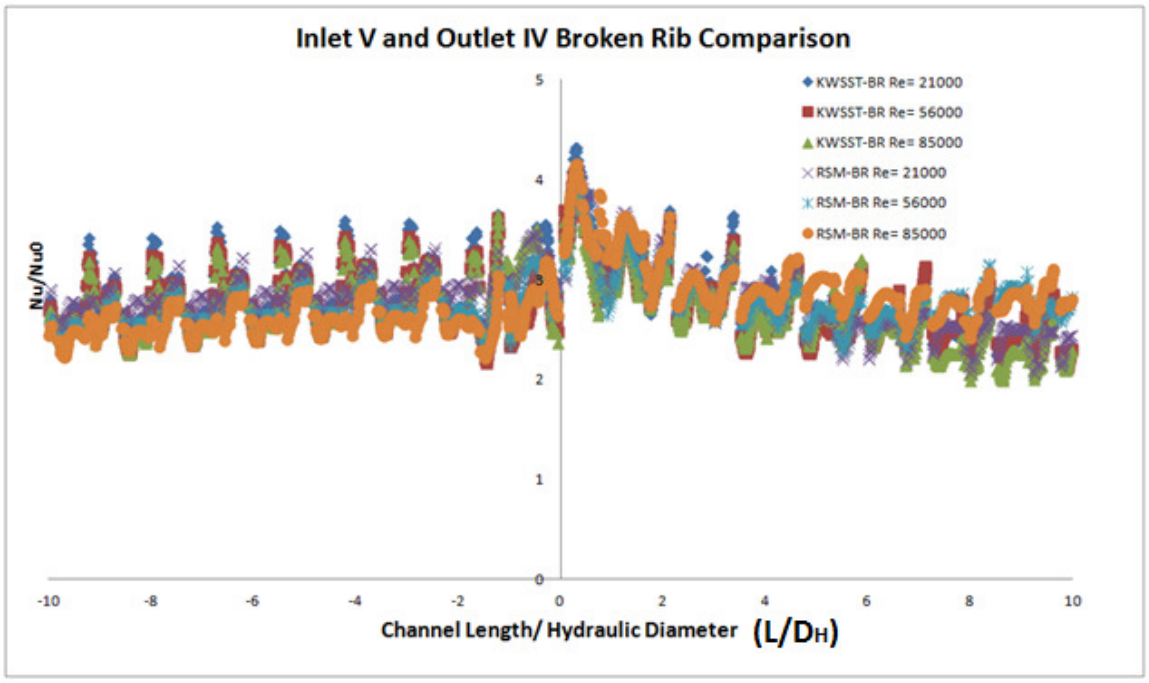

Figure B.15: Broken Rib V-IV for *k*-ω SST and RSM model

Figure B.15 to B.18 show the Nusselt Number ratio throughout the channel starting from inlet which is represented as negative on the x-axis to the second pass of the channel represented on the positive x-axis. -2 to 2 is considered as turn region of the channel. These figures show the spanwise averaged Nusselt Number distribution for each of the four configurations of broken rib case.

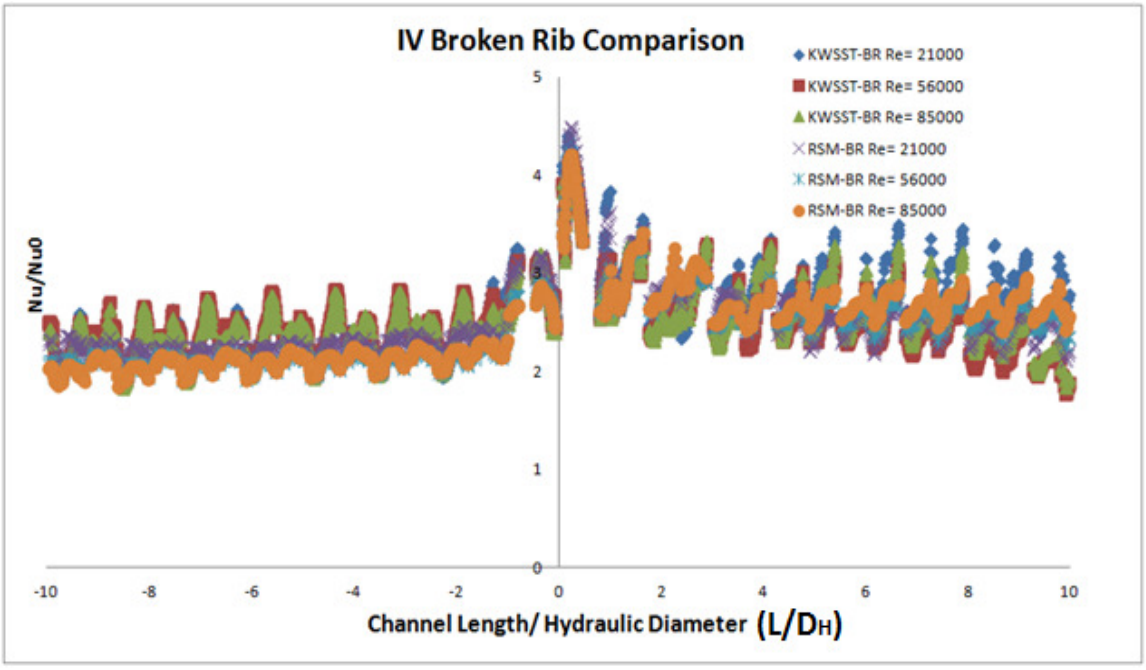

Figure B.16: Broken Rib IV for *k-ω* SST and RSM model

In Fig. B.15, Nusselt Number ratios for both the turbulence models are compared. As can be seen in this figure, the ratio changes periodically or spikes throughout the inlet section; which is because of the ribs present in the section .There are two spikes seen, each due to the two broken parts of the rib. The numerical results overall is able to predict the phenomenon of heat transfer throughout the channel. The numerical simulation replicates the experimental result by showing the inverse relationship between Reynolds Number and the Nusselt Number ratio for all the rib configurations. The Nusselt Number is highly affected by the presence of rib orientation along the flow; when V ribs are towards the flow the ratio is on the higher side as compared to when V is pointed opposite to the flow.

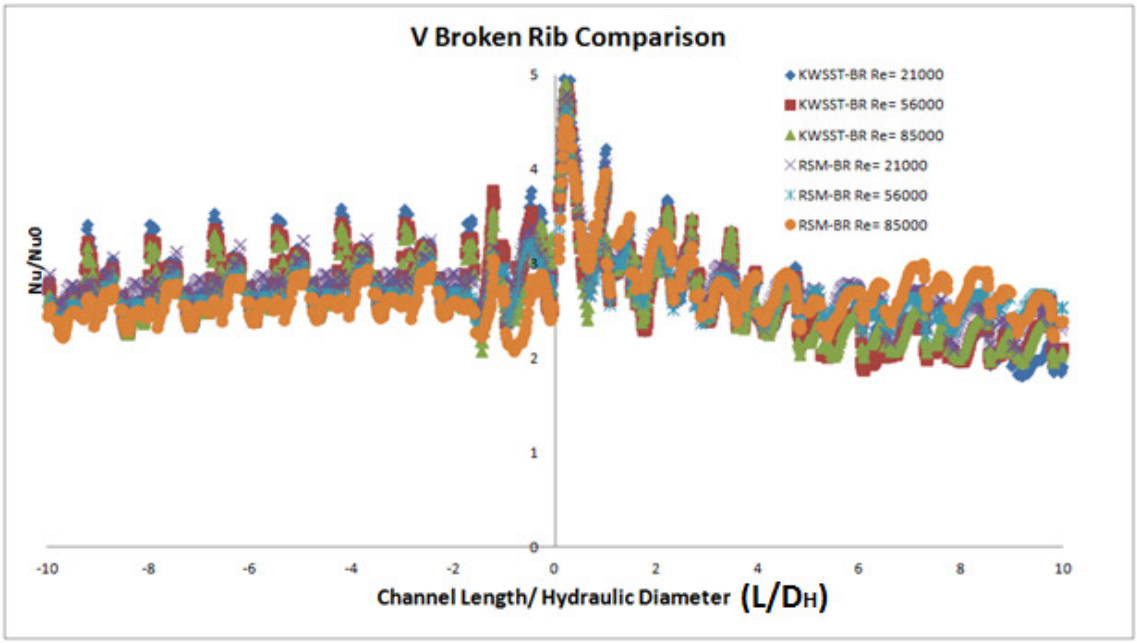

Figure B.17: Broken Rib V for *k*-ω SST and RSM model

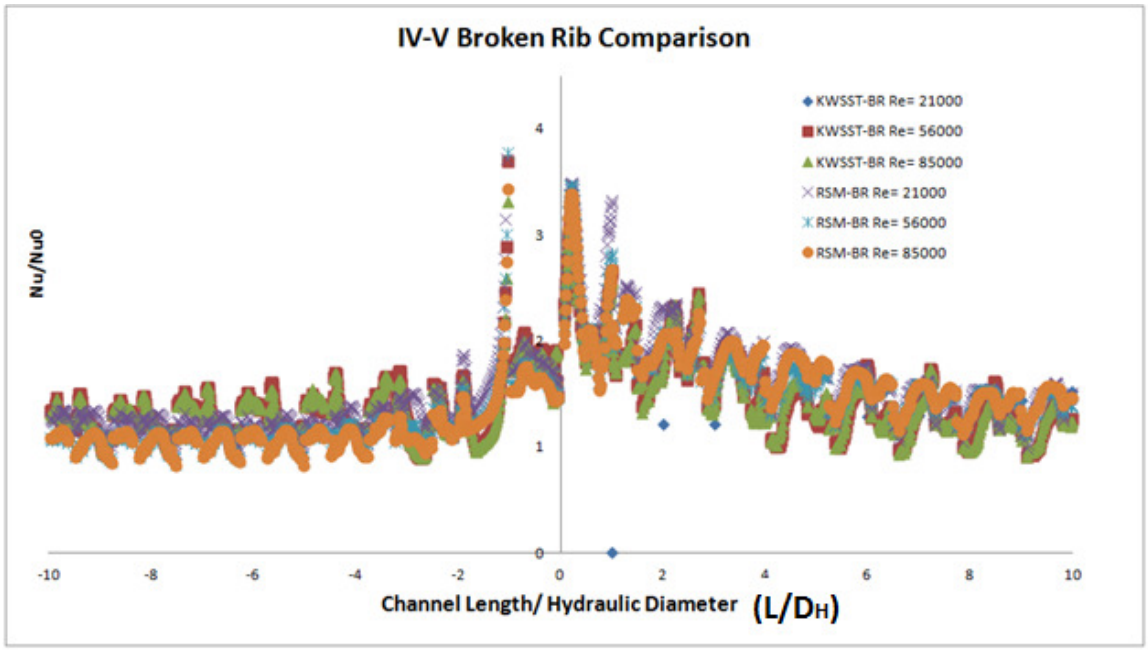

Figure B.18: Broken Rib IV-V for *k*-ω SST and RSM model

Again, in the turn region the value goes up because of the turn effect and the presence of ribs. This turning effect is reduced after a certain distance along the flow.

Overall, the heat transfer enhancement is more around the ribs and the variation is consistent along the flow.

B. Continuous Ribs:

Figures B.19 to B.22 show the Nusselt Number ratio throughout the channel starting from inlet of the channel (represented as negative on the x-axis) to second pass of the channel (represented on the positive x-axis). -2 to 2 is considered as turn region of the channel. These figures show the spanwise averaged Nusselt Number distributions for each of the four configurations of continuous rib case.

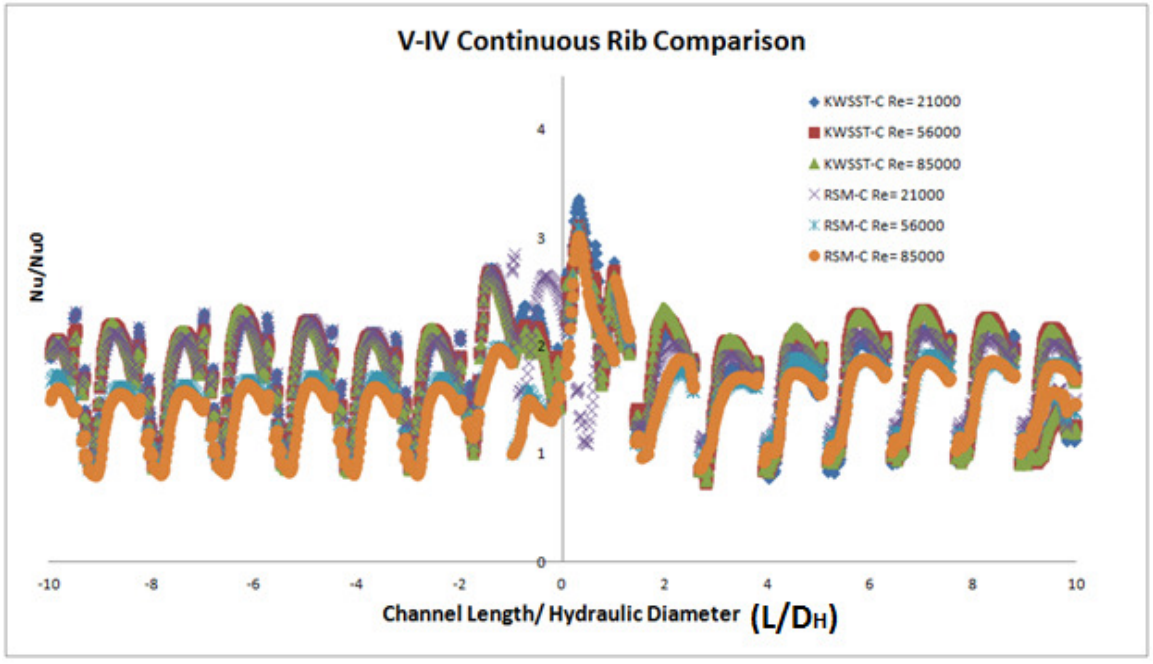

Figure B.19: Continuous Rib V-IV for *k-ω* SST and RSM model

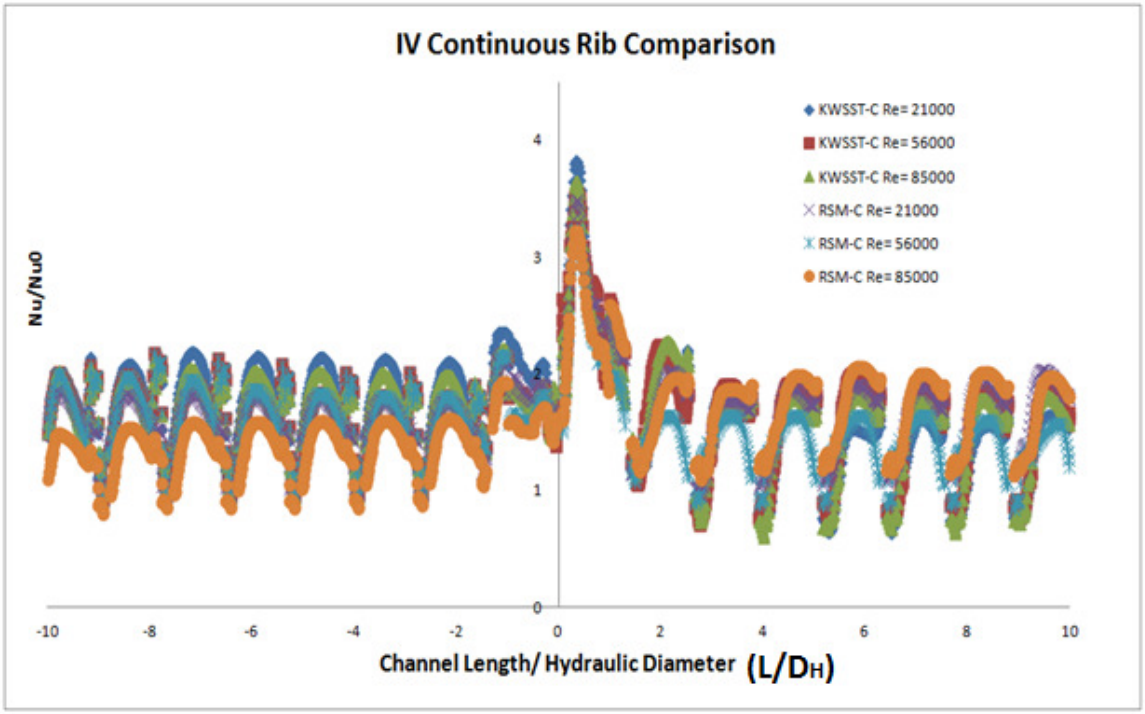

Figure B.20: Continuous Rib IV for *k-ω* SST and RSM model

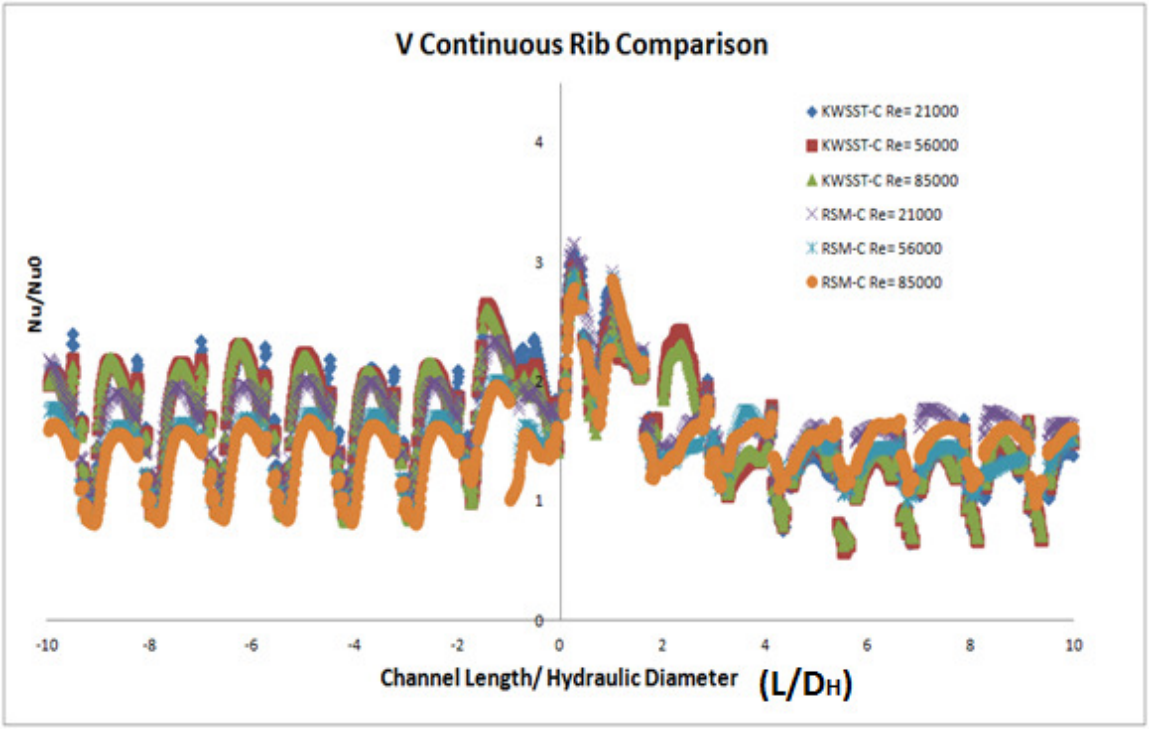

Figure B.21: Continuous Rib V for *k-ω* SST and RSM model

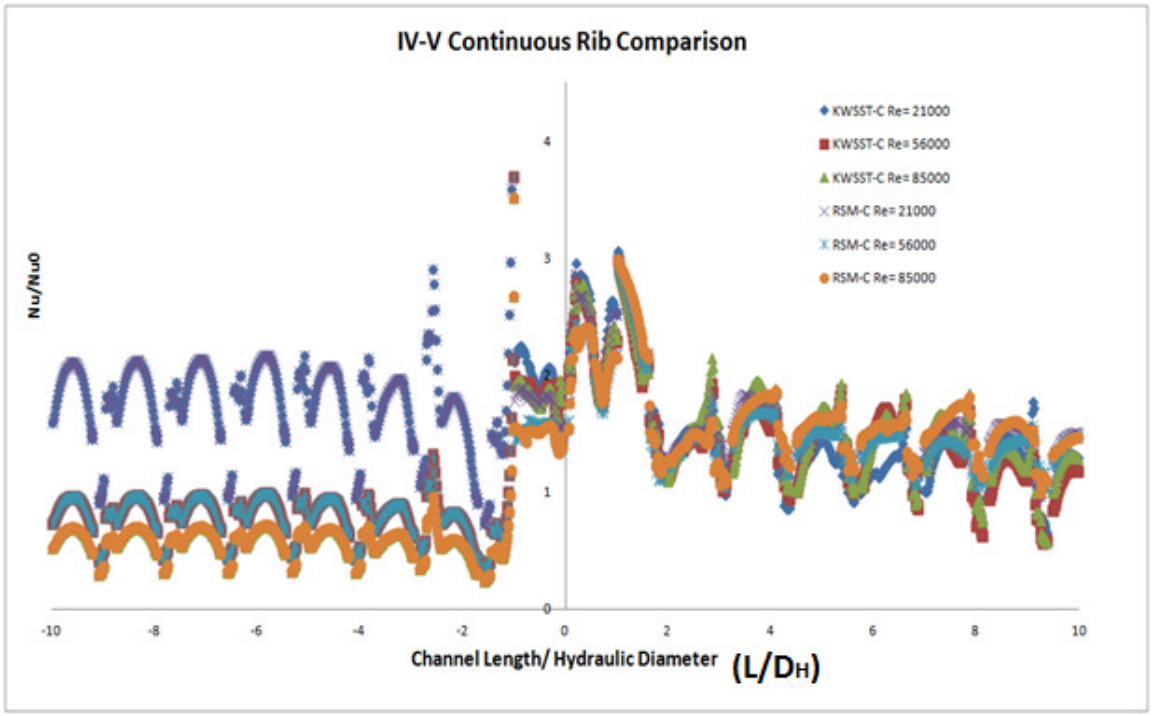

Figure B.22: Continuous Rib IV-V for *k*-ω SST and RSM model

In these figures, Nusselt Number ratios for both the turbulence models are compared. As can be seen, throughout the inlet section, the ratio changes periodically or spikes because of the presence of ribs along the flow. In case of continuous ribs, there is a small spike in between. The numerical result is able to predict the phenomenon of heat transfer throughout the channel. Again, same inverse correlation between Reynolds Number and Nusselt Number Ratio can be observed as in the case of experimental results. The Nusselt Number is highly affected by the presence of rib orientation along the flow. When V ribs are towards the flow, the ratio is on the higher side as compared to when V is pointed away from the flow. Again, in the turn region the value goes up because of the turn effect and the presence of ribs. This turning effect is reduced after a certain distance along the flow. Overall, the heat transfer enhancement is more around the ribs and the variation is consistent along the flow.

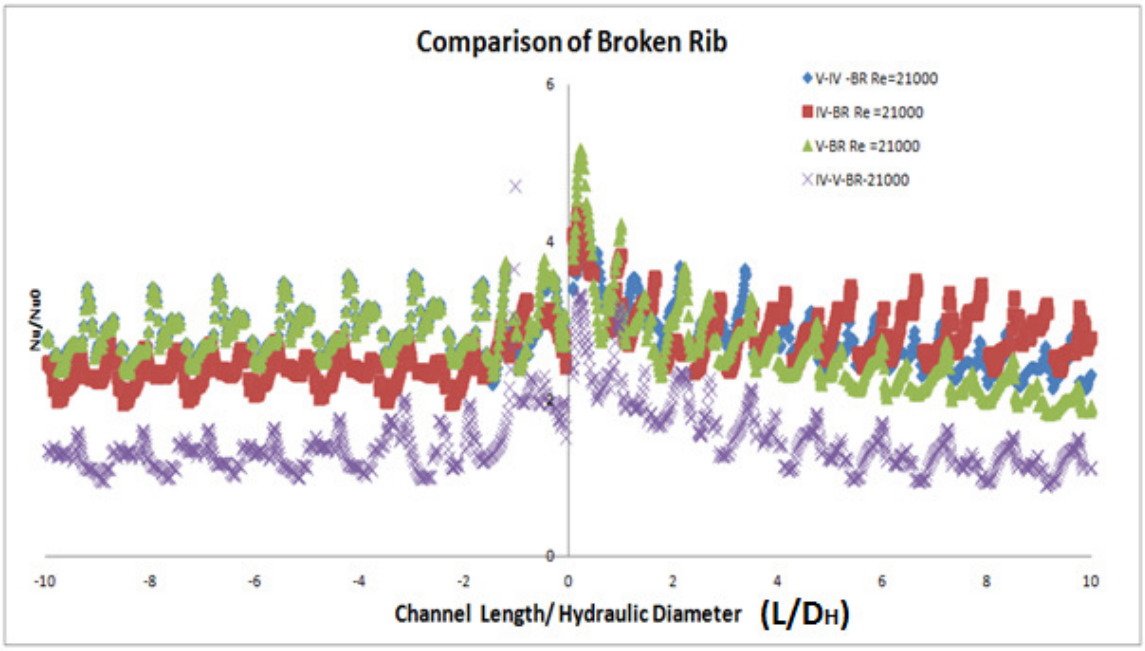

Figure B.23: Broken Rib *k*-ω SST for all the rib arrangement

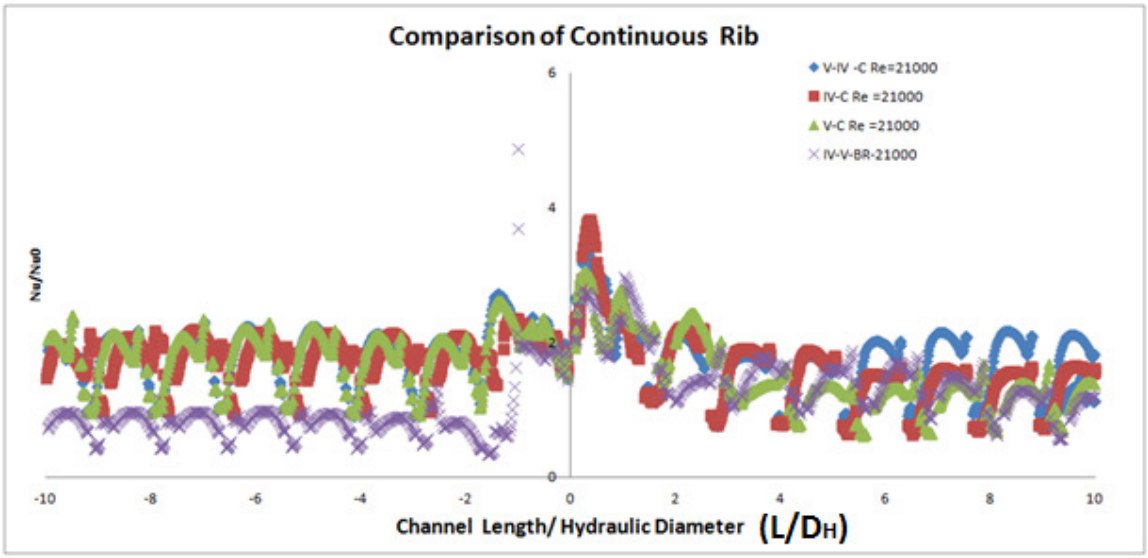

Figure B.24: Broken Rib *k*-ω SST for all the rib arrangement

Figures B.23 and B.24 show, comparison of broken and continuous ribs for Reynolds Number of 21,000. The figure shows that throughout the channel, there is variation in Nusselt Number, the highest increase or enhancement being in V-IV case. This is because

of location of the ribs in upstream. To further prove that the V-IV ribs are the best available configuration, comparative results are presented in chapter 6.

CURRICULUM VITA

Sourabh Kumar

Education:

B.E (Bachelor of Engineering), Bangalore Institute Of Technology
Major: Mechanical Engineering

M.S (Master Of Science), University Of Wisconsin-Milwaukee, 2009
Major: Mechanical Engineering

PhD, University Of Wisconsin-Milwaukee, Dec. 2012
Major: Mechanical Engineering

Work Experience:

Senior Engineer (Production Department), VAFS Pvt. Ltd.
Jan 2003- June 2007

Affiliation/ Membership: AIAA/ASME

Dissertation Title:

INVESTIGATION OF HEAT TRANSFER AND FLOW USING RIBS WITHIN GAS TURBINE BLADE COOLING PASSAGE: EXPERIMENTAL AND HYBRID LES/RANS MODELING

Journal Publications:

1. Modeling of energy usage for refining of ethanol from corn, International Journal of Sustainable Energy, **Sourabh Kumar**, Dr. John R Reisel, June 2010.

2. Numerical prediction of heat transfer distribution of a two-pass square channel with V-rib turbulator and Bleed Holes, Heat and Mass Transfer, **Sourabh Kumar**, Krishna Guntur and Dr R.S Amano, 2012 (Submitted).

Conference Publications: (more than 10)

1. Internal Cooling of two pass gas turbine blades channel with 90 degree rib with varying height. **Sourabh Kumar** and Dr. R. S Amano. IMECE 2012.

2. Experimental and Numerical Evaluation of Geometric Modifications in Gas Turbine Blade Cooling Channel. **Sourabh Kumar**, Krishna S Guntur & R.S. Amano, ASM 2012.